ISBN 978-82-471-1479-7 (printed ver.)
ISBN 978-82-471-1480-3 (electronic ver.)
ISSN 1503-8181

Doctoral theses at NTNU, 2009:53

Trygve Kristiansen

Two-Dimensional Numerical and Experimental Studies of Piston-mode Resonance

Trygve Kristiansen
Doctoral Thesis

NTNU
Norwegian University of
Science and Technology

Doctoral theses at NTNU, 2009:53

NTNU

NTNU
Norwegian University of
Science and Technology
Thesis for the degree of
philosophiae doctor
Faculty of Engineering and Technology
Department of Marine Technology

NTNU
Norwegian University of
Science and Technology

Trygve Kristiansen

Two-Dimensional Numerical and Experimental Studies of Piston-mode Resonance

Thesis for the degree of philosophiae doctor

Trondheim, April 2009

Norwegian University of
Science and Technology
Faculty of Engineering and Technology
Department of Marine Technology

NTNU
Norwegian University of
Science and Technology

NTNU
Norwegian University of Science and Technology

Thesis for the degree of philosophiae doctor

Faculty of Engineering and Technology
Department of Marine Technology

ISBN 978-82-471-1479-7 (printed ver.)
ISBN 978-82-471-1480-3 (electronic ver.)
ISSN 1503-8181

Doctoral Theses at NTNU, 2009:53

Printed by Tapir Uttrykk

Acknowledgements

This work has been carried out under the supervision of Professor Odd M. Faltinsen at the Centre for Ships and Ocean Structures (CeSOS) / Department of Marine Hydrodynamics, Norwegian University of Science and Technology (NTNU). I want to thank him for his excellent supervision during the present PhD study. His guidance and suggestions have been most appreciated, and the present work would not have been possible without these.

The major part of work has been financed by the Centre for Ships and Ocean Structures (CeSOS). My employer, Marintek, has also partly contributed. I would like to thank Marintek for giving me leave of absence for this study.

I would also like to thank all my fellow students and the staff at the department for providing an inspirational environment during the work. In particular this goes to my room-mate David Kristiansen. The collaboration with him during the first year of studying courses was most valuable. Later, he has been continuously involved in my work through discussions and by providing suggestions. Also my second room-mate Eivind Ruth and also Bjørn Christian Abrahamsen have contributed in terms of interesting discussions. Also Professor Marilena Greco has provided important suggestions during the work. Karl Gunnar Aarsæther and Csaba Pakozdi have been key persons regarding the computer setup needed for all the numerical simulations.

The following persons are acknowledged for proof-reading: Jan Roger Hoff for proof-reading the whole thesis, and Linlin Jiao, David Kristiansen, Bjørn Christian Abrahamsen and Rolf Baarholm for proof-reading parts of the thesis.

My love and gratitude go to my wife, Stina, for her continuous encouragement and appreciable patience. I must also thank my now six months old son, Torstein, for sleeping most of the night during the last stages of my PhD work.

Abstract

When a ship is moored alongside a terminal, the ship and the fluid entrained in between the ship and the terminal may both experience large motion. The large motion occur at the resonance frequency of the coupled ship and piston-mode motion. Large ship motions induce significant wave frequency forces in moorings and fenders, while large piston-mode amplitude causes large drift forces. Linear theory in general over-predict the resonant ship and fluid motions rather severely. For example, if in reality the piston-mode amplitude is found to be five times that of the incoming wave, linear theory may typically predict a factor of ten - twenty, or even more.

It is with this discrepancy between linear theory and that observed in reality we are mainly concerned in the present work. The possible candidates explaining the discrepancy are probably (1) effects due to the nonlinear free-surface conditions, (2) flow separation and (3) boundary layer effects. We investigate these three candidates with special attention to the flow separation from the bilges of the ship. We limit ourselves to a two-dimensional setting. A two-dimensional ship section will resemble the mid-ship section of a long ship in beam sea waves.

Our work is mainly of numerical and experimental character. We assume potential flow and implement a linear numerical wavetank as well as a fully nonlinear numerical wavetank. Both wavetanks are implemented in the time-domain. We use the Boundary Element Method (BEM), and employ the Mixed Eulerian-Lagrangian (MEL) formalism. Flow separation is modelled in the nonlinear numerical wavetank by an inviscid vortex tracking method where a thin free shear layer is evolved. The in- and out-flow of the boundary layers is modelled in the linear wavetank by a semi-analytical method involving a convolution integral. Two-dimensional physical model tests are carried out as well.

The free shear layer will become entangled if not continuously simplified. An algorithm for automatic simplifications is developed and implemented. The simplification procedure is found necessary for long-time simulations in order to reach steady-state. By long-time we here mean typically 20 - 50 wave periods or more. The simulations will break down after about one single wave period if the simplifications are not carried out.

We consider both a fixed ship section, forced motion of a ship section and a ship section that is free to oscillate in sway, heave and roll. In the last case the coupled fluid- and body-motion is solved. To overcome the problem that the φ_t term in the Bernoulli equation is not defined in the MEL approach when the boundaries are moving (nonlinear wavetank only), an alternative formulation of the force where the time derivative is moved outside the integral is derived and implemented in the nonlinear numerical wavetank.

Results from numerical simulations are compared to experimental results. Three main studies are carried out, including a fixed ship section in incoming waves, a ship section in forced motion and a moored ship section oscillating in incoming waves. The influence

of geometric parameters like the distance between the ship and the terminal and the water depth as well as wave steepness is investigated. The linear simulations over-predict the piston-mode motion by about 30 - 300% in the considered cases. Qualitatively, the ship motion is over-predicted by an equal amount. The nonlinear wavetank without flow separation show the same over-predicting trends. Exceptions are in shallow water waves, where our results are somewhat inconclusive. The results from simulations by the nonlinear wavetank including flow separation from the ship bilges do on the other hand compare well with the experimental results. Our work hence strongly suggests that flow separation from the ship bilges is found to cause the majority of the discrepancy, and this serves also as a validation of our numerical work. The effect from the boundary layer flow is found negligible to all purposes.

The present study has direct relevance also to other problems within marine hydrodynamics that inhibit gap resonances, such as moonpools, multi-hull vessels or two ships in side-by-side configuration.

Nomenclature

General rules

- Only the most used symbols are listed in the following sections
- Meaning of symbols given at least when introduced in the thesis
- Sometimes the same symbol is used to indicate different quantities
- Vectors are represented by bold-face letters

Subscripts

n	Normal derivative, or natural period
s	Tangential derivative
0	Deep water limit

Roman Letters

A	Amplitude of incoming, undisturbed wave ($A = H/2$)
A_g	Piston mode amplitude, amplitude in terminal gap ($A_g = H_g/2$)
b	Distance from ship section to terminal (terminal gap width)
B	Ship section beam (also called ship breadth)
C_g	Group velocity
d	Clearance from ship bottom to sea floor
D	Ship section draft
F_x, F_y	Horizontal and vertical force in inertial frame
g	Acceleration of gravity ($g = 9.81\mathrm{m/s}^2$)
h	Water depth
H	Wave height
H_g	Piston mode crest to trough height
$\mathcal{I}$	Roll moment of inertia
KC	Keulegan-Carpenter number (defined where it appears)
m	Ship section mass

$\mathcal{M}$	Roll moment
p	Pressure
r	Radius of curvature, or distance from field point to position of singularity
Rn	Reynolds number (defined where it appears)
s	Arc length along a boundary
S	Boundary of closed domain of numerical wavetank
S_B	Boundary of ship section
S_F	Boundary of free surface
S_V	The free shear layer
t	Time
T	Wave period of regular wave
T_n	Natural period of coupled ship and piston mode motion
T_p	Natural period of piston mode
U_s	Shedding velocity just outside boundary layer
x, y	Horizontal and vertical axes of inertial frame
x_G, y_G	Horizontal and vertical coordinates of center of gravity

Bold Roman Letters

$\mathbf{n}$	Unit normal vector
$\mathbf{s}$	Unit tangential vector
$\boldsymbol{U_c}$	Velociy of the free shear layer
$\mathbf{x}$	Field point (x, y) in two-dimensional space
$\mathbf{x}_G$	Center of gravity, i.e. (x_G, y_G)
$\mathbf{x}_v$	Position (parametrized by s) of the free shear layer

Greek Letters

α	Internal angle along the boundary S, or cumulative angle between free shear layer elements
β	Parameter in cosine squared distribitution of elements, or angle between two free shear layer elements
Γ	Circulation
η_j	Ship section motion in j'th degree of freedom
λ	Wavelength
φ	Velocity potential
ρ	Fluid density
θ	Roll angle of ship section
ζ	Free surface elevation
ω	Wave frequency (rad/s)
Ω	Computational domain

Contents

Chapter 1

Introduction

Gap resonances are resonant fluid motion within semi-entrained vertical gaps between two or more structures or within one structure defining a gap of some sort. Considerable vertically oscillating fluid motion may occur in such gaps under forcing at particular frequencies. Typical examples where vertical gaps are introduced within marine hydrodynamics are moonpools, multi-hull vessels, two ships in side-by-side configuration and a ship alongside a terminal. In the two latter cases, large ship motions and not only large fluid motion is associated with the resonance problem.

The gap resonances are what we consider external resonance problems and differ from the internal resonance problem, i.e. sloshing, in that the fluid within the gap communicates with the outer, or external, flow. The consequence is that liquid volume conservation is satisfied in sloshing, while this is in general not true for the gap problem. The latter fact allows for a piston-mode resonance in the gap problem, which is not present in the sloshing problem.

Linear potential flow theory predicts infinite fluid motions in the sloshing problem. In the gap resonance problem, except in some rare cases called wave trapping, the communication allows for outgoing waves. This introduces potential flow damping. In gap resonance problems the fluid motion hence remains finite at resonance even within linear theory.

However, although present, the potential flow damping may be very small in gap resonance problems, and the response near the resonance frequency is often highly over-predicted by linear theory relative to that observed in reality. The over-prediction by linear theory poses a practical problem when analyzing this kind of problems using e.g. a three-dimensional linear frequency domain code. Sharp spikes occur in the response curves that are not associated with irregular frequencies which are of mathematical character, but rather existing physical resonance frequencies of the system. The level of response predicted by linear theory at these frequencies may be several times that observed in reality.

Although not as drastic as that predicted by linear theory, the ship and water motions may still be large in reality. It is therefore of interest to be able to predict the level of response correctly, something linear theory fails to do. The two main possible candidates causing the discrepancies are (a) effects associated with the nonlinear free-surface conditions and (b) viscous effects. Postulations that viscous effects provide damping and thereby explain the discrepancies have been made in the literature. The problem was investigated by means of a Navier-Stokes solver by Maisondieu et al. (2001), but to the

Figure 1.1: Illustration of planned Gravity Based Structure (GBS) type offshore Liquefied Natural Gas (LNG) terminal. Actual site: Port Pelican, coast of Louisiana in Gulf of Mexico (ChevronTexaxo). Water depth $h = 25$m, distance from land 50km, GBS dimensions 364m $\times$ 89m $\times$ 57m and storage capacity 330.000m^3. The capacity of the LNG carriers is at the present time typically up to 140.000m^3 and typical dimensions are $L \times B \times D = 300\text{m} \times 45\text{m} \times 12\text{m}$, where L is length, B the beam and D the draft. The LNG is first off-loaded to the terminal where re-gasified and transported to land by pipelines.

author's knowledge the postulations have not explicitly been investigated in other works.

This is what we investigate in detail in the present work. Within the framework of potential flow theory, we investigate the effect of flow separation from the bilges of the ship on the resonant behaviour of a ship alongside a terminal by means of time-domain numerical wavetanks based on the boundary element method including an inviscid vortex tracking method.

1.1 Offshore LNG terminals - Challenges

Through increased focus on risk regarding the off-loading of Liquefied Natural Gas (LNG) from LNG carriers to terminals traditionally located within harbors, there has recently evolved a trend of moving LNG terminals offshore, say 10 - 50 km from land. The carriers off-load their cargo to the terminals where the LNG is re-gasified and transported to land by pipelines. The situation is illustrated in Figure 1.1, where the terminal dimensions and particulars of the site are given. This particular terminal is of Gravity Based Structure (GBS) type, the type used in water depths h of $h \simeq 15 - 30$m. At larger depths, fixed platform systems involving jacket type installations are used for water depths of $h \simeq 30 - 100$m, and floating systems at water depths $h \gtrsim 100$m.

Along the US coast, sixteen offshore terminals were projected by mid 2007 (cf. Maritime Administration (2007)). Some projects have apparently been withdrawn due to high economical costs. The Port Pelican depicted in Figure 1.1 is among those put on hold for this reason. Several projects are also planned in Japan and Europe, where one, the

Figure 1.2: The North Adriatic LNG terminal tested at MARINTEK.

so-called North Adriatic LNG terminal off the coast of Italy has recently been installed. A photo from model tests of this terminal performed at MARINTEK is shown in Figure 1.2.

Aside from a risk perspective, the concept of offshore terminals offer additional advantages such as reducing port congestion as well as accommodation of larger LNG vessels. Due to the increasing activity in LNG transportation using vessels of increasing size these matters inspire the utilization of the offshore areas for LNG terminals.

However, along with the advantages there are also challenges associated with moving offshore. Intuitively there is an issue with the environmental loads experienced at such unsheltered areas relative to those in harbors, introducing concerns about available operational time. The duration of an off-loading is typically 12 - 24 hours. The system will be exposed to wind, current and waves.

In the present work we consider the hydrodynamic problem, and more specifically, the wave-structure interaction of relevance for an LNG carrier alongside a GBS type offshore terminal as those shown in Figures 1.1 and 1.2.

The terminal introduces a fixed vertical wall extending from the sea floor and thereby a vertical gap between itself and the ship. Hence the system is prone to gap resonances.

Around resonance the ship may experience resonant motion in all six degrees of freedom. Vertical motions, including both pitch and roll in addition to heave, then may become an issue with respect to contact with the sea floor due to the small bottom clearance.

Large forces exerted on the moorings and fenders is yet another concern. The fenders and moorings exhibit nonlinear characteristics. These are in general designed such as to withstand drift and slowly varying forces and not the first order ship motions. However, large first order fluid motions in the gap between the ship and the terminal introduce large drift forces.

Large vertical fluid motions in the gap also involves hazards in relation to the actual operation of off-loading. One may in severe cases experience damage of the structures involved in the off-loading by the large water motion.

In addition to the gap resonances there are also issues regarding shallow water wave aspects given the relatively small water depths. Waves of periods $T \gtrsim 10$s - 14s entering the terminal area of water depths of $h \simeq 15 - 30$m are true shallow water waves, with their associated nonlinear behaviour and complexity of modelling. Further, a consequence

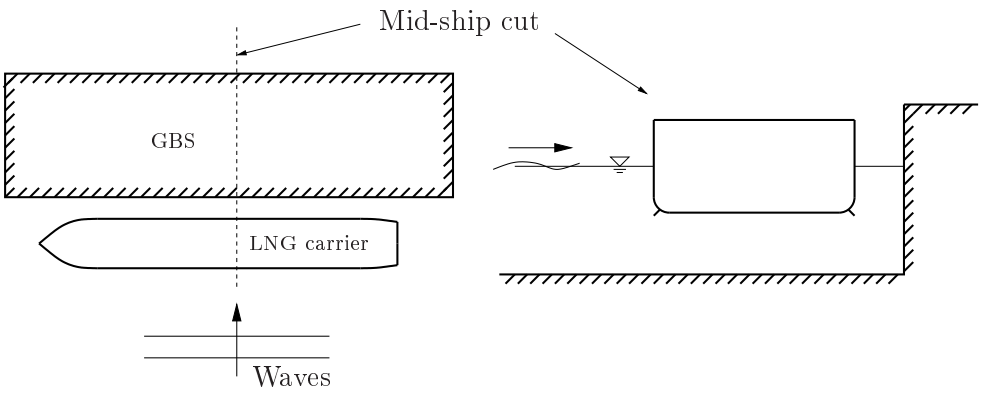

Figure 1.3: The hydrodynamic problem of an LNG ship alongside a terminal is in principal three-dimensional (left). In the present work we consider a mid-ship cut and beam sea waves. We restrict ourselves to a two-dimensional approach as illustrated to the right.

of shallow water is small bottom clearance of the ship. Although the main focus of the present work is on the damping effect of flow separation from the ship bilge keels, we also investigate to a certain extent the behaviour of a the system in shallow water waves.

1.1.1 Scope and limitations of the present work

In the present work we limit ourselves to long-crested, beam sea waves and no current or wind. Since the longitudinal dimensions of the problem is rather large relative to the lateral dimensions, and with the restriction of beam sea waves we may to a certain extent allow for a two-dimensional approach. This corresponds to an infinitely long ship and terminal and is a reasonable approximation regarding the mid-ship cut. We will throughout the text refer to the two-dimensional setting illustrated in the right part of Figure 1.3 as a "ship section by a bottom mounted terminal". We restrict our work to such a two-dimensional setting. We consider rigid body motions in sway, heave and roll. The three-dimensional fluid flow related to the longitudinal ends of the structures are hence not investigated in the present work, nor are the surge, pitch or yaw motions of the ship.

A motivation for a two-dimensional study is that it more easily than a three-dimensional study allows for detailed and controlled numerical and experimental studies of the physics of the problem.

Throughout our work we shall denote the gap between the ship and terminal by the "terminal gap". Within the terminal gap the free surface may undergo resonant motion of any mode. The zeroth mode, being the massive bulk of fluid in the terminal gap oscillating with a flat free surface, is often referred to as the piston mode. We shall concern ourselves with the piston mode, and do not consider resonance of the higher modes, i.e. the sloshing inside the terminal gap. This means we consider wave frequencies away from the sloshing frequencies. Although pure piston-mode motion will in general not exist, as in reality also some disturbance of the free surface will inevitably occur, we will most often denote the near piston-mode motion simply by piston-mode motion.

We will refer to *piston-mode resonance* as well as *coupled ship and piston-mode resonance*. If two-dimensional linear potential flow theory is considered, piston-mode reso-

nance is associated with peaks in the piston-mode amplitude in the diffraction or radiation problem, that is, for fixed ship section or forced motion of the ship section. Coupled ship and piston-mode resonance is the coupled resonant motion of the ship section and piston-mode when the ship is free to oscillate and associated with peaks in the ship motion amplitude. These resonance frequencies are in general different.

Our work is carried out within the framework of potential flow theory of an incompressible fluid. We assume the water to be inviscid outside boundary and free-shear layers. Viscous effects are, however, modelled. We model flow separation from sharp corners as well as the in- and out-flow of viscous boundary layers. Vorticity is then introduced, but assumed to be limited to thin free shear layers within the water or in thin boundary layers. The flow in the main bulk of the water is hence irrotational. We solve the Laplace equation under the restraint of the usual boundary conditions, both linearized and fully nonlinear. Two time-domain numerical wavetanks are implemented, one linear wavetank and one fully nonlinear wavetank. Both are based on a Boundary Element Method (BEM) and within the Mixed Eulerian Lagrangian (MEL) framework.

Flow separation is modelled by an inviscid vortex tracking method. In order to reach steady-state conditions, an automatic simplification algorithm for the free shear layer is developed and implemented. There are certainly limitations associated with the inviscid vortex tracking method and the presently developed simplification procedure, but it has proved useful in our work regarding accurate predictions of the effect of flow separation.

Integration of the equations of motion need special treatment in the nonlinear wavetank. We assume slip conditions. The sway and heave forces as well as roll moment are obtained by integration of the pressure given by Bernoulli's equation over the ship section. However, in the Mixed Eulerian-Lagrangian approach we have adopted, the time-derivative of the velocity potential, φ_t, in Bernoulli's equation is not defined over the ship section when this is moving. To overcome this problem, an alternative formulation of the force and moments are derived and implemented in this work.

1.2 Previous related work

The problem of a ship by an offshore terminal in shallow water was treated by Buchner et al. (2001). Their study was three-dimensional and within linear theory. Calculated drift forces about four times that observed in corresponding model tests were predicted for frequencies near gap resonance. The discrepancy was remedied by applying a numerical damping lid on the free surface in the gap. The damping coefficient of the numerical lid was tuned using the model test results, with improved correspondence between simulations and model tests as a result. Similar works are reported in Buchner et al. (2004) and Buchner et al. (2004), where also significant run-up on the ship was observed due to nonlinearity introduced by the shallow water. Pauw et al. (2007) considered two ships in a side-by-side arrangement with emphasis on the effect on linear versus second order quantities when tuning the damping parameter of the numerical lid. They recommended that the damping parameter be tuned in such a way that the drift forces are optimal rather than the linear quantities.

The numerical lid approach as used in these works is explained in Huijsmans et al. (2001). The damping is achieved using the same approach as for removing irregular frequencies. While irregular frequencies are of pure mathematical character appearing

as a consequence of artificial internal resonance problems associated with the structures involved, the gap resonances are physical. In that regard the empirical damping lid approach is perhaps somewhat questionable, as it does not reflect the physics. Since the model requires experimental input, its practical usefulness in studying new concepts without doing model tests is limited. Similar numerical damping lid approaches have also been used by Newman (2004), Newman and Lee (2005) and Chen (2005).

Practical problems for engineering purposes associated with gap resonances are discussed by Pinto et al. (2008) for moored ships in harbors. A moored ship in harbor was also studied by Bingham (2000) where he introduces a hybrid method coupling two established methods; a time-domain method based on Boussinesq type equations for propagating waves from deeper waters and into the shallow waters of the harbor, and a linear frequency domain panel method for the wave-structure interaction. The latter uses the wave spectrum at the position of the ship given by the Boussinesq model as input, assuming these are free waves. Bingham argues that sub-harmonics are generated as waves propagate over a sloping sea floor, and these become important with respect to the excitation of resonant ship motions, and should therefore be carefully modelled. This is achieved fairly well with the Boussinesq model as the method shows promising results in comparison with model tests. The used Boussinesq model is well documented in Madsen, Bingham, and Hua (2002) and previous work cited therein. We note that since nonlinearities in the incoming wave field is important, we expect similar nonlinear interaction between the ship generated waves and the incoming waves. This is not modelled in the hybrid model by Bingham (2000). Bingham also mentions that in constricted waters as in a harbour, seiching, the resonant fluid motion associated with the basin, may also induce resonant ship motions. In the present case there is no harbour. The modelling of the incoming waves by e.g. a Boussinesq model would nevertheless be applicable also in our case when considering the transformation of the waves when entering the associated shallow waters at the offshore terminals.

A review of literature related to gap resonances, inviscid vortex tracking methods and force calculations in the nonlinear numerical wavetanks follows.

Gap resonances. Molin (2001) studied, within linear potential flow theory, the eigenvalue problem for gap flows. Infinite water depth was assumed. A simplified, quasi-analytical approach to calculate approximately the resonance frequencies for the piston-mode as well as the sloshing modes in rectangular moonpools was presented. Also the corresponding shapes of the sloshing modes were calculated. The work was both for the two-dimensional (infinitely long moonpool) and three-dimensional case. The effect of beam to draft ratio of the moonpool was considered in particular.

Faltinsen et al. (2007) studied, also within linear potential flow theory, the piston-mode problem in a moonpool in a more exact manner. The work was restricted to the two-dimensional problem, but for arbitrary finite water depth. They followed the strategy of domain decomposition and derived applicable Green functions for the problem along the so-called Neumann traces dividing the different domains. Under forced heave of the two rectangular ship hulls defining the moonpool, they considered both the natural frequency and the amplitude of the piston-mode motion. They defined the natural frequency of the piston mode as that with the largest corresponding piston-mode amplitude after considering forced motion for a range of frequencies. The calculated natural frequencies reported therein were found correct to at least the seventh digit.

McIver (2005) investigated the problem of a freely floating body with a gap of some sort, for instance a moonpool. He considered the radiation and diffraction problems. He denoted by the resonant coupled ship and fluid motion the "motion resonance". He further denoted the resonant fluid motion where the body is fixed or forced to oscillate by the "sloshing resonance". We remark that in his nomenclature, the first sloshing mode is what we in the present denote the piston mode. He showed analytically that the natural frequencies of the coupled fluid and ship motions are in general different from the sloshing frequencies. He also showed that the response near the sloshing resonances (which are for fixed body or forced motion of the body) will be nearly annulled when the ship is free to oscillate. An exception was in case the ship was restrained from oscillating in one or more degrees of freedom. In that case, large fluid motion also at the sloshing frequencies could be attained, although the body is free to oscillate in some degrees of freedom.

An interesting feature of gap resonance is the so-called trapped modes. There exists geometries where under certain conditions resonant fluid motion may occur without radiating waves. The first such was discovered by McIver (1996) - the McIver toroid, and other have been found and studied later. We have not found any evidence that our present problem exhibit wave trapping. This was also the conclusions by Faltinsen et al. (2007) in their investigation of resonant piston-mode motion in moonpools.

Eatock Taylor et al. (2008) generalized the three-dimensional method of Molin (2001) to study the gap resonances of a ship by a terminal by substituting the Neumann conditions with Dirichlet conditions at the longitudinal ends. They compared their approximated theory with results from a linear diffraction code with promising results both in terms of estimation of natural frequencies as well as level of fluid response in the gap. They used the theory to introduce an artificial damping on the frequency response function, in order to investigate the influence of this damping on the ship response due to transient wave trains with peak period around resonance.

Inviscid vortex tracking models. A number of inviscid models for vortex shedding has been developed over the years, falling mainly into two categories characterized by approximating the shed vorticity either by discrete vortices or by a continuous distribution of vorticity. Continuous representation of the free shear layer has the advantage relative to discrete methods that the actual vortex shedding is well defined, and the fine structures of the free shear layer is represented in a more rigorous way. Further, problems associated with the unphysical infinite velocity at the discrete vortex cores are avoided. A disadvantage, however, is the requirement that the whole free shear layer be connected at all times leading to increasingly complicated structures during time evolution in unsteady flow. We shall in the following refer to both the terms *free shear layer* and *vortex sheet* meaning the same thing.

Clements (1973) gives a comprehensive overview of earlier works on discrete vortex methods. We here refer to key points of the evolution for the reader to get acquainted. Perhaps the first to represent a vortex sheet by an array of discrete vortices for numerical purposes was Rosenhead (1932). He examined the so-called Rayleigh instability of an initially perturbed straight line of constant vorticity representing e.g. the layer between two velocities of a stream. The numerical calculations were in that work done by hand. As in all discrete vortex methods, the velocity of each vortex was calculated and the positions stepped forward in time. He was successful in showing perpetual growth of the instabilities also beyond the valid regime of linear theory, with the sheet forming shapes resembling

breaking waves. Later, the calculations were re-done with a finer discretization by Birkhoff and Fisher (1959) and the method was shown to be unstable, considered therein to be due to the higher influence of the unphysical infinite velocities at the center of each vortex in their case of higher resolution. Chorin and Bernard (1973) introduced in this respect a small cut-off near the vortex origin, giving the stream function constant values near the origin and hence avoiding the infinite velocities. They concluded that in any successful application of discrete vortex models such a cut-off or other similar strategy is necessary, otherwise solutions will diverge under increasing resolution. Similar conclusions were made by Clements (1973) where they investigated the roll-up of the end of a vortex sheet.

When considering vortex shedding from a structure using a discrete vortex method, ambiguities arise on where to place a newly shed vortex. This is discussed in several works, see e.g. Sarpkaya (1975). He gives a nice overview of discrete vortex methods with emphasis on the numerical treatment of the Kutta condition. The Kutta condition says that the fluid flow must remain finite at the point of separation, and that it must leave tangentially from the body. The Kutta condition is a matter of observation in physical experiments. During his literature review he found that there were a different numerical treatment of the Kutta condition in almost each publication. The position and strength of each new vortex was different. In most works mapping was used to identify the positions.

For discrete vortex methods there are therefore issues both regarding how to satisfy the Kutta condition rigorously and how to treat the singular behaviour at the vortex cores. However, since these issues have been understood for quite some time, several authors report satisfactory results. Application of a discrete vortex method to a ship heaving with consequent flow separation around the bilge keels is discussed in Soh and Fink (1971).

A continuous vortex method was developed by Faltinsen and Pettersen (1987). They investigated separation from both blunt and sharp edged bodies with emphasis on marine applications. They performed boundary layer calculations to obtain the separation points on the blunt bodies. Dipoles were distributed over the free shear layers which were discretized by piecewise linear elements. Over each free shear layer element a linear variation of the dipole distribution was assumed. We mention that assuming piecewise constant values is similar to a discrete vortex method, as each node connecting two elements will then be like a discrete vortex. A difference is, however, that velocities are calculated on the mid-point of each element in their work, and not at the nodes. The method was used by Braathen (1987) to study roll damping of ships, with satisfactory results reported, and further by Lian (1986) for more general cases. The method was also used by Aarsnes (1984) to study current forces on ships. He considered flow separation from continuously curved surfaces by coupling the global solution to viscous boundary layer calculations in order to determine the separation points. Difficulties occured at the separation points that were remedied by introducing the so-called "triple-deck" method. The entanglement of the free shear layer was in all these works a major issue.

More recently, a higher order representation of the vortex sheet was developed by Jones (2003) and applied to oscillatory flow past sharp edges. He put, like Faltinsen and Pettersen (1987), emphasis on the treatment of the Kutta condition in the unsteady case, giving what he denotes a generalization to that in the well established case of steady flow. The method of Jones was further developed by Shukla and Eldredge (2007) where they investigated the flow separation from a deforming body of prescribed motion, with propulsion from aquatic organisms in mind, with aims at the possible improvement of

propulsion systems. The numerical results were promising showing non-entangled, quite impressive, vortical structures for long time simulations in oscillatory flow. In the works by Jones (2003) and Shukla and Eldredge (2007), there was in addition to the oscillatory flow induced by the body, also a mean steady flow implying that the vorticity was convected away from the body. This considerably simplifies the problem.

Three dimensional vortex sheets have been modelled by Winckelmans and Leonard (1993) and Brady, Leonard, and Pullin (1998). In the former a discrete distribution was applied. In the latter a continuous distribution was used. There, they introduced a length scale cut-off in order to suppress small scale deformations. The suppressions were implemented such as to work in an automatic manner. Their results are in general not compared to measurements, although they compare well in a two-dimensional case of axisymmetric flows. The three-dimensional vortical structures appear by all means reasonable.

Analytically based approaches has also been applied. Faltinsen and Sortland (1987) used a single vortex tracking method, and investigated the drag force on a ship due to separation from the bilge keels of the ship. Downie, Bearman, and Graham (1988) studied roll damping of a ship section. They used a technique where the local solution of the vortex shedding, which was assumed to be localized to the corner of separation, was matched to an outer solution.

We also mention the so-called vortex-in-cell method. Actually, here, the Navier-Stokes equation is the basis, and so it is not an inviscid vortex tracking method. It has, however, the similarity that it tracks the vorticity. One formulate an equation for vortex transportation and use an operator-splitting technique, i.e. the vortices are first convected and next diffused. The Poisson equation for the stream function is solved for. This was used to study the flow separation around two-dimensional finned bodies by Yeung (2002). They also refer to the method as the "vortex blob" or random-vortex method. In Yeung et al. (2008) they used the method to study the three-dimensional problem of yaw moments on a slender body in terms of a strip theory approach.

As far as (attached) boundary layer effects are concerned, Liu and Orfila (2004) modelled the in- and out-flow of boundary layers as boundary conditions on the sea floor in a Boussinesq model in order to study viscous effects on propagating shallow water waves.

Force calculations. The Mixed Eulerian-Lagrangian (MEL) approach is adopted in the present study in order to numerically solve the fully nonlinear potential flow problem. In the Eulerian step the boundary integral equation is solved given the instantaneous potential and geometry. Next, based on the solution from the Eulerian step, the potential on the free surface and geometry of the free surface are stepped forward in time in the Lagrangian step. This allows for solving the problem involving a deforming geometry. The MEL approach was suggested by Ogilvie (1967) in a numerical study on ship resistance and later used by Longuet-Higgins and Cokelet (1976) where they investigated numerically the breaking of waves. Faltinsen (1978) used Ogilvie's ideas in a semi-Lagrangian manner to study numerically the nonlinear problem of a surface-piercing body undergoing forced heave motion. Faltinsen (1978) used the method to also study nonlinear sloshing in tanks. The MEL approach has later been used by many authors e.g. to study waves in wavetanks and their interaction with fixed structures or structures subject to forced motions.

Introducing free body motions, a challenge is introduced in solving the equations of motion. In the nonlinear numerical wavetank the φ_t term in Bernoulli's equation is

not defined at boundaries that evolve, so calculating the force on an oscillating ship by integrating the pressure requires special care. Evaluating φ_t simply by finite differences in time leads inevitably to numerical instability.

To our knowledge three main strategies have been adopted to overcome the problem. One is to evaluate φ_t in a separate problem. We mention that in the literature the φ_t term is commonly referred to as the "acceleration" term, referring to its gradient being the fluid acceleration at a fixed point. The second is to manipulate the force expression in such a way that the time derivative is moved outside the integral. The third is to introduce a generalized total derivative.

For the first main strategy, according to Tanizawa (2000) four methods have been employed which he denote iterative methods, decomposition methods, indirect methods and implicit boundary condition method. Iterative methods imply estimating φ_t by finite differences and then iterating until some criteria is met. A problem with the method is time consumption as the boundary value problem is solved in each iteration. Decomposition methods involve decomposing the force in that from a unit acceleration multiplied by an effective mass defined in the actual application, and that from a fixed body. This was used by Cointe (1989), and further elaborated in Cointe et al. (1991). They posed a boundary value problem for φ_t similar to that of φ. The indirect method also solves a boundary value problem for φ_t, but at the same time also an artificial problem is introduced and solved for. This approach has been employed by Wu and Eatock Taylor (1996) and Kashiwagi (2000). In all these works the additional computational cost associated with solving the boundary value problem for φ_t is small, but as with all numerical procedures these methods exhibit challenges, such as estimating higher order derivatives, e.g. φ_{ns}, along the body. Here, the subscripts n and s means partial derivative in the normal and tangential directions respectively. The implicit boundary condition method was employed in earlier works by Tanizawa (see references in Tanizawa (2000)), but it is not clear to the author what this theory involved.

The second strategy was followed by Faltinsen (1977), where he re-cast the force expression by integrating over a closed contour involving the body, the surrounding free surface and a surface at "infinity" (a distance b from the body). In the present work we follow this approach, although re-formulating the expression to overcome the limitation that the fluid had to be still exterior to b. In the case of incoming waves, as in most of the present work, this would not be applicable.

The third method was used by Zhao and Faltinsen (1993) in a study on water entry of a wedge. They introduced the derivative $\mathrm{D}'/\mathrm{D}t = \partial/\partial t + \mathbf{U} \cdot \nabla$ where the velocity $\mathbf{U}$ was not the fluid velocity, but rather the body velocity. They showed convergence of the numerical results.

1.3 Present work - structure and findings

In the present study we have implemented and applied numerical models as well as performed several sets of model tests. All work has been restricted to two dimensions. Model tests performed rather early in our study provided valuable insight to the author on resonant fluid behaviour and the appearance of shallow water waves that would otherwise not be as accessible. They further provided inspiration in connection with the work of implementing the numerical models, a task that at times may be experienced not so

inspirational in itself.

We wish to emphasize the following aspects regarding model tests and numerical models. Validation and verification of a numerical code is always a necessity, and model tests are in that respect very useful. However, one should be careful about considering model tests as the "truth" from the fact that bias errors may be present. Then comes precision errors. We regard the numerical and experimental work, of course together with analysis, as tools to study a problem. They are like partners with different skills; both posses unique features that may provide valuable information and they complement each other. In this respect rather extensive efforts have been made both in debugging and verifying the numerical codes as well as on identifying bias errors in the model tests. Bias errors such as wave reflections, reduced wave making capacity and slight flexing of structures which were supposed to be rigid have been discovered during post-processing of our model test data. Some were discovered from arguments of analytical character, but others in fact through direct use of the numerical codes.

Associated with model tests there are scale effects relative to full scale, for instance associated with the Reynold's number. In case of flow separation from blunt parts of structures this is an important issue. In the present work flow separation from sharp corners have been studied, and hence model scale effects are considered not to be of great importance.

1.3.1 Structure of the present thesis

The structure of the present thesis is as follows. In Chapter 2 the mathematical formulations upon which we base our numerical work are given. We first formulate the standard set of equations describing potential free-surface flow, next the theory of inviscid flow separation, then the viscous boundary layer flow, and last state the equations of motion of a rigid body.

In Chapter 3 we discuss physical and numerical issues regarding wave generation in wavetanks with emphasis on reaching steady-state when starting from calm conditions.

In Chapter 4 we discuss the relevant dimensions of our problem and present the basic problem of resonant piston mode and resonant coupled ship and piston-mode behaviour.

The numerical work is presented in the next four chapters, i.e. Chapters 5 - 8. In Chapter 5 the basics of the numerical wavetanks are presented. We introduce the spatial discretization and time integration. Some attention is paid to the treatment of intersection points between the free surface and solid boundaries. Our chosen methods of wave making and wave absorption is explained. In Chapter 6 the inviscid vortex tracking method is presented, along with some verification by foil theory. Special attention to the algorithm for automatic simplifications of the free shear layer during nearly sinusoidal ambient flow is made, as this is new to the present work, and considered a contribution to the field. In Chapter 7 the modelling of the in- and out-flow of boundary layers in the present linear numerical wavetank is presented. In Chapter 8 the derivation of the alternative formulation of the force and moment is given. The implementation is verified to the extent a fully nonlinear method may be verified.

The model tests are presented in Chapter 9. This involves four sets of model tests carried out within the present work, as well as a recapitulation of a set of previously performed model tests whose results are used in the present work. The first two sets involved a fixed rectangular ship section with rounded bilges by a terminal in incoming

shallow water waves. The focus in the first of these was shallow water effects on forces and wave kinematics, while in the second resonant piston-mode motion. The last two sets involved a moored rectangular ship section with sharp corners in resonant motion by a terminal in incoming waves. The recapitulated model tests, called the moonpool tests, were originally performed to study resonant piston motion in moonpools under forced heave of two rectangular sections with sharp corners. With the symmetric geometry in the set-up, this is equivalent to a ship by a terminal in forced heave. The range of model tests thus include the three sub-problems in linear theory: Diffraction, radiation and freely floating ship section, all by a bottom mounted terminal.

In Chapter 10 our studies on resonant behaviour are presented. They all involve a ship section by a bottom mounted terminal. The studies involve results from present numerical simulations as well as the model tests. There are three main studies, directly related to the experimental work described above, and two supplemental studies involving numerical simulations only. The three main studies are (1) the diffraction problem involving a fixed ship section, and no flow separation, (2) the radiation problem involving forced heave of the ship section with flow separation and (3) a moored ship including flow separation. The two supplemental studies involve forced sway of a ship section with flow separation and a fixed ship section in incoming waves including flow separation.

A summary with recommendations to further work is given in Chapter 11.

1.3.2 Main contributions

We summarize what we consider the main contributions of the present work as follows:

- Linear theory over-predict the ship and piston-mode motion near resonance. Our conclusions are that (1) the discrepancy is mainly caused by the damping effect from flow separation at the ship bilges, (2) nonlinear potential flow effects are small and (3) the damping effect of the in- and out-flow of boundary layers is negligible
- An algorithm for automatic simplification of the free shear layer in nearly sinusoidal ambient flow is developed and implemented
- A new alternative expression for the force and moment on a surface piercing body in a nonlinear wavetank is derived and implemented

As for the first, linear theory over-predicts the piston-mode motion around the piston-mode resonance frequency in the case of a fixed ship section or forced motion of the ship section. Linear theory also over-predicts both the ship motion and the piston-mode motion near the coupled ship and piston-mode resonance frequency when the ship is free to oscillate. In the latter case, the discrepancies are larger than in the former. Our results strongly indicate that the observed discrepancy between linear theory and model tests is explained practically in full by the damping effect caused by flow separation. The nonlinear potential flow effects due to gravity waves are not dominant. That is, satisfying the boundary conditions at the instantaneous free surface as well as including the square term in the Bernoulli equation is not important in the present resonance problem. Further, the effect of the in- and out-flow of boundary layers is negligible for all practical purposes. We emphasize that since our conclusion is based on numerical work and not analytically derived results, we have not actually shown this fact. We feel, however, that the good agreement with model tests provide strong evidence that the conclusion is feasible.

In order to reach these conclusions, we needed to handle the free shear layer in a rational manner. We developed an algorithm for automatic simplifications of the free shear layer in near sinusoidal ambient flow, providing a means to apply the inviscid vortex tracking method involving a continuous representation of the vortex sheet for long-time simulations until steady-state. Without the automatic simplification procedure our results regarding flow separation could not have been achieved as the free shear layer becomes entangled. We also regard the automatic simplification algorithm as a contribution by itself.

We also needed to deal with the problems associated with calculation of the forces and moment in the nonlinear wavetank. In this respect we derived and implemented a new alternative expression for the hydrodynamic force and moment on a body in a closed nonlinear numerical wavetank. By alternative we mean the following. The integral of the pressure over the body is re-written by introducing a closed control surface involving the body, a part of the free surface and a connecting surface within the fluid. By manipulations employing Gauss' theorem for force and Stokes' theorem for moment, the time derivative of the φ_t term is moved outside the integrals. The alternative expression hence avoids the need to evaluate φ_t directly. The free shear layer is included explicitly in the formulation.

A limitation to the presently adopted BEM model with free shear layer is that it is most applicable to separation from sharp corners, as the separation point is hard to predict in case of blunt bodies. In the present implementation, separation from sharp corners only are considered. One may ask why a Navier-Stokes solver (CFD) was not chosen to investigate the present problem. There are a large variety of CFD methods such as FDM, FVM, FEM, SPM etc., and different ways of handling the free surface by either free-surface tracking or capturing methods. There is no method that a priori stands out as the perfect choice, and the chosen method has to undergo a verification phase in the same way as is done in the present thesis with the adopted BEM model with free shear layer. When that is said, we note two aspects that are of significance from a practical point of view and that perhaps inspires the use of the present method. First, the CPU time when simulating typically 40 - 50 wave periods in a rather long wavetank is probably modest using the present BEM method compared to that of a CFD code. Second, the present method has the convenient feature that flow separation may be turned on or off simply by a flag specifying whether flow separation should be included in the simulation or not. This allows for an easy way of investigating the effect of flow separation.

Chapter 2

Mathematical formulations

2.1 Potential free-surface water flow

In the present work we consider the two-dimensional motion of an incompressible and inviscid fluid with the objective of studying the fluid interaction with a ship section by a bottom-mounted terminal. We model flow separation from sharp corners by an inviscid vortex tracking method. Further, the in- and out-flow of viscous boundary layers is modelled by a semi-analytical method, under the assumption of laminar boundary layer flow. Vorticity is in both cases introduced, but assumed to be limited to thin free shear layers within the main bulk of the water, or within thin boundary layers along the solid boundaries. The flow in the main bulk of the water is hence irrotational.

The work is carried out within a closed tank as illustrated in Figure 2.1. We denote the domain of the tank by Ω and its boundary by $S+S_V$. We make a distinction between the "physical" boundary S and that excluding the free shear layers S_V. We define S to consist of the solid surfaces $S_0 + S_B$ as well as the free surface S_F, such that $S = S_0 + S_B + S_F$. There may be an arbitrary number of free shear layers. They are collectively denoted S_V. They are not allowed to enter a solid boundary or cross the free surface. Although S_V in the figure appears to be within the domain Ω, it rather is introduced to exclude the vorticity from the free shear layers from Ω. The modelling of the free shear layer is treated in Section 2.2.

We define an Earth-fixed right-handed coordinate system with Cartesian coordinates (x, y) where y is positive upwards, and the horizontal axis defined by $y = 0$ is in the mean water line as indicated in the figure. The surface S_B represents a ship section, while S_0 typically a wavemaker, sea floor and bottom mounted terminal. The domain Ω bounded by the closed surface S is hereafter usually referred to as the numerical wavetank.

We make a distinction between the linear wavetank and the nonlinear wavetank. In the linear wavetank, the domain and its boundary is fixed in time. The free-surface elevation is in this case denoted $\zeta(x, t)$. In the nonlinear wavetank, the domain and its boundary do evolve with time, i.e. $\Omega = \Omega(t)$ and $S = S(t)$.

We now introduce the governing Laplace equation in Ω and the standard boundary conditions on S.

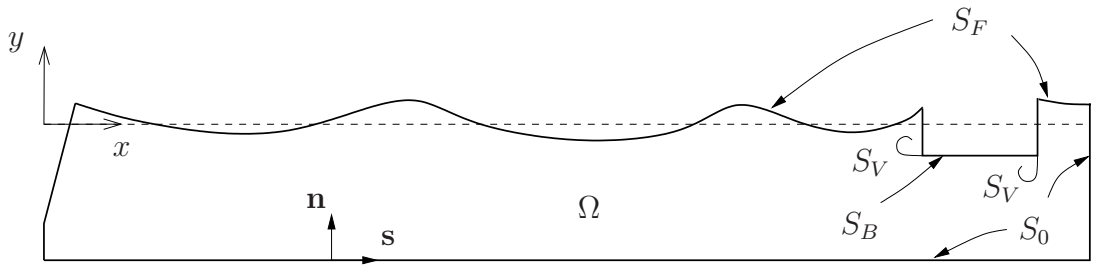

Figure 2.1: Illustration of the closed tank considered in the present work. The domain is denoted Ω and its boundary $S + S_V = S_0 + S_B + S_F + S_V$. All free shear layers are collectively denoted S_V. The Cartesian coordinate system denoted (x, y) is defined such that $y = 0$ is in the mean water line. The unit normal vector $\mathbf{n}$ is defined positive into the water, and $\mathbf{s}$ is the unit tangential vector with positive direction as shown.

2.1.1 Governing equation

With the fluid assumed incompressible, conservation of mass may be described by the usual zero divergence of the velocity, i.e. $\nabla \cdot \mathbf{u} = 0$, where $\mathbf{u}$ is the fluid velocity at any point and at any time, and $\nabla = (\partial/\partial x, \partial/\partial y)$. Further, with the fluid assumed inviscid, and upon excluding any vorticity from the main bulk of the fluid, the velocity may be represented by the gradient of a velocity potential φ, such that $\mathbf{u} = \nabla\varphi$. Our governing equation for the fluid motion is then the Laplace equation,

$$\nabla^2\varphi = 0 \quad \text{in } \Omega. \tag{2.1}$$

We aim at solving for the unknown φ over the domain Ω. The governing equation (2.1) implies that we have an elliptic problem. This means that the solution at any point of the domain depends on the solution everywhere else in the domain. We therefore need boundary conditions along all the boundary S.

2.1.2 Boundary conditions

Along S_F we have the dynamic and kinematic free-surface conditions, while along $S_0 + S_B$ we have the zero-penetration boundary condition. Along S_V we impose a zero pressure drop condition. This is explained further in Section 2.2. In the present section, we state the free-surface conditions only.

The necessary evolution equation for the velocity potential on the free surface is the so-called dynamic free-surface boundary condition derived from Bernoulli's equation which relate the pressure p to the fluid velocity and gravitational force per fluid volume at any point in the fluid,

$$p + \rho\frac{\partial\varphi}{\partial t} + \rho\frac{1}{2}\left(\frac{\partial\varphi}{\partial x}\right)^2 + \rho\frac{1}{2}\left(\frac{\partial\varphi}{\partial y}\right)^2 + \rho gy = C, \tag{2.2}$$

where ρ is the fluid density, g is the acceleration of gravity and y the vertical coordinate being zero at the mean free surface and with positive direction upwards as illustrated in Figure 2.1. Here C is uniform in space and constant in time. If we consider the special condition of zero flow everywhere, we have from (2.2) that $p + \rho gy = C$, and it follows

that $C = p_a$ at $y = 0$, where p_a is the atmospheric pressure. We may subtract p_a on both sides of the equality sign in (2.2). The net pressure $p := p - p_a$ in the resulting equation must then be interpreted as the net pressure when the atmospheric is subtracted. In this thesis, it is the net pressure we consider. We further neglect surface tension. There should then be no pressure drop across the free surface, and we obtain from (2.2) the standard dynamic free-surface condition on S_F,

$$\frac{\mathrm{D}\varphi}{\mathrm{D}t} = \frac{1}{2}\left(\frac{\partial\varphi}{\partial x}\right)^2 + \frac{1}{2}\left(\frac{\partial\varphi}{\partial y}\right)^2 - gy \quad \text{on } S_F \tag{2.3}$$

where $\mathrm{D}\varphi/\mathrm{D}t = \partial\varphi/\partial t + \mathbf{u}\cdot\nabla\varphi$ is the total derivative. As above, $\mathbf{u} = \nabla\varphi$.

The evolution of the free surface with coordinates denoted by $\mathbf{x}_F(t)$ is governed by the kinematic free-surface condition such that S_F is tracked by following the velocity of the fluid at the free surface itself,

$$\frac{\mathrm{d}\mathbf{x}_F}{\mathrm{d}t} = \nabla\varphi \quad \text{on } S_F, \tag{2.4}$$

where $\mathrm{d}/\mathrm{d}t$ is the usual differentiation operator with respect to time.

On solid boundaries we impose the zero-penetration condition, that is the fluid velocity normal to the boundary is imposed as

$$\frac{\partial\varphi}{\partial n} = \mathbf{U}\cdot\mathbf{n} \quad \text{on } S_0 + S_B, \tag{2.5}$$

where $\mathbf{U}$ is the velocity of the boundary $S_0 + S_B$ relative to the defined Earth-fixed coordinate system (x, y) and $\mathbf{n}$ is the unit normal vector defined positive into the fluid as shown in Figure 2.1.

In the linearized problem the boundary S itself does not evolve in time. The boundary conditions are hence imposed on the initial position of the boundary S, so (2.3) and (2.4) are reduced to

$$\begin{aligned} \frac{\partial\varphi}{\partial t} &= -g\zeta \quad \text{on } y = 0, \\ \frac{\partial\zeta}{\partial t} &= -\frac{\partial\varphi}{\partial n} \quad \text{on } y = 0, \end{aligned} \tag{2.6}$$

where by $y = 0$ we here mean the part of the mean water line outside the body. Note that $\partial/\partial n = -\partial/\partial y$ due to the direction of the normal vector pointing into the water. The solid boundary condition is also in the linearized problem that of (2.5).

2.2 Flow separation - Inviscid vortex tracking model

An essential feature of a viscous fluid is that the fluid separates from convex corners forming a free shear layer. The free shear layer contains vorticity shed into the main bulk of the fluid domain from the separating boundary layer. The vorticity in the boundary layer is a consequence of the no-slip condition on solid surfaces. The situation is illustrated in Figure 2.2. One may say that the flow separation provides a means for the fluid to retain a finite velocity at the corner of separation. In "standard" potential theory, an infinite fluid velocity will be predicted at convex corners. This is not physical. The physical behaviour is recovered by imposing a *Kutta condition*. The Kutta condition says that the

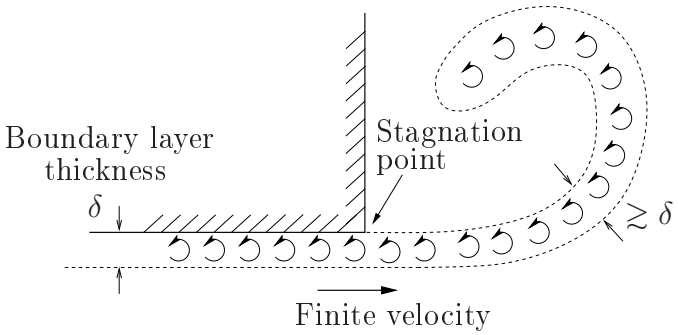

Figure 2.2: Conceptual illustration of a free shear layer representing vorticity shed into the fluid by flow separation from sharp corner. In reality, the free shear layer has a finite width ($\simeq \delta$) which will increase away from the separation point due to diffusion. In the present vortex tracking model the whole free shear layer is assumed infinitely thin, i.e. $\delta \to 0$.

flow must leave tangentially from the body at the point of separation, and that the fluid velocity must be finite. The means to ensure this is in the present model is described in this section.

2.2.1 Validity of the vortex tracking model

The free shear layer is in the present model assumed to be thin, i.e. the vorticity is assumed to be concentrated in a thin strip in the fluid domain. This means that the model is only valid for high Reynolds numbers. In the cases we have studied, the Reynolds numbers have been sufficiently large.

We illustrate that the Reynolds numbers have been sufficiently large in the following. We emphasize that the Reynold's number does not explicitly enter the computations. A sufficiently large Reynold's is purely a matter of having the right conditions for which the model is valid, i.e. that the free shear layers are thin. We start out by assuming steady-state sinusoidal ambient flow above a straight plate in a semi-infinite fluid. In that case the Reynold's number is

$$Rn = \frac{2\,\omega\,a^2}{\nu}, \tag{2.7}$$

where ω is the imposed circular frequency, a is the amplitude of the relative ambient flow and ν is the kinematic viscosity. In the present problem, none of the above assumptions are strictly speaking fulfilled. First, the flow past the ship section is not that of an infinite fluid. Second, since we investigate the nonlinear problem, the ambient flow may in principle undergo rather complicated flow, and further, we investigate the transient problem with the flow starting from rest. However, the flow around the ship section corner will behave similar to that around one corner of a rectangle in infinite fluid. This applies at least if the vortical structures are confined to the vicinity of the corner such that the bottom, terminal, the other corner of the ship section and free surface are considered in the far-field. Further, in all the investigated cases, when the system has reached steady-state, the piston-mode motion has been quite sinusoidal. This means that in steady-state conditions, we may take the piston-mode amplitude as a relevant measure of the ambient

flow amplitude a in (2.7). Also, in the transient part, taking the "instantaneous" piston-mode amplitude over one period, (2.7) provides in our opinion a relevant measure of the "instantaneous" Reynold's number.

For a measure of the boundary layer thickness we use the distance δ from the wall where the actual flow differs from the outer flow by 1%. This is $\delta \simeq 4.6\sqrt{2\nu/\omega}$ for laminar boundary layer flow (see e.g. Faltinsen (1990)). In the main part of the present work, we have had the following situation regarding the boundary layer thickness and the Reynold's number range in steady state conditions. We take the ship section beam $B \simeq 0.5$m (model scale) as a typical structural length, $\omega \simeq 2-9$rad/s and $a \simeq 0.01-0.05$m as representative values for the circular frequencies and ambient flow amplitudes. We then get that $Rn \simeq 10^3 - 5 \times 10^4$ and $\delta/B \simeq 5 \times 10^{-3} - 10^{-2}$. These Reynold's numbers are considered large enough for the inviscid vortex tracking model to be valid. The boundary layer thickness, and hence the thickness of the free shear layer, are also considered small relative to the body geometry. Although this is not a direct criterion, it provides qualitative information of interest for the user. It is, however, directly relevant in the modelling of the in- and out-flow of thin boundary layers which will be treated in the next section.

In full scale the boundary layers in the terminal gap are most probably turbulent, and estimations of the boundary layer thickness becomes more involved. The model test scale above is roughly 1:100. We denote the inverse of the scale by κ, so that $\kappa = 100$ in this case. Since the Reynold's number Rn scales like $\kappa^{3/2}$, we have full scale values of $Rn \sim 10^6 - 5 \times 10^7$. In oscillatory flow over a smooth bed, the critical Reynold's number for transition between laminar and turbulent boundary layer flow is $\mathcal{O}\{10^5\}$. In our case then, the lower bound is in the regime of transition from laminar to turbulent boundary layers, while the upper is well into the turbulent regime. An estimation of the boundary layer thickness for a turbulent boundary layer is given in Fredsøe and Deigaard (1992) (see p. 29) as $\delta/a = 0.093 Rn^{-0.11}$. They give no formal definition of what is meant by boundary layer thickness, but the formula is based on the assumption of a hydraulically smooth surface and a log-law for the velocity distribution. Using this formula, we get $\delta/B \simeq 4 \times 10^{-4} - 10^{-3}$.

In order to reduce possible confusion, we want to make the following remark. Although the boundary layer flow is laminar, the free shear layer is likely to be turbulent. Whether the free shear layer is turbulent or not is not, however, an issue regarding the applicability of the inviscid vortex tracking model. On the other hand, whether the boundary layers are laminar or turbulent, becomes an issue in case of separation from a rounded part of a body. The separation point will differ in the two cases. In the case of separation from blunt bodies without sharp corners, a boundary layer calculation would be required in order to determine the separation points. The point of separation would vary in time. We mention that the boundary layer calculations needed for blunt bodies without sharp corners is quite troublesome, as discussed by Aarsnes (1984). A complication is that the boundary layer cannot be considered thin in the vicinity of the separation point. Also, a distinction between laminar and turbulent boundary layers is necessary. This is a practical matter when considering model testing versus full scale behaviour. This is not relevant, however, for bodies with sharp corners. In the present work we restrict ourselves to flow separation from sharp corners only, meaning that the separation points are well defined.

2.2.2 Recapitulation of the theory

In the following we recapitulate the theory presented by Faltinsen and Pettersen (1987). The vortex tracking model is based wholly on Bernoulli's equation (2.2). Following similar arguments as those behind Prandtl's boundary layer equations and assuming the free shear layer to be thin, the pressure is impressed onto the shear layer from the ambient flow from both sides, and so, there may be no pressure drop through the layer. Denoting the two sides by + and − as indicated in Figure 2.3 means we may write $p^+ = p^-$, yielding

$$\frac{\partial \varphi^+}{\partial t} - \frac{\partial \varphi^-}{\partial t} + \frac{1}{2}\left(\frac{\partial \varphi^+}{\partial x}\right)^2 - \frac{1}{2}\left(\frac{\partial \varphi^-}{\partial x}\right)^2 + \frac{1}{2}\left(\frac{\partial \varphi^+}{\partial y}\right)^2 - \frac{1}{2}\left(\frac{\partial \varphi^-}{\partial y}\right)^2 = 0. \tag{2.8}$$

This may be re-arranged as

$$\frac{\partial(\varphi^+ - \varphi^-)}{\partial t} + \frac{1}{2}\left\{\frac{\partial \varphi^+}{\partial x} + \frac{\partial \varphi^-}{\partial x}\right\}\frac{\partial(\varphi^+ - \varphi^-)}{\partial x} + \frac{1}{2}\left\{\frac{\partial \varphi^+}{\partial y} + \frac{\partial \varphi^-}{\partial y}\right\}\frac{\partial(\varphi^+ - \varphi^-)}{\partial y} = 0, \tag{2.9}$$

and defining

$$\Gamma = \varphi^+ - \varphi^-, \tag{2.10}$$

we may write (2.9) as

$$\frac{\partial \Gamma}{\partial t} + \boldsymbol{U_c} \cdot \nabla \Gamma = 0, \tag{2.11}$$

where

$$\boldsymbol{U_c} = \frac{1}{2}\left[\frac{\partial \varphi^+}{\partial x} + \frac{\partial \varphi^-}{\partial x}, \frac{\partial \varphi^+}{\partial y} + \frac{\partial \varphi^-}{\partial y}\right]. \tag{2.12}$$

Since (2.11) is the advection equation, Γ is advected with the velocity $\boldsymbol{U_c}$, or put in another way, Γ does not change when following a path defined by this velocity. This means that the geometry $\mathbf{x}_v$ of the free shear layer at any time t may be found by integrating (2.12) from zero to t, or on differential form

$$\frac{\mathrm{d}\mathbf{x}_v}{\mathrm{d}t} = \boldsymbol{U_c}. \tag{2.13}$$

The free shear layer is fully described by $\mathbf{x}_v$ and Γ. These quantities are parametrized by the arc length s of the free shear layer, such that $\mathbf{x}_v = \mathbf{x}_v(s)$ and $\Gamma = \Gamma(s)$. It is here implied that $\mathbf{x}_v$ and Γ both are functions of time as well, although not stated explicitly. We define $s = 0$ to be at the separation point and $s = L_v$ at the far end free shear layer, where L_v is the free shear layer length.

The discontinuity in the potential $\varphi^+ - \varphi^- = \Gamma$ along the free shear layer is illustrated in Figure 2.3. The circulation along any closed path enclosing the free shear layer such as S_c (which resides in the xy-plane) is given by the integral $\int_{S_c} \partial\varphi/\partial s \, \mathrm{d}s = \varphi^- - \varphi^+$, where the integration direction is positive in the counter-clockwise direction. This is equal to $-\Gamma$, meaning that here, $\Gamma(s)$ is the negative value of the circulation at any point along the free shear layer.

Kutta condition. The Kutta condition involves two aspects. First, the fluid is required to leave tangentially from the body. This may be from either of the two sides

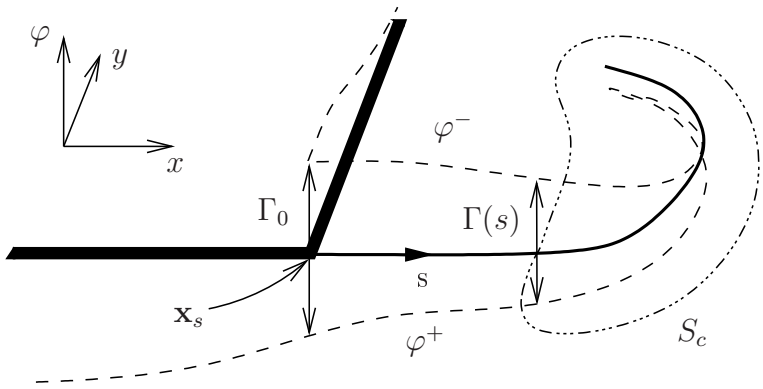

Figure 2.3: Illustration of the potential jump $\Gamma(s) = \varphi^+(s) - \varphi^-(s)$ along the free shear layer. The dashed line indicates the value of φ along the free shear layer and body. The dash-dotted line S_c is an arbitrary closed curve in the xy-plane enclosing the free shear layer.

of the body. The side from which it should leave depends on the water flow in the near vicinity of the separation point. We use the tangential fluid velocity along the ship section sides on both sides of the separation point as measures of the flow. These are measured a small distance away from the separation point. We choose the side of separation as that which has the highest velocity towards the separation point. Choosing the side may be a somewhat delicate matter in practice, and how this is implemented in the present code is explained in sub-section 6.3.3. The second aspect of the Kutta condition is that the velocity at the point of separation is finite. This is imposed in the BEM by requiring that the quantity $\varphi^+ - \varphi^-$ must vary smoothly from the fluid and onto the body. This is required on the side of shedding only. There will be a discontinuity of the potential from the body and into the fluid along the opposite side of the body. Now, given such a smoothly varying Γ along the free shear layer, we may require the jump in the potential *on the body* at the corner of separation to be exactly the value of Γ on the free shear layer at the point of separation, that is $(\varphi^+ - \varphi^-)_{\text{body}} = \Gamma_0$, where $\Gamma_0 = \Gamma(0)$. The implication of this requirement is perhaps not so obvious at the present stage. However, it provides a mean of imposing the proper flow in the numerical model as shown later in the text.

The time rate of change of Γ at the separation point, Γ_0, is also found from the Bernoulli equation. Following the definitions above and in Figure 2.3, and because the lee side of the point of separation $\mathbf{x}_s$ is a stagnation point (cf. Figure 2.2) as a consequence of the Kutta condition, we get from (2.8) that

$$\frac{\mathrm{d}\Gamma_0}{\mathrm{d}t} = \pm\frac{1}{2}U_s^2, \tag{2.14}$$

where U_s is the fluid velocity just outside the boundary layer at the corner on the side where shedding occurs, i.e. $U_s = \partial\varphi/\partial s(\mathbf{x}_s)$. The sign on the right hand side is negative when the flow separates from the +-side, and positive when the flow separates from the other.

2.3 Viscous boundary layer - In- and out-flow

In this section we consider attached, viscous boundary layers. We explain how the in- and out-flow of the viscous boundary layers is modelled such that it may be used in the present BEM.

As mentioned above, a consequence of the no-slip condition is that vorticity is generated. The generated vorticity is localized to a thin boundary layer close to the wall. This has, due to continuity of mass, the effect of inducing an in- and out-flow, say $\tilde{v}$, of the "outer limit" of the boundary layer. In all physical flows the in- and out-flow will act globally as damping. This follows from the fact that there is energy dissipation in the boundary layer. This means that the sum of the kinetic and potential energy in the whole fluid must be reduced, or damped.

We are interested in the effect of the in- and out-flow in the present problem of a resonant piston-mode motion. Under certain assumptions, the steady-state periodic solution of $\tilde{v}$ is found in standard textbooks, as noted somewhat further below. However, since we investigate this problem by means of an initial value problem starting from rest, we have unsteady conditions. After deriving the expression for $\tilde{v}$ in unsteady flow, we use it as right-hand-side in the body boundary conditions (2.5), i.e. $\partial\varphi/\partial n = \tilde{v}$.

Liu and Orfila (2004) considered the in- and out-flow in the unsteady case, and presents a solution for $\tilde{v}$ in a similar form as will be done below, but without derivation. The solution is therefore derived in the following.

We assume that the boundary layer flow is laminar. Since the in- and out-flow of the boundary layers are imposed directly on the solid boundaries, the layer should be thin relative to a typical dimension of the geometry. We require that $\delta/B \ll 1$. Further, the curvature of the boundary, κ, must be small compared to the boundary layer thickness, that is $\delta\kappa \gg 1$, so that we may solve the problem locally in s in a curvilinear manner, where s is the local tangential coordinate. The boundary layer thickness is as before denoted δ. We denote by n the local normal coordinate as indicated in the left part of Figure 2.4. The domain is assumed to extend infinitely far in both the positive and negative s-direction as well as in the positive n-direction. We let the velocity immediately outside the boundary layer be given by $(U_e(s,t), V_e(s,t))$ with $V_e = 0$. This is the external flow. We further write the total velocity as $(u, v) = (\tilde{u}, \tilde{v}) + (U_e, 0)$, where u is required to satisfy the no-slip condition on the wall, i.e. $u = 0$ at $n = 0$.

In steady-state conditions the expression for $\tilde{v}$ is found in many text books, e.g. in Faltinsen (1990). With $U_e(s,t) = U_0(s)\cos\omega t$ this is

$$\tilde{v} = \frac{\partial U_0}{\partial s}\sqrt{\frac{\nu}{\omega}}\cos(\omega t - \pi/4). \tag{2.15}$$

There is a phase lag of $\pi/4$ relative to the outer horizontal flow, meaning there are equal contributions in phase with acceleration and in phase with the velocity, where the latter has a damping effect.

We expect a similar behaviour also in the case of arbitrary unsteady flow. We take the linearized Prandtl equations as a starting point. We mention that the linearized Prandtl equation is equivalent to the heat equation. Relevant theory may be found e.g. in Landau and Lifschitz (1987) (see discussion around the heat equation in §52). We have the following initial boundary value problem for $\tilde{u}$, where the initial condition is assumed

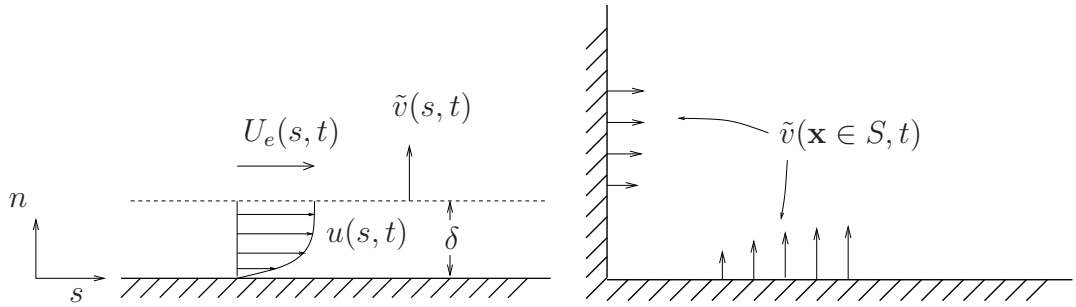

Figure 2.4: In- and out-flow $\tilde{v}$ of a boundary layer. Left: Near field with curvilinear coordinates (s, n). Right: Far field where the in- and out-flow $\tilde{v}$ imposed directly on solid parts of the boundary S. This may be done since δ is small relative to a characteristic length of the problem.

that of starting from rest:

$$\begin{gathered}\frac{\partial \tilde{u}}{\partial t} - \nu \frac{\partial^2 \tilde{u}}{\partial n^2} = 0, \quad \tilde{u}(s,0,t) = -U_e(s,t), \quad \tilde{u}(s,\infty,t) = 0, \\ \tilde{u}(s,n,0) = 0, \quad U_e(s,0) = 0.\end{gathered} \tag{2.16}$$

Note that instead of δ we write ∞ in the boundary condition. We take the Laplace transform of (2.16), where we define the transform $\hat{f}(b)$ of a function $f(t)$ by

$$\hat{f}(b) = \mathcal{L}\{f(t)\} = \int_0^\infty e^{-bt} f(t)\, \mathrm{d}t, \tag{2.17}$$

and get

$$b\,\hat{u} - \nu \frac{\partial^2 \hat{u}}{\partial n^2} = 0, \quad \hat{u}(s,0,b) = -\hat{U}_e(s,b), \quad \hat{u}(s,\infty,b) = 0. \tag{2.18}$$

b is here a complex variable. Note that we have here used that the flow is initially at rest, or $\tilde{u}(s,n,0) = 0$. The solution must be of the form $\hat{u} = A(s,b)\ \mathrm{e}^{\alpha n}$, and using the two boundary conditions at zero and infinity we get that $\alpha = -\sqrt{b/\nu}$ and $A(s,b) = -\hat{U}_e(s,b)$, so that

$$\hat{u} = -U_e(x,b)\ \mathrm{e}^{-n\sqrt{b/\nu}} \tag{2.19}$$

The vertical velocity at $n = \delta$ is obtained by integrating the equation of continuity from $n = 0$ to infinity, $\hat{v} = -\int_0^\infty \partial \hat{u}/\partial s\, \mathrm{d}n$, yielding

$$\hat{v}(s,\infty,b) = \frac{\partial \hat{U}_e}{\partial s}(s,b)\sqrt{\frac{\nu}{b}}. \tag{2.20}$$

The right hand side consists of a product of the two transforms $\hat{f}_1 = \sqrt{\nu/b}$ and $\hat{f}_2 = \partial \hat{U}_e/\partial s$, and the inverse of the product is hence a convolution integral between the inverse transforms $f_1 = \nu/\sqrt{\pi t}$ and $f_2 = \partial U_e/\partial s$. The convolution integral is defined as

$$\mathcal{L}^{-1}\{\hat{f}_1(b)\hat{f}_2(b)\} = \int_0^t f_1(t-\tau) f_2(\tau) \mathrm{d}\tau, \tag{2.21}$$

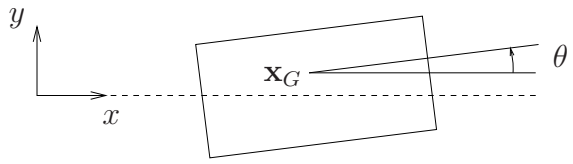

Figure 2.5: Roll is denoted by θ, and is taken to be positive counter-clockwise. Centre of gravity is denoted by $\mathbf{x}_G = (x_G, y_G)$.

and so the solution to our problem is

$$\tilde{v}(s,t) = \sqrt{\frac{\nu}{\pi}} \int_0^t \frac{\partial U_e}{\partial s}(s,\tau) \frac{1}{\sqrt{t-\tau}} \, \mathrm{d}\tau. \tag{2.22}$$

As discussed, under the assumption of a thin boundary layer, we may impose the velocity (2.22) directly on the solid boundaries, providing a slightly different boundary condition than the classical zero penetration condition. This is illustrated by the far-field representation in the right part of Figure 2.4.

Near corners of the solid boundaries and intersection points between the free surface and solid boundaries we still apply (2.22), although the situation in the vicinity of these positions is strictly speaking not as assumed.

2.4 Rigid body motion

In the present work we are primarily interested in a ship section by a terminal, with the section either fixed or moving and with the motion either forced or free. In the case of free body motion, the equations of motion must be solved for. We consider rigid-body ship motions in three degrees of freedom; sway, heave and roll. In the inertial coordinate system $0xy$ as used throughout the present work and illustrated in Figure 2.5, the equations of motion are

$$\begin{aligned} m\,\ddot{x}_G &= F_x, \\ m\,\ddot{y}_G &= F_y, \\ \mathcal{I}\,\ddot{\theta} &= \mathcal{M}, \end{aligned} \tag{2.23}$$

where m is the body mass, $\mathcal{I}$ the roll inertia about the center of gravity of the ship section $\mathbf{x}_G = (x_G, y_G)$, F_x and F_y the horizontal and vertical forces and $\mathcal{M}$ the roll moment about the center of gravity. We denote by motion of the center of gravity in the x-direction sway and in the y-direction heave. Roll is denoted by θ and measured in radians. The roll motion and moment are considered positive in the counter-clockwise direction as indicated in Figure 2.5.

Although in the previous section we described a method to include the viscous effect of in- and out-flow of boundary layers we neglect shear stress when calculating the forces and the moment. We only consider the contribution from the pressure. The fluid force $\mathbf{F} = (F_x, F_y)$ and moment $\mathcal{M}$ acting on the body are then the pressure given by the

Bernoulli equation multiplied by the body normal vector and integrated over the body,

$$\begin{aligned} \mathbf{F} &= -\int_{S_B} p\,\mathbf{n}\,\mathrm{d}s, \\ \mathcal{M} &= -\int_{S_B} p\,n_\theta\,\mathrm{d}s, \end{aligned} \tag{2.24}$$

where $\mathbf{n} = (n_x, n_y)$ and $n_\theta = (x - x_G)n_y - (y - y_G)n_x$. The expression for n_θ is explained in more detail in Section D.1.

Chapter 3

Wave modelling in a wavetank

We are basically concerned with wave-body interaction and some knowledge on the matter of water waves has proved useful throughout our study. In the present chapter we discuss some aspects regarding generation of steady-state waves in a wavetank. This applies to both physical and numerical modelling.

There are no new results presented in this chapter. We do however, devote a separate chapter to aspects concerning obtaining steady-state, or at least nearly steady-state, wave conditions, as we find the issues discussed herein of appreciable importance to keep in mind during studies such as the present one. Special attention is paid to shallow water waves.

Relevant to offshore terminals in small water depths, we give a short overview over developments in shallow water wave modelling by Boussinesq type of equations made over the last one or two decades.

3.1 Linear propagating waves

For a linear, regular wave we denote by T the wave period, λ its wavelength and H its trough-to-crest height. From these we have the wave frequency $\omega = 2\pi/T$, the wave number $k = 2\pi/\lambda$ and the wave amplitude $A = H/2$. We also introduce the wave steepness H/λ. In other contexts, such as in perturbation schemes of the velocity potential, a more convenient definition is perhaps kA which is π times larger.

Assuming constant water depth h in a fluid extending infinitely in the horizontal direction, a steady-state harmonic solution may be found, giving the linear dispersion relation relating the wave frequency ω, wave number k and acceleration of gravity g, which is the well known

$$\omega^2 = gk \tanh kh. \tag{3.1}$$

From an energy consideration of a narrow banded wave train, in the limit, we recover the propagation velocity of the energy associated with the wave, denoted the group velocity $C_g = \mathrm{d}\omega/\mathrm{d}k$, which is

$$C_g = \frac{C}{2}\left(1 + \frac{2\,kh}{\sinh\,2kh}\right), \tag{3.2}$$

where $C = \omega/k$ is called the phase velocity. In the deep water limit when the wavelength becomes negligible compared to the water depth, or $kh \to \infty$, we get $C_g = C/2$. In the shallow water limit where $kh \to 0$, we get $C_g = C = \sqrt{gh}$.

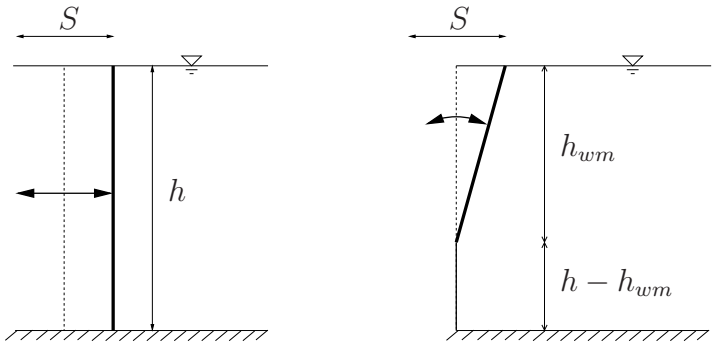

Figure 3.1: Two types of wave making devices. Left: Piston type. Right: Hinged flap type.

We also mention that when a regular wave enters from one water depth to another over a gently sloping bottom, not only the wavelength, but also the amplitude will change somewhat according to linear theory. This problem is discussed e.g. in Mei (1989) where the solution to the linearized problem is obtained assuming multiple scales. The behaviour is governed by the so-called wave action equation, which is in three-dimensional space $\partial/\partial t(E/\omega) + \nabla \cdot (\mathbf{C_g}E) = 0$, where $E = 0.5\rho g A^2$ for long crested waves. With no temporal changes in the topography or current, there is no temporal change in period or energy, which means that in two dimensions $C_g E = \text{const}$, or

$$\frac{A}{A_0} = \sqrt{\frac{C_{g0}}{C_g}}, \tag{3.3}$$

where subscript zero means a reference water depth, e.g. deep water. The wavelength decreases appreciably when entering an area of smaller water depth, but the amplitude changes to a lesser extent. The steepness hence increases until finally breaking at sufficiently small water depths. We make use of (3.3) when defining the environmental conditions in the model tests presented in Section 9.1.

3.2 Steady-state wavemaker theory

We next present linear wavemaker theory and discuss aspects that have consequences in a wavetank. The theory is found in many textbooks, see e.g. Hughes (1993), Dean and Dalrymple (1984) or Faltinsen (2005).

Given a wave period T and a desired far-field waveheight H for a regular wave in steady-state, the solution of the linearized problem of the motion of different types of wavemakers has been found and referred to in the above references. The solutions are given in terms of transfer functions expressing the ratio between the waveheight and the stroke S of the wave making board, sometimes referred to as Bièsel transfer functions. The stroke S is the horizontal distance between the two extrema of the paddle motion taken in the still free surface as indicated in Figure 3.1. The motion of the wavemaker is assumed sinusoidal. Perhaps the most common type of wave making devices are (1) the piston type being a vertical plate typically extending the full water depth h for shallow

water waves, and (2) hinged flap of arbitrary height h_{wm} for deeper water, both illustrated in Figure 3.1. The transfer function for these are

$$\begin{aligned} \frac{H}{S} &= \frac{2\left(\cosh 2kh - 1\right)}{\sinh 2kh + 2kh} \quad \text{(Piston)}, \\ \frac{H}{S} &= \frac{4\sinh kh}{\sinh 2kh + 2kh}\left(\sinh kh + \frac{\cosh k(h - h_{wm}) - \cosh kh}{kh_{wm}}\right) \quad \text{(Hinged flap)}. \end{aligned} \tag{3.4}$$

A special flap-type wavemaker that is commonly used is the double-hinged flap. It will typically be proper for generating waves over a large range of wave frequencies; the top flap may generate the shortest waves, while the lower plus upper flap the longer waves.

Note that in the linearized problem the actual geometry does not change, that is the boundary conditions are satisfied on the mean position of the paddle. Therefore, the validity of (3.4) becomes questionable if the paddle motion is large, e.g. large flap angles. This is, however, in many cases not a practical problem.

As stated, the transfer functions provide relations between the far-field waveheight and the stroke. There are, however, also near-field disturbances that do not propagate, often called evanescent modes. The evanescent modes appear since the paddle motion does not in general satisfy the exact fluid kinematics under a steady wave train. They vary sinusoidally with depth and decay exponentially in the horizontal direction as $A_n \exp(-k_n x)$. Here $x = 0$ corresponds to the wave board at rest and the water domain is for $x > 0$ in a linear analysis. There is an infinite number of evanescent modes with k_n the positive roots of the equation $\omega^2 = -gk \tan kh$. Note the minus sign and tan rather than tanh. The solution procedure for obtaining A_n is given in detail in Faltinsen (2005) (see p. 283). The amplitude of the evanescent modes depends on the type of wavemaker, wave period and water depth. A rule of thumb is that undisturbed outgoing waves appear about $2 - 3\lambda$ away from the wavemaker. However, this depends on a reasonable choice of type of wave making device. Two extreme cases are (1) attempting to create deep water waves with a piston type paddle extending to the tank bottom and (2) creating shallow water waves with a flap hinged far from the bottom. In the former case, the amplitude of the evanescent modes A_n will be large and give significant disturbances beyond that of the rule of thumb above. In the latter case the ability to produce waves with any significant amplitude will be very limited.

3.3 Reaching steady-state

The linear dispersion relation and its derived results such as group velocity, is strictly speaking valid in steady conditions only. It is perhaps somewhat confusing how steady-state might exist, but in our case it means that there is an infinitely long wave train caused by a local disturbance, sinusoidal in time, located infinitely far away that started at $t = -\infty$. In practice we have only a finite length wavetank and a finite amount of time to produce waves, so that we may obtain only near steady-state behaviour. This has practical implications. Assume that the fluid is initially at rest in a closed wavetank. When a wave making device at one end of the wavetank starts undergoing regular motion, a wave train will start to propagate along the tank. The wave train front experiences a different reality than the waves further behind which, at least some distance from the wavemaker experience a near steady-state condition. The wave front may be described

by an infinite sum of frequencies, and therefore, some energy will travel with the velocity $\sqrt{gh}$ (the zero frequency limit), and its disturbance will be vertically uniform. This is relevant for seiching, which may occur in a basin or wave flume. Disregarding the detailed behaviour of the wave front, we note that the velocity of the wave train front is limited by the velocity that the energy is transported which is C_g. In the deep water limit, the waves travel twice as fast as the wave front, since $C_g = C/2$, whereas in the shallow water limit the waves travel with the same velocity as the energy propagates, since $C_g = C$. A body in the wavetank will reflect waves that are in turn re-reflected from the wavemaker. The time of re-reflection is roughly $3l/C_g$, where l is the distance from the wavemaker to the body. The number of periods where the incoming waves at the position of the body attain a near steady-state behaviour is therefore dependent on the relation C/C_g and the distance l. In the shallow water limit this is at most half that in the deep water limit, but in practice somewhat less due to the somewhat transient behaviour typically of the first two or three wave crests in the wave train front. This is indeed a practical limitation that must be considered if performing physical or numerical work on shallow water.

3.4 Shallow water aspects

For deep water waves nonlinearity is associated by a large wave amplitude, with the relevant non-dimensional parameter being the steepness kA. In finite water depths, another relevant parameter is kh. There are thus the two independent parameters kA and kh, that are both measures of nonlinearity. They relate the horizontal dimension to the vertical dimensions of the wave, i.e. the wavelength to the wave amplitude and water depth, respectively.

kh becomes important when the water depth becomes shallow. The deep water limit is usually considered $\lambda_0/h \leq 2$, while the traditional limit for a shallow water wave is $\lambda_0/h \geq 10$. The latter is equivalent to $k_0 h \leq \pi/5 \simeq 0.63$. The subscript 0 means deep water limit. We mention that shallow water waves are often also denoted long waves, referring to their length compared to the water depth. Nonlinearity is introduced when kh becomes small, as may be seen from the ratio of the two acceleration terms in the Euler equations, $uu_x/u_t \sim kA/\tanh kh$. Given A, the nonlinear advection term becomes important when kh becomes small. When $kh \to 0$, the ratio tends to A/h, and so in very shallow waters, the degree of nonlinearity is associated with the ratio of the amplitude to the water depth. Ursell (1953) further found that the parameter $U_r = kA/(kh)^3$, commonly known as the Ursell parameter, is a more descriptive parameter regarding the amount of nonlinearity introduced by the finite water depth relative to that from the wave amplitude. Relative to the above discussion, we see that $U_r = 1/(kh)^2\, A/h$.

3.4.1 Permanent shape of the waves

We present in Figure 3.2 four snapshots of waves produced by four simulations using the present nonlinear wavetank. For each simulation, the water depth h was changed, otherwise, the conditions were the same. The motion of the piston wavemaker was sinusoidal at period $T = 1$s with stroke S corresponding to deep water wave steepness is $H_0/\lambda_0 = 1/50$. The parameter relating the deep water wavelength to water depth λ_0/h is included for each of the four snapshots in the figure. The lower snapshot represent deep water con-

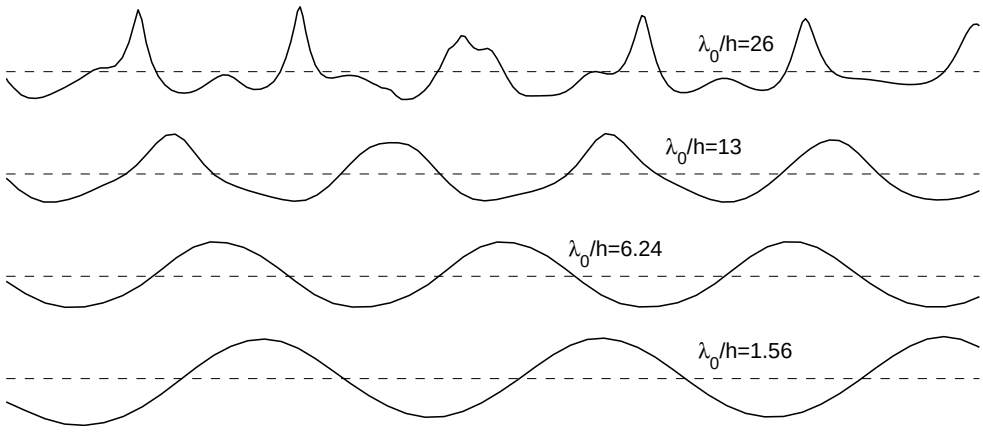

Figure 3.2: Snapshots showing typical shallow water effects on propagating waves. Simulations from the present nonlinear wavetank. Same wave period in all four simulations, but different constant water depths h. The horizontal axis represent distance x along the wavetank.

dition, the second lowest an intermediate depth, while the two upper represent shallow water conditions. We want to mention the following two features. First, the shape of the free-surface elevation changes drastically upon exceeding the shallow water limit, almost unrecognizable when comparing to the well-known near sinusoidal deep water wave. Second, the presented shallow water waves do not attain profiles of permanent shape, the profile varies along the tank. In shallow water, waves of permanent shape do, however, exist. These are called Cnoidal waves. Generation of Cnoidal waves requires a paddle motion other than sinusoidal, as discussed e.g. in Mei (1989). In the case of sinusoidal motion, so-called parasitic free second-order waves are propagated, as discussed e.g. in Hughes (1993). With second order we here refer to an expansion of the potential in the wave steepness parameter kA. In very shallow water as that in the upper snapshot, this expansion becomes less valid from the discussion around the Ursell parameter above, but the main feature is still explained in a qualitative manner.

The features discussed here introduce practical issues when modelling long waves in a wavetank. In case of sinusoidal wave paddle motion, the lack of permanent shape suggests that one should perform wave calibration tests without the model present in order to measure the wave at the position where the model will later be placed. The far from sinusoidal shape further complicates the matter on what is actually a representative value for the waveheight H. An obvious option is to take the crest-to-trough height over one paddle period. This is what has been done during the present work in the parts involving shallow water waves. There is a question, however, if the crest-to-trough height at e.g. the mid-position of the model is an adequate measure of say, the energy in the wave. These kinds of issues illustrates some difficulties regarding shallow water waves. Not only do they involve a great deal of care in modelling, but once modelled, the way to extract of information from the results are not obvious.

3.4.2 Boussinesq models

With respect to the modelling of shallow water waves we feel that so-called Boussinesq type of equations deserves to be mentioned. These equations basically keep some of the nonlinearity in the dynamic free-surface condition, and makes implicit restrictions on the dispersive character of the waves. They are based on expansion of the velocity potential in the two parameters $\mu = kh$ as well as $\epsilon = kA$. One may associate with kh the dispersive characteristics of the waves, and with kA the nonlinearity introduced by the nonlinear free-surface conditions. What is characteristic by the traditional Boussinesq models is that ϵ and μ^2 are assumed to be of the same order of magnitude. In newer formulations, the two parameters are treated more separately. The variation in the vertical direction y is assumed small and represented traditionally as a power expansion in ky. The order of the method with respect to dispersion is the highest order of ky kept. Since the range of y is in the order of h, one usually refers to kh rather than ky when discussing the order of the method. So an expansion to $(ky)^2$ is referred to as an expansion up to $(kh)^2$. Expansions other than power expansions, like Padé approximants has more recently been applied.

The basic idea behind a Boussinesq model is that some of the nonlinearity of the water wave problem is retained through the expansion in kA. Since shallow water waves attain nonlinear behaviour, this may be essential in a given physical problem. The capability of the model to capture the nonlinear characteristics depends on how the nonlinear free-surface conditions, or expansion in kA, is treated. This varies from model to model.

A Boussinesq model will not model the exact dispersive character of the waves. It will be valid only for a certain range of kh. The range of water depth to wavelength ratios (kh) for which a given Boussinesq model is applicable must be investigated for each specific model. It is a question of settling a limit for kh where the model captures global linear wave characteristics like the wave celerity C and group velocity C_g reasonably well. Beyond this limit, the errors typically increase very fast with increasing kh. The dispersive characteristics of the wave field is modelled improvingly well the higher the order of the Boussinesq model is. One may then in theory expand to a very high order in kh. However, the resulting equations become very complex if expanding to orders higher than, say, $4 - 6$.

The classical Boussinesq equations were derived by Peregrine (1967), and is applicable for $\lambda_0/h \gtrsim 8$, or equivalently $kh \lesssim 0.75$. Significant progress has been made in the last one or two decades in the treatment of medium deep to shallow water waves. A wealth of suggested models improving both nonlinearity of the free surface as well as extending the ranges of kh have been published. Recently, so called enhanced Boussinesq type of equations have been developed and presented in Madsen et al. (2002), applicable for $\lambda_0/h \gtrsim 0.15$ or $kh \lesssim 40$. Interesting to note is that, compared to Peregrine's model, the water depth may be about 50 times greater. Note also that the water depth may in the latter model be about seven times greater than the wavelength, and that is definetely a true deep water wave. In practice this removes the restriction to shallow water almost completely. They used a so-called Padé approximant rather than a power expansion in ky. A Padé approximant type of expansion involves a quotient in the shape $p(ky)/q(ky)$. For example, keeping the first order term in each function gives a second order method, as $(1 + a(ky))/(1 + b(ky)) \simeq (1 + a(ky))(1 - b(ky))$ when $b(ky)$ is small. According to their work such an expansion gives a higher range of kh where the model is applicable

relative to that for a traditional power expansion to the same order (second order in this case). Further, one may choose pairs of a, b such as to maximize this range.

We mention last that originally our purpose was to study shallow water effects related to offshore terminals, and so we considered coupling a Boussinesq type of model with a BEM. The idea was to evolve the waves from deep sea waves entering a sloping bottom and thereby undergoing transformations. The advantage of Boussinesq models is that discretization is needed only along one horizontal strip, e.g. along the bottom. In a BEM the whole boundary is discretized and thereby more computationally demanding. A disadvantage of the Boussinesq models is maybe that they involve spatial derivatives in the horizontal directions. Solving the equations numerically typically involves using a finite difference scheme, and in that respect, numerical damping may be an issue. Numerical solution of a set of Boussinesq equations by finite elements is, however, reported in Sørensen et al. (2004) with application of waves entering a medium steep slope. Interesting results are also reported by Fuhrman et al. (2005) in an application of wave interaction with a bottom-mounted surface-piercing structure using the high-order Boussinesq type equations presented in Madsen et al. (2002). In all these work, two horizontal dimensions are considered.

We chose at an early stage not to pursue the approach of coupling Boussinesq and BEM type solvers. We have developed numerical wavetanks based on the BEM only. The wavetanks have been implemented such as to account for arbitrary bathymetry. The present nonlinear wavetank was used for studying waves interacting with a ship located near a steeply sloping bottom by Fredriksen (2008). In all the present applications of the numerical models, however, the water depth has been constant. We have not considered the nonlinear aspects of the transformation of waves entering from deep to shallow water.

We now turn to the formulation of the two-dimensional problem of a ship section by a bottom mounted terminal and the associated resonance problems.

Chapter 4

The physical resonance problem

In this chapter we introduce the two-dimensional hydrodynamical problem of a rectangular ship section by a bottom mounted terminal. We first present in Section 4.1 the geometric parameters in the problem. Next, for the reader to get acquainted with the two resonance phenomena that we denote the *piston-mode resonance* and the *coupled ship and piston-mode motion resonance*, we present in Section 4.2 a schematic and descriptive overview with some direct references to specific parts of the results from our analysis which are presented in Chapter 10. We emphasize that some parts of the discussion is not based on analysis only, but rather from observations during our case studies by means of model tests and simulations. However, we feel that several key features are enlightened and the evidence for our reasoning quite strong.

4.1 Formulation of the basic two-dimensional problem

Throughout the present study we have considered our ship section to be of a simple rectangular shape with sharp or rounded corners. A rectangle with sharp corners will resemble a typical mid-ship section of an LNG carrier which has rounded bilges including bilge keels. In the present study we have not investigated the effect of bilge keels; we have not considered ship section geometries with that degree of detail. We have only considered ship sections with 90° corners or with rounded corners. The details of the separated flow will certainly be different around a bilge keel compared to those around a corner of a rectangle, but the flow will always separate in both cases. This is illustrated in Figure

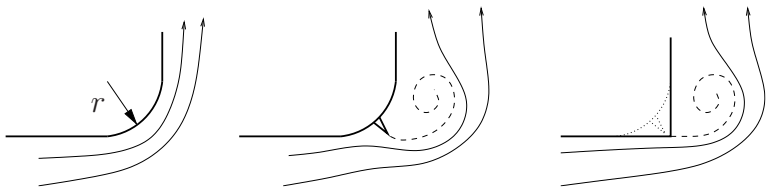

Figure 4.1: Instantaneous scenarios of flow around bilges. The flow will always separate around a sharp corner. Left: No bilge keel. The flow will still separate at sufficiently large KC-numbers, but not in the illustrated case. Middle: Bilge keel. Right: Sharp corner with bilge keel superimposed for illustration purposes.

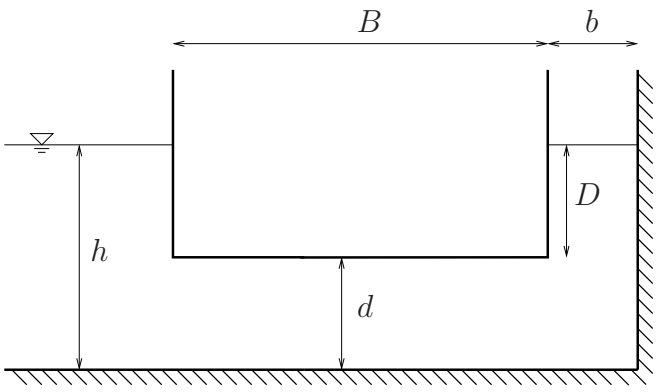

Figure 4.2: Dimensions in the problem of a ship section by a bottom mounted terminal: Water depth h, bottom clearance d, ship section beam or breadth B, ship section draft D and terminal gap width b.

4.1, where streamlines indicate the imagined flow pattern. The effect of the depth or size of the bilge keels on drag forces were investigated in Faltinsen and Sortland (1987). They showed significant increase in the drag with increasing bilge keel depth. This means the effect of separation increases with the bilge keel depth. We imagine that there would be a similar significant effect of bilge keel depth in the present case of a ship section by a terminal. This has not been investigated, though.

In Figure 4.1 we also define the bilge radius r. In the case of finite radius r the flow will separate provided the KC-number is sufficiently large, although in the figure we have illustrated non-separated flow. More discussion on that matter is provided in Section 10.1 in connection with the study involving a ship section with rounded bilges.

We define by B the ship beam or breadth and D the ship draft as illustrated in Figure 4.2. In the figure the vertical wall to the right of the ship section represents the bottom mounted terminal, and the distance from the ship section to the terminal is denoted b. We will throughout the work call the area between the terminal and the ship section the terminal gap, and b the terminal gap width. The still water depth is denoted h and the bottom clearance d.

There is a fair number of dimensions to consider in this problem. The beam-to-draft ratio B/D is a main parameter for the ship section hull itself. For an LNG carrier this is typically around $B/D = 4$. The ratio between the beam and the water depth B/h is a relevant parameter when considering finite water depth effects on ship section motion. Considering the terminal, the ratios between the terminal gap width and the ship section beam and draft, b/B and b/D, are relevant. If we consider forced motion of the ship section, these parameters describe the ability the ship has to disturb the fluid in the terminal gap when forced to move in heave and sway.

Choosing one single dimension to characterize our problem in full is of course not possible. However, if forced to make a choice, perhaps B is a reasonable candidate. It defines in a way the relative extent of the terminal gap and further, the distance from the "external" flow to the left of the ship section and to the "inner" flow in the terminal gap. We have in the present work mostly chosen B as our typical dimension of the problem and hence present variations of the other dimensions as nondimensional parameters with respect to B.

We will consider ship sections of different B/D ratios in settings with different water depths h and terminal gap widths b. The ship section will be subject to incoming regular waves of varying regular wave period T and wave steepness H/λ. It will also be forced in sinusoidal motion in heave with varying heave amplitude η_{3a}, or sway with varying sway amplitude η_{2a}. The results will in general be presented as function of the nondimensional wave frequency $\omega/\sqrt{g/B}$.

4.2 Resonant behaviour

In the gap resonance problem that we study in the present work, there is in principle an infinite number of resonance frequencies. Most of these are associated with modes of the free surface localized in the terminal gap. We refer to these localized modes as the sloshing modes. Note that we make a distinction between the sloshing modes and the piston mode, which is of a more global character. This should become clear shortly.

We want to remark that the approach taken in the present work is solving the linear and fully nonlinear problems by means of a BEM and not that of a modal method. With the chosen BEM we may not separate modes as such. We solve in principle the full problem without assumption of participating modes. We do, however, nevertheless find it useful to use the notion of modes in our discussion.

Now, unless the ship section draft D is very small relative to the terminal gap width b, that is, unless $D/b \ll 1$, these modes are similar to those in a closed rectangular tank of breadth b and water depth D. This is due to the exponential decay of the fluid motion under a traveling or standing wave, and that the fluid motion is near zero at $y = -D$, i.e. it is as if a horizontal solid boundary encloses the gap from below. The first mode is under the above restriction roughly that of a standing wave of wavelength $2b$. Then comes the higher modes. The first and higher modes all have their associated resonance frequencies. We note that there are also disturbances of the free surface in the terminal gap other than those caused by the sloshing modes. These are evanescent-like disturbances.

In addition to the sloshing modes, there is a zeroth mode which is usually referred to as the *piston mode*. The piston mode is characterized by that the fluid entrained in the terminal gap undergoes near uniform vertical oscillatory motion with a flat, horizontal free surface. This is illustrated in the left part of Figure 4.3. The piston mode has an amplitude which we call the *piston-mode amplitude* and denote it by A_g. More specifically, we define $A_g = H_g/2$, where H_g is the trough-to-crest height of the free surface averaged over the terminal gap. Following this definition of the piston-mode amplitude, it also holds in the nonlinear case where the magnitude of the trough might typically be slightly different from the magnitude of the crest. Associated with the piston mode is a resonance frequency which we denote the *piston-mode resonance frequency*. This will typically be lower than those of the sloshing modes. Hence, if the excitation frequency is in the vicinity of the piston-mode resonance frequency, the dominating part of the fluid motion is that of the piston mode, although also local evanescent-like disturbances of the free surface will be present. We denote this as piston-like behaviour. The piston-like behaviour is illustrated in the right part of Figure 4.3.

It is the piston-like behaviour we study in the present work. We hence do not study violent sloshing behaviour involving run-up and wave breaking, which is a typical feature of the internal resonance problem. The internal problem we refer to here is that of a closed

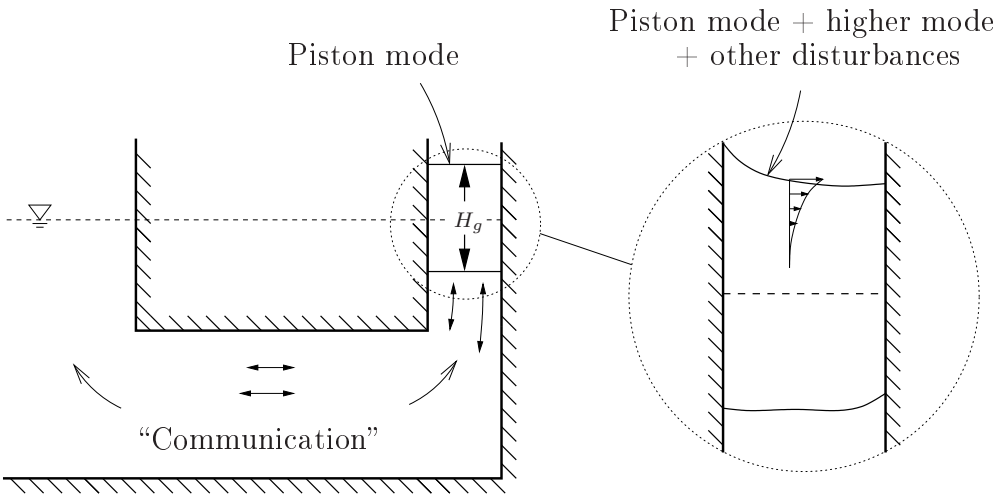

Figure 4.3: Illustration of the piston-mode motion. Piston-mode amplitude is $A_g = H_g/2$ where H_g is the crest-to-trough height of the free-surface elevation averaged over the gap. Higher modes hardly communicate with the outer flow while the piston mode must do so due to continuity of mass.

tank partially filled with liquid. The present external resonance problem differ from the internal one basically in the following two ways. First, in the external problem there exists a piston mode as just discussed. As a consequence of mass conservation this does not exist in the internal problem. Under forced heave of a partially filled tank, linear theory predict zero sloshing. We mention, however, that nonlinear effects may cause parametric resonance in that case. Second, in the external problem energy may in general escape via radiated waves. The radiated waves generated by the fluid motion in the terminal gap introduces damping, and hence the motion is kept at a finite level. The system is therefore, one might say, not forced to act in an essentially nonlinear manner. In the internal problem, under forced oscillation in sway at the natural frequency of an anti-symmetric mode, linear theory predicts infinite fluid response. In reality, the behaviour of that system around resonance is essentially nonlinear as described e.g. by Faltinsen (1974). If the depth is finite, in a two-dimensional tank, nonlinear Duffing type behaviour limits the fluid motion. See also thorough description of the three-dimensional case in Faltinsen et al. (2005) and Faltinsen et al. (2003).

The damping effect due to radiated waves in the external problem applies in principle to all modes in the terminal gap, although most pronounced for the piston mode, since the basic nature of the piston mode is such that it communicates appreciably with the external flow due to continuity of mass. This is illustrated as "Communication" in the left part of Figure 4.3. The higher modes will communicate with the external flow to a considerably lesser extent as the fluid motion decays roughly exponentially from the free surface.

There are two separate resonant problems associated with the piston-like behaviour. One is the resonant motion of the piston mode when the ship section is fixed or forced to oscillate. These are the usual diffraction and radiation sub-problems respectively. The resonant piston-like motion will be triggered whether excited by waves entering the system or by forced ship section motion, so disregarding which sub-problem, there is one single

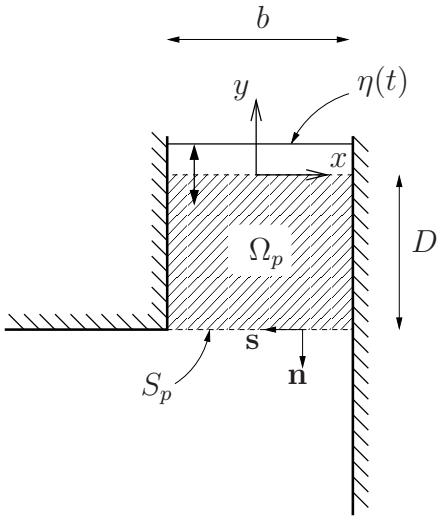

Figure 4.4: Simplified, linear hydrodynamical problem of piston-mode motion. The fluid motion within Ω_p is assumed uniform, so the shaded mass acts like a rigid body. S_p is the dashed (horizontal) curve only.

resonance frequency of the piston-mode motion, which we denote ω_p. This is what we have so far referred to as the *piston-mode resonance frequency*. Since the type of external resonance we investigate is also called gap resonance, we will use terms like *terminal gap* resonance and *piston-mode* resonance interchangeably. The other resonant problem appears when the ship section is free to oscillate. The system of the coupled ship section and piston-like fluid motion then exhibits two other natural frequencies, one associated with the stiffness in heave and the other with the stiffness in roll. We note that if the ship section is moored by linear, horizontal springs there will be another third resonance frequency associated with sway. We choose to call the one associated with the stiffness in heave the *coupled ship and piston-mode resonance frequency*, and denote it by ω_n.

In the following we describe how to obtain the piston-mode resonance frequency ω_p and the coupled ship and piston-mode frequency ω_n. We also include some discussion on the dependence on the geometric parameters as well as the overall behaviour of the system. We will throughout the work also refer to the resonance periods which are $T_p = 2\pi/\omega_p$ and $T_n = 2\pi/\omega_n$. Also, we will use the terms resonance and natural frequency, or resonance and natural period interchangeably.

4.2.1 Piston-mode resonance

An approximate method to estimate natural periods in gaps such as in the present case was derived within linear theory by Molin (2001) for the case of infinite water depth. The problem for finite water depth was treated by means of domain decomposition and finding relevant Green functions in Faltinsen et al. (2007). We have not in the present work undertaken a frequency domain analysis such as in their works. Rather, a time-domain approach has been taken. The resonance frequency of the piston mode ω_p is then found by performing forced motion of the ship section for a range of frequencies using the linear time-domain numerical wavetank which is described later in the text, and the

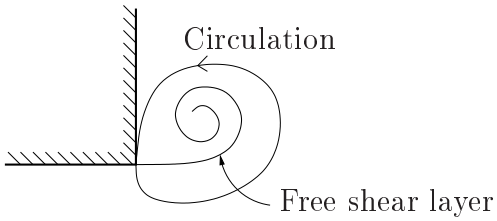

Figure 4.5: Illustration of the circulation introduced by the shed vorticity. The shed vorticity is in the present work assumed to be contained in thin free shear layers.

simulations run to steady-state. The resonance frequency of the piston mode, ω_p, is taken as the frequency for which the averaged amplitude of the free surface in the terminal gap attains a local maximum when plotted versus frequency.

The piston "body". The existence of a natural period of the piston mode is a consequence of the mass-spring type behaviour of the piston-mode motion. We illustrate this by the following simplified, linear analysis. The starting point of the analysis is as that of a moonpool in Faltinsen (1990) (see p. 99). We assume that the fluid motion in the whole terminal gap is uniform, and denote the flat free surface by $\eta(t)$ as illustrated in Figure 4.4. This means that all the fluid in the shaded area denoted Ω_p in the figure oscillates vertically with velocity η_t. Under the assumption of uniform fluid motion within Ω_p, the fluid in Ω_p will act just as a rigid body on the surrounding fluid. The equation of motion in heave of the piston "body" Ω_p is then

$$(\rho Db + A_p)\,\eta_{tt} + B_p\,\eta_t + \rho gb\,\eta = F_D. \tag{4.1}$$

where $A_p(\omega)$ and $B_p(\omega)$ are the added mass and damping coefficients of the piston body, respectively, and F_D is the excitation force. If we in (4.1) assume harmonic motion, $\eta = \eta_a e^{i\omega t}$, we may solve the homogenous problem to find the natural period $\tilde{T}_p$. The homogenous equation is $-\omega^2(\rho Db + \tilde{A}(\omega)) + i\omega\tilde{B}(\omega) + gb = 0$. The undamped natural period is, from this,

$$\tilde{T}_p = \frac{1}{2\pi}\sqrt{\frac{\rho Db + \tilde{A}_p}{\rho gb}}, \tag{4.2}$$

where $\tilde{A}_p$ is the added mass at the natural period.

We see from (4.2) that the natural period increases with the square root of the draft D. It further depends on the added mass term $\tilde{A}_p$. The added mass term will depend on all geometric parameters B, D, b and h. The exact behaviour is captured through a dedicated analysis only. It is not easy even to give a rough estimate on the dependence of $\tilde{A}$, as the added mass typically varies appreciably in such gap problems. In any case, it is maybe not so rewarding to make a detailed investigation of this simplified problem of uniform flow in the present gap-resonance context, as it is not an exact approach; the fluid flow along the lower parts of Ω_p will not behave as the assumed uniform flow. However, what we have illustrated in this description, is that the piston mode to a certain extent may be thought of as a rigid body. An explicit approximate formula for T_p is given by Molin (2001) in the case of deep water and small b/B ratio. The error in his formlula is $\mathcal{O}\{(b/B)^2\}$.

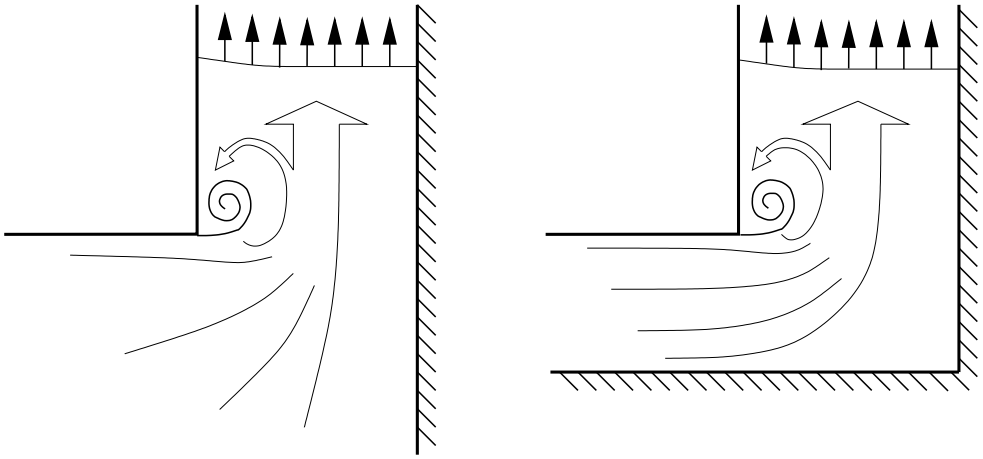

Figure 4.6: Schematics of the effect of circulation. Left: Deep water. Right: Finite water depth.

Effect of flow separation. What we have shown in the previous paragraphs is that the piston mode in the terminal gap behaves like a damped, linear harmonic oscillator. Therefore, the response level relative to the level of excitation is at resonance directly dependent on the level of damping, where linearly, damping is manifested through wave radiation only. This is the potential flow damping. In reality, however, the flow separates at the sharp corner. In other words vorticity is shed into the bulk of the fluid with the main consequence that circulation is introduced as illustrated in Figure 4.5. The circulation is roughly speaking 45deg out of phase with the relative ambient flow, such that the phase creates a back-flow acting as a damping. This is further conceptually illustrated in Figure 4.6. The damping effect of flow separation on the piston-mode amplitude due to forced heave of the ship section is found significant in the study presented in Section 10.1, as also described in Kristiansen and Faltinsen (2008). The results from the study further indicate that nonlinear effects associated with the nonlinear boundary conditions are small.

4.2.2 Coupled ship and piston-mode resonance

The terminal gives rise to a coupling between the fluid flow and all three modes of rigid-body motion of the ship section; sway, heave and roll. This is in contrast to a ship section in open waters, where there is for symmetric bodies a coupling between sway and roll only. The coupling between all three modes of motion and the piston-mode motion is an essential feature of our problem. There is in particular no pure heave resonant motion, only that of the coupled ship section and fluid motion.

If considering the steady-state velocity potential as a function of complex frequency, resonances are related to poles in the complex-frequency domain that lies close to the real frequency axis, see e.g. McIver (2005). In that work, he analyzed the gap problem for both the radiation, diffraction and freely oscillating problem by a linear potential flow analysis. He investigated the behaviour around simple poles of the complex potential. He first shows that the poles are the same in all the three radiation problems and the diffraction problem. He next considers the homogenous solution of the equations of motion. The added mass

and damping as well as excitation forces from the radiation and diffraction problems are hence included. He checks for what he calls consistence to see if the radiation/diffraction natural frequency ω_p is existent in the equations of motion. His analysis shows that this is not so. An exception exists if the ship section is fixed in one or two degrees of freedom. The system may then retain the ω_p resonance. Further, he shows that in general, $\omega_p \neq \omega_n$. He describes this as a shift in the resonance frequency, from ω_p to ω_n. The coupled ship and piston-mode behaviour is thus, when free to oscillate in all three degrees of freedom, in resonance at ω_n only. The practical implication is that when the ship section is free to oscillate, the coupled ship and piston-mode motion will be considerable around ω_n only.

Assuming no moorings, there are two resonance frequencies. These are found from the two zeros of the determinant of the system of the three coupled equations of motion when assuming steady-state motion $e^{i\omega t}$. That is, the equations of motion in sway, heave and roll. As we stated earlier, the one associated with the stiffness in heave is what we call the coupled ship and piston-mode resonance frequency ω_n. The required added mass and damping coefficients are in the present work found from forced motion simulations using the linear time-domain wavetank presented later in the text. The simulations are run to steady-state and the hydrodynamic coefficients extracted from steady parts of the time-series. The procedure is standard and explained in more detail in Section 10.3.

We now discuss the mechanisms that drives the coupled ship and piston-mode motion. In the discussion we consider only sway and heave. The reason we do not include roll, is that it was not included in the concrete example that will be given shortly. Roll should in principle also have been considered.

Now, considering sway and heave only, there are three excitation mechanisms for the piston-mode motion; sway, heave and the external flow. By external flow we mean the incident waves. The relative phasing between the three excitation mechanisms is crucial for the level of response in the terminal gap, i.e. the achieved steady-state piston-mode amplitude A_g. As a special case, if the ship motion resonance period T_n is low enough so that the fluid motion induced by the incoming wave does not "reach" into the terminal to any significant extent, the direct communication between the external flow and that in the terminal gap is small and the ship motion becomes the major excitation mechanism of the fluid in the terminal gap. Large piston-mode amplitudes are then achieved when the sway and heave motion is close to 180deg out of phase, meaning the ship moves downwards and towards the terminal simultaneously. However, with a relative phasing of around 0deg, the terminal gap response may be almost canceled. Large ship motions may, however, be experienced also in this case. The relative phasing between sway and heave motion in steady-state conditions seems in our experience to be quite sensitive to the b/B ratio. This matter is discussed more in Section 10.3.

On the other hand, from a ship section point of view the excitation forces acting on the ship are due to the fluid flow which we may conceptually divide into two parts; the external flow and the terminal gap flow. The relative phasing between the external forces are then crucial for the ship motion response level. It is the net force that the ship section responds to.

At resonance, the amplitude of the ship motion is proportional to the net force and also inversely proportional to the damping. Waves radiated both as a consequence of the ship section motion and the piston-mode motion contribute to the potential damping.

A concrete example. We now give a concrete example taken from the study of

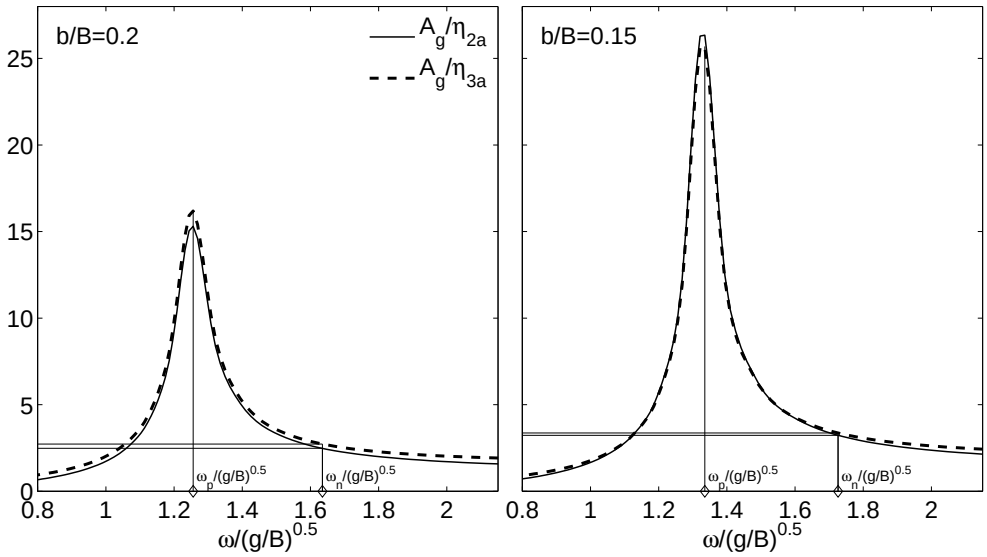

Figure 4.7: Nondimensional piston-mode amplitude due to forced motion of the ship section. Left: $b/B = 0.2$. Right: $b/B = 0.15$. A_g is the piston-mode amplitude. η_{2a} is the amplitude of the forced sway motion and η_{3a} is the amplitude of the forced heave motion. The natural frequencies of piston mode $\omega_p = 2\pi/T_p$ and coupled ship and piston-mode motion $\omega_n = 2\pi/T_n$ are indicated.

a moored ship in Section 10.3. The rectangular ship section has beam to draft ratio $B/D = 4$, the water depth is $h/B = 2.2$ and we consider two terminal gap widths $b/B = 0.2$ and $b/B = 0.15$. The natural frequencies of the coupled ship motion and piston-mode motion were $\omega_n/\sqrt{g/B} \simeq 1.635$ and $\omega_n/\sqrt{g/B} \simeq 1.726$ for the two cases respectively. From the linear solution the steady-state amplitudes of the piston-mode motion and sway and heave motion was in both cases

$$\begin{aligned} A_g/A &\simeq 15, \\ \eta_{2a}/A &\simeq 2.5 - 3, \\ \eta_{3a}/A &\simeq 2 - 2.5, \end{aligned} \tag{4.3}$$

where A is the amplitude of the undisturbed, incoming wave.

In both cases the direct communication between the external flow and that in the terminal gap was quite weak around the resonance frequency ω_n. This conclusion was reached based on the following check. We performed simulations with the ship section fixed and subject to incoming waves at the frequency ω_n, with a resulting piston-mode amplitude of $A_g/A \simeq 0.4$. Since a piston-mode elevation $A_g/A \lesssim \mathcal{O}(1)$ is negligible in the current discussion, the communication between the external flow and that in the terminal gap was mainly via the ship motion.

Further, from the simulations it was clear that around ω_n, the relative phasing between sway and heave was close to 180deg. This means the ship section moved downwards and towards the terminal simultaneously. In light of the discussion above, the achieved piston-mode amplitude should then be a superposition of that resulting from forced sway and forced heave separately. This was in fact what we found. This should become clear from the following.

The piston-mode amplitude due to forced sway and heave is presented as function of forcing frequency in Figure 4.7. The amplitude of the forced sway motion is denoted η_{2a} and the amplitude of the forced heave motion is denoted η_{3a}. In these two particular cases, the terminal gap response due to sway and heave is very similar, but the behaviour will depend on the beam to draft ratio B/D. With a smaller B/D ratio, sway will induce larger piston-mode amplitudes than heave, and with a larger B/D value, the heave will induce the largest piston-mode motion. What is the key information in the figure, is the level of response at the natural frequency ω_n. This is indicated by vertical and horizontal lines in the figure. We see that the piston-mode amplitude per unit motion of the ship in both sway or heave at ship motion resonance ω_n is approximately 2.5 - 3. This means that superposing a unit amplitude in sway and and a unit amplitude in heave with a relative phasing of 180deg should result in 5 - 6 units piston-mode amplitude. Now, with approximately 2.5 units of ship section motion in both sway and heave as that indicated in (4.3), we shold get about 12 - 15 units of piston motion. This is what we got, as seen from (4.3).

Effect of flow separation. So far we have discussed the linearized solution only. What we have illustrated is that, given the ship motion, and under the condition that the excitation of the piston-mode motion was mainly via the ship, the terminal gap elevation was predicted well by linear theory using forced motions. The problem which is not taken into account by linear theory is of course the flow separation. In reality, the flow separation must be modelled in order to find the actual ship motion near resonance. And so, we need to include the flow separation directly in our analysis. This is what we have done in the present work and present in the main study in Section 10.3.

A comment on three-dimensional effects. We want to comment on that the present work has only considered the two-dimensional problem, whereas all realistic situations are three-dimensional. In the problem of a ship by a terminal, waves will be scattered in all directions and in particular radiate from the fore- and aft ends of the structures. This means there is a further damping effect associated with these openings, as the wave radiation represents an energy flux out of the system. This radiation is captured by linear potential flow theory. However, a three-dimensional viscous effect is that investigated in Aarsnes (1984), where the effect of flow separation from the fore- and aft ends of a ship in open waters (i.e. without terminal) was considered. Seen from above the flow separation from the longitudinal extremities induces a back-flow, thereby reducing the in-flow velocity on the bilge keels resulting in less vorticity shed from these. In the present context, the net effect from this phenomenon on the piston-mode resonance is not easily deducted without detailed investigation.

Chapter 5

Numerical wavetank - the basics

In this chapter we explain the basics of our time-domain numerical wavetanks. The plural form "wavetanks" refers to a linear as well as a fully nonlinear wavetank. The inclusion of the free shear layer and in- and out-flow of boundary layers are explained in the two next chapters. We here introduce the boundary integral equation on which all of the numerical work is based, and its discretized version in terms of a set of boundary element equations leading to a Boundary Element Method (BEM). Evolution in time is achieved by adopting the Mixed Eulerian - Lagrangian (MEL) approach. In the Eulerian phase we solve the boundary element equations, whereas in the Lagrangian phase the free surface as well as the potential on the free surface are stepped forward in time according to the free-surface conditions using the solution acquired in the Eulerian phase.

None of the theories in this chapter are new to this work; the boundary integral equations, the BEM as well as the MEL approach are well established in the literature. One may therefore argue that some of the following text is, strictly speaking, unnecessary. We feel, however, that neglecting to include the following theory would leave the present text incomplete and the work nearly impossible to reproduce, in particular that regarding the alternative force expression in Chapter 8, where e.g. sign conventions are crucial. We therefore proceed by introducing the boundary integral equation.

5.1 Boundary integral equation

The Laplace equation (2.1) is our governing equation for the fluid flow in $\Omega \cup S$ (cf. Figure 2.1) given in so-called strong, or differential form. This may, along with proper boundary conditions, be recast into a weak, or integral form upon applying Green's second identity, leading to a boundary integral equation. The re-writing is of a purely mathematical character. Therefore, after the statement of the integral equations, we include a short discussion on how to interpret the boundary integral, which in our opinion is quite useful for understanding the physical fluid flow of our problem.

We assume that the velocity potential $\varphi(\mathbf{x})$ that we aim at solving for is analytic for all $\mathbf{x} \in \Omega \cup S$. In order to apply Green's second identity we need to introduce another function ψ. If this is harmonic in Ω, we have $\nabla^2\psi = 0$. Then,

$$\int_\Omega \left(\varphi\nabla^2\psi - \psi\nabla^2\varphi\right) \mathrm{d}\Omega = 0 \tag{5.1}$$

We now take $\psi = \log r$, which is the fundamental solution of the Laplace equation in free space. This function is singular at the point $r = 0$, where $r = ((x-\xi)^2 + (y-\eta)^2)^{1/2}$. We call $\mathbf{x} = (x, y)$ the field point and $\boldsymbol{\xi} = (\xi, \eta)$ the location of the singularity. If we let $\mathbf{x} \in \Omega \cup S$, from (5.1) and Green's second identity we get

$$0 = \int_{S_1} \left(\varphi \frac{\partial \psi}{\partial n} - \frac{\partial \varphi}{\partial n} \psi \right) \, \mathrm{d}s + \int_S \left(\varphi \frac{\partial \psi}{\partial n} - \frac{\partial \varphi}{\partial n} \psi \right) \, \mathrm{d}s, \tag{5.2}$$

where the integration is with respect to $\boldsymbol{\xi}$. S_1 is introduced in order to exclude the singularity. This is explained in connection with Figure A.1. After the limiting process described there, we obtain the boundary integral equation that we will use for our numerical work, which is

$$\alpha(\mathbf{x})\varphi(\mathbf{x}) = \int_S \varphi(\boldsymbol{\xi}) \frac{\partial \psi(\boldsymbol{\xi}, \mathbf{x})}{\partial n_\xi} \, \mathrm{d}s - \int_S \frac{\partial \varphi(\boldsymbol{\xi})}{\partial n_\xi} \psi(\boldsymbol{\xi}, \mathbf{x}) \, \mathrm{d}s. \tag{5.3}$$

Here, $\alpha(\mathbf{x})$ is the internal angle measured counter-clockwise, being e.g. -2π when the field point $\mathbf{x}$ is away from the boundary and $-\pi$ when on a flat part of the boundary. $\partial/\partial n_\xi = n_x \, \partial/\partial \xi + n_y \, \partial/\partial \eta$ is the normal derivative with respect to the integration parameter. When the field point $\mathbf{x}$ is on the boundary, the first integral in (5.3) must be interpreted as a principal value integral. The contribution from that integral is explicitly given by the term on the left hand side.

$\psi = \log r$ is within the theory of fluid mechanics referred to as a source. Differentiating the source with respect to $\boldsymbol{\xi}$ one obtains what is referred to as a dipole. The dipole has a direction, and when differentiating in the n_ξ-direction, it is called a normal dipole. The functions are

$$\begin{aligned} \psi(\boldsymbol{\xi}, \mathbf{x}) &= \log r \qquad && \text{(Source)}, \\ \frac{\partial \psi(\boldsymbol{\xi}, \mathbf{x})}{\partial n_\xi} &= \frac{\partial}{\partial n_\xi} \log r \qquad && \text{(Normal dipole)}, \end{aligned} \tag{5.4}$$

which are also often referred to as Rankine singularities in the present context. These are singularities that do not satisfy any boundary conditions, they are solutions of the infinite fluid case. With the present choice of ψ, the boundary integral equation (5.3) expresses a distribution of Rankine singularities over the boundary S.

The dipole attains a stronger singularity at $r = 0$ than the source. A source has a range of influence far beyond that of a dipole of the same strength, but the dipole has a more pronounced influence in its immediate neighbourhood, for physically, the range is proportional to the induced velocity which is the gradient of the potential, being proportional to $1/r$ for the source and $1/r^2$ for the dipole. These facts are keys in understanding how the fluid reacts when disturbed.

The source distribution represents the motion of a boundary. In the boundary integral equation (5.3), the source strength $\partial\varphi/\partial n_\xi$ represents the normal velocity of the solid boundaries, and is known via the solid body boundary condition (2.5). The role of the dipoles is not interpreted as easily. It is two-fold. Firstly, they ensure locally that no flow induced by sources or dipoles elsewhere induces flow through the wall at its position, and secondly induce flow felt in its neighbourhood, which depending on the characteristics of the problem may be globally significant or not. In any case, the dipole strength represented by φ is known on the free surface via the free-surface boundary condition (2.3).

We mention that the so-called desingularized boundary element methods exists where point singularities are distributed along fictitious lines outside the boundary S of the domain, as well as outside the fluid domain. According to the principle of distributing sources and dipoles for constructing a solution as discussed above, this is another way of doing that. However, the method is actually based on assuming analytic continuation of the potential outside the considered domain. Due to this assumption, there are limitations on how to go inside a body with sharp corners and also how to treat the intersections between the free surface and solid boundaries. Singularities must be distributed there, and care must be taken in doing that. We have not in the present work used or investigated this method, but the desingularized method has been applied e.g. by Schønberg and Rainey (2002) to study green water loading and Lalli (1997) to study the wave resistance problem. They point out that a disadvantage of the desingularized method is that an ill-conditioned matrix system appears if the position of the point singularities are not carefully chosen. The argument for using the desingularized method, however, is according to Lalli (1997) a faster solver, ease of implementation and avoiding strong singularities associated with higher order methods. On the other hand, it is expected that the accuracy of the solution at intersection points between the free surface and a solid surface such as a body, is reduced relative to the method applied in the present case where singularities are distributed along the boundary itself.

5.2 Wave making and absorption

There are two main strategies for generating waves in a time-domain numerical wavetank. The first is by moving a part of the solid boundary. This is rather straight-forward in a BEM, and the chosen strategy in the present work. This was found most convenient since we have a closed tank. The second is by imposing analytic values for the fluid velocity along a vertical control surface as well as imposing the corresponding free-surface elevation there. This is a convenient way to do it if the wavetank is not closed. This strategy has been adopted e.g. by Baarholm (2001) where he investigated the two-dimensional problem of slamming underneath platform decks using a fully nonlinear time-domain wavetank. He modelled parts of the free surface only, and the water depth was infinite. The domain was restricted laterally by a control surface on one side, and a numerical damping zone on the other. On the control surface he applied the analytic results in infinite water depth as given by Bryant (1983). The fully nonlinear solution is there given as a series, which in practice is truncated. In finite depth, similar solutions are given by Rienecker and Fenton (1981).

In the present work, both the piston and single flap type wavemakers are implemented. During the present study only regular waves have been considered. See Figure 3.1. The user prescribes the wavemaker type and height of the paddle h_{wm}, the wave period and a desired (linear) steepness, and the stroke S is calculated from the Bièsel transfer functions (3.4). Alternatively, the wavemaker stroke $S(t)$ may be given as a time-series provided by means of a text-file generated a priori, allowing e.g. for reproduction of model tests or for irregular wave generation. We have used the latter extensively during the present work. We have not, however, considered irregular waves.

A numerical damping zone is used to damp out waves in the far-field. There are several possible ways to achieve wave damping as discussed e.g. in Newman (2008). We

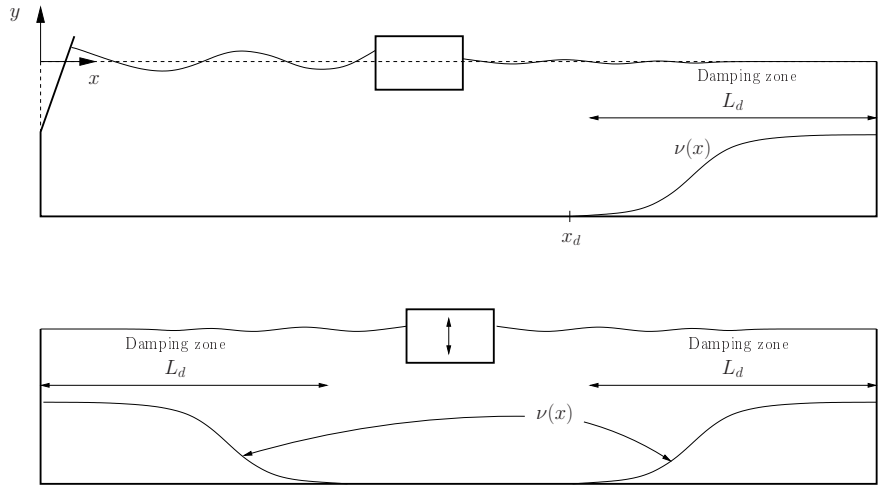

Figure 5.1: Illustration of numerical damping zone parameter $\nu(x)$. Typical scenarios of a body in incoming waves (upper) or in forced heave motion (lower).

follow that described by Clement (1996), where artificial dissipation terms are added in the free-surface conditions, here chosen to be proportional to the vertical coordinate of the free surface y and the potential φ in the kinematic and dynamic free-surface conditions, respectively,

$$\begin{aligned} \frac{\mathrm{D}\mathbf{x}}{\mathrm{D}t} &= \nabla\varphi - \nu y \quad \text{on} \;\; S_F, \\ \frac{\mathrm{D}\varphi}{\mathrm{D}t} &= \frac{1}{2}\left(\frac{\partial\varphi}{\partial x}\right)^2 + \frac{1}{2}\left(\frac{\partial\varphi}{\partial y}\right)^2 - gy - \nu\varphi \quad \text{on} \;\; S_F. \end{aligned} \tag{5.5}$$

Here $\nu = \nu(x)$ is typically a smooth function which is nonzero in the damping zone, and zero elsewhere. See Figure 5.1. It is taken such as to smoothly increase up to a value ν_{max}. The interval over which $\nu(x)$ is nonzero is denoted L_d. Since the function should be smooth to minimize reflections, it must vary with x. The function ν is from (5.5) not explicitly a function of x, it rather has the dimension of frequency $1/s$. This indicates a dependence on wave frequency or equivalently wave number, or equivalently, wavelength. The dependence on wavelength justifies the spatial variation. Choosing the actual shape of $\nu(x)$ is a matter of experience, and we have chosen the shape of a third order polynomial as $\nu(x) = \nu_{max}(-2\hat{x}^3 + 3\hat{x}^2)$, where $\hat{x} = (x - x_d)/L_d$, where x_d is described in Figure 5.1. During our work we have usually taken L_d to be a multiple of the wavelength. Typical values are $L_d = 3\lambda - 6\lambda$. The actual value of ν_{max} is determined empirically, typically depending on water depth and L_d. The empirically based damping zone is found to work satisfactory.

As kh decreases, the effectiveness of the damping strategy in (5.5) will decrease. The strategy provides no damping in the shallow water limit. This was discussed in detail by Clement (1996). So for example the front of a wave train is not effectively damped out. A piston-type strategy at the far end of the tank is then appropriate, as suggested by Clement (1996). He presented a simple piston-type damping strategy based on control theory, and demonstrated its effectiveness for small kh. Such a piston-type damping device has not been implemented in the present work.

5.3 The Boundary Element Method

The BEM is the discretized version of the boundary integral equation (5.3). The boundary of the fluid domain, S, is divided into elements of some prescribed shape, and the variation of the unknowns over each element assumed to be of a certain order. A so-called low order method assumes constant value of variation of the unknowns over each element, while a higher order method assumes a linear or higher order of variation of the unknowns over each element. Typically, one assumes a similar order of the shape of the elements as that assumed of the variation of the elements. What one chooses is more or less a matter of taste.

Assuming a constant variation over each element, the boundary conditions are typically satisfied at the mid-point of each element, and with a higher order variation it is satisfied at several collocation points on each element. Methods with constant variation has been applied in studies on slamming by several authors and with good results, e.g. Baarholm (2001) and Zhao and Faltinsen (1993). Note that in their works, a parabolic fit of the free surface was introduced in order to properly conserve mass near the body in connection with the kinematic free-surface condition. Linear variation over each element, with piecewise straight elements, has been adopted with success for a nonlinear numerical wavetank by Greco (2001). A method for free-surface flows using arbitrary high order is presented in Landrini, Grytøyr, and Faltinsen (1999).

A consequence of choosing a higher order method is that we satisfy the boundary conditions at singular points involving convex corners of the domain as well as the intersection between the free surface and solid boundaries. Although a higher order variation provides a better description of the solution in the main part of the domain, it does not provide a more accurate solution at the singular points. It is perhaps natural to expect problems of numerical character associated with the singular points due to the lack of proper mathematical modelling. However, the works referred to above presents numerical results that are of good quality.

In the present work we have chosen piecewise linear elements and a piecewise linear variation of the unknowns over each element. When dealing with propagating wave problems, higher order variation (including linear) is perhaps more commonly used than constant variation, judging from the literature. We believe that for propagating waves over several wavelengths and over many periods it is proper to use a linear variation.

We divide the boundary S into a total of N straight elements. A linear variation of some quantity z over element j is then

$$z = \frac{z_{j+1} - z_j}{s_{j+1} - s_j} s - z_j \quad \text{on } S_j. \tag{5.6}$$

In the present context, z represent φ, φ_n or $\mathbf{x}_F$, and s is the arc length along the element. As introduced earlier, $\mathbf{x}_F$ are the free-surface coordinates. The boundary integral equation (5.3) is satisfied at the N end points $\mathbf{x}_i$ of the elements, hereafter called nodes. The two integrals in (5.3) become sums of $2N$ integrals, each over an element S_j, and the discrete version of (5.3) is given by (A.1). Re-arranging the terms such that the known quantities are on the right hand side and the unknowns on the other, we obtain a linear system of N equations in N unknowns, say

$$Ax = b, \tag{5.7}$$

where the unknowns in x are the values of φ_n and φ on the free-surface and the solid boundary nodes, respectively.

We require the potential to be continuous at the intersections between the free surface and solid boundaries, such that φ is known through the dynamic free-surface condition at these points. The unit normal vector is here essentially discontinuous and the normal velocity therefore double valued, with that on the wall known through the body boundary condition while that on the free surface is an unknown.

5.4 Time-stepping - the Lagrangian phase

Once the solution x in (5.7) is obtained as just described, the potential and the free-surface position are updated according to the free-surface conditions (2.3) and (2.4) respectively. The free-surface conditions are both ordinary differential equations of type $\dot{z} = f(t, z)$, with z being the potential φ or the free-surface position $\mathbf{x}_F$, while f is $0.5\,\varphi_n^2 + 0.5\,\varphi_s^2 - gy$ or $\nabla\varphi$ in the two free-surface conditions respectively. In the present work we use an explicit Runge-Kutta method of order m for time integration scheme. The explicit Runge-Kutta methods are predictor-corrector type of schemes, that is the right hand side of the ordinary differential equation f is estimated, iteratively, m times at positions updated from the previous estimate, and the final f taken as a weighted sum of the estimates. This means that the boundary value problem must be solved at least m times each main time-step. When solving the fully nonlinear problem, the system matrix A in (5.7) must be constructed each sub-step, whereas in the linear case where the computational domain does not change, the system matrix is constructed and inverted once at the beginning of the simulation. The system (5.7) must, however, be solved each sub-step also in the linear case.

The present implementation is such that an arbitrary order up to $m = 4$ may be chosen. For higher orders, the number of predictions needed is higher than the achieved order, see e.g. Iserles (1996). Typical choices in our field is order two or four. Order one is also used, but seems from the literature to be less popular in the context of time-domain BEM codes. There is always a trade-off between computational time and accuracy, and in the present work we have preferred the fast convergence provided by the fourth order scheme on the expense of doubled computational time relative to order two. The classical explicit Runge-Kutta fourth order scheme is

$$z^{n+1} = z^n + \frac{\Delta t}{6}\,(f_1 + 2\,f_2 + 2\,f_3 + f_4) \tag{5.8}$$

where Δt is the length of the main time-step, the super-script n means main time-step number, and

$$f_1 = f^n, \quad f_2 = f^n + 0.5\,\Delta t\,f_1, \quad f_3 = f^n + 0.5\,\Delta t\,f_2, \quad f_4 = f^n + \Delta t\,f_3. \tag{5.9}$$

Choosing the type of time integration scheme is a matter worth attention. Attention must, however, also be given to how to actually update the position of the nodes, i.e. how to calculate the right hand side f. Due to our choice of having the collocation points at the nodes, the unit normal and tangential vectors are not uniquely defined there. We have chosen to introduce averaged unit vectors $\bar{\mathbf{n}}_j$ and $\bar{\mathbf{s}}_j$ at the nodes as illustrated in Figure 5.2. In the present a second order polynomial $y(x)$ is fitted through the node j

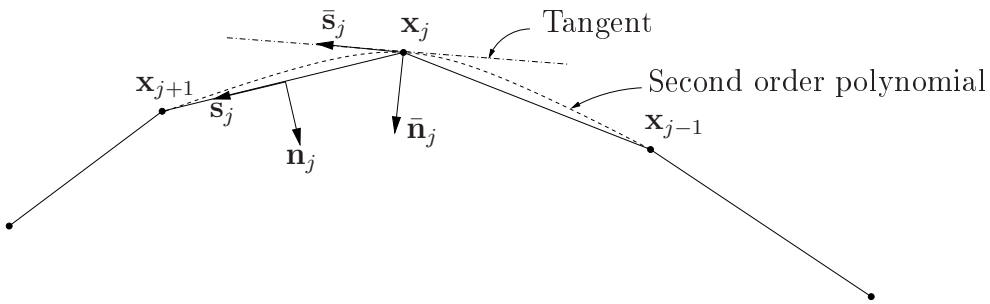

Figure 5.2: Average unit normal and tangential vectors $\bar{\mathbf{n}}_j$ and $\bar{\mathbf{s}}_j$ at nodes estimated by the tangent of a second order polynomial fitted through the node itself and its two neighbouring nodes.

and its two neighbouring nodes. The tangent of the polynomial at node j is taken to represent the tangential direction. At intersection points, $\bar{\mathbf{n}}_j$ and $\bar{\mathbf{s}}_j$ are taken as $\mathbf{n}$ and $\mathbf{s}$ at its neighbouring element. The position of node j is hence updated by the velocity

$$(\nabla\varphi)_j \simeq (\varphi_n)_j\,\bar{\mathbf{n}}_j + (\varphi_s)_j\,\bar{\mathbf{s}}_j, \tag{5.10}$$

where the normal velocity $(\varphi_n)_j$ is the solution from (5.7), and the tangential velocity $(\varphi_s)_j$ estimated by difference-schemes correct to second order in a curvilinear manner, using central differences at the main part of the free-surface nodes, while forward and backward differences at the intersections. Expressions for the difference schemes are given by the expressions (A.4) - (A.6).

In the construction of the second-order polynomial above, we represent the free surface by the vertical coordinate as a function of the horizontal coordinate, $y(x)$. This limits the applicability to a non-overturning free surface. This is, however, a limitation which has no practical limitations in the present work. Throughout our studies, we did not consider any breaking waves. A plunging breaker would introduce problems in long-time simulations without proper handling of these, and this was outside the scope of the present project. In case one wishes to study overturning waves, however, the method is easily modified by the following approach. For each node j, rotate the two neighbour elements S_{j-1} and S_j such that the two far end-points $\mathbf{x}_{j+1}$ and $\mathbf{x}_j$ lie in the horizontal plane. Then compute the second order polynomial in this rotated plane to obtain the tangent there. Calculate the unit vectors in the rotated plane based on the tangent. The unit vectors $\bar{\mathbf{n}}_j$ and $\bar{\mathbf{s}}_j$ in the physical plane are obtained by rotating these back to the physical plane.

5.4.1 The intersection point between the free surface and a solid boundary

Since, as discussed earlier, within the framework of potential theory the intersection points between the free surface and solid boundaries are singular, there is no way that we may represent the physics in an absolute sense here. Thorough analysis of the problem of a wavemaker of both sudden and infinitely smooth start-up assuming linear potential flow theory is presented in Roberts (1987), where he demonstrates that the solution in the very near vicinity of the wavemaker attains a spatially oscillatory behaviour with the amplitude finite, but the wave number increasing to infinity when approaching the singular point.

Note that this is a consequence of assuming linear theory. The oscillatory behaviour is not captured in the present linear wavetank, as we in general discretize the free surface such that these oscillations are on a much smaller scale than the first element. This lack of modelling is thought not to be of significance in the present work.

However, there are inconsistencies introduced by the discretization; the velocity computed based on φ_n and φ_s on the free surface is in general not consistent with that imposed on the solid surface. Effort should be made on treating this matter as consistent as possible. We tried two methods, where the latter was found superior to the first, providing more stable long-time simulations. In the first method, the position of the intersection node was updated simply according to (5.10), and next extrapolated/interpolated along the newly defined free-surface element onto the new position of the solid boundary. This was found to work satisfactory except for long time simulations with large motion of the solid boundary. This caused saw-tooth type of instabilities on the free surface in the terminal gap in cases of large ship section motion. An improved, probably more consistent method was as follows. First denote by $\mathbf{u}$ the velocity from (5.10). Next, this is projected onto the solid boundary providing a velocity component along the wall $u_{sw} = \mathbf{u} \cdot \mathbf{s}_w$, where the subscript w refers to "wall". The node velocity is then taken as

$$\nabla\varphi = u_{nw}\,\mathbf{n}_w + u_{sw}\,\mathbf{s}_w, \tag{5.11}$$

where $u_{nw} = \mathbf{U} \cdot \mathbf{n}$ is given by the solid boundary condition (2.5). This is thought to give a more consistent motion seen from the solid boundary point of view.

There are also other, similar choices, such as the "double node" approach explained in Tanizawa (2000). The idea of the double node approach is to require that $\mathbf{n}_w \cdot \mathbf{u} = u_{nw}$ and $\mathbf{n}_f \cdot \mathbf{u} = u_{nf}$. Here, $\mathbf{u} = (u_x, u_y)$ is the unknown and desired velocity vector of the intersection point, u_{nw} is the prescribed normal velocity of the wall at the intersection point, and u_{nf} the normal velocity of the free surface at the intersection point. This yields two equations for the two unknown velocity components, u_x and u_y, which is readily solved for. We see that the double node approach does not make use of the tangential velocity along the free surface, φ_s, and hence avoids the use of a finite difference scheme which is necessary for estimation of that quantity.

5.4.2 Mass conservation in the numerical scheme

Mass conservation is the core of our method, expressed by the Laplace equation and reformulated in the boundary integral equations. At each time-step we calculate the exact volume V of the discretized surface using Gauss's theorem (see Section D.2), for example by

$$V = \int_S y\, n_y \,\mathrm{d}s \tag{5.12}$$

since $V = \int_\Omega 1 \,\mathrm{d}\Omega$ and $\nabla \cdot (0, y) = 1$.

The spatial discretization naturally introduces errors, as does the temporal discretization. Throughout our work we have checked the level of error in this respect in all cases. We typically observe a nearly sinusoidal variation of V, but in no cases any sign of increase or decrease of the volume. The oscillation amplitude decreases with decreasing time-step. Except for some of the very early work, the amplitude has been within $V/V_0 \sim \mathcal{O}\,(10^{-6})$, where V_0 is the initial volume at still water conditions.

5.5 Dynamic re-gridding of the boundaries

Dynamic re-gridding of the discretized boundary is applied in the nonlinear wavetank in order to make it possible to impose a resolution at a certain level. The discretization of the boundary S is initially prescribed. Typically, a cosine distribution of elements is used along each part of the boundary, as described by (A.8). Note that the parameter β in (A.8) indicates the degree of refinement towards one or both ends of the selected part of the boundary. What we mean by a "parts of a boundary" in this context is either one side of the ship section, the terminal wall, the wavemaker, the sea floor or the two separated parts of the free surface. A gradually refined grid with refinement near the ends as provided by this kind of distribution is considered good practice, in particular towards intersection points between the free surface and a solid part of the boundary. However, with a fine discretization near an intersection point the need for re-gridding is evident.

The implementation of dynamic re-gridding was in the present work mainly inspired by the large vertical piston-mode motion in the terminal gap. Re-gridding the right side of the ship section and the terminal was found necessary. The implementation was, however, done slightly more general than only to include the terminal gap area. The two closest elements near any of the intersection points between the fluid and the solid boundaries are split upon exceeding 1.8 of their original lengths, and removed if smaller than 0.4 of the original lengths. There is no re-gridding applied on other parts of the boundary other than the elements closest to the intersection points. The re-gridding is applied at the end of each main time-step.

The potential is linearly interpolated when splitting a free-surface element. During our work we experienced some parasitic oscillatory saw-tooth like behaviour of the free surface nodes closest to an intersection point following re-gridding of the free surface. We believe that the parasitic oscillations are associated with the linear interpolation of the potential when splitting an element, which we suspect is too crude. We have not considered more refined interpolation strategies, such as using cubic spline interpolation, but have from communication with other researchers the feeling that the goodness of the re-gridding of the free surface is sensitive to these issues. We have hence tried to keep the occurrence of re-gridding of the free surface at a minimum. In our application of a ship section by a terminal, re-gridding is typically associated with two phenomena: Stokes drift and large sway or roll motion of the ship section. As for the first, the Stokes drift will stretch the element closest to the wavemaker, but any pronounced Stokes drift is associated with larger amplitude waves than those generated for the most part in the present work. For the second, since we have studied piston-like behaviour, i.e. a near flat free surface in the terminal gap, there has been no need to apply a fine discretization of the free surface in the terminal gap. The number of elements on the free surface in the terminal gap has mainly been chosen such as to avoid splitting of the elements there. Saw-tooth instabilities would arise and become significant typically after about 5 - 10 wave periods after a splitting.

We also want to mention a few words regarding smoothing of the free surface. We have seen that many authors mention that smoothing every time-step or at periodic time intervals is a necessity for stable long-time simulations, e.g. for the propagation of wave trains. They report that saw-tooth instabilities quickly arise and eventually lead to simulation break-down if neglecting smoothing. For example, Longuet-Higgins and Cokelet (1978) used a stencil providing a weighting procedure of nearby points, and prefers what they call the five-point stencil. Koo and Kim (2004) refers to this as five-point

Chebyshev smoothing.

In the present work we have used no such smoothing. There has been no need for this. In our experience there are three situations that give rise to the mentioned saw-tooth instabilities. First, as discussed, improper re-gridding of the free surface, with particular reference to the re-distribution of the potential φ. Second, improper handling of the intersection points. And third, implementation errors, in particular those associated with creating the system matrix A in (5.7). For instance, bugs may easily be introduced if not careful with respect to the principal value integrals, the internal angle α or the treatment of the atan-function. We emphasize that these three situations are those experienced by the author during work with weakly nonlinear flow only, e.g. with no overturning of the free surface or wave run-up, and does not constitute a complete list of reasons for the occurrence of saw-tooth instabilities in general for more violent free-surface flow.

Chapter 6

Numerical modelling of the flow separation

In this chapter we present the numerical aspects of including the free shear layer in the numerical wavetank. This involves the limiting process of excluding the vorticity from the domain to obtain an extended version of the boundary integral equation (5.3), the discretization of the resulting thin free shear layer and an explanation on how the Kutta condition is imposed numerically. We next present an algorithm for automatic simplifications of the free shear layer which was developed in order to be able to run long-time simulations without excessively complex vortical structures in near sinusoidal flow. We last present an application of the method to foil in infinite fluid serving partly as a verification of the present implementation.

The method of including the free shear layer as a dipole distribution into the boundary integral formulation is not new to this work, including also its discretization and some numerical aspects as how to enforce the Kutta condition and a method of re-gridding the free shear layer. However, the algorithm for the automatic simplifications is new and considered a contribution from the present work to the field of flow separation modelling.

6.1 Boundary integral equation including the free shear layer

The free shear layer is included in the boundary layer equation by excluding the thin strip containing vorticity, S_V, in a similar manner as the singular points are excluded as described earlier in connection with equation (5.3). The integration path is shown in the left part of Figure 6.1. The limit is taken such that S_1, S_2 and S_5 tend to zero length, while S_3 and S_4 tends to S_V, resulting in the configuration shown in the right part of Figure 6.1. The boundary integral equation (5.3) is then extended to

$$\begin{aligned}\alpha(\mathbf{x})\varphi(\mathbf{x}) = &\int_S \varphi(\boldsymbol{\xi})\frac{\partial\psi(\boldsymbol{\xi},\mathbf{x})}{\partial n_\xi}\,\mathrm{d}s - \int_S \frac{\partial\varphi(\boldsymbol{\xi})}{\partial n_\xi}\psi(\boldsymbol{\xi},\mathbf{x})\,\mathrm{d}s \\ &- \int_{S_V} \Gamma(\boldsymbol{\xi})\frac{\partial\psi(\boldsymbol{\xi},\mathbf{x})}{\partial n_\xi}\,\mathrm{d}s,\end{aligned} \tag{6.1}$$

for all points $\mathbf{x} \in \Omega \cup S \cup S_V$. If the field point $\mathbf{x}$ is on one of the boundaries S or S_V, the corresponding integral over the dipole distribution must be interpreted as a principal value

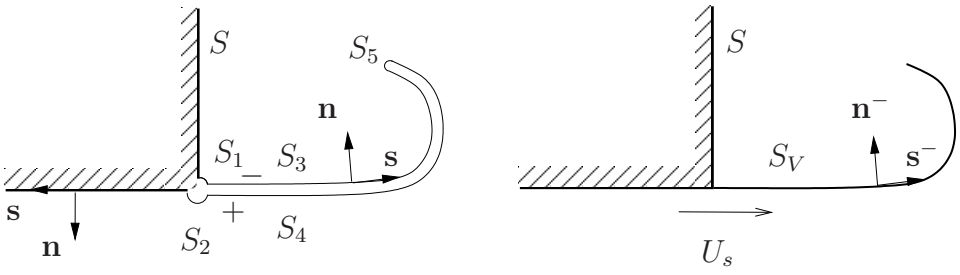

Figure 6.1: The limiting process of a thin free shear layer. S_{1-5} are shrunk to a single line. The unit normal vector on the - side is denoted $\mathbf{n}^-$. We finally let $\mathbf{n} := \mathbf{n}^-$ and $\mathbf{s} := \mathbf{s}^-$ along S_V.

integral. The source terms along $S_3 + S_4$ cancel due to the assumption of an infinitely thin shear layer and opposite signs of the normal vectors on each side, while the normal velocity is continuous across the free shear layer. The Γ-term appears since $\Gamma = \varphi^+ - \varphi^-$, and since $\varphi^+ \neq \varphi^-$, these terms do not cancel. We recognize the negative value of the circulation $-\Gamma$ as the strength of the dipole distribution along the free shear layer.

We mention that, in reality, the free shear layer has a finite width actually expanding from the time the shedding occurs, as indicated in Figure 2.2. If modelling a finite width free shear layer, the source terms would model the spreading of the shear layer, a diffusion effect.

The velocity of the free shear layer, $\boldsymbol{U_c}$, is given formally by (2.12). We may, however, express $\boldsymbol{U_c}$ explicitly as the gradient of (6.1). Some care must be taken in this procedure, as described in the following. In the limiting procedure for the exclusion of the free shear layer described above, we now take the field point $\mathbf{x}$ to be on the free shear layer. As the two sides S_3 and S_4 are shrunk towards each other, a full circle remains enclosing the field point, with the two halves of the circle residing on each side of the free shear layer. So the value of the potential is φ^- over one half of the integral and φ^+ over the other half of the integral, giving $-\pi\varphi^- - \pi\varphi^+ = -2\pi\bar{\varphi}$, where $\bar{\varphi} = 0.5(\varphi^- + \varphi^+)$. Considering now equation (6.1) we get $\bar{\varphi}$ on the left hand side and on the right hand side the last integral becomes a principal value integral. The velocity of the free shear layer, being $\boldsymbol{U_c} = \nabla\bar{\varphi}$, is then

$$\begin{aligned} -2\pi\,\boldsymbol{U_c}(\mathbf{x}_v) = &\int_S \varphi(\boldsymbol{\xi})\nabla\frac{\partial\psi(\boldsymbol{\xi},\mathbf{x})}{\partial n_\xi}\,\mathrm{d}s - \int_S \nabla\frac{\partial\varphi(\boldsymbol{\xi})}{\partial n_\xi}\psi(\boldsymbol{\xi},\mathbf{x})\,\mathrm{d}s \\ &- \fint_{S_V} \Gamma(\boldsymbol{\xi})\nabla\frac{\partial\psi(\boldsymbol{\xi},\mathbf{x})}{\partial n_\xi}\,\mathrm{d}s, \end{aligned} \tag{6.2}$$

where $\nabla = (\partial/\partial x, \partial/\partial y)$ is as before the usual gradient operator, and the last term is a principal value integral.

Riemann cuts. Before we proceed with the discretization of the free shear layer, we introduce so-called *Riemann cuts*. We define by a Riemann cut a curve of any shape in the (x, y)-plane with a discontinuity of the potential φ across the cut, and with the restriction that there is no change in Γ along it. Since Γ is constant along it, there is no shear along a Riemann cut. The Riemann cuts are of purely mathematical character and

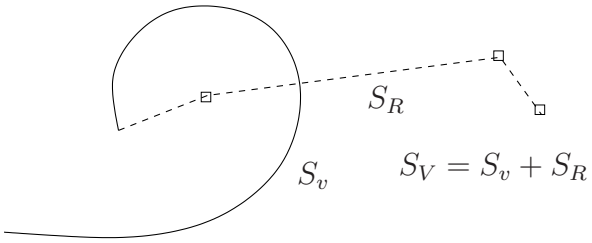

Figure 6.2: Illustration of Riemann cuts represented by the three dashed lines collectively called S_R. The solid line S_v represents the unsimplified part of the free shear layer. Across the Riemann cut S_R, the potential φ is discontinuous, while the normal and tangential velocities, φ_n and φ_s, are continuous. Expections are at the connection points denoted by squares. These points are singular and each point represents a point vortex.

is introduced basically as a means of simplifying the structure of the free shear layer. The shape of the Riemann cut may typically be that of a straight line.

In the present methodology a Riemann cut is modelled as a curve with constant dipole distribution Γ. There are singularities at the ends of the Riemann cuts that need special care. Introducing a Riemann cut is mathematically equivalent to introducing a point vortex at its far end, and typically we want to simplify the free shear layer such that a near circular vortical structure is represented by a point vortex. Since there is no shear along the main parts of a Riemann cut both the tangential and normal velocities are continuous along this part. All the shear is concentrated to the end vortex which is singular. An example of a Riemann cut made up from three straight lines is shown in Figure 6.2. We denote the unsimplified part of the free shear layer by S_v and the Riemann cuts by S_R. Together they represent what we consider the whole free shear layer in our model, i.e. $S_V = S_v + S_R$. Along each Riemann cut the dipole strength Γ is constant. If the value of Γ on two neighbouring Riemann cuts differ, the effect is a point vortex at the connecting point, indicated by the squares. The far end square will represent a point vortex as long as $\Gamma \neq 0$ along the last straight segment of the Riemann cut. We will often refer to this set-up as having three Riemann cuts, meaning the three straight curves.

There may in principle be several Riemann cuts connecting several unsimplified parts of the free shear layer. We have in our work always considered Riemann cuts to represent the far end of the free shear layer. The reason is that we cut the end parts of the free shear layer twice each wave period. This will become clear when we shortly discuss the automatic simplification procedure of the free shear layer. We first present the discretization procedure for the free shear layer.

6.2 Discretization of the free shear layer

We discretize the unsimplified part of the free shear layer S_v into N_v piecewise linear elements, and assume Γ to vary piecewise linearly along each element. Choosing the lowest order method with constant dipole distribution along each element would provide poor accuracy of the induced velocities close to the free shear layer, as each node would effectively act as a discrete vortex, with resulting insufficient modelling of the spiraling

vortices. Anyway, since we assume the same variation of φ and φ_n along S, including the free shear layer into the system of equations is a straightforward extension. We further include the N_R Riemann cuts as straight elements with constant dipole strength Γ over each cut. A Riemann cut is thus in this sense treated similar to an element of the unsimplified part of the free shear layer, except it has always a constant dipole distribution. We denote by N_V the sum of the free shear layer elements and Riemann cuts, that is $N_V = N_v + N_R$.

The discrete version of (6.1) is given by (B.1). This is the same as (A.1) except with also a sum over the dipoles of S_V with strength Γ_j. The contribution from the integral over the free shear layer enters the right hand side of the system (5.7) as known quantities since Γ is known.

6.2.1 Kutta condition

As stated earlier, there are two requirements in the Kutta condition. First, the flow must leave tangentially from one side of the body, and second, the potential must be continuous from the body and into the fluid. In the numerical model these are imposed by the following procedure.

First, the flow is imposed to leave tangentially by imposing the direction of the free shear layer element closest to the separation point to be in the direction of the tangent of the body element closest to the point of separation (on the shedding side). Node 2 of the free shear layer, which is the end of the first free shear layer element, is forced to move in the tangential direction with the velocity $0.5U_s$.

Second, the continuity of φ from the body and into the fluid is imposed in the following manner. When flow separation is enforced, we avoid to explicitly satisfy the boundary value integrals at the node defining the separation point $\mathbf{x}_s$ as we do in the case without separation. In that case the boundary integral equation was satisfied at the corner with $\alpha = -3\pi/2$ in (5.3). Instead, extrapolation from both sides along the body is used. Not solving for this node means we loose one equation. Further, since the potential is discontinuous over the free shear layer, i.e. $\varphi^+ \neq \varphi^-$ in general at the corner, we implicitly add one unknown. This means we are two equations short. However, we require the potential jump on the body to be equal to Γ_0, hence introducing one additional equation since the circulation is known. Next, we represent the two values of the potential at the separation point by extrapolating φ linearly along the walls using the values at the two elements on each side next to the elements closest to the separation point. This introduces two more additional equations, meaning there is an overhead by one equation. We resolve that by not satisfying the boundary integral equations at the end point of one of the elements adjacent to the corner. We have chosen to exclude φ_{i-1} as unknown in our calculations, where node i defines the separation point. We get that

$$\begin{gathered} \varphi^+ - \varphi^- = \Gamma_0, \\ \varphi^+ = a\,\varphi_{i+1} + b\,\varphi_{i+2}, \quad \varphi^- = c\,\varphi_i + d\,\varphi_{i-1}, \end{gathered} \tag{6.3}$$

where $a = 1 + \Delta s_i/\Delta s_{i+1}$, $b = -\Delta s_i/\Delta s_{i+1}$, $c = 1 + \Delta s_{i-1}/\Delta s_{i-2}$ and $d = -\Delta s_{i-1}/\Delta s_{i-2}$. Δs_i is the length of element i which has end-points $\mathbf{x}_i$ and $\mathbf{x}_{i+1}$.

6.3 Evolution of the free shear layer

Once the system of equations (5.7) are solved, we may calculated the velocity $\boldsymbol{U_c}$ at the nodes of the free shear layer as well as the separation velocity U_s. Using these and the position of the free shear layer $\mathbf{x}_v$ and the circulation Γ may be stepped forward in time according to (2.13) and (2.14).

The chosen time integration scheme for the free shear layer is the simple explicit Euler scheme, that is, in the numerical wavetank where the fourth order Runge Kutta method is used, the free shear layer is updated only once at the beginning of each main time-step. Choosing the simple explicit Euler method must be seen in context with the re-gridding and automatic simplifications applied to the free shear layer which will be discussed in detail in the next section. Also, the explicit Euler scheme was found to be adequate in earlier works, e.g. in Faltinsen and Pettersen (1987). This means, given the solution of φ and φ_n along S, and Γ along S_V at the beginning of time-step n, we calculate the separation point velocity U_s and $\boldsymbol{U_c}$ based on these, and the updated solutions $\mathbf{x}_v$ and Γ are next used as forcing on the right hand side of (5.7) in all the four sub time-steps of the fourth order Runge Kutta scheme for the free surface.

6.3.1 The velocity of the free shear layer nodes

We need to distinguish slightly the way to obtain the velocity at the nodes of the unsimplified part of the free shear layer, and that of the point vortices. The latter is explained in the next sub-section.

The discrete version of the velocity of the mid-point of an element of the unsimplified part of the free shear layer is given by (B.2). Note that the summation over the free shear layer is both the free shear layer elements and the Riemann cuts, altogether N_V terms. The free shear layer velocities at each node, except for the end node, is found by linear interpolation of the calculated velocities at the mid-points of the two neighbouring elements in a curvilinear fashion.

The velocity at the end node, that is node $N_v + 1$, is obtained as follows. First, the value from linear extrapolation using the values at the mid-points of elements N_v and $N_v - 1$ is calculated, call it u_a. Next, the value based on fitting a second order polynomial through the mid-point of element $N_v - 1$ and that of nodes $N_v - 1$ and N_v is calculated, call it u_b. Upon using only u_a, the end node tends to cross the inner spiral core after some time, and upon using only u_b the end element tends to rotate around its hinge point. Since extrapolation in general is a dubious affair, we chose to experiment with different combinations of u_a and u_b following the strategy of trial and error. The final combination was taken as $0.6\,u_a + 0.4\,u_b$ (for node $N_v + 1$).

We mention that the computer time associated with calculating the velocity of the N_v nodes of the free shear layer is not negligible, at least when $N_v/N \sim \mathcal{O}\{1\}$. This is due to the summation in (B.2) over all $N + N_V$ elements when calculating the velocity at each of the N_v free shear layer element mid-points.

6.3.2 The velocity of the point vortices

The velocity of a point vortex, or the far end of a Riemann cut, needs special treatment. Basically, the expression (B.2) is used, but modified in two ways. First the sum is over all

free shear layer elements, so the "$j \neq i$" should be neglected. Second, and more importantly, a point vortex does not induce any velocity on itself. Therefore, the contribution from its one or two neighbouring Riemann cuts must be treated specially. If S_R^k is the k'th Riemann cut with end coordinates $\mathbf{x}_d$ and $\mathbf{x}_e$, then $\mathbf{x}_e$ is the location of the point vortex for which we want the velocity. The velocity induced by S_R^k, call it $\mathbf{U}_{de}$, at some position $\mathbf{x}$ is

$$\mathbf{U}_{de}(\mathbf{x}) = -\frac{\Gamma_k}{2\pi}\left(\frac{1}{r_e^2}(y-y_e) - \frac{1}{r_d^2}(y-y_d), -\frac{1}{r_e^2}(x-x_e) + \frac{1}{r_d^2}(x-x_d)\right). \tag{6.4}$$

The two terms involving $1/r_e^2$ must be interpreted as the contribution from the point vortex located at position $\mathbf{x} = \mathbf{x}_e$. When calculating the velocity of the point vortex at $\mathbf{x}_e$, these two terms should be excluded. The procedure must be carried out for both the neighbouring Riemann cuts if not considering the very end vortex.

6.3.3 Separation velocity

The separation point velocity U_s is in the present taken positive towards the separation point, and basically taken as the largest of the two candidates on each side, being

$$\begin{aligned} U_{s1} &= -((\nabla\varphi)^+ - \mathbf{v}_B)\cdot\mathbf{s}, \\ U_{s2} &= ((\nabla\varphi)^- - \mathbf{v}_B)\cdot\mathbf{s} \end{aligned} \tag{6.5}$$

where $\mathbf{v}_B = \dot{x}_G + \boldsymbol{\omega}\times\mathbf{r}$ is the ship section motion at $\mathbf{x}_s$ and $\mathbf{s}$ is the unit tangential vector along the body. Ideally, there is a stagnation point on the lee side of separation. However, the fluid velocities in (6.5) are calculated over the elements not next to, but second next to $\mathbf{x}_s$, and hence will take non-zero value in general. The chosen criterion for swapping side of separation in case of unsteady flow has in our experience only small consequence regarding the accuracy, but is, however, a matter of importance with respect to numerical stability. We believe that the treatment of the free shear layer element closest to the body should be considered in connection with this as well. We have chosen the following strategy for deciding separation direction. Given a shedding direction with velocity, say U_{s1}, this is changed whenever U_{s2} exceeds $(1+\varepsilon)U_{s1}$ with ε a small value, and left unchanged otherwise. We found that simulations using $\varepsilon = 0$ often resulted in numerical instabilities in the case of oscillatory ambient flow around a ship section corner due to the small velocities occurring at both sides around the time of the flow separation changing direction. This typically caused frequent changes back and forth every other time-step leading eventually to entanglement of the free shear layer elements closest to the separation point. We found a value of $\varepsilon = 0.1$ to improve this matter significantly. There is, however, still room for further improvements in order to ensure a more globally robust numerical method. We report some problems related to the flow direction change in connection with the study of a ship section moored to a terminal in Chapter 10.

6.4 Automatic simplifications of the free shear layer

In order to apply the present method to oscillatory flow, repeated simplifications of the free shear layer geometry as the simulation progresses is crucial. We begin by posing the

two rules that (1) the free shear layer is not allowed to become too complex, and (2) the free shear layer must not be over-simplified. We exploit our knowledge regarding the main features of the free shear layer in order to define a physically sound set of simplifications which obeys these two rules. Ignoring the simplification procedure, even after one single period the free shear layer structures become exceedingly complex, as will become clear in this section.

6.4.1 Characteristics in sinusoidal flow

In arbitrary oscillatory ambient flow, there is no simple characteristic of the free shear layer, while for sinusoidal ambient flow there is. Basically, in sinusoidal ambient flow four single vortices, or two pairs of vortices, are shed each period. The two single vortices shed each half period form a vortex pair, that is, they are formed in such a way that they remain close to each other and once created they travel along under mutual influence. Their vortex strengths are of opposite sign due to opposite sign of the shed vorticity from the two sides of the body, and typically they travel away from the body and return in a large circular motion. The circular motion appears when the absolute value of the strength of each of the two are not equal. With identical absolute values of the strengths they would in infinite fluid travel in a straight line, and most likely away from the body.

We illustrate the behaviour by means of an example. Figure 6.7 presents snapshots of the free shear layer geometry during the first few periods of a typical simulation. The time step number is indicated in each sub-plot. References to the figures will be made in the following explanations of the four main tools that we use: Re-gridding, dumping, cutting and resolution limitation (both temporally and spatially). None of these four tools are new to this work. However, the automatic identification of the main vortical structures allowing for continuous simplifications crucial to long time simulations is new, and is considered as a contribution to the area of vortex tracking methods. We discuss this matter in some length and detail, as we have found, in accordance with earlier users of the method (e.g. Braathen (1987), Faltinsen and Pettersen (1987)), that a substantial amount of details must be dealt with properly in the practical use of the method.

6.4.2 Re-gridding of the free shear layer

Since a spiral core will tend to stretch the rest of the free shear layer, the actual length L_v is in general longer than the sum of the lengths of the shed elements. Areas of large vorticity curls up and stretches areas with less vorticity, thereby causing element lengths to become increasingly different. Our re-gridding strategy is as in Faltinsen and Pettersen (1987)) based on keeping all elements of the free shear layer, except the two closest to the separation point, of equal length at all times. As illustrated in Figure 6.3(a), the nodes on the $N_v - 2$ free shear elements are after each time-step slided along the existing free shear layer geometry such that each element obtain the length $\Delta s_v^0 = L_v/(N_v - 2)$. The length L_v is conserved in this manner.

More refined re-gridding strategies may have been chosen, such as having $\Delta s_v \propto 1/\kappa_v$ where κ_v is the local curvature of the free shear layer, providing more elements to regions of high curvature and hence providing higher resolution to fine structures. The present strategy, however, although perhaps somewhat crude, has the advantage of stabilizing the

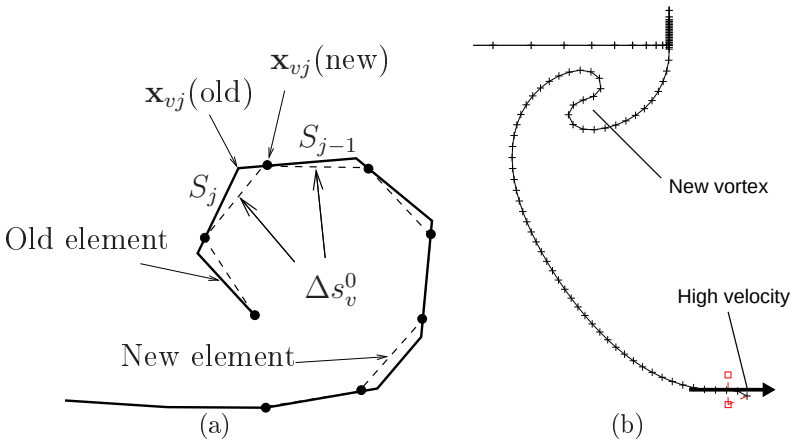

Figure 6.3: Left: Re-gridding of the free shear layer. Equal free shear element length strategy. Forcing equal length prevents large differences in element lengths as vortical structures curls up. Two secondary effects are that it (1) prevents unwanted perturbations growing, but also (2) partly prevents formation of new vortices. Right: Explanation of effect (2). The high velocity induced in between the two vortices defining a vortex pair stretches the free shear layer.

free shear layer in the sense of preventing the growth of perturbations. This is in our experience in practice crucial for the survival of the simulation.

On the other hand, a negative effect of the present strategy is the partly prevention of new vortex formation in connection with the pronounced stretching from a newly formed vortex pair. This is illustrated in Figure 6.3(b). Here, the newly forming vortex is struggling to curl up due to the stretching by the vortex pair. This problem may, however, be overcome by replacing the long flat part of the free shear layer by a Riemann cut. The replacement is plausible since there is next to zero vorticity along this part anyway, that is Γ is near constant, so the exact shape, which is more or less a straight line, is just as well represented by a Riemann cut with constant Γ. This procedure is called dumping.

6.4.3 Dumping

By dumping we mean that a certain number of elements of the free shear layer forming a near circle are replaced by a single discrete vortex. This is feasible since a closed circle with uniform vorticity distribution, or equivalently, linearly varying dipole strength, induces identically the same velocities outside the circle as a discrete vortex located at its origin. A spiral which in shape is close to a closed circle exhibits approximately the same properties. The discrete vortex is represented by a constant distribution of dipoles along a Riemann cut. The Riemann cut is connected to the remaining free shear layer in one end, while the other end is located at the origin of the spiral core. This position, $\mathbf{x}_d$, is the weighted mean of the positions of the mid-points of the dumped elements, weighted by the vorticity over each element, i.e.

$$\mathbf{x}_d = \frac{1}{\Gamma_{k+1} - \Gamma_i} \sum_{j=i}^{k} \gamma_j \, \bar{\mathbf{x}}_{vj} \tag{6.6}$$

$\gamma_j = \Gamma_{j+1} - \Gamma_j$, $\bar{\mathbf{x}}_{vj} = 0.5(\mathbf{x}_{vj+1} + \mathbf{x}_{vj})$, and the sum is over an appropriate set of elements defining the near circle, or spiral core, in this case elements i to k. The criteria that we use are purely geometrical, based on accumulated angles as well as distance of the spiral core from the separation point. The algorithm for identifying a spiral core as well as the criteria for dumping are described in detail in the following.

We first denote by β_j the angle between the neighbouring pair of elements at node $\mathbf{x}_{vj}$, being the elements S_j and S_{j+1}. The angle between two elements are determined using the standard function atan2 along with the dot and cross products. For unit vectors we have that $\cos\beta = \mathbf{a}\cdot\mathbf{b}$ and $\sin\beta = (\mathbf{a}\times\mathbf{b})\cdot\mathbf{k}$, where $\mathbf{k}$ is the unit normal vector pointing out of the paper, i.e. $\mathbf{k} = \mathbf{i}\times\mathbf{j}$. We use the unit tangential vector along free shear layer element j, that is $\mathbf{s}_j = (\mathbf{x}_{vj+1} - \mathbf{x}_{vj})/(\Delta s)_j$, and get that

$$\beta_j = \text{atan2}\,(c_j, d_j) - \pi, \tag{6.7}$$

where $c_j = (\mathbf{s}_j \times \mathbf{s}_{j-1})\cdot\mathbf{k}$ and $d_j = \mathbf{s}_j \cdot \mathbf{s}_{j-1}$. This gives the angle β_j in a robust manner from -2π to 0. Next, we define the accumulated angle α_i at node i as that calculated from $s = 0$ and further the accumulated angle α_I at node I as that calculated from node I to $s = L_v$, i.e.

$$\alpha_i = \Sigma_{j=2}^{i}\,\beta_j\,, \quad \alpha_I = \Sigma_{j=I}^{N_v}\,\beta_j\,. \tag{6.8}$$

Note the convention of upper- and lower-case i.

The first dumping occurs as the spiralling vortex reaches four turns, or $|\alpha_I| \geq 16\pi$ with $I = 2$. The elements forming the inner turn, identified by the node I which is such that α_I just exceeds 2π, are then dumped. This process is repeated as long as the single vortex continues to roll up, and is illustrated in Figure 6.7(a-c).

When a vortex pair has established its shape such as that shown in Figures 6.7(c) and 6.4(a), two criteria has to be met before dumping to a vortex pair. First the point i_1 as indicated in Figure 6.4(a) is identified by an accumulated angle $|\alpha_{i_1}| \geq 3\pi/2$ where the sign of β_j for $j = 1, .., i_1$ are required all to be equal. Next, the distance from the node $\mathbf{x}_{vi_1}$ to the separation point $\mathbf{x}_s$ must be larger than a given characteristic length, that is $|\mathbf{x}_{vi_1} - \mathbf{x}_s| \geq D_0$. A certain distance from the corner is required so as not to violate the rule of not over-simplifying. The impact of the dumping on the body will in general be smaller the larger the distance is. D_0 is in the present taken as the mean of the maximum extent of the vortex in the x- and y-directions, disregarding the part of the free shear layer from $s = 0$ and to the point i_1, as illustrated in Figure 6.4(a). If both criteria are met, the point i_2 is identified as one node of the element being closest to perpendicular to the shedding direction, that is such that $|\alpha_{i_2}| \simeq \pi/2$ with the sign of α_{i_2} opposite to that of α_{i_1}. The part beyond this point is dumped into the existing end vortex, while the part between i_1 and i_2 are dumped into the second vortex. The situation is then typically as illustrated in Figure 6.7(d) which is just after the vortex structure in Figure 6.7(c) has been dumped to the shown vortex pair.

When a new vortex has started forming, such as that illustrated in Figures 6.7(e,i) and 6.4(b), the point i_3 as indicated in Figure 6.4(b) is identified as that with accumulated angle $|\alpha_{i_3}| \geq 3\pi/2$. If this exists, all elements beyond i_3 are dumped into a new, single vortex. Since the vorticity is highly concentrated in the near vicinity of i_3, the long tail extending to the vortex pair with almost zero vorticity has a negligible contribution to the position of the dumped vortex.

There are now three Riemann cuts, representing three discrete vortices. At this stage, however, the double pair is removed, as described in connection with the description of

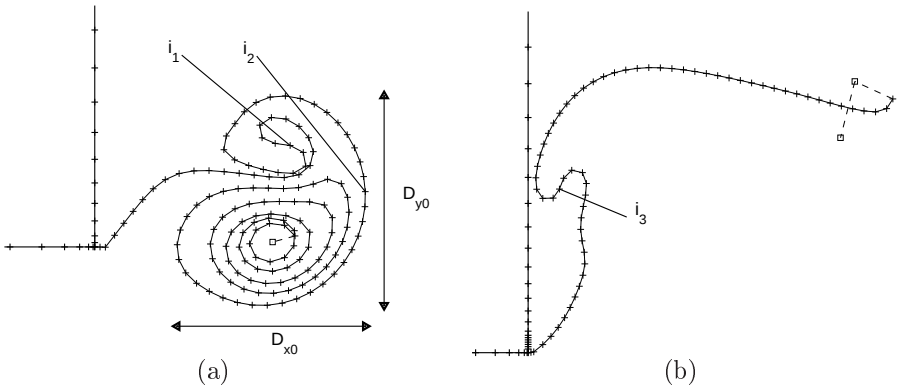

Figure 6.4: Illustration of characteristic length scale for a double vortex $D_0 = 0.5\,(D_{x0} + D_{y0})$ and the nodes $i_1 - i_3$ identified and used in the automatic dumping process.

cutting. The situation after dumping to a new single vortex at i_3 and removal of the double pair is depicted in Figures 6.7(f,j). The process of dumping to a new double pair repeats in Figure 6.7(h) and the simulation goes on.

Dumping has two main effects. First, it simplifies the inner core of the evolving spiral vortex, vital to avoid too few elements per turn resulting in inadequate resolution. A typical situation is the end element crossing the second innermost spiral which in general is inevitable if dumping is ignored. A positive side effect is the reduction of the number of free shear layer elements which in turn reduces the computational costs.

The second main effect is to effectively "disconnect" the free shear layer from a newly formed vortex pair. Since the nature of the free shear layer is such that it stretches due to roll up, the forming of the new single vortex at i_3 (see Figure 6.4(b)) is partly denied if the free shear layer is allowed to roll up between the vortex pair as discussed earlier under re-gridding and illustrated in Figure 6.3(b). Therefore, some time after the double vortex is formed, all the free shear layer elements in its vicinity are dumped. The stretching of the remainder of the free shear layer is then avoided, allowing the new vortex to form. The fact that the new vortex formation is partly denied by the stretching is of purely numerical character, while dumping is a matter of simplified representation of the physics. However, the dumping is to our understanding physically sound in this situation just as when dumping the inner spiral core.

To give an idea of the complications arising when dumping is ignored an example is provided in Figure 6.5. Also, cutting, which is described shortly, is ignored in the example. The free shear layer enters into the body right after the situation shown in Figure 6.5(b). The entering of the body occurs in connection with the formation of a new single vortex. Although the simulation proceeds, the numerical solution becomes unphysical. Perhaps the situation could have been avoided by decreasing the element size on the ship section side, with the zero penetration condition thereby enforced to a higher degree, but perhaps also the somewhat messy behaviour of the free shear layer introduces the necessary numerical errors for the penetration to happen. The vortex pair reaches and penetrates also the terminal wall some time later, where the resolution is poor relative to the vortex dimensions as shown in Figure 6.5(c). Again, perhaps this could have been avoided by decreasing the element size on the wall. However, the required resolution

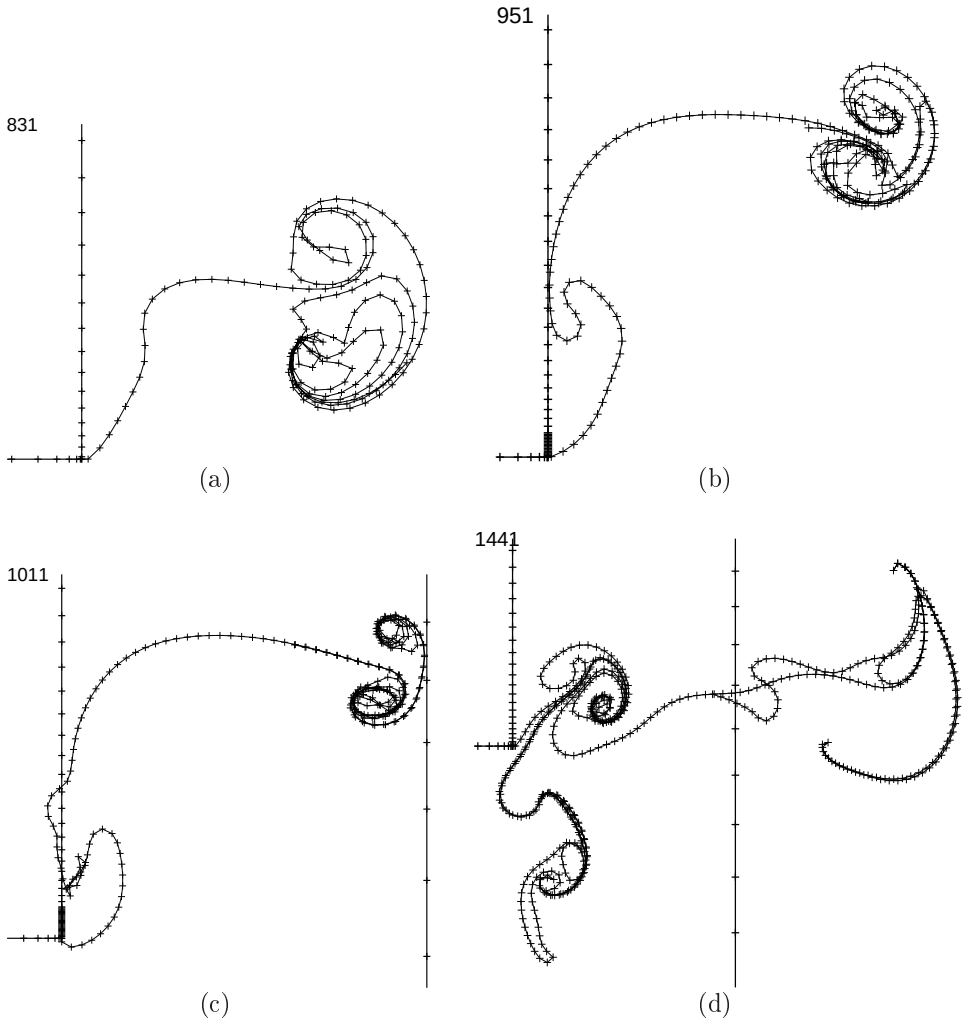

Figure 6.5: Illustration of typical breakdown when dumping is disregarded. In this example, the simulation breaks down because the free shear layer penetrates the wall near the separation point, where-after the evolution is unphysical.

would lead to excessive use of computer time. Also, the structures will quickly become too complicated for the present method to resolve properly. As a curiosity the situation about three quarters of a period later, just before the simulation breaks down, is shown in Figure 6.5(d).

6.4.4 Cutting

Cutting is in the present work associated with the action of removing a vortex pair. Cutting allows the simulation to go on for any wanted number of periods, as it basically serves as a restart of the system. If cutting is not performed the vortex pair will remain forever and eventually be entangled in the new developing double vortex or interfere with the free surface. This is most probably occurring also in nature, but there, the vortex strength will not be preserved. In reality, the vortex strength of the double vortex will weaken due to turbulent dissipation. A vortex pair will dissipate at a higher rate than a

single vortex, since the two vortices which remain close inhibit opposite sign of vorticity causing a cancellation effect due to viscosity. Further dissipation occurs if the vortex pair "slides" along the wall interfering with the boundary layer which may inhibit vorticity of opposite sign. The interaction between vortices and a boundary layer is in general not well understood.

With dumping only, and no cutting, the simulations in general survive for some time, perhaps a couple of periods, but the behaviour becomes to our understanding unphysical. A typical scenario is presented in Figure 6.6. Dumping is performed as described above, but a number of vortex pairs are accumulated as they are not removed, in this case two pairs. The firstly shed vortex pair travels towards the terminal wall as indicated by the arrow in Figure 6.6(a). This was also the case in the discussion above where dumping was suppressed, but now, the free shear layer does not penetrate the solid walls. However, as this vortex pair reaches the wall, the two individual vortices start travelling along the wall in opposite directions as illustrated by the arrows in Figure 6.6(b), both remaining close to the wall. They would interfere with the boundary layer and further, in reality, feel the no-slip conditions here. The second shed vortex pair travels in a circle and nearly infiltrates the vortex sheet as shown in Figure 6.6(c). The simulation eventually breaks down as one of the discrete vortices from the first vortex pair infiltrates the free surface, see Figure 6.6(d).

The method of suddenly removing a pair may seem crude. A possibility is of course to model the decay of vortex strength, i.e. the decay of Γ, and then eventually remove the vortex pair when its strength is below some threshold. This requires a mathematical model for the decay, and one such model is due to Oseen, see e.g. Venkatalaxmi et al. (2007). However, any substantial decay of single Oseen vortices that we investigated takes in the order of ten or more periods, while the double vortices seem from informal physical experiments to dissipate faster. An explanation to this discrepancy may be that an Oseen vortex only considers laminar viscous effects, while in reality the flow is turbulent. Therefore, without further reasoning we cut the pair at the instant the first dumping is performed for the new single vortex, i.e. at the instant just before that e.g. in Figure 6.7(f). The double vortex has then in general travelled a fair distance away from the body and is considered not to induce considerable velocities there. A small, sudden jump in the potential on the body in the vicinity of the separation point is experienced in these cases. The implications related to the force calculations and integration of the equations of motion are to our experience of little practical importance as discussed in Chapter 8.

The free surface seems free from such jumps if the intensity of the circulation is not too large and if the vortical structures are confined to an area close to the corner of separation. We require the vortical structures to be confined in the vicinity of the corner of separation if $D_0/D << 1$, where D is the ship section draft as before and D_0 is illustrated in Figure 6.4. If this is the case, also the vortex pairs will typically be removed when still in the far-field of other boundaries such that the terminal and sea floor. The nature of the vortical structures are also of course a function of its strength, which in principle is independent of the size D_0, but in practice strongly related. In our experience the cutting strategy and hence the automatic simplification procedure works well if $D_0/D \lesssim 0.25$, given that the other structural dimensions are in the order of the draft or larger, in this case that $b/D \sim 1$ and $d/D \sim 1$, where b and d are the terminal gap width and the bottom clearance respectively.

We illustrate in Figure 6.8 how the free surface is affected in a case where $D_0/D \simeq 1$.

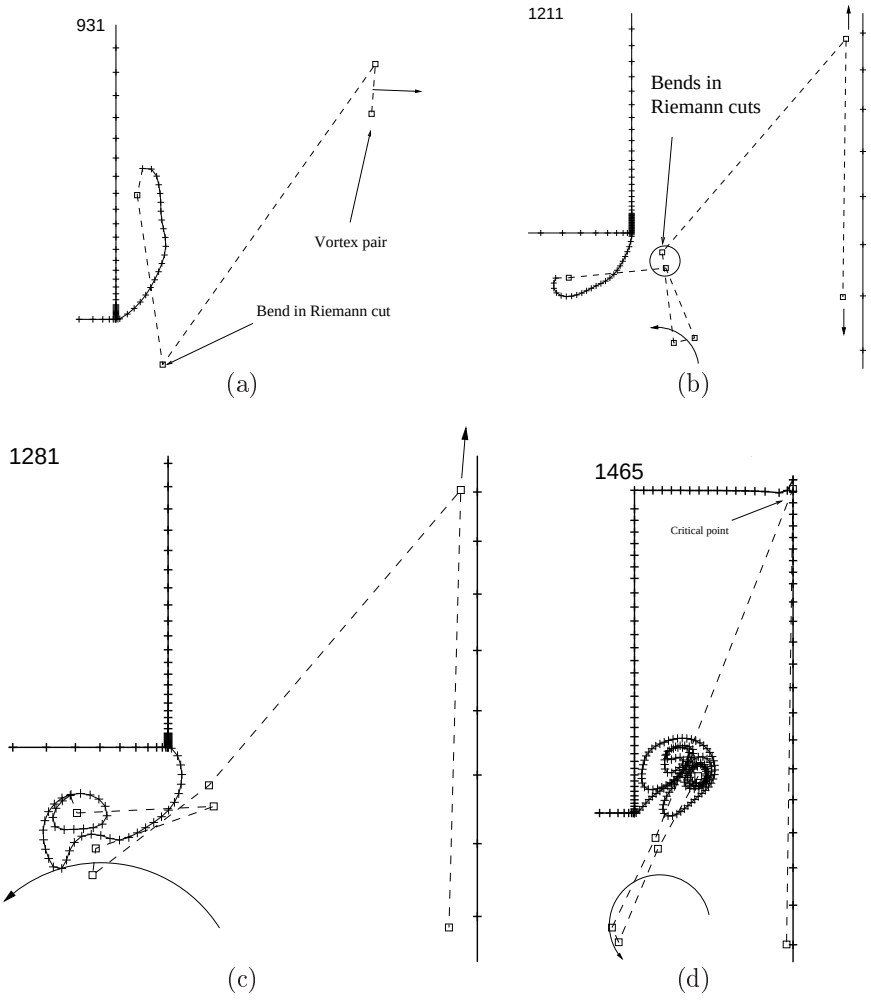

Figure 6.6: Illustration of typical breakdown when cutting is disregarded. All vortex pairs are kept. The arrows indicate the direction the discrete vortices travel. The Riemann cuts are represented by the dashed lines, and these are bent in order to avoid possible crossing of the corner of the body.

A regular wave with period close to the natural piston-mode period enter a fixed ship, and the fluid motion in the terminal gap builds up. Velocity vectors are included in order to visualize qualitatively the strength of the vortical structures. The time-step number is also shown, and there are $N_p = 600$ time-steps per wave period. In the initial stage (Figure 6.8 (a - b)), the vortical structures are reasonably confined to the vicinity of the corner. As the flow builds up, however, the size and also its strength increases. At a later stage (Figure 6.8 (p - r)), the free-surface kinematics become somewhat violent. Although not clear from the figures, shocks are induced by each cutting which occurs twice each wave period, and the induced sloshing behaviour hence considered artificial. From Figure 6.8 (n - o) it is clear that the fluid flow in the lower part of the terminal gap is altered appreciably by the removal of the vortex pair. The influence from the pair on the flow near the free surface perhaps looks quite insignificant, but it does have a disturbing effect. We also show the time of break-down in Figure 6.8 (r) when the free shear layer enters

the ship section. The simulation survives about six wave periods. This is not enough in this case to reach steady-state. In case of surviving sufficiently amount of periods to reach steady-state we would still, however, deem the results unphysical in this case where $D_0/D \simeq 1$.

Note that from the velocity vectors in Figure 6.8 one may at least qualitatively feel confident that the Kutta condition is fulfilled by the present implementation. That is, the flow leaves tangentially from the corner of separation and stagnation of the fluid flow on the lee side is indicated by only very short velocity vectors there.

The discussed limitation on vortical structure size implies a limitation to the validity of the algorithm, but in all the cases investigated during the present work, the requirement has been fulfilled, i.e. $D_0/D \lesssim 0.25$. In case of investigating more severe vortex shedding, we would recommend using other numerical methods.

6.4.5 Spatial and temporal resolution

The free shear layer has an unstable nature in the sense that short wave instabilities arise. In fact, an infinitely long and straight vortex distribution is unstable to any perturbation. A stabilizing effect is that the core of the vortex, if sufficiently strong, stretches the free shear layer as described earlier. During one period there are, however, several stages where the majority of the free shear layer may adopt small scale instabilities whose growth cause destruction of the major structures. This typically happens when very small elements or time-steps are allowed.

A crucial parameter is therefore the lower limit of the length of the free shear layer element closest to the separation point until a new first element is born, Δs_v^{min}. This length should be related to the characteristic dimension of the free shear layer D_0. We have found $\Delta s_v^{min} \simeq D_0/m$ with $m \simeq 20 - 30$ a reasonable choice through trial and error.

The chosen value of Δs_v^{min} should not be too large either. If chosen too large, the vortical structures are poorly resolved, leading among other things to large vorticity in the end free shear layer element which then rapidly swirls around its hinge point, which is unphysical, as the free shear layer should not cross itself. This is basically a resolution problem.

The choice of the time-step length Δt seems in our experience also to be crucial. Too small time-steps allows the free shear layer to grow small scale instabilities, and with too long time-steps typically the free shear layer enters the body, after which the results are rendered unuseful. More specifically, our experience points to that $N_p = 600$ time-steps per period is a good choice. While e.g. $N_p = 400$ is slightly too coarse and the structures tend not to be adequately resolved with the risk of free shear layer entering the body, $N_p = 800$ is slightly too fine with small scale instabilities evolving.

The recommended values of the parameters Δs_v^{min} and Δt must be seen in context with the fact that the re-gridding algorithm is applied each time step. Using other re-gridding strategies would probably yield other values of the parameters. In our experience, though, a successful simulation depends on re-gridding each time-step, as attempts with every second, fourth and eight all resulted in devastating small scale instabilities.

6.4.6 Start-up and element shedding

The start-up of the free shear layer is implementation-wise straightforward. U_s is calculated and a free shear layer element of length $0.5\,U_s\Delta t$ is created. In the following time-steps, this is prolonged by advecting node 2 which is the far end of the first element, with the velocity $0.5\,U_s$, until reaching the length Δs_v^{min}. The element is then split in two. The node 2 is forced to move along the tangent direction of the body from the side the shedding occurs as explained in connection with the Kutta condition. The shedding velocity is hence applied to a point somewhat away from the separation point (node 2), but only by a small distance and so considered feasible. The physics are not well described in the very early stages of the start-up process, but the free shear layer curls up under the influence of its own induced velocities, as e.g. shown in Figure 6.7(a) in an early stage. An improved description of the physics in the early stages may perhaps be achieved by introducing a starting vortex, but this has not been done in the present work; it was not found necessary.

We next present an application of the vortex tracking method to a foil in infinite fluid. The focus is there not on the automatic simplification procedure, rather on verification of the basic implementation. The automatic simplification procedure is validated through the main studies in Chapter 10.

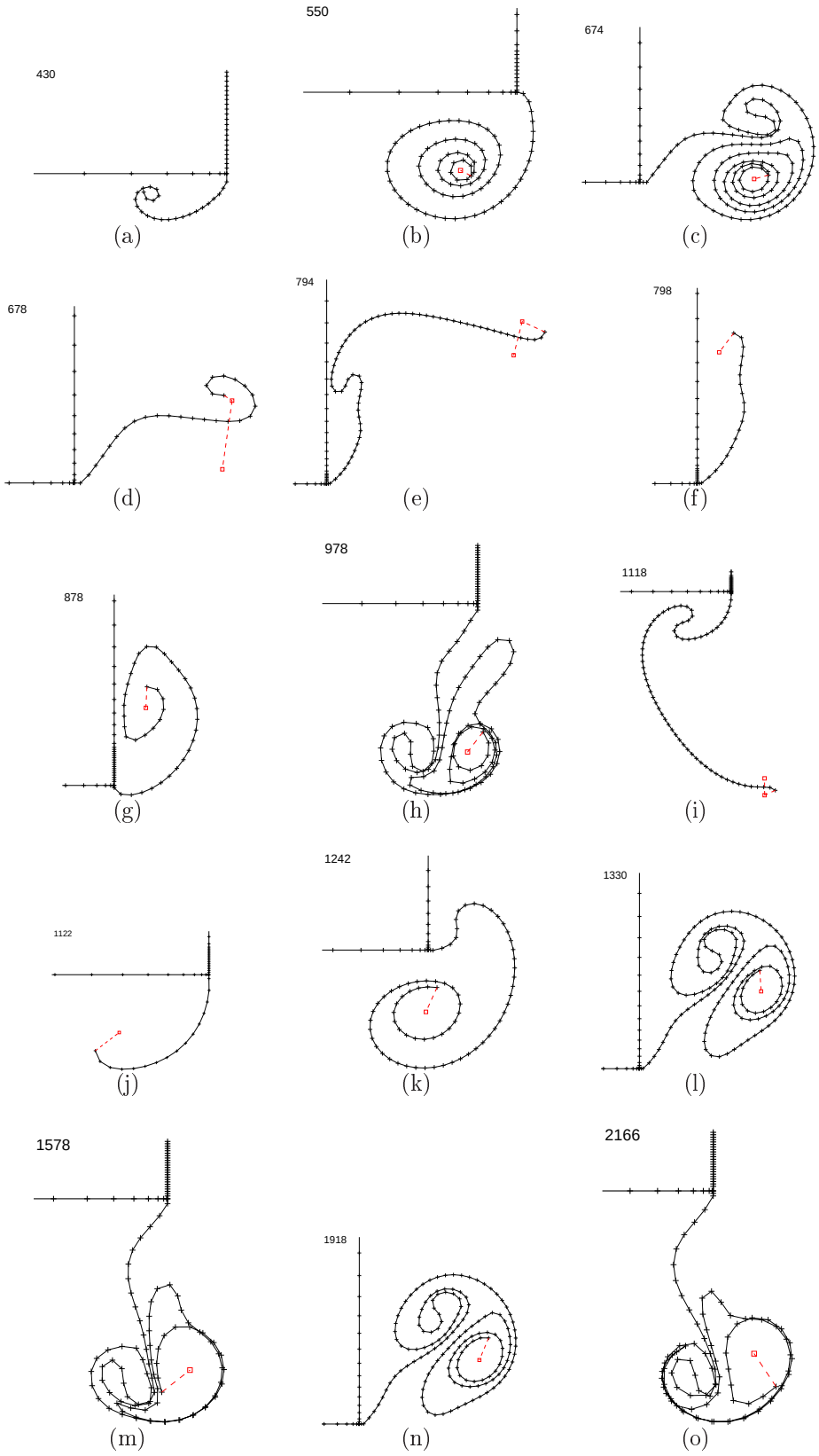

Figure 6.7: Typical behaviour of the free shear layer from the initial stage and up to steady-state. Time step number is given. (a-h) describe roughly the first period. The free shear layer started at time step $n = 391$ and number of time steps per period is $N_p = 600$.

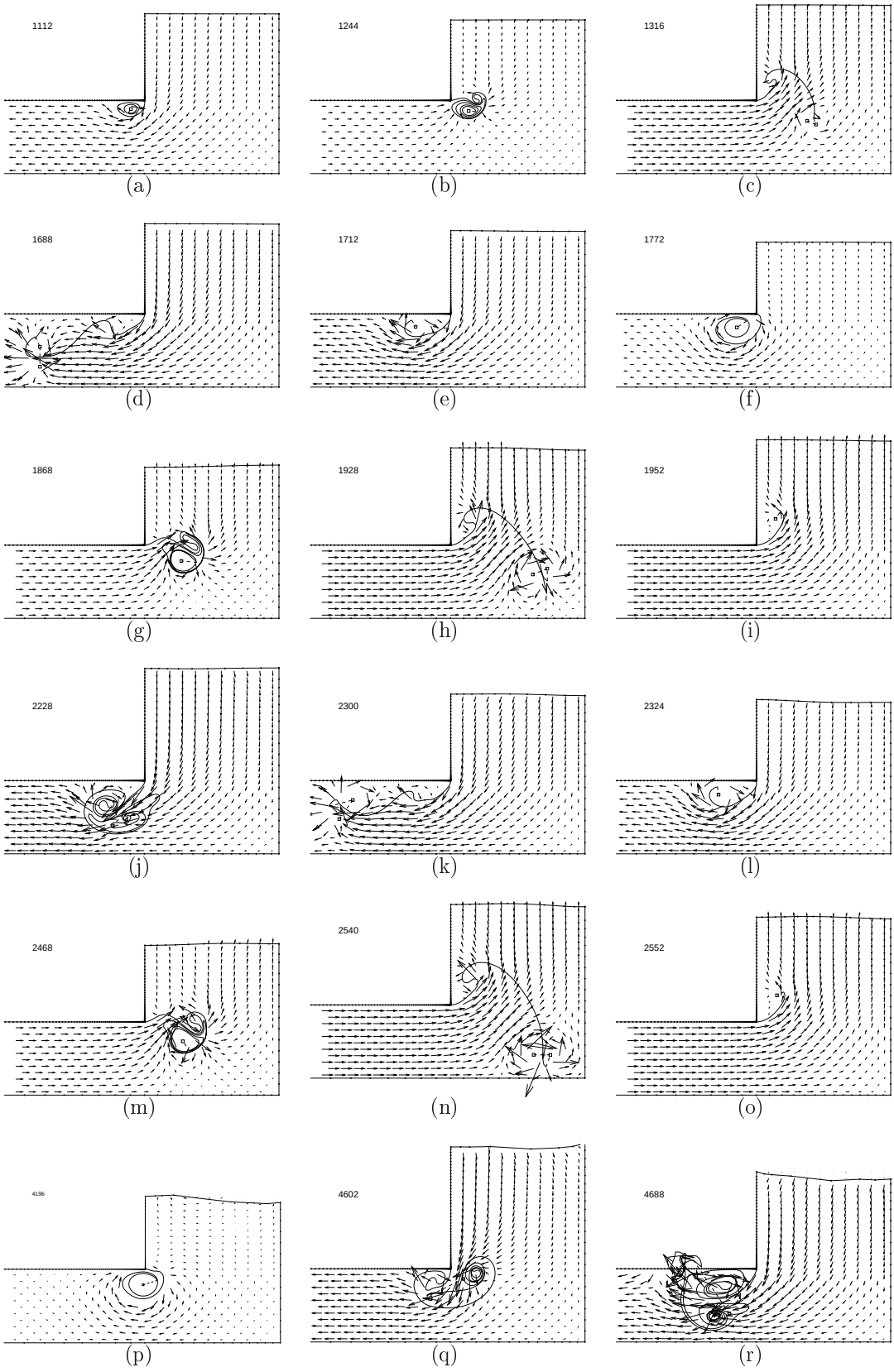

Figure 6.8: The free shear layer and velocity field in a case of waves entering a fixed ship section in piston-mode resonance condition. Time step numbers are shown. The piston-mode amplitude builds up and the vortical structures become too large for the present method to be valid, with $D_0/b \sim 1$ and $D_0/d \sim 1$.

6.5 Application to foil in infinite fluid - A verification

The first implementation of the inviscid vortex tracking method was in the present work done for a foil in infinite fluid, and next further developed for arbitrary number of separation points in oscillatory flow around a rectangular box also in infinite fluid. The resulting code was finally exported nearly as a separate module into the existing numerical wavetank. Choosing the case of foil in infinite fluid was a matter of providing a safe environment for the early development. The results serve, however, as a first verification and we present some of the results in the following.

In the steady case, analytical solutions of the flow exist for Joukowski foils, see e.g. Milne-Thomson (1968). In the unsteady case linear theory gives the lift for an impulsively started flat plate in terms of the Wagner function (see e.g. Newman (1977)). For a foil in oscillatory flow physical model tests show that under certain circumstances a mushroom like wake is formed as in e.g. the experiments presented by Giesing (1968).

The boundary value problem is posed in the xy-plane in the usual manner where a total potential ϕ is introduced as $\phi = \varphi_I + \varphi$, where φ_I represents the ambient flow taken in the present case to be $\varphi_I = U(x\cos\beta + y\sin\beta)$. Here, U is the magnitude of the ambient flow. The angle β is measured from the x-axis with positive direction in the counter-clockwise direction. We impose a zero penetration condition on the foil boundary S, which means that $\partial\varphi/\partial n = -\partial\varphi_I/\partial n$, and solve for φ through (6.1). In the absence of a free surface in the case of infinite fluid, the only unknown is φ along the foil. In the steady case the boundary value problem is solved once, while in the unsteady case the MEL approach as described earlier is used with a first order explicit Euler scheme for time stepping.

6.5.1 Joukowski foil in steady flow

We first consider the steady solution of a Joukowski foil at an angle β relative to the incoming flow of constant velocity U as described above. By steady we mean that the magnitude and direction of the ambient flow has been constant for a very long time, and further that there is a stagnation point both on the lower and upper sides of the trailing edge. The flow is assumed to leave with half the apex angle from the trailing edge. We note two things. First, the flow hence does not leave tangentially from any of the sides of trailing edge of the foil, as in the case of unsteady foil. In that case the side of shedding will change with time; the flow will leave from the upper or lower side of the foil in an oscillating manner under steady inflow condition. Second, the so-called homogeneous solution is obtained with an infinite valued transverse flow at the trailing edge if not imposing the Kutta condition.

We first revisit the essentials of Joukowski foil theory, being the analytic expression for the complex velocity and the circulation by which we may directly compare with our present simulations. Note that the complex mapping is such that one may directly compare velocities in the physical plane with those in the auxiliary plane, but not the values of the complex potential itself.

The foil geometry in the physical complex z-plane is expressed by the Joukowski transformation

$$z = \zeta + \frac{l^2}{\zeta} \tag{6.9}$$

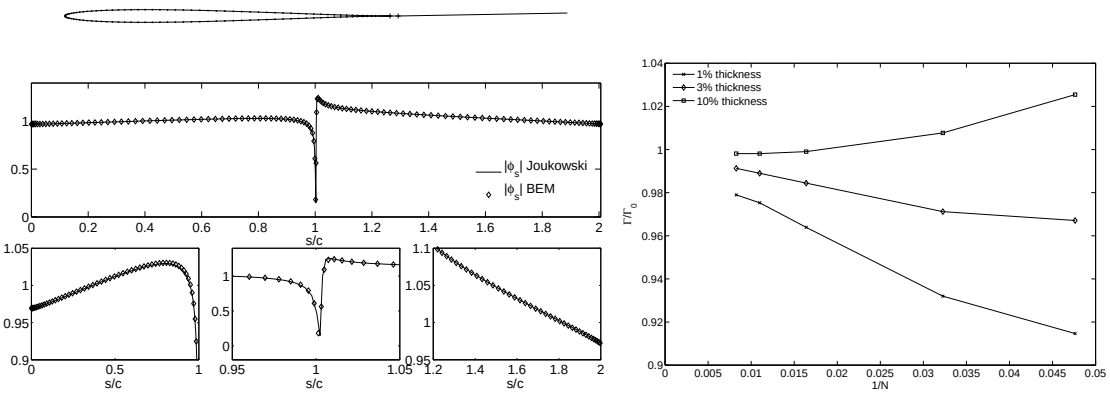

Figure 6.9: Joukowski foil in steady flow. Angle of attack $\beta = 1\,\text{deg}$. Upper: Example of foil geometry ($l = 0.97$ and $\mu = -0.03$ corresponding approximately to 3% thickness, and $N = 121$). The free shear layer extends approximately $100c$ to the right. Lower left (four plots): The computed and theoretical tangential velocity along the foil. The correspondence is good. Right: Convergence study of the circulation Γ with respect to refinement of the body discretization (increasing N) for three foil thicknesses.

where $\zeta = \xi + \mu$ with $\xi = Re^{i\theta}$ describing a circle of radius R in an auxiliary complex plane. The coordinate point $\xi = R$ maps to the trailing edge of the foil. The chord length of the foil is $c = 2R + l^2((R+\mu)^{-1} + (R-\mu)^{-1})$. Choosing $\mu < 0$ has the effect of "twisting" the right part of the circle. Choosing l and μ such that $l - \mu = 1$ provides a foil with a smooth leading edge and sharp trailing edge. Taking $\mu = 0$ yields a flat plate, and for small values it gives approximately the thickness of the foil, with e.g. $\mu = -0.01$ being a foil with thickness approximately 1% of the chord length. The complex potential describing the flow is $f(\xi) = U\left(\xi e^{-i\beta} + R^2 e^{i\beta}/\xi\right) + \Gamma \log \xi / 2\pi i$. The complex velocity is $u - iv = \mathrm{d}f/\mathrm{d}z$ which is

$$u - iv = \left(U\left(e^{-i\beta} - \frac{R^2}{\xi^2}e^{i\beta}\right) + \frac{\Gamma}{2\pi i \xi}\right)\frac{1}{1 - (l/(\xi-\mu)^2)}. \tag{6.10}$$

Stagnation points on both the lower and upper sides of the trailing edge is enforced by requiring that $u - iv = 0$ at $\xi = R$. From (6.10) a circulation of

$$\Gamma = 4\pi U R \sin\beta \tag{6.11}$$

is required to satisfy the zero flow condition. Note that this is consistent with linear foil theory for a flat plate which predicts a circulation $\Gamma = \pi U c\,\beta$, where $c \simeq 4R$.

We model the free shear layer by two elements of equal and constant vorticity as illustrated in the upper left of Figure 6.9. Only a small portion of the second element extending to the far-field is shown in the figure. We do the following reasoning to justify this representation. A constant dipole distribution along a straight element is mathematically equal to two point vortices of opposite strengths located at each end of the element. As is well known, and will be exemplified below for an impulsively started foil, the initially shed vorticity from a foil starting from rest will create what we for simplicity may call a starting vortex which is convected to infinity with the ambient flow. The exact path is not known, but in the present case not of interest as long as the second element

represents a vortex in the downstream far-field. The first element may be short compared to the foil and has the direction of the half apex angle of the trailing edge. The required length of the second element for it to represent a vortex in the far-field depends on the magnitude of the circulation $(-\Gamma)$. In the case presented in Figure 6.9 a distance $\gtrsim 100c$ was needed. In the lower left part a comparison between the calculated and theoretical tangential velocity along the foil is shown, and the comparison is promising.

A convergence study on Γ with respect to body discretization for the circulation is presented in the right part of Figure 6.9, which shows a reasonable convergent behaviour. In the figure, Γ_0 is the analytic value given by (6.11), while Γ is the circulation obtained by the present BEM.

We experienced some problems with divergence when increasing the number of elements N on the body to higher values than those shown. We believe this is a numerical effect due to the very fine elements near the trailing edge giving a near zero angle between the two elements constituting the trailing edge and hence a nearly singular system matrix A. We did not pursue this further, as the problem of near zero angle is not relevant for our main study, namely flow separation from a rectangular ship section. Even in the case of modelling a bilge keel, the angle would exceed by at least an order of magnitude that encountered when refining the grid of the Joukowski foil.

6.5.2 Thin foil in impulsively started flow

We next consider what we call a thin foil in impulsively started flow and compare with the solution for the linearized problem of a flat plate as given by the Wagner function. The chord length of the flat foil is as before denoted c. The shape of the foil is like a diamond. That is, the thickness increases linearly, both in the upper and lower parts, from zero at the two ends to the middle point $c/2$, where it attains its maximum thickness a. The foil in the present study has a thickness of 1% ($a/c = 0.01$). The angle of attack is $\beta = 4$deg. The geometry is shown in the middle part of Figure 6.10. The grid is refined towards the trailing edge. For all grids the two elements defining the trailing edge was of length $\Delta s \simeq 0.002c$.

The steady-state circulation given by the linearized problem of a flat plate is $\Gamma_\infty = \pi U c \beta$. The Wagner function which represents $\Gamma(t)/\Gamma_\infty$ attains a value of 0.5 at $t = 0$. In the numerical solution we model this by a starting vortex with strength equal to $\Gamma_\infty/2$. The numerical solution may not capture this behaviour directly without such a starting vortex. This is seen from the following. Consider the homogeneous solution which predicts an infinite velocity at the tip of the foil. We obtain numerically the homogeneous solution if solving the boundary value problem without enforcing the Kutta condition, that is, when solving without any free shear layer elements or Riemann cuts, say, at the first time-step. The separation velocity U_s is taken as the velocity over the lower aftmost element on the foil by a simple finite difference estimator $U_s = (\varphi_2 - \varphi_1)/\Delta s$, where φ_1 and φ_2 are the values of the potential at the element ends, and Δs the element length. The evolution of the circulation is governed by (2.14), such that when discretized, the solution at time-step n is $\Gamma^n = \Gamma^{n-1} \pm 0.5\,\Delta t\, U_s^2$. Now, if $\Gamma^0 = 0$ (no starting vortex), the circulation after the first time-step is $\Gamma^1 = 0.5\,\Delta t\, U_s^2$. Now, since U_s calculated as described is finite, the expression tends to zero with decreasing time-step, not to $\Gamma_\infty/2$, and provides hence by no means a convergent numerical scheme.

The starting vortex is modelled by a Riemann cut connected to a short free shear layer

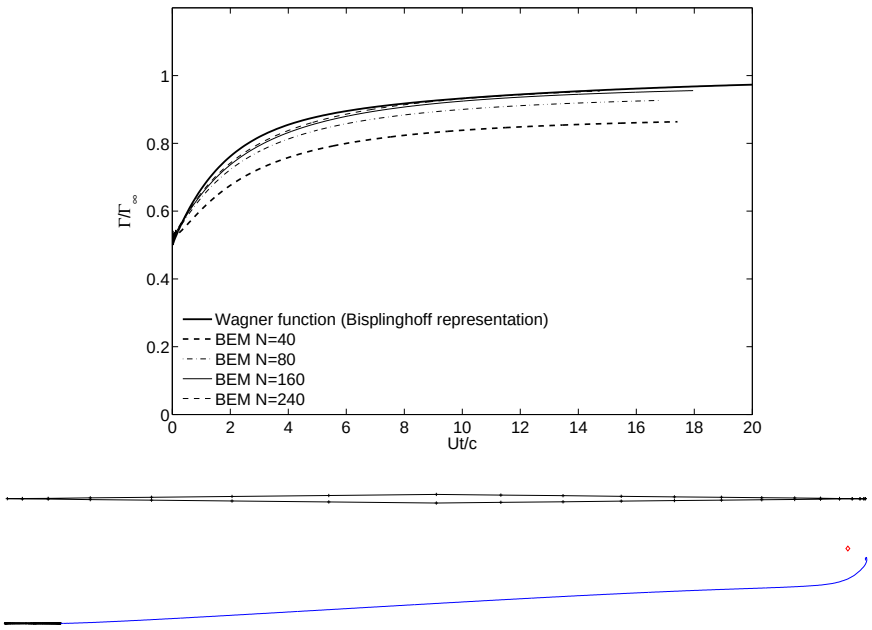

Figure 6.10: Thin foil in impulsively started flow. Upper: Circulation Γ/Γ_∞ for a foil in infinite fluid with impulsively started flow. $\Gamma_\infty = \pi U c \beta$ is steady-state lift for a flat plate (linear theory). Wagner function representation given in Bisplinghoff et al. (1996): $\Gamma/\Gamma_\infty \simeq 1 - 0.165\exp^{-0.091Ut/c} - 0.335\exp^{-0.6Ut/c}$. Numerical results referred to as BEM are from the present simulations for a flat foil of 1% thickness and angle of attack $\beta = 4$deg. N refers to number of elements on the body. Nondimensional time-step is $\Delta t\, U/c = 0.02$. Middle: Flat foil geometry. Lower: Snapshot of the foil and free shear layer after $Ut/c = 14$.

element of length $0.01c$. The Riemann cut extends to a position $\mathbf{x}_{sv}$. The position is not determined analytically, rather by numerical experiments. In the present case, the position was taken as $(0.2c, 0.38c)$ relative to the trailing edge of the foil. The dipole strength over the Riemann cut is taken as $\Gamma_\infty/2$, and as discussed earlier, this is equivalent to a single potential vortex at position $\mathbf{x}_{sv}$. The boundary value problem is solved, giving U_s, and the time-marching procedure of shedding free shear layer elements starts. The evolution of the circulation should then follow quite close to that of the Wagner function. We note that the numerical results represent the fully nonlinear solution, whereas the Wagner function is the solution to the linearized problem. We will expect some discrepancies due to the nonlinearity in the problem. The nonlinearity is, as pointed out by Giesing (1968), basically only associated with the vortex structure which involves a curled up free shear layer. This means we expect some discrepancy at the initial stages, but this should vanish for long times. The discrepancy should also decrease with decreasing angle of attack β. For our chosen rather small angle of attack of $\beta = 4$deg, there should be quite small discrepancies.

Time-series of the circulation are presented in the upper part of Figure 6.10. The Wagner function is that of a representation given in Bisplinghoff et al. (1996). The number of elements on the foil N is varied to check the convergence. The results seem to converge quite well. The time-step is in all cases $\Delta t\, U/c = 0.02$. There was no visual

difference when using half the time-step. Choosing twice the time-step gave a slightly less comparable result for $Ut/c \lesssim 4$, otherwise the same.

A snapshot of the foil and free shear layer including the Riemann cut whose far end is represented by the small square is also presented in the figure. The snapshot is taken at $Ut/c = 14$ for the case with $N = 240$.

We also performed simulations of the impulsively started foil without a starting vortex. The circulation Γ then starts with zero value as discussed. It does, however, approach quite close to the theoretical solution after the foil has travelled about 6-8c. This indicates that a starting vortex is basically needed only to capture the initial stages of the evolution. The steady-state value seems to be quite insensitive to the start-up of the process.

6.5.3 Foil in oscillatory inflow

Since we are in the main part of the present work investigating oscillatory flow, we lastly present some results from simulations of a Joukowski foil with 1% thickness in uniform oscillatory ambient flow. Application of the present BEM qualitatively gives the wake picture as observed in physical model tests presented in Giesing (1968). In the model tests presented there a NACA 0015 foil profile was used. Around a certain oscillatory frequency, or Strouhal number UT/c, he obtained a mushroom like behaviour of the wake. An example of a simulation with the present BEM is shown in Figure 6.11. The obtained structures as shown in the figure do compare qualitatively well with those obtained experimentally by Giesing (1968). The amount of details captured in the wake was found quite strongly dependent upon the time-step. With twice the time-step there was no strong curling up of the structures furthest away from the foil as that in Figure 6.11, only similar to those closest to the foil. This is in a way natural. The finer time-step, the finer the problem is modelled. With increasing time-step the physics is modelled in a more averaged way. In reality, however, viscosity will cause dissipation of the free shear layers, diffusing the structures with time, so a more detailed representation of the free shear layer than that shown is perhaps not correct in that respect anyhow.

We conclude that the present BEM with vortex tracking method reproduces analytic and experimental results in the setting of foils in infinite fluid satisfyingly well. This goes for both steady and unsteady conditions.

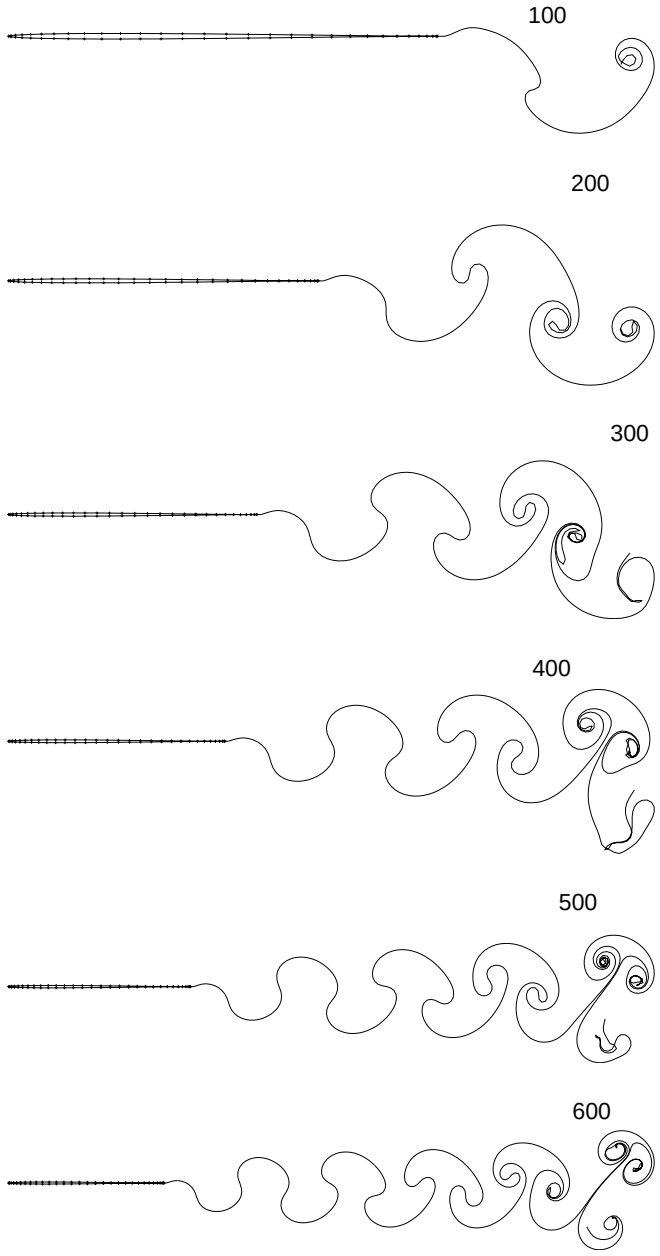

Figure 6.11: Foil with 1% thickness in oscillatory flow with angle varying sinusoidally with amplitude 17.8 deg. $UT/c = 0.537$. Simulation with $N_p = 100$ time steps per period. Time step number is shown in each subplot.

Chapter 7

Numerical modelling of the in- and out-flow of boundary layers

The expression for the in- and out-flow velocity $\tilde{v}$ of a laminar boundary layer along a smooth solid surface in unsteady ambient flow was derived and given by (2.22). The expression involved a convolution integral. In the present chapter we describe how the matter is treated numerically.

The in- and out-flow was implemented in the linear wavetank only, and not in the nonlinear wavetank. In the linear case where the boundary of the domain S is fixed, the implementation was straight-forward, and in our experience involving no numerical problems e.g. such as instabilities or large associated computation time. The implementation involved evaluating the convolution integral (2.22) numerically at each time-step and at each node of the solid parts of the discretized boundary. This was done each sub time-step in the fourth order Runge Kutta scheme in order to provide a consistent boundary condition on the solid boundaries at all times.

We considered also implementing the in- and out-flow into the nonlinear wavetank, but the damping effect of the attached boundary layer was found by all means negligible in the present context of a ship by a terminal, or resonant piston-mode motion in a moonpool (see Figure 10.9), and we therefore decided not to. We mention, however, some thoughts around implementing the in- and out-flow effect in the nonlinear wavetank. In the nonlinear case, a question on how to treat the free-surface zone would arise. First of all, the basic idea behind modelling a viscous boundary layer is to incorporate the effect of the no-slip condition. A physical modelling problem then arises, since there is a conflict between the no-slip condition at the wall and the treatment of the intersection between the free-surface and the wall in the BEM. In this regard we stress that the no-slip condition is in the present viscous boundary layer model not enforced explicitly in the BEM, we rather impose the resulting in- and out-flow on the solid boundaries. Next, a practical problem is that the parts of the solid boundaries that are in the free-surface zone will alternately be dry and wetted. If one should attempt to implement the method in the nonlinear case, we suggest the following strategy: Re-start the convolution integral associated with positions in the free-surface zone each time the fluid enter that position. Now, since (2.22) is derived assuming locally the flow to be of semi-infinite extent, this approach would perhaps be somewhat questionable in the initial phase of wetting of a position. Further, nonlinear terms in the boundary layer calculations should be included in the nonlinear BEM case. We did not investigate the matter further.

7.1 Numerical integration of the convolution integral

There is no analytic solution to the convolution integral (2.22) for general unsteady ambient flow U_e, and so, it must be integrated numerically. Being of the form

$$I(t) = \int_0^t \frac{f(\tau)}{\sqrt{t-\tau}}\,\mathrm{d}\tau, \tag{7.1}$$

we see that some care must be taken due to the square root singularity at $\tau = t$. The square-root singularity is a weak singularity that we may remove in at least two standard ways. One is by integration by parts and another by substitution of variables. Although we chose integrating by parts, we first briefly outline a possible strategy if choosing substitution of variables. In the following, we take $f = \sqrt{\nu/\pi}\,\partial U_e/\partial s$.

7.1.1 Substitution of variables

The method of substitution of variables may be applied by introducing an auxiliary variable u. Substituting $u^2 = t - \tau$ into (2.22) leads to the integral $\int_0^{\sqrt{t}} f(s, t-u^2)\,\mathrm{d}u$. In this expression the integration parameter appears in the argument of the integrand as u^2, which means that numerically, where the integral is approximated by a sum, the integrand would be evaluated at time-steps n, $n-1$, $n-4$ etc., where time-step n is the present time-step. The sum hence involves only $\sqrt{n}$ and not n terms, which reduces the cost of evaluating the sum. Note that this is so in the case of constant time-step length Δt. With a varying time-step some interpolation would be necessary.

7.1.2 Integration by parts

In the method of integration by parts, which we have chosen to use, all n terms are in principle involved in the sum, but due to the $1/\sqrt{\tau}$ term the sum may in practice be truncated, as the value of the integrand in (7.1) vanishes as τ becomes large. The perhaps seemingly excessive time consumption associated with the summation is therefore avoided. The reason we discuss time consumption is that in some applications, this may become an important issue. However, in the simulations performed in the present work all n terms were included with only a minimum of time consumption experienced.

The following approximate expression for the integral is derived in Appendix C:

$$I(t) = \left(\sum_{i=1}^{n-1} \frac{f^{n-i}}{\sqrt{i}} + f^n + \frac{1}{2} f^{n-1} - \frac{1}{2} \frac{f^1}{\sqrt{n-1}} \right) \sqrt{\Delta t}\,. \tag{7.2}$$

In the derivation, constant time-step Δt is assumed, and the expression is correct to second order in time. The expression (7.2) was implemented into the linear numerical wavetank with the outer flow taken as that on the solid boundary itself, i.e. $\partial U_e/\partial s = \partial^2\varphi/\partial s^2$. The second derivative of the potential was estimated numerically by the difference scheme given by (A.7) and using the known values for the potential along the solid boundary from the previous (sub) time-step.

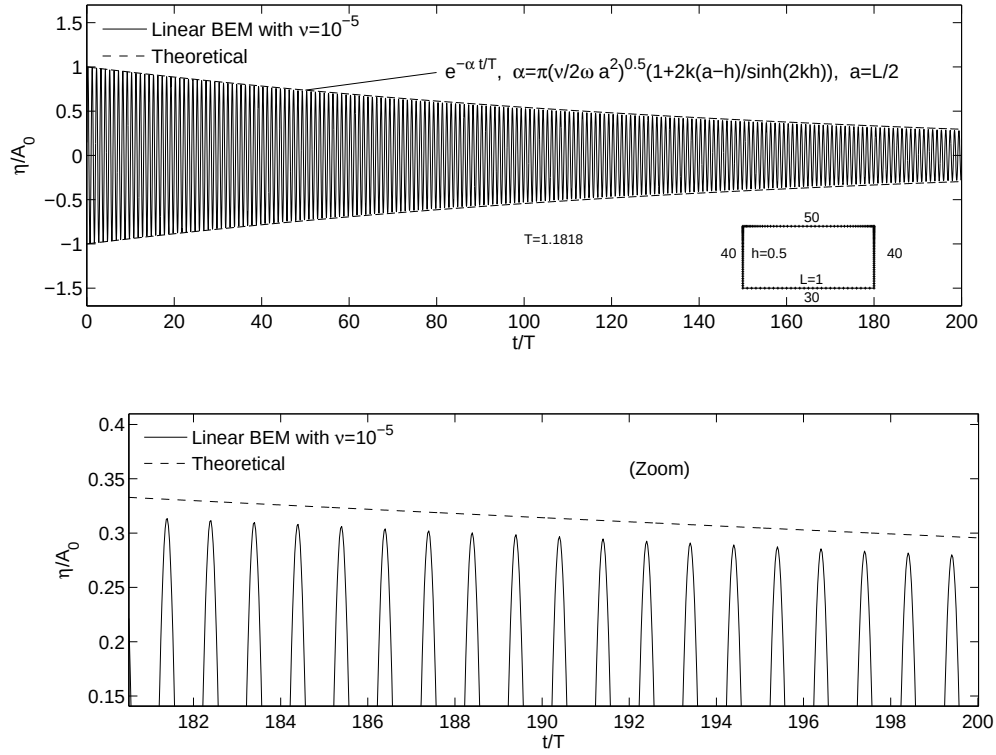

Figure 7.1: Decay of a standing wave in a rectangular tank. Simulations using the present linear wavetank compared to theoretical decay. The decay is due to the damping introduced by the in- and out-flow of the boundary layers along the tank bottom and walls. Lower plot is zoom-in of the upper. Tank length is $L = 1$m, still water depth $h/L = 0.5$ and $\nu = 10^{-5}\text{m}^2/\text{s}$. Initial amplitude is $A_0/L = 0.0147$.

7.2 Standing wave in a rectangular tank - A verification

A verification of the current method and implementation of (7.2) into the linear numerical wavetank is presented in the following by means of a free decay test. The test involves a fixed rectangular tank, partially filled with water. The tank length is $L = 1$m, and still water depth $h/L = 0.5$. We investigate the decay of the standing wave of wavelength $\lambda/L = 2$, that is, the first linear mode. The initial condition for the potential φ and the free surface ζ is taken from the analytic linear solution. The free-surface elevation is initially at a maximum, such that the fluid velocity is zero in the whole domain. The initial standing wave amplitude is $A/L = 0.0147$. The kinematic viscosity that enters (7.2) is here chosen to be $\nu = 10^{-5}\text{m}^2$.

The simulated time-series of the wave elevation ζ at the left wall is presented in Figure 7.1. The numerical results are compared to theory as presented by Keulegan (1959) where the decay of the amplitude is, for small values of ν, assumed to be exponential $\exp(-\alpha t/T)$ where α is found from an energy consideration. The expression for α is shown in the figure along with the analytic solution $\exp(-\alpha t/T)$ represented by the dashed curve. The number of elements along the boundary as well as the actual grid is also indicated in the figure. The element size was refined near the two intersections between the free surface and the vertical walls according to a cosine squared spacing with the resolution

parameter $\beta = 0.7$ in the formulation given in (A.8). The number of time-steps per period was $N_p = 120$. From the figure it is clear that the numerical solution recovers that of the theoretical quite nicely. From the zoomed view in the lower part of the figure we may estimate the discrepancy to approximately 2 - 3% after 200 periods of oscillations. We performed no systematic convergence study. However, we did some checks with different grids. The results were slightly improved with the refined grid near the intersections relative to constant element size. Further, they approached the theoretical solution with increasing number of elements.

We feel comfortable that the present method of modelling the in- and out-flow of boundary layers is feasible, and that its implementation in the linear wavetank has been verified through this example.

Chapter 8

Numerical force calculations

We have in the three preceding chapters introduced and discussed the numerical wavetanks including the free shear layer as well as the in- and out-flow of boundary layers. In this last chapter on numerical issues we present the numerical force calculations and integration of the equations of motion.

Rigid body motion may be forced or free, where in both cases the normal velocity is imposed as a boundary condition in the boundary integral equations (6.1). The difference between the two cases is that in the latter the velocity must be solved for simultaneously and in a way becomes another unknown requiring an additional set of equations to solve. The equations of motion provide the required additional set of equations.

The right hand side of the equations of motion are the force and moment on the body. When imposing a slip-condition as we do here, these are found by integrating the pressure given by the Bernoulli equation multiplied with the unit normal vector along the full body boundary. The integration of the pressure involves integration of the instantaneous time rate of change of the potential, φ_t. In the linear case, the boundary is fixed at all times and the force calculations rather straight-forward. However, in the nonlinear case, φ_t is not defined over a moving boundary, since we have adopted the MEL approach. The MEL approach is explained in Chapter 5.

There are to our knowledge three main strategies to overcome this problem, and we refer the reader to the introduction chapter of the present text for a review of these. There are challenges associated with each strategy. In the present work we chose to pursue the strategy of manipulating the force and moment expression in such a way that the time derivative of φ_t is moved outside the integral.

In this chapter we start by deriving the alternative formulations for the forces and moment. We next discuss some characteristics of these expressions. As a result of the manipulation, the equations of motion are cast into a set of so-called differential algebraic equations. We point at problems related to solving these. We last present some verification cases.

8.1 Alternative formulation of the forces and moment

In the present work we derive an alternative expression for the force and moment on a freely floating, surface piercing body in a nonlinear wavetank. The basic idea is as that presented in Faltinsen (1977), where the time derivative is moved outside the integrals.

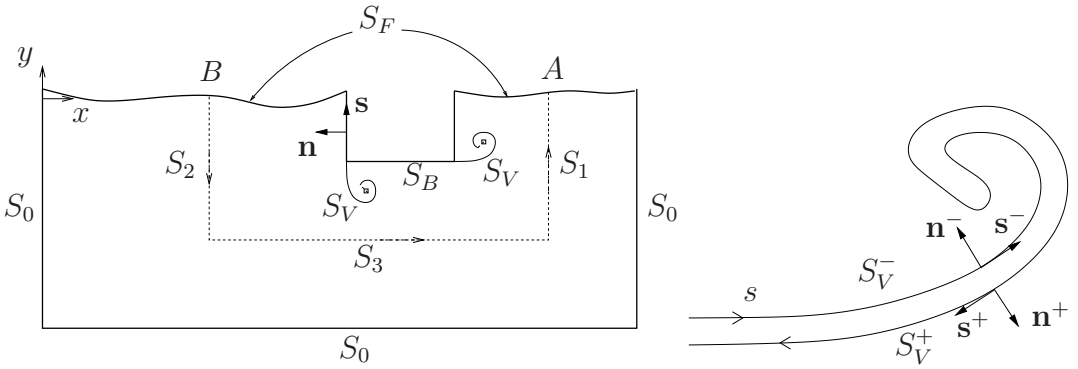

Figure 8.1: Closed path of integration in force calculations $S_I = S_B + S_F + S_V^{\pm} + S_1 + S_2 + S_3$, enclosing a domain called Ω_I. Here, S_F is the part of the free surface between A and B. S_0 denotes the solid boundaries of the closed wavetank. Right: Path of integration along $S_V^{\pm} = S_V^- + S_V^+$, where S_V^- is denoted simply as S_V after collapsing S_V^- and S_V^+ to one single curve.

In his work disturbances all the way to infinity was allowed, but only vertical dipole-like. There were no waves allowed beyond a distance "b" from the body. This assumption was suitable for cases with forced body motion with radiating waves in otherwise still fluid. In the case of a body in a closed wavetank subject to incoming waves that are generated at one of the lateral boundaries, however, we may not make the assumption of no waves far away. We therefore derive an expression which is basically a generalization of the formula presented therein. More terms are involved in the present expression.

8.1.1 Derivation of the alternative formulation

In short, moving the time derivative outside the integral is achieved by manipulation by use of Gauss' theorem for the force and Stokes' theorem for the moment, as well as the Transport theorem. We first introduce a closed control surface as that shown in Figure 8.1 enclosing and including only the body of interest. Here the closed surface is denoted $S_I = S_B + S_F + S_V^{\pm} + S_1 + S_2 + S_3$. By S_F we here mean the part of the free surface limited by the body and the intersection points between S_1 and S_2 with S_F, denoted A and B in the figure. By $S_V^{\pm} = S_V^+ + S_V^-$ we mean a surface enclosing the whole free shear layer, including the unsimplified part as well as Riemann cuts. This is illustrated in the right part of Figure 8.1. We will later collapse $S_V^{\pm}$ to S_V. The horizontal coordinates of the vertical parts of the control surface, S_1 and S_2, as well as the whole of surface S_3, are fixed. Only the upper ends of S_1 and S_2 change with time, and only vertically. For convenience in the derivation we define $S_C = S_1 + S_2 + S_3$. The vertical axis is as before denoted y being positive upwards, and the normal points into the fluid as before. We derive the expression for the force only. The moment may be derived in the same manner, only using Stokes' instead of Gauss' theorem.

We write the force (2.24), after adding and subtracting the integral of $p\,\mathbf{n}$ over $S_I - S_B$, as

$$\mathbf{F} = -\int_{S_I} p\,\mathbf{n}\,\mathrm{d}s + \int_{S_F+S_C+S_V^{\pm}} p\,\mathbf{n}\,\mathrm{d}s. \tag{8.1}$$

In the second term on the right hand side, the integrals of the pressure over S_F and $S_V^{\pm}$ vanish, that is $\int_{S_F+S_V^{\pm}} p\,\mathbf{n}\,\mathrm{d}s = 0$. This is so since on the free surface the pressure is assumed zero in the present application of Bernoulli's equation. Over the free shear layer, the pressure drop is zero while the normal vector is opposite along S_V^- and S_V^+ when taking the limit of a thin free shear layer. Substituting the pressure given by Bernoulli's equation (2.2) into (8.1) we now get

$$\mathbf{F} = \rho \underbrace{\int_{S_I} \varphi_t \mathbf{n}\ \mathrm{d}s}_{I_1} + \rho \int_{S_B+S_F+S_V^{\pm}} 0.5\,|\nabla\varphi|^2\,\mathbf{n}\ \mathrm{d}s + \rho g \int_{S_B+S_F} y\mathbf{n}\ \mathrm{d}s - \rho \int_{S_C} \varphi_t \mathbf{n}\,\mathrm{d}s. \quad (8.2)$$

Here, the integral of gy over the free shear layer $S_V^{\pm}$ vanishes for the same reason as just explained above, since y is equal along both sides. We proceed by rewriting I_1. First, using Gauss' theorem (D.3) we have that

$$I_1 = \int_{S_I} \varphi_t \mathbf{n}\ \mathrm{d}s = -\int_{\Omega_I} \nabla\varphi_t\,\mathrm{d}\Omega. \quad (8.3)$$

Next, from the Transport theorem (D.4), we get

$$\begin{aligned} I_1 &= -\frac{\mathrm{d}}{\mathrm{d}t}\int_{\Omega_I} \nabla\varphi\,\mathrm{d}\Omega - \int_{S_I} \nabla\varphi\, U\ \mathrm{d}s \\ &= \frac{\mathrm{d}}{\mathrm{d}t}\int_{S_I} \varphi\,\mathbf{n}\,\mathrm{d}s - \int_{S_B+S_F+S_V^{\pm}} \nabla\varphi\,\varphi_n\ \mathrm{d}s, \end{aligned} \quad (8.4)$$

where U is the normal velocity of the boundary, defined positive into Ω_I. In the last equality, Gauss' theorem and the fact that $U = 0$ on S_C and $U = \varphi_n$ on $S_B + S_F + S_V^{\pm}$ is used. Inserting this expression for I_1 into (8.2), we get

$$\begin{aligned} \mathbf{F} = \rho\frac{\mathrm{d}}{\mathrm{d}t}\int_{S_I} \varphi\,\mathbf{n}\,\mathrm{d}s + \rho g\int_{S_B+S_F} y\,\mathbf{n}\ \mathrm{d}s \\ + \rho\int_{S_B+S_F+S_V^{\pm}} \left(0.5(\varphi_s^2-\varphi_n^2)\mathbf{n} - \varphi_n\varphi_s\mathbf{s}\right)\ \mathrm{d}s - \rho\int_{S_C} \varphi_t\,\mathbf{n}\,\mathrm{d}s. \end{aligned} \quad (8.5)$$

where the expression in the second last integral is obtained due to the equality

$$0.5\,|\nabla\varphi|^2\,\mathbf{n} - \nabla\varphi\,\varphi_n = 0.5(\varphi_s^2-\varphi_n^2)\mathbf{n} - \varphi_n\varphi_s\,\mathbf{s}, \quad (8.6)$$

since $\nabla\varphi = \varphi_n\mathbf{n} + \varphi_s\mathbf{s}$. Over $S_V^{\pm}$ we show in Section D.3 the following equality,

$$\int_{S_V^{\pm}} \left(0.5(\varphi_s^2-\varphi_n^2)\mathbf{n} - \varphi_n\varphi_s\mathbf{s}\right)\ \mathrm{d}s = \int_{S_V} (U_{cn}\mathbf{s} - U_{cs}\mathbf{n})\,\Gamma_s\ \mathrm{d}s, \quad (8.7)$$

where $U_{cs} = \boldsymbol{U_c}\cdot\mathbf{s}$ and $U_{cn} = \boldsymbol{U_c}\cdot\mathbf{n}$ where $\boldsymbol{U_c}$ is the wake velocity given by (2.12), and $S_V := S_V^-$ in the limit that S_V^- and S_V^+ collapses to one single line. Note that the contribution over the Riemann cuts vanish in this integral. Strictly speaking, the integration is therefore over S_v only, although we write S_V.

We see that there still remains an integral with φ_t in the integrand of (8.5). We reduce this term into two much simpler terms as follows. We use the one-dimensional version of

the Transport theorem (D.5). Take the function f in (D.5) to be $f = \varphi\,\mathbf{n}$. We may then, according to (D.5), write

$$\frac{\mathrm{d}}{\mathrm{d}t}\int_{S_C}\varphi\,\mathbf{n}\,\mathrm{d}s = \int_{S_C}\varphi_t\,\mathbf{n}\,\mathrm{d}s + [u\,\varphi\,\mathbf{n}\,]_A + [u\,\varphi\,\mathbf{n}\,]_B. \tag{8.8}$$

The points A and B are the contact points between S_C and the free surface as shown in Figure 8.1. u_A and u_B are the vertical velocities of the free surface at points A and B. Both must be taken as positive in the positive y-direction. This is so since the direction of expansion of the curve S_C is in the positive y-direction. This means that the direction out of the "domain" S_C in the Transport theorem is in that direction. The values of the potential is that at the time instant of evaluation. The normal vectors are those of the control surface S_1 and S_2 at the contact point, i.e. pointing horizontally (not vertically). We may now substitute (8.8) into (8.5), and we arrive at the alternative force expression where the φ_t term is eliminated,

$$\begin{aligned}\mathbf{F} = {}& \rho\frac{\mathrm{d}}{\mathrm{d}t}\int_{S_B+S_F}\varphi\,\mathbf{n}\,\mathrm{d}s - \rho\frac{\mathrm{d}}{\mathrm{d}t}\int_{S_V}\Gamma\,\mathbf{n}\,\mathrm{d}s + \rho g\int_{S_B+S_F} y\,\mathbf{n}\;\mathrm{d}s + \rho[u\,\varphi\,\mathbf{n}\,]_A + \rho[u\,\varphi\,\mathbf{n}\,]_B \\ & + \rho\int_{S_B+S_F}(0.5\left(\varphi_s^2-\varphi_n^2\right)\mathbf{n} - \varphi_n\varphi_s\mathbf{s})\;\mathrm{d}s + \rho\int_{S_V}(U_{cn}\,\mathbf{s} - U_{cs}\,\mathbf{n})\,\Gamma_s\;\mathrm{d}s.\end{aligned} \tag{8.9}$$

The moment is derived in the same manner, only using Stokes' theorem rather than Gauss' theorem, cf. (D.3), and the result is analogous to (8.9), being

$$\begin{aligned}\mathcal{M} = {}& \rho\frac{\mathrm{d}}{\mathrm{d}t}\int_{S_B+S_F}\varphi\,n_\theta\,\mathrm{d}s - \rho\frac{\mathrm{d}}{\mathrm{d}t}\int_{S_V}\Gamma\,n_\theta\,\mathrm{d}s + \rho g\int_{S_B+S_F} y\,n_\theta\;\mathrm{d}s + \rho[u\,\varphi\,n_\theta\,]_A + \rho[u\,\varphi\,n_\theta\,]_B \\ & + \rho\int_{S_B+S_F}(0.5\left(\varphi_s^2-\varphi_n^2\right)n_\theta - \varphi_n\varphi_s s_\theta)\;\mathrm{d}s + \rho\int_{S_V}(U_{cn}\,s_\theta - U_{cs}\,n_\theta)\,\Gamma_s\;\mathrm{d}s,\end{aligned} \tag{8.10}$$

where n_θ and s_θ are given by (D.1), except here, they apply to all surfaces, not only S_B as indicated in that expression.

Note that the present formulations may readily be used in multi-body problems. One simply defines a separate control surface enclosing each body. Each control surface must then enclose its associated body only, and not other bodies. If the bodies drift, such that one body drifts across another body's control surface, one must redefine the positions of the control surfaces at some stage. This will presents no considerable practical problem in a numerical implementation. This strategy of redefining the control surface may also be followed for a ship in forward speed.

8.1.2 Some characteristics of the alternative formulation

There are two key features of the alternative expressions (8.9) and (8.10). First, they involve several integral terms as opposed to the original single integral term over the body itself. Second, and this was the primary goal, the time derivative is moved outside those integrals involving φ_t. As for the first, the additional cost of evaluating the extra terms is negligible as they are over known quantities. A problem that arises, however, is

that pairs of terms may attain large amplitude of opposite sign which in theory should nearly cancel, but in practice may pollute the numerical solution. This is so in particular when calculating the roll moment. As far as the second goes, moving the time derivative outside the integral means that the integral itself represents momentum, giving velocity directly without time integration. This may at first sight seem attractive, but represent in practice what we might consider a phasing problem with respect to the remaining integrals. In mathematical terms we are left with a set of so called *differential-algebraic* equations which in general is not trivial to solve. This means the present method also has its challenges, where suggested resolutions will be discussed shortly in connection with time integration of the equations of motion.

We first shortly discuss some characteristics of the contribution of each of the terms in (8.9) or (8.10) and consider one of the force components F_x, F_y or the moment $\mathcal{M}$ and denote this simply by F. We refer to F as force, although it also applies to the moment. We further denote by n and s the corresponding components of the unit normal and tangential vectors respectively. We write

$$F = \rho \frac{\mathrm{d}}{\mathrm{d}t} \sum_{j=1}^{3} K_j + \rho \sum_{j=4}^{10} K_j, \tag{8.11}$$

where the K_j-terms are

$$\begin{aligned} K_1 &= \int_{S_B} \varphi\, n \,\mathrm{d}s, \quad K_2 = \int_{S_F} \varphi\, n \,\mathrm{d}s, \quad K_3 = -\int_{S_V} \Gamma\, n \,\mathrm{d}s, \\ K_4 &= g \int_{S_B} y\, n \,\mathrm{d}s, \quad K_5 = g \int_{S_F} y\, n \,\mathrm{d}s, \; K_6 = [u\, \varphi\, n\,]_A, \; K_7 = [u\, \varphi\, n\,]_B, \\ K_8 &= \int_{S_B} f_1 \,\mathrm{d}s, \; K_9 = \int_{S_F} f_1 \,\mathrm{d}s, \; K_{10} = \int_{S_V} f_2 \,\mathrm{d}s, \end{aligned} \tag{8.12}$$

where $f_1 = 0.5\,(\varphi_s^2 - \varphi_n^2)\, n - \varphi_n \varphi_s\, s$ and $f_2 = (U_{cn}\, s - U_{cs}\, n)\, \Gamma_s$.

Assuming linear theory, and neglecting flow separation, we indeed recover the linear force due to the following. All terms K_{6-9} are of second order and therefore vanishes in the limit of linear theory. Further, since S_F and S_B are in the linear case the fixed mean position of the free surface and the body, the time derivative goes under the integral sign of K_1. Then, $\mathrm{d}K_2/\mathrm{d}t + K_5 = 0$ due to the linear free-surface condition, and we are left with only $\mathrm{d}K_1/\mathrm{d}t$ representing the added mass and damping force and K_4 the restoring force. Removing the assumption of linear theory we may perhaps still associate with K_1 the "added mass and damping" and with K_4 the "restoring term", at least for small ship motion, although strictly speaking, these are no longer defined.

To second order we observe the following. The terms K_1, K_2 and K_3 do not contribute to the mean force since any constant term is differentiated away. K_6 and K_7 do not contribute to the heave force at all, since the normals of the vertical parts of the control surface S_C point horizontally. The two terms do, however, contribute significantly to the mean drift force in sway. Except from K_6 and K_7, all the other terms K_4 - K_{10} contribute to the mean force or moment in all three degrees of freedom.

8.2 Numerical integration of the forces and moment

The numerical treatment of the spatial integrals as well as the integration of the equations of motion are discussed in the following. We begin with the rather straight-forward implementation of the spatial integrals and next describe in some detail that of the temporal integration.

8.2.1 Spatial integration

Numerically, the K_j terms in (8.12) are obtained by summation over the body, free surface and free shear layer elements. Since the potential etc. vary linearly over linear elements, the expressions are straight-forward to deduce consistent to second order accuracy in space as other quantities in the present work. The sums representing the integrals are given by (D.8). Note that for the term K_9 there is a contribution from the Riemann cuts, while it was shown in the derivation of (8.7) that the contribution from Riemann cuts was zero for K_{10}.

8.2.2 Time integration of the equations of motion

The force is integrated to velocity and the velocity to position. As a standard mathematical procedure the equations of motion (2.23), being a set of second order differential equations, may be converted into another set of twice as many first order differential equations by introducing the velocities in the three degrees of freedom v_x, v_y and v_θ, and we write the six equations of evolution

$$\begin{aligned} \dot{x}_G &= v_x, \quad \dot{v}_x = F_x/m \\ \dot{y}_G &= v_y, \quad \dot{v}_y = F_y/m \\ \dot{\theta} &= v_\theta, \quad \dot{v}_\theta = \mathcal{M}/\mathcal{I} \end{aligned} \tag{8.13}$$

where for each there is an initial value at $t = 0$. Although necessary in the boundary integral formulation (6.1), the velocities may in a sense be considered auxiliary functions. As a mean of further studying the nature of the alternative force expression (8.9) we introduce yet another set of auxiliary functions as follows. We express the motion x and velocity v in one of the degrees of freedom, each by a sum of two auxiliary terms $x = x_a + x_b$ and $v = v_a + v_b$ such that $\dot{v}_a = \mathrm{d}K_a/\mathrm{d}t$ and $\dot{v}_b = K_b$ where $K_a = \Sigma_{j=1}^{3} K_j$ and $K_b = \Sigma_{j=4}^{10} K_j$. In the selected degree of freedom we therefore have the set of four equations of evolution

$$v_a = K_a, \quad \dot{v}_b = K_b, \quad \dot{x}_a = v_a, \quad \dot{x}_b = v_b, \tag{8.14}$$

where we have assumed $v_{a0} = 0$. We see that one part of the velocity, v_a, is governed by an algebraic equation and is known explicitly at time t given the geometry and potential at that instant in time, while for the second part of the velocity, v_b, and for the positions x_a and x_b first order ordinary differential equations govern the solutions.

Now, considering all three degrees of body motion, we have three algebraic and nine ordinary differential equations. Further, for the coupled fluid-structure problem, we also have the two free-surface conditions, (2.3) and (2.4), as well as the evolution equation of the free shear layer (2.13) and that of the circulation (2.14). In the MEL approach,

where total derivative is like a normal time derivative, we then have thirteen ordinary differential equations, and these together with the three algebraic equations constitute a so-called set of differential-algebraic equations (DAE).

Differential-algebraic equations are known to be non-trivial to solve, and some aspects of the numerical solution are discussed e.g. in Hairer, Lubich, and Roche (1989). Here we only give a quick outline of our understanding of the implied difficulties. As an example, consider the motion of some arbitrary object in three-dimensional space with solution $(x(t), y(t), z(t))$ with the motion governed by

$$\begin{aligned} \dot{x} &= f(x, y, z, t), \\ \dot{y} &= g(x, y, z, t), \\ 0 &= h(x, y, z, t), \end{aligned} \tag{8.15}$$

together with proper initial conditions. Note the zero on the left hand side of the last equation. This is a set of two ordinary differential equations and one algebraic equation. Now, the algebraic equation is not an equation of evolution, but rather a constraint as to where the object might travel. The solution is thus defined over a manifold, i.e. lives in this case on a surface in three-dimensional space, with the surface possibly of complex shape. Intuitively, keeping the solution on that surface is harder than having available the whole three-dimensional space. This goes in particular for a numerical method where one in a discrete time stepping algorithm is prone to "fall off" the surface.

Accuracy and stability. The consequence of the above discussion is in a way two-fold, although the two matters are inter-related. The first matter is regarding the order of accuracy of the time-stepping algorithm. This will become clear in a while. The other is regarding numerical stability. Both matters are related directly to the difficulties with the numerical solution of DAE. Here we explain the way the problems are overcome thus far, regarded sufficient for the present problem. More efforts would nevertheless be welcome in order to handle the problems in an improved manner in future works.

As for the first, from a practical point of view, the DAE represent a phasing problem. For example, consider the linearized problem and resonant heave motion of a ship section. The relative phasing between the added mass and damping force represented by $\mathrm{d}K_1/\mathrm{dt}$ and the restoring force represented by K_4 is crucial at resonance. The only way we have managed to model this in a proper way with convergent results is using a sense of averaging during the four sub-steps of the fourth order Runge Kutta scheme. The implication is that we recover a numerical method only first order in time, not fourth order. Although the ship motion is in this way only captured to first order in time we still use the fourth order Runge Kutta method as it gives a truly superior numerical solution of the free surface in the far field, e.g. the propagation of the incoming wave train.

As far as the numerical stability goes, a technique as used by several other authors is adopted in the present implementation. The first one known to the auther to use the technique was Kvaalsvold (1994). Later it has been used by e.g. Wu and Eatock Taylor (2003), Sun and Faltinsen (2006). The technique is simple and robust. In the equations of motion an artificial "added mass" term is added on each side of the equality sign. For example, in the equation of motion for heave, where we denote the artificial added mass by A_{yy}, we get $(m + A_{yy})\ddot{y}_G = F_y + A_{yy}\ddot{y}_G$. In the numerical scheme, the acceleration on

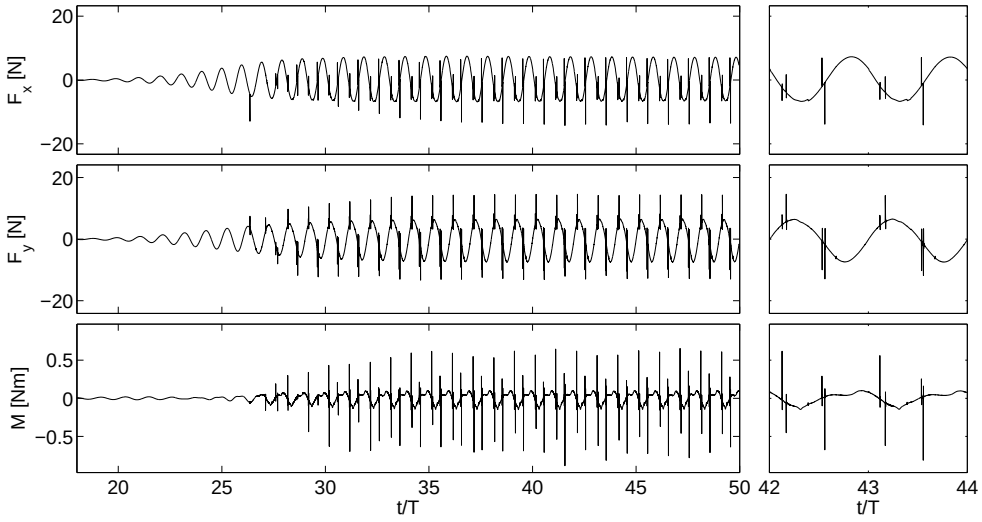

Figure 8.2: Illustration of peaks occurring in the force and moment time-series due to simplifications of the free shear layer.

the left hand side is the unknown to be solved for, while that on the right hand side is taken as that of the previous time-step or sub time-step. This does not reduce the order of accuracy, as it is already first order as described above. In our experience the results are not sensitive to the chosen value for A_{yy} as long as it is in the same order of magnitude as the actual added mass. We have found this technique to be strictly necessary in heave, as neglecting its use leaves an unconditionally unstable numerical scheme, the simulation will break down after only few time-steps even in still water tests. In our experience it also stabilizes the roll motion in cases with more pronounced roll than in the present. We have not applied the technique for sway as was done by Wu and Eatock Taylor (2003), as it was not found necessary. Recommended values for the added mass terms for all degrees of freedom is given therein. This may not, however, be adopted directly here due to a different formulation of the problem relative to the present.

An observation regarding this stabilizing technique which has to our knowledge not been noted in the literature on the matter is the following. The described technique is intrinsically similar to a finite impulse response (FIR) filter commonly used among other places in control theory, see e.g. Rabiner and Gold (1975). It basically averages new estimates and existing known values. In this respect, we performed a quick study by applying a FIR filter for reproduction of a sinusoid when solving a second order differential equation similar to the equation of motion. With $A_{yy} = m$, this gave a reproduction lagging one time-step disregarding the size of the time-step, and an error in the reproduced amplitude which was by all means negligible. The small discrepancies found in this simple test explains qualitatively the goodness of the method experienced by others as well as the present author.

8.2.3 Problems related to large roll motion

We now look closer into some problems of the method based on the alternative formulation of the moment to calculate roll motion. In cases of considerable roll we found it necessary

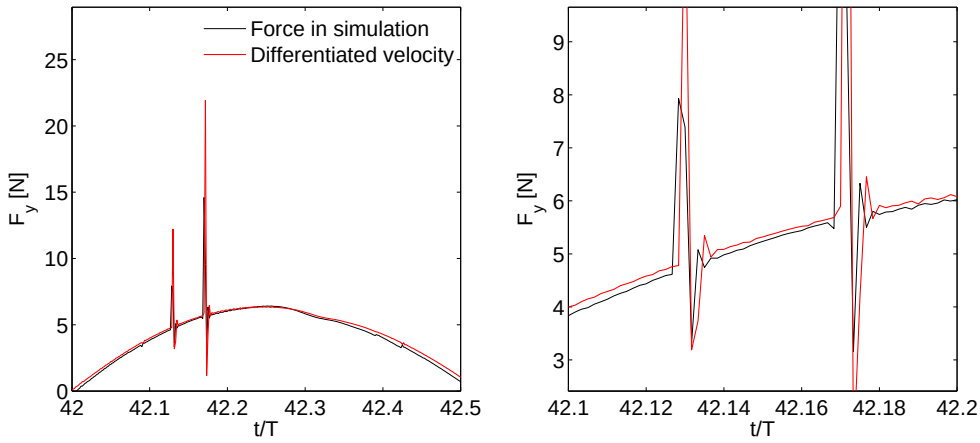

Figure 8.3: Close-ups of the heave force time-series presented in Figure 8.2.

to neglect all other terms than $\mathrm{d}K_1/\mathrm{dt}$ and K_4. That is, we keep only the "linear" terms. The main problem was that the sum of the terms over the free surface $\mathrm{d}K_2/\mathrm{dt}$ and K_5, which in theory only should contribute to second and higher order, in general gave contributions in the same order as the "linear" terms, gave rise to inaccuracies that in turn caused instabilities. One reason that the numerical inaccuracies arise is perhaps that in the integration over the free surface, each term involve multiplication with the distance from the center of gravity, which may become large depending on the extent of the control surface. We did not resolve this problem satisfactory during the present work, and we recommend for future use a proper investigation possibly resolving the problem. We can not, for example, neglect the possibility of a bug in the code.

We emphasize that in case of small roll angle, the instability does not arise, and all terms may be kept. We realize that "small" roll angle is not well defined in this discussion. However, for example in the study of a moored ship by a terminal presented in Section 10.3, the roll amplitude was "small", and no sign of instability was observed during that study. We did, however, perform numerical experiments with a rectangular box floating in a sloshing tank. The motion was started from rest, and a sinusoidal motion of the tank walls was prescribed. The frequency was that of the first sloshing mode of the tank. The box was placed in the middle of the tank. The roll moment of inertia was taken such that the roll motion of the box should be equal to the slope of the free-surface at its position in the tank, i.e. in the quasi-static roll regime. In the initial stages of the simulations, the box behaved well in both sway, heave and roll. However, as the free-surface motion built up, the roll motion of the box became unstable. This was in the case all the K_j-terms were kept. Neglecting all terms except the "linear", however, the roll motion was stable, and did follow the free-surface slope, even up to the stage where the free-surface was near breaking.

8.2.4 Effect of free shear layer simplifications

As was explained in Chapter 6 we automatically simplify the free shear layer during a simulation. We argued that dumping near circular vortical structures to a single vortex and cutting pairs of vortices of near opposite strength were acceptable actions both based

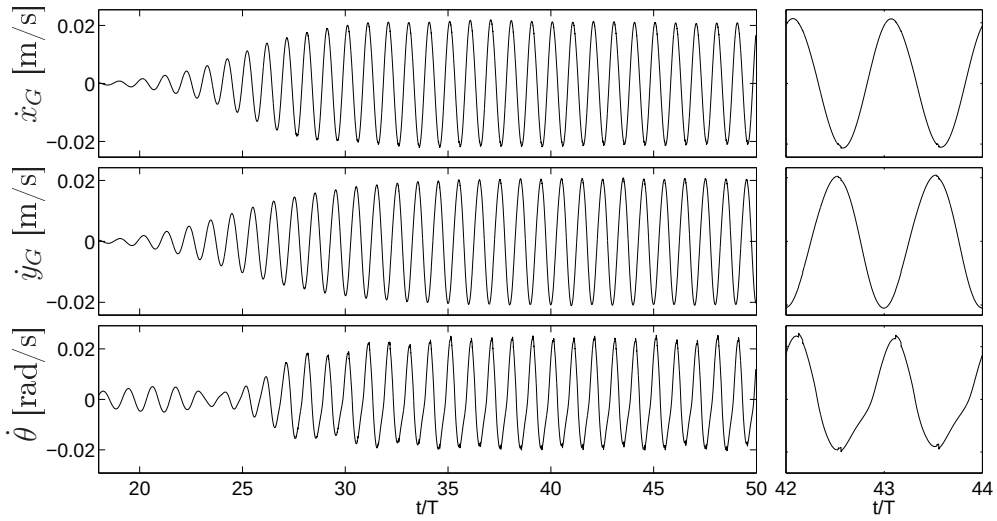

Figure 8.4: The velocities resulting from integration of the forces in Figure 8.2.

on physical reasoning as well as in a mathematical sense. The surroundings do, however, feel these simplifications as a shock. The experienced level of the shock depends on the size of the vortical structures and of course their strengths relative to the magnitude of the ambient flow. For example, cutting a vortex pair will have an influence on the potential φ near the corner of the ship. A vortex pair of large strength relative to the ambient flow will naturally cause a larger influence on the surroundings than a pair of modest strength. An example involving large vortical structures was given and discussed in connection with Figure 6.4. In all of the present work, however, the flow has been such that the vortical structures have been constrained to the vicinity of the corner of separation.

In any case, removing a part of the free shear layer either by dumping or cutting will inevitably lead to a peak in the force time history, since parts of S_V disappear with a jump in the velocity v_a in (8.14) as a consequence. We illustrate this by an example from simulations using the present nonlinear wavetank with flow separation from the ship bilges. The example involves a moored ship in incoming waves, and is taken from the same simulation as that presented later in Figure 10.21, with further specifics explained there. The specifics are not important to the present discussion. The force and moment time-series in all three degrees of freedom are presented in Figure 8.2 with close-ups of the heave force in Figure 8.3. We observe from Figure 8.2 that four main peaks occur each wave period. These are associated with cutting of the two free shear layers emanating from each of the two ship bilges. Each free shear layer is, as explained in Section 6.4, cut twice each wave period. Other irregularities in the time-series are associated with dumping, but these are very small.

From Figure 8.3 it seems that the force simply continues on "its track" after some high-frequency oscillation lasting about five to six time-steps. The way it continues back on track is consistent with the findings of Braathen (1987). The curve denoted "Differentiated velocity" is the time derivative of the velocities as written to file after each main time-step during the simulation and multiplied by the body mass. The other curve represents the force or moment as written to file. There is a small discrepancy between the reconstructed force and that written to file. This is a consequence of the difficulties associated with

the DAE discussed earlier. The discrepancies are so small that they have no practical relevance.

At first sight the force peaks may look devastating. However, the influence on the resulting velocities is small as illustrated in Figure 8.4. The shock are smoothed out. The shocks are further smoothed out when integrating to position. Physically we may say that the large peak in the force occurs over such a small interval of time that any momentum of significance is not transferred to the body.

8.3 Solving the equations of motion - Verification tests

In this section we seek to verify the alternative force and moment expressions (8.9) and (8.10), and their implementation into the nonlinear numerical wavetank. We may not verify all aspects regarding this problem due to lack of theoretical results of the fully nonlinear problem. Only "linear" motion and "second order" drift forces are verified. No verification associated with flow separation is done. The method is, however, validated through the study on a moored ship section by a terminal presented in Section 10.3.

We have chosen to investigate three cases. First, free heave and roll under wave excitation. Second, heave decay of an initially displaced ship section in still water. Third, horizontal mean drift force on fixed ship sections. In all the cases we investigate surface piercing, rectangular ship sections of beam to draft ratios $B/D = 2$ or 4. An important feature in the present work is a correct reproduction of heave damping, crucial to the level of response around ship motion resonance. This is verified by the first two cases. Another feature is the mean drift away from the terminal in resonant condition. The third case serves qualitatively as a verification in that respect.

Since we have adopted a time-domain approach, the simulations are run until steady-state. Here, as well as later on the applications to ship by terminal, we have based our chosen time-windows on the group velocity C_g as well as visual inspection. In the verification cases presented in the following, we have deep water conditions with $h = 2\lambda$.

8.3.1 Free heave and roll

Assuming linear theory, the ship section behaviour in a free, single degree of freedom motion is described as a damped harmonic oscillator. The nonlinear numerical wavetank should be able to reproduce this behaviour in case of a body in heave or roll in vanishingly small amplitude waves. Given an incoming wave of prescribed steepness we compare the computed ship section response to the theoretical. For the theoretical solution we need the added mass and damping coefficients. These are provided by Skejic (2008) using a frequency domain boundary element code for infinite water depth. The provided coefficients are assumed to be of high accuracy, and hence regarded as benchmark results for our purpose.

We follow the standard six degree of freedom convention of sway being direction 2, heave 3 and roll 4. The vertical coordinate is y as shown in the lower right part of Figure 8.5. The linearized equations of motion are in heave and roll given as

$$\begin{aligned} (m + A_{33})\,\ddot{y}_G + B_{33}\,\dot{y}_G + C_{33}\,y_G &= F_3, \\ (I_{44} + A_{44} + 2y_G A_{42} + y_G^2 A_{22})\,\ddot{\theta} + (B_{44} + 2y_G B_{42} + y_G^2 B_{22})\,\dot{\theta} + C_{44}\,\theta &= F_4, \end{aligned} \tag{8.16}$$

where I_{44} is the moment of inertia calculated around the center of gravity $\mathbf{x}_G = (x_G, y_G)$, that is, around the origin of the coordinate system $0\tilde{x}\tilde{y}$ indicated in the lower right of Figure 8.5. A_{ij} and B_{ij} are the added mass and damping coefficients in the i'th degree of freedom due to motion in the j'th degree of freedom. C_{ii} is the stiffness in the i'th degree of freedom. The coupling terms between sway and roll, being the third, fourth, sixth and seventh terms in the second equation of (8.16) appear since the hydrodynamic coefficients A_{ij} and B_{ij} are calculated with respect to the $0xy$ coordinate system, and not with respect to $0\tilde{x}\tilde{y}$.

In steady-state, the ratio between the amplitude of the motion x_a to the amplitude f_a of the excitation force is for a linear damped mass-spring system given by the transfer function

$$\frac{x_a}{f_a/c} = \frac{1}{1 - \omega^2 a/c + i\omega b/c}. \tag{8.17}$$

If we relate the equations of motion (8.16) to (8.17), the parameters a, b and c are given by the added mass, damping and restoring coefficients. For heave, $a = m + A_{33}$, $b = B_{33}$ and $c = C_{33}$. For roll $a = I_{44} + A_{44} + 2y_G A_{42} + y_G^2 A_{22}$, $b = B_{44} + 2y_G B_{42} + y_G^2 B_{22}$ and $c = C_{44}$. The roll moment of inertia is taken as $I_{44}/(mB^2) = 1/6$. The restoring coefficients are $C_{33} = \rho g B$ and $C_{44} = \rho B^3/12 + \rho g(y_b - y_G)$, where y_b is the center of buoyancy. In the present case $y_G = y_b$.

We investigate free heave for two ship sections of $B/D = 2$ and 4, and free roll for a ship section of $B/D = 2$. We mention that we also attempted to investigate free roll for a ship section of $B/D = 4$, but due to the very small potential damping for this B/D ratio (see Figure 3.17 in Faltinsen (1990)), we were not able to reach anywhere near steady-state around resonance within acceptable CPU times.

The steepness of the incoming waves was small, with $H/\lambda = 10^{-4}$. We emphasize that it is the nonlinear wavetank we are verifying. With the small wave steepness used, we adopt the strategy of linear theory where we solve several sub-problems. First, the ship is restrained to oscillate and subject to incoming waves. This provides the amplitude of the excitation forces or moments F_{ex}. Next, the ship is subjected to the same waves while free to oscillate in the chosen degree of freedom, providing the amplitude of the motion. This is performed for a range of wave frequencies from the small frequency, stiffness dominated regime through the resonance and to the high frequency, mass dominated regime.

The dimensions of the nonlinear wavetank are shown schematically in the upper part of Figure 8.5. The still water depth was $h = 2\lambda$, providing deep water conditions. Ten wavelengths in front of the ship section provided a sufficient amount of wave periods so that steady-state could be achieved before re-reflections from the wavemaker reached the ship section. The damping zone started two wavelengths downstream of the ship section and extended four wavelengths. This was through testing found to sufficiently damp out the transmitted waves. The spatial resolution was in all cases the same. $N_F = 300$, with 200 elements on the free surface upstream of the ship section and 100 downstream with increasing element length along the tank. $N_B = 60$ on the ship.

The results are presented in three of the sub-plots of Figure 8.5. Convergence with respect to temporal resolution was performed, with $N_p = 40$, 80, 120 and 160 time-steps per period. The results from the simulations are presented by markers, while the results from using (8.17) with the coefficients obtained by the frequency domain code is represented by the solid curve. For five selected frequencies the values of the transfer function from

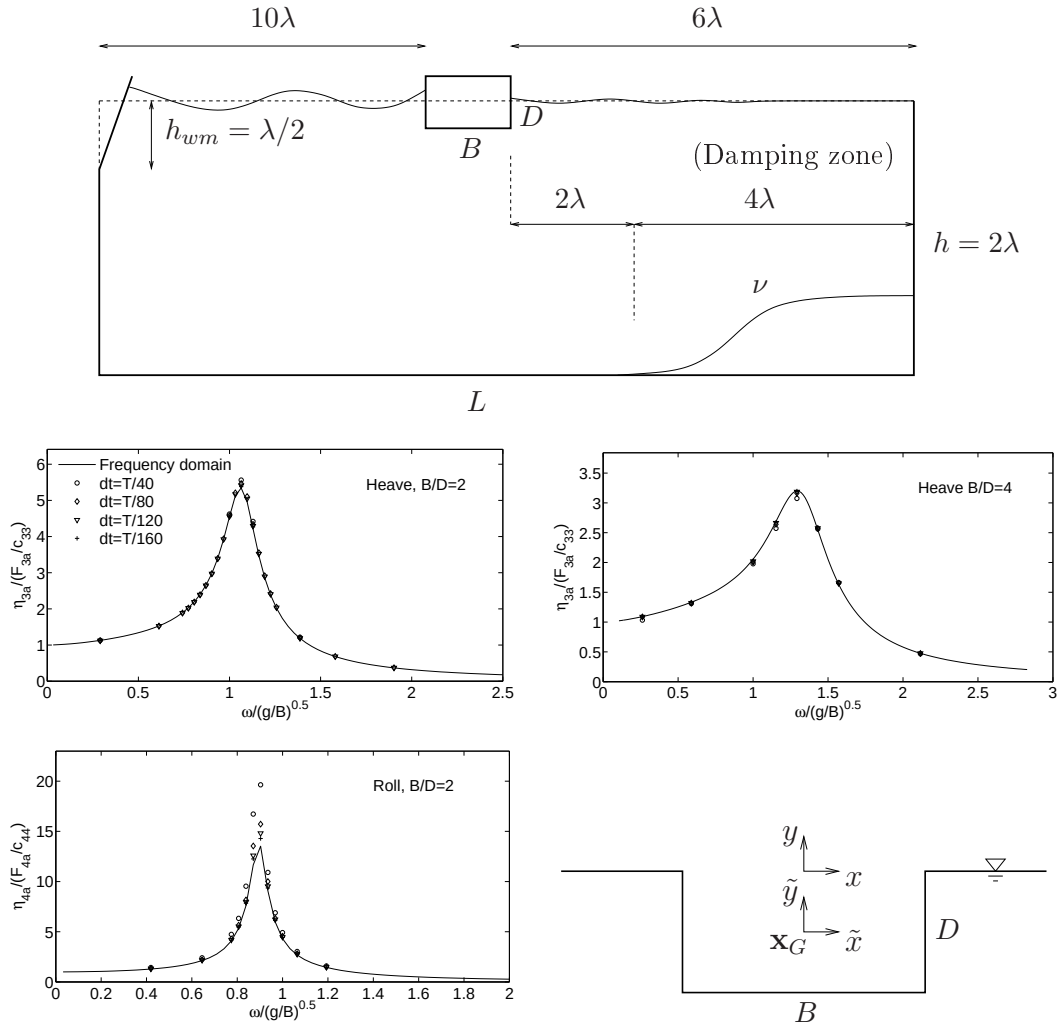

Figure 8.5: Transfer function between response and forcing for a square ship section. Upper: Schematics of numerical wavetank. Middle left: Heave ($B/D = 2$). Middle right: Heave ($B/D = 4$). Lower left: Roll ($B/D = 2$). Lower right: Coordinate systems. Nonlinear numerical simulations with $H/\lambda = 10^{-4}$ and $h = 2\lambda$.

the present simulations are presented as function of temporal resolution $1/N_p$, nondimensionalised by those acquired from the frequency domain code, are presented in Figures 8.6 and 8.7. The selected frequencies are indicated in the figure. The results indicate a convergence rate approximately first order in time, as argued earlier in the chapter. Considering that the spatial resolution is fixed, the results converge rather nicely for heave. For roll, it is clear that a sufficient number of time-steps per period is necessary around resonance in order to reach an acceptable level of error. We tried running these simulation both with only K_1 and K_4 as well as with all K_j-terms included, with no difference. The reason is the very small amplitude waves. The remaining terms introduce inaccuracies and instabilities only when the steepness becomes appreciable.

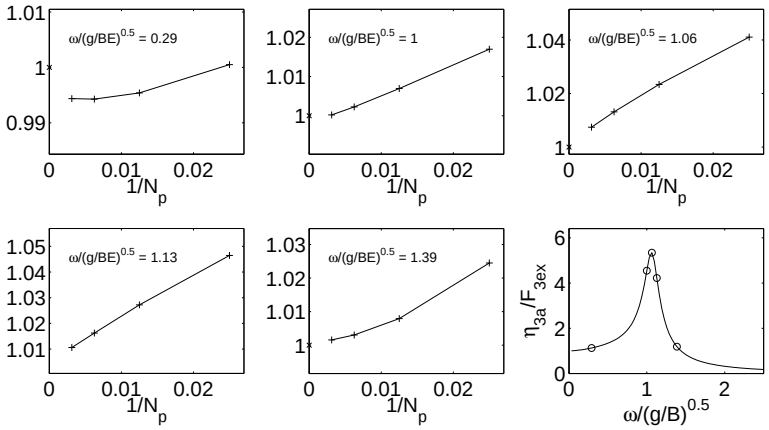

Figure 8.6: Convergence results for heave transfer functions $\eta_{3a}/(F_{3a}/c_{33})$ at five selected frequencies. $B/D = 2$.

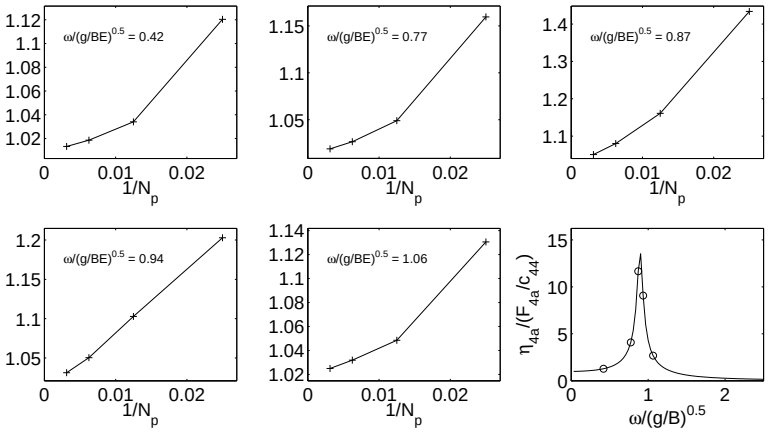

Figure 8.7: Convergence results for roll transfer functions $\eta_{4a}/(F_{4a}/c_{44})$ at five selected frequencies. $B/D = 2$.

8.3.2 Heave decay

We next study heave decay of a square section with $B/D = 4$ with initial displacement $\Delta y_G/D = 10^{-2}$ and zero initial velocity. In this study we use both the linear wavetank as well as the nonlinear wavetank. The results are compared with digitized data from theoretical results on free decay presented by Yeung (1982).

The parameters used in the present numerical simulations were identical for the linear and nonlinear wavetanks. The ship section was located in the middle position of the wavetank which had length $L/B = 50$. The still water depth was $h/B = 7.5$. The number of elements on the free surface was $NF_{=}240$ with half on each side and a cosine spaced variation with $\beta = 0.5$ (cf. Equation (A.8)) and increasing element size away from the body. On the body the number of elements were $N_B = 120$, with refinement towards the intersection points, using also here $\beta = 0.5$. Two damping zones extending from $10B$ away from the ship section and to both tank ends were used. Several different

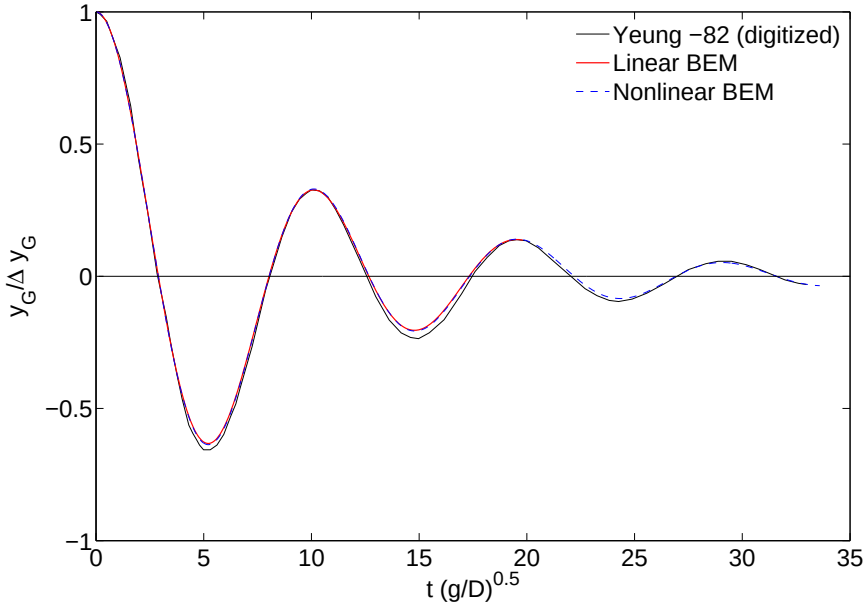

Figure 8.8: Heave decay of a rectangular body with $B/D = 4$ using the present linear and nonlinear numerical wavetanks, and comparing with the theory of Yeung (1982). Initial displacement $\Delta y_G/D = 10^{-2}$ and zero initial velocity.

time-steps were used, ranging approximately from $N_p = 60$ to 600 per "period", with the "period" taken in the case of this transient behaviour, as the time from the first to the second positive peaks in the time-series of the vertical displacement. For values higher than about 120, there was no visible change in the behaviour. We also tried varying the artificial added mass term A_{yy} described earlier, and the behaviour proved insensitive to the actual value, except when exceeding about 20 times the body mass m. For $A_{yy} = 0$, the simulations broke down after five-six time-steps.

The time-series of the vertical displacement of the rectangular section obtained by the linear wavetank, nonlinear wavetank and from Yeung's theory are presented in Figure 8.8. The comparisons are in general good. There are no nonlinearities predicted by the nonlinear simulations on the chosen scale of the figure. This is as expected. There are, however, some discrepancies between Yeung's theory and our simulations, in particular around the two first negative peaks. We attempted to run simulations with several larger water depths h as we suspected that perhaps the initial wave front which is induced at the time of release, experiencing finite water depth in any finite depth condition, in some way could cause the discrepancies, but the results seemed absolutely insensitive to variation in h beyond that used here. The discrepancies are, however, very similar to those noted by Yeung (1982) between the theory and model tests reported therein, in that case for a circular cylinder.

With the good comparison to Yeung's theory and the numerical method proving insensitive to the choice of A_{yy}, we feel quite confident that the heave damping properties are well described in the present numerical work.

8.3.3 Mean drift force

In the last case of the verification process, we investigate the mean horizontal drift forces due to incoming waves on fixed rectangular ship sections of beam to draft ratios $B/D = 2$ and $B/D = 4$. Knowing the incoming wave amplitude A as well as transmitted wave amplitude A_T we may compare with the analytical expression known as Maruo's formula, which is correct to second order in deep water,

$$\begin{aligned} \bar{F}_x &= \frac{1}{4}\rho g(A^2 + A_R^2 - A_T^2) \\ &= \frac{1}{2}\rho g(A^2 - A_T^2), \end{aligned} \tag{8.18}$$

where A_R is the amplitude of the reflected wave and the overbar indicates mean value. We mention that in the case of finite water depth, a formula due to Longuet-Higgins is

$$F_x = \frac{1}{4}\rho g \left(A^2 + A_R^2 - A_T^2\right) \left(1 + \frac{2kh}{\sinh 2kh}\right), \tag{8.19}$$

where k is as usual the wave number given by the linear dispersion relation (3.1).

The wave steepness was in our numerical tests taken to be $H/\lambda = 1/100$. The wavetank arrangement in the numerical simulations is presented in the upper part of Figure 8.9, and the specifications are as follows. The still water depth $h = 2\lambda$, i.e. deep water conditions. The total length is $L = 38\lambda + B$ with the ship section front 16λ from the wavemaker, and a downstream tank length of 22λ. The numerical beach starts at $x_d = 22\lambda$ giving a relatively long beach of length 16λ in an attempt to avoid reflections from the transient wave front. The spatial resolution was taken quite high, with $N_F = 600$ elements on the free surface, 400 upstream and 200 downstream of the ship section. In the downstream part the element size increased along the tank according to $\beta = 0.6$. The number of elements on the ship section was $N_B = 120$, with a variation according to $\beta = 0.6$ along each of the sides. 100 elements were used on the tank bottom. The number of time-steps per period was $N_p = 120$. We did not perform a systematic convergence test, but found that the resolution needed in order to approach good solutions was higher than in the two previous cases validating linear quantities. This is perhaps not a surprise.

Results from the simulations with the nonlinear wavetank by means of the normalized mean force are presented as a function of the scattering parameter kB in Figure 8.9. The markers represent the mean forces taken from a part of the force time-series that seemed stationary. The values for A and A_T was taken as steady-state values from the same part of the time-series and used in (8.18). These values are represented by the solid curves and indicated as "Maruo" in the figure. Although the comparison is qualitatively quite good, there are noticeable discrepancies. The discrepancies are small for small wavelengths, say less than 2 - 3% for $kB > 4$. For $1 < kB < 4$ the discrepancies are within 10%. For the smallest scattering parameters, the relative error is large. However, the values are very small since nearly all the wave energy is transmitted, as the long waves do not feel the presence of the body. The discrepancies may be due to numerical errors in the estimated amplitudes. Since $A_T \to A$ as kB tends to zero, only small errors in the wave amplitudes will cause significant relative errors in the mean force as seen from (8.18).

Reaching steady-state of the mean force. Some effort was made to understand the discrepancies more in-depth. Using the same arguments based on group velocity as

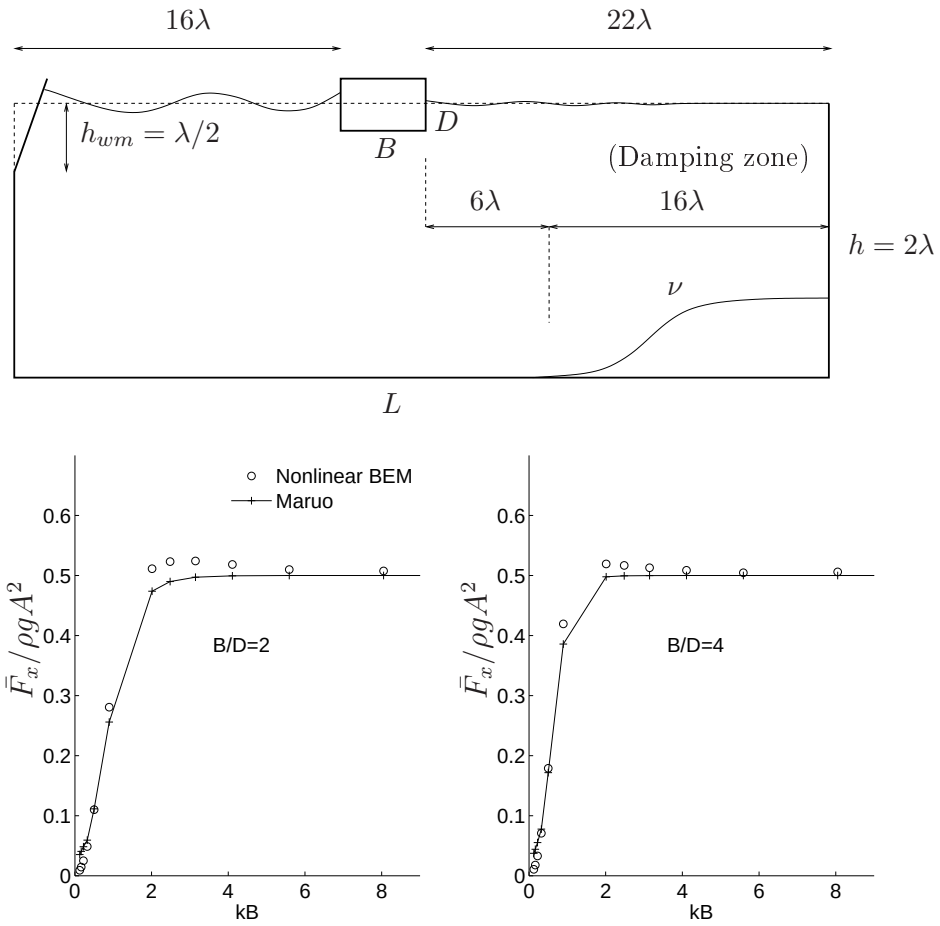

Figure 8.9: Upper: Schematic overview of the nonlinear numerical wavetank in Maruo tests. Total tank length is $L = 38\lambda + B$, length from wavemaker to ship front is 16λ, while the damping zone extends from 6λ downstream the ship until the far tank end. Deep water conditions ($h = 2\lambda$). Flap type wavemaker hinged at $y = -\lambda/2$. Bottom: Results from simulations with the present nonlinear numerical wavetank. ($\circ$): $\bar{F}_x$ taken directly from the force time-series. (-): $\bar{F}_x$ taken from Maruo's formula (8.18) with the amplitudes A and A_T from the simulations using the nonlinear numerical wavetank.

above, the wave elevation time-series from visual inspections seemingly reached steady-state. However, the second order quantities perhaps did not really reach a proper steady-state. We base our speculation on the following. Consider two wave-trains propagating in opposite directions in a domain extending to infinity in the horizontal direction. This may for example be the incoming wave-train and that reflected from the ship section. Then, a spatially uniform and oscillatory second order disturbance is created below these wave fields, with the solution of this second order potential given in Faltinsen (1990) (see p. 168). In the present nomenclature the solution is $\varphi_2 = 0.5AA_R\,\omega \sin(2\omega t + \delta)$. The solution oscillates with the sum-frequency 2ω, and has an amplitude of $0.5AA_R\,\omega$. Upon visual investigation of the potential at the mid position between the wavemaker and the ship section at $y = -h$, we found this to seemingly approach the value $0.5AA_R\,\omega$, but approaching in a manner much slower than what we have observed the linear quantities to do. The linear quantities such as A and A_T typically reach steady-state condition

about 10 - 15 periods after the wave-train has reached the position of measurement. The amplitude of the second order 2ω oscillation was still increasing about 40 wave periods after the wave-train had reached the ship section, and was at the end-time about 10% off the theoretical value. Since mean values may not undergo visual inspection in the same manner, we do not know whether this quantity also experience a similar slow convergence to steady-state, but it is possible.

The above discussion indicates that a time-domain fully nonlinear numerical wave-tank does experience challenges regarding nonlinear effects despite the seemingly straightforward handling of these. However, in the application of the nonlinear numerical wave-tank used in the main part of the work related to a moored ship by a terminal as presented in the next chapter, the scattering parameter is $kB \gtrsim 2$, a regime where the error is thought to be acceptably low for our purposes.

Chapter 9

Model tests

Altogether four sets of model tests were performed during the present work. Two related sets were performed in September and November 2006, and another two related sets in April and June 2008. In all four sets a two-dimensional rectangular shaped ship section by a bottom mounted terminal subjected to waves was considered. In the 2006 tests a fixed ship section with rounded bilges was used, while in the 2008 tests we considered a moored ship section with sharp bilges. For convenience we shall henceforth refer to these as the September and November 2006 tests and April and June 2008 tests.

In the September 2006 tests the aim was to investigate shallow water effects on the forces as well as the kinematics considering waves of full scale periods 6s - 15s. The resulting forces and free-surface kinematics contained considerable nonlinearities associated with the shallow water. However, more interestingly the results suggested we were approaching a resonant behaviour of the fluid column in the terminal gap at the highest wave periods, and we decided to perform another set of tests around the natural periods which resulted in the November 2006 tests. Only the results from the November tests have thus far been published, see Kristiansen and Faltinsen (2009a).

In the 2008 tests the ship section was moored by horizontal, linear springs and thereby free to move in three degrees of freedom, this time essentially in deep water. The purpose was two-fold, first to validate the numerical work involving solving the equations of motion in the nonlinear numerical wavetank, and second to investigate resonant behaviour also in the more realistic case of a moored ship as opposed to the fixed ship in the previous model tests. It turned out, however, that during the April 2008 tests the terminal, being only an unstiffened and hardly horizontally supported 3mm aluminum plate had slightly flexed due to the hydrodynamic pressure. This caused additional damping, and the model tests had to be repeated. This resulted in the June 2008 tests. Results from the June tests have been published in Kristiansen and Faltinsen (2009b).

In addition, model test results from moonpool experiments performed in 2005 and reported in (Faltinsen, Rognebakke, and Timokha (2007)) were re-analyzed for further investigation of some rather surprising results reported therein. The model tests involved forced heave of two surface piercing rectangular sections in a wave flume resembling the present problem of a ship by a terminal under the assumption of symmetry around the mid-line of the moonpool. The re-analysis showed that the somewhat surprising results were caused by wave reflections. The re-analyzed data have been published in Kristiansen and Faltinsen (2008).

In the first three sections of the present chapter, we describe the test set-up, test

Table 9.1: Key parameters in the September 2006 model tests. Full scale and 1:70 model scale. Full scale dimensions are based on a typical mid-ship section of an LNG carrier.

Quantity	Term	Full scale	Model scale 1:70
Beam [m]	B	45.0	0.64
Draft [m]	D	12.0	0.17
Bilge radius [m]	r	4.2	0.06
Water depth [m]	h	16.0 - 20.0	0.23 - 0.29
Bottom clearance [m]	d	4.0 - 8.0	0.06 - 0.12
Terminal gap [m]	b	15.0 - 22.0	0.22 - 0.32
Periods [s]	T	6 - 15	0.72 - 1.79
Wave steepness	H/λ	1/60 - 1/40	1/60 - 1/40

conditions, some results and a discussion around sources of model test errors and its possible influence on the results from the 2006 and 2008 tests. In the last section we present the re-analysis of the moonpool tests.

9.1 Fixed ship section in shallow water - Sept 2006

The nearly two-dimensional model tests of a fixed ship section by a bottom mounted terminal subject to incoming medium deep to shallow water waves were conducted in a 26.5m long and 0.595m wide wave flume at the Division of Marine Civil Engineering at NTNU. The flume had plexiglas walls, and was equipped with a piston-type wavemaker from DHI with a paddle extending from the bottom. The wave paddle controller included an active wave absorption system (AWACS). The system proved to effectively damp out reflections during the tests, and was useful also for damping out the waves in between runs. A parabolic beach was used at the far end as wave absorber during wave calibration.

In this section we first present the choice of parameters in these model tests, next describe the models, rigging and instrumentation, and last discuss sources of error and a brief look at some results. Results from the present model tests have not been published earlier.

9.1.1 Model test overview - choice of parameters and test conditions

The dimensions and environmental conditions used for the model tests were chosen based on a mid-ship section of a typical LNG carrier subject to near regular waves of periods corresponding to typical deep water wave spectra at sea. The full scale wave period range was $T = 6$s - 15s. LNG carriers typically have beam of $B \simeq 45$m, a beam to draft ratio as large as $B/D \simeq 4$, and a bilge radius of $r \simeq 4$m. In reality, bilge keels extend about half the length of the ship, but these were not modelled. The bilges were rounded such as to avoid flow separation as far as possible, with the KC-number bringing relevance to the problem. The water depths were chosen according to typical water depths were Gravity Based Structure (GBS) type of offshore terminals are to be installed, which are $h \simeq 15 - 30$m. The carrier is typically fendered out from the terminal with relatively

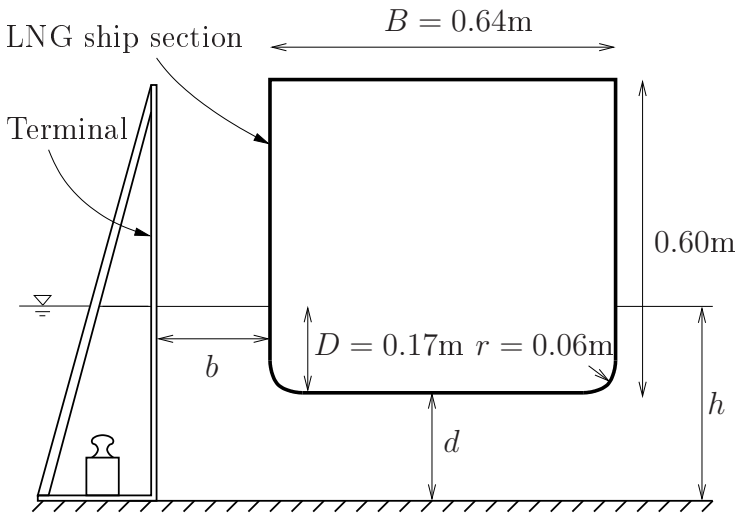

Figure 9.1: Schematics of the ship section and terminal wall used in the fixed ship section tests of September and November 2006.

large terminal gap widths of typically $b/B \simeq 0.2 - 0.35$.

The model scale was chosen to be 1:70. The main parameters and environmental conditions are listed both in full scale and model scale in Table 9.1. The still water depth h and implicitly the bottom clearance d, the terminal gap width b as well as the incoming wave period and steepness were varied. The draft D was not changed during the tests. The ship section dimensions in model scale are presented in detail in Figure 9.1. The ship section height of 0.6m was chosen to ensure no fluid overturning the model. The terminal was modelled as a straight wall extending from the sea floor.

The test matrix is presented in Table E.2 and additional information about the waves such as group velocity and finite water depth steepness is presented in Table E.5. The true shallow water conditions according to the usual definition of $\lambda_0/h > 10$ are indicated by light grey background in the tables. The test numbering convention was as the following. Each run was named by a four digit number where the first number corresponds to b, the second number to h, the third to T and the last is reserved for either repetition or re-running. Each of the eight test conditions indicated in the test matrix by two test numbers connected by a hyphen were run in total five times for repeatability check. Except for these, all other tests with other than zero last digit is a re-run. In particular, the 8000-series was originally run as H_0/λ_0=1/30 steepness, but this was found too steep for our purpose as breaking occured for the two longest waves on water depth of $h = 0.29m$, so the 8000-series and 8100-series were re-run with the indicated H_0/λ_0=1/40 steepness and named 8005 - 8095 and 8105 - 8185.

Among the parameters subject to variation as mentioned above was the wave steepness H_0/λ_0 where subscript 0 means deep water limit. The finite depth waveheights H were chosen based on the following philosophy. When a deep water wave with steepness H_0/λ_0 propagates up a very gentle slope it will become shorter and also loose some height. The (linear) wavelength at finite water depth λ is then calculated using the linear dispersion relation (3.1), whereas the (linear) waveheight H is given by the steady wave action equation (3.3). Since in the model tests, the wave flume was such that only the finite

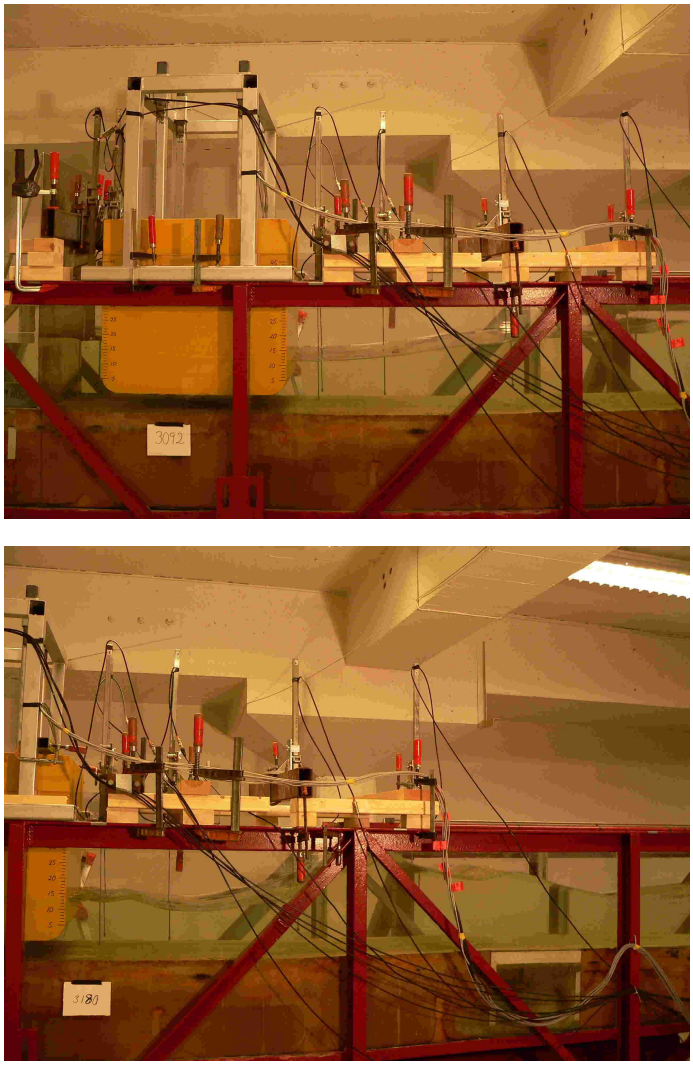

Figure 9.2: Two snapshot from the September 2006 tests. The ship section is fixed and subject to waves entering from the right. The water depth is $h = 0.23$m.

depth part was modelled, the finite water depth waveheight H was that input to the wavemaker. The stroke of the paddle was then automatically found through the transfer function (3.4).

9.1.2 The models, rigging and instrumentation

The ship section was constructed by steel plates of 1.5mm thickness. The section was connected to a vertically adjustable steel rig through a six degree of freedom (dof) force transducer. The force transducer was constructed by two horizontal 0.45m x 0.45m and 1.5cm thick aluminum plates connected to each other at six positions. The model and the rig are shown Figure 9.2 and also in the lower part of Figure 9.3. The force transducer is shown in the upper left part of the upper photo of Figure 9.3. The force transducer produced at MARINTEK was of high quality, but not very robust. Stiffeners were therefore placed in between the top and bottom plates when being moved during rigging and

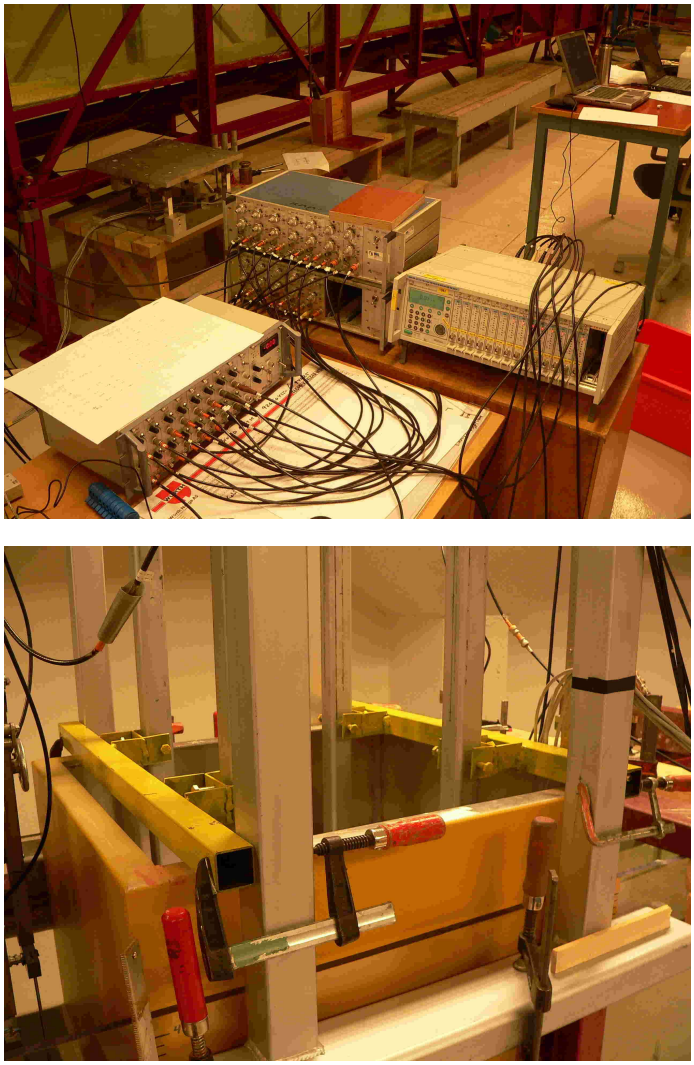

Figure 9.3: Upper: Force transducer (top left corner), filter box (lower left corner), wave gauge amplifier (middle) and force amplifier of type Hottinger MGCplus (right). Lower: Reinforcement of the rig by two steel bars.

transportation. Further, the model was loaded with weights in order to balance the buoyancy force, such that the force transducer experienced a minimum of pretension. The transducer was mounted with its midline in the still water line, that is, 0.17m above the bottom of the model in order to minimize moments. Each of the six connection points between the two plates were associated with a force measuring unit, one in the transverse direction, two in the x-direction and three in the (vertical) y-direction, giving a total need of six channels for logging. Total forces and moments were obtained by summation.

Using a six dof force transducer when a three dof is ideally enough for two-dimensional model tests was a matter of availability. It proved, however, useful to measure transverse forces due to some transverse sloshing in the wave flume during the model testing.

The terminal was fastened to the wave flume frame by clamps, and loaded with about 30kg of weights, as illustrated in Figure 9.1.

A total of twelve wave gauges denoted by w1 - w12 were mounted for measurement

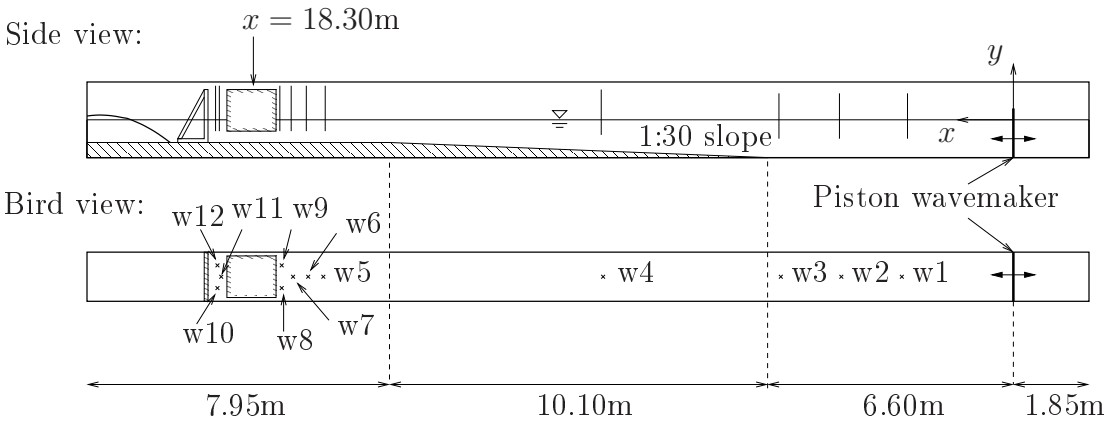

Figure 9.4: Schematics of the wave flume in the September 2006 tests including the 1:30 sloping bottom. See Table E.1 for positions of the wave gauges w1 - w12. Mid-ship position is $x = 18.30$m as indicated. The terminal gap width b was varied by changing the position of the terminal.

of free-surface elevation. The location of these are shown schematically in Figure 9.4 and listed in Table E.1. The wave gauges were of standard capacitance type with two metal bars 1cm apart, each with diameter of approximately 1mm. The length of these ranged from about 35cm to 46cm. Manual calibration was done at least once per day, and except for two of the wave gauges only very small drift was observed. The zero level and gain was sensitive to temperature changes, that is, when adding water or changing the water, the drift was large until room temperature had been reached. After completely refilling the tank, it typically took one day and night to reach a steady temperature, while the actual process of filling in itself only took about one minute. For wave calibration runs, all twelve wave gauges were used, whereas in the tests with ship section only ten were used in order to fit six force channels in the sixteen channel filtering box which is shown in the lower left corner of the upper photo in Figure 9.2. The amplifier receiving the wave gauge signals is shown in the middle part of the same photo.

The amplifier of type Hottinger MGCplus receiving the force signals is shown in the lower right corner of the upper photo in Figure 9.2. The force and wave elevation signals were acquired at a sampling frequency of F_s=200Hz, while the wavemaker signals were by default acquired at 40Hz.

9.1.3 Estimation of measurement error and observed artefacts

Although we believe that the model test results in general were of fairly high quality, in our opinion, a careful identification of possible sources to error with attempts to provide estimates of these is crucial. There are two kinds of error; random error and bias error. The random errors may be quantified by repetition tests. Other means of investigations are needed in order to identify possible bias errors. The process of identifying possible sources of bias error includes actions such as quantifying known limitations of the equipment, utilizing your own and others' experience, "brain storming" as well as careful observation during the model testing. During the model testing, continuous efforts were hence made to observe and identify artefacts of possible significance to the results.

A summary of the possible sources of error and observed artefacts with their assumed significance, quantitative or qualitative, is given in Table 9.2, and each discussed in the following.

A parabolic beach, or any shaped beach, will not in general be a perfect wave absorber. The strategy of such a beach is inducing wave breaking. This will never remove all the energy in a wave. This is true in particular for shallow water waves. In fact, a parabolic beach is basically a low-pass filter. Therefore, some reflection was inevitable in the present tests. No quantitative analysis of the reflection intensity has been performed, although the available data would allow such an analysis, but some non-negligible reflection is expected for the longest waves, say for $T \gtrsim 1.5$s. Wave reflections are typical examples of bias errors in model tests.

Capacitance type wave gauges consist of two parallel steel wires penetrating the free surface. Bias error is introduced through nonlinearity in the voltage created, the surface tension causing the water to "climb" on the steel wires, also known as the meniscus effect, as well as drifting over time. A semi-quantitative estimate of that introduced by nonlinearity based on our experience from daily calibration is in the present $\lesssim 0.5$mm. Drifting was kept under control by daily recalibration, and no significant drift was observed. The meniscus effect is said to introduce an error in the order of the diameter of the steel wires. In our case this would mean 1mm. However, based on our experience it is much less than that, perhaps an order of magnitude lower. This is shortly discussed later in connection with the June 2008 tests. There, we did a short investigation using wave gauges of different diameters. Based on this we would say that the error introduced by the meniscus effect is negligible in the present context.

A slight motion of the ship in the order of 1 - 2mm was observed during the tests with the longest waves. The motion was caused by that the rig was originally not constructed adequately stiff with respect to forces in the x-direction. The mounting brackets were placed near the top of the rig implicitly indicating large moments. This was mended by mounting additional steel bars to the rig at a lowest possible position as shown in the lower left picture in Figure 9.2. About half of the runs were made prior to this remedy, but were not re-run. Another related effect was an observed indentation of the ship side due to the hydrodynamic forces exerted on the unstiffened 1.5mm steel plate constituting the ship section. The indentation might have been in the order of 1 - 2mm as well. Whereas the motion of the whole model was of a rigid body character, the latter effect was a hydroelastic effect. Assuming the ship motion was repeatable, this introduced a bias error. The measured forces may have been somewhat affected by the motion as well as the indentation, but we have not investigated quantitatively the significance. We also mention that during a few tests the screws connecting the force transducer (and hence the model), to the rig were loose, and a clear 6Hz disturbance was introduced in the force measurements due to the sudden jerky movements of the ship. These tests were re-run, however.

Seiching is a low-frequency oscillation of the fluid corresponding to the first longitudinal eigenperiod of the basin, that is, a standing shallow water wave. This is in theory always triggered in any flume or basin. Typically the standing wave has a very low ampli-

Table 9.2: Summary of possible error sources and their estimated or assumed significance in the September 2006 tests.

Artefacts	**Significance**
Beach reflections	Non-negligible for longest waves
Wave gauge random error	$\lesssim 0.5$mm
Ship moved slightly (rig stiffness)	Little
Indentation of the ship side	Some
Seiching	Negligible
Transverse sloshing and glass wall gap	Little (except when $T = 0.96$s)
Three dimensional effects near model	Unknown

tude, but results in fluid motion of possibly appreciable horizontal extent, i.e. it basically acts as an oscillating current. As the AWACS is based on wave elevation, the seiching was not effectively damped out. It typically took 3 - 5min and sometimes closer to 10min to adequately damp out seiching following the tests with the longest waves. Oscillating shear type currents, both in the vertical plane as well as in horizontal plane, were also observed to some extent, although of significantly smaller amplitude than that of the seiching. The seiching and shear currents were observed until almost vanished before starting a new run, and any effect therefore considered negligible.

Transverse sloshing is the corresponding transverse standing wave of the first eigenperiod in the transverse direction of the flume. With a breadth of 0.595m, the resonant period using the deep water limit of the dispersion relation is 0.87s. Transverse sloshing was observed in particular during the tests with wave periods $T = 0.84$s, 0.96s and 1.79s. For the latter wave period, the second harmonic triggered the transverse instability. The onset of transverse sloshing is a consequence of the three dimensional instability inherent in wave trains as investigated theoretically in e.g. McLean et al. (1981). In our case, the slightly three-dimensional flow introduced e.g. by the gaps formed between the wave paddle and the glass walls would provide the necessary perturbation from pure two-dimensional flow. In the measurements the transverse sloshing is manifested as a slight phase difference between the side-by-side mounted wave gauges, that is, between w8 and w9 as well as between w10 and w12, accompanied by a transverse force of appreciable magnitude for these periods on the model as seen in Figure E.1.

Glass wall gap. The transverse force must be seen in context with the 3 - 4mm wide water column in the gap between the model and the glass wall, hereby denoted by the glass wall gap. The gap was a matter of necessity in connection with force measurements. The ship section had to be denied any mechanical contact except through the force transducer. Using a quasi-static approach, the amplitude of the transverse force due to the water columns in the glass wall gaps on each side is $F_z = 0.5\rho g B\left((D + A_T)^2 - (D - A_T)^2\right)$ where $B = 0.64$m is the beam, $D = 0.17$m the draft and A_T the amplitude of the standing wave. As two examples, in tests 2120 ($T = 0.96$s) and 2130 ($T = 1.08$s), the amplitude of the linear force was 4N and 13N, and this is achieved if A_T is 2mm and 6mm respectively. From visual observations and qualitative inspection of wave elevation time series from w8 and w9 in front of the ship these predicted values of A_T are probable. Although of appreciable amplitude for some wave periods, the transverse sloshing is considered not to

have influenced the other results significantly. For example, no transverse motion of the ship section leading to mechanical contact with the glass walls occured.

Slight tilt. Another three-dimensional effect of unknown significance was a slight transverse variation of the distance b between the terminal and the ship of about 0.5cm, due to a small mounting angle of the ship as seen from above. From video recordings we observed slightly three dimensional kinematics in terms of higher modes in the terminal gap during the tests with the longest and steepest waves.

9.1.4 Short discussion of the results

The results of the September model tests were not used further throughout the present work as our focus turned to resonant behaviour in general water depth rather than shallow water effects, and an extensive analysis has therefore not been performed. However, following the testing condensed results as well as all time series were included in a model test report. The condensed results included steady-state values taken from steady time windows of the time series of the first three harmonics, mean value as well as peak to peak values of the forces and the wave kinematics. A selection of results are presented in Figure E.1.

The repeatability proved to be good, even in some rather extreme test cases with transverse sloshing induced. A selection of results from the random error analysis of the repetition tests is shown in Figure E.2 where bars represent mean values from the five tests in each of the eight test groups as indicated in the test matrix, and diamonds and numbers the corresponding standard deviation relative to the mean value in percentage. In general for all cases and all channels, the standard deviation is less than 0.5% for the first harmonic, and for the second and third harmonics in the cases with an appreciable mean value, below 3% and 10% respectively.

9.2 Fixed ship section with piston-mode resonance - Nov 2006

The November 2006 tests were performed in order to investigate the resonant piston-mode motion in the terminal gap. The model test set-up was very similar to the September tests; the same facility, ship section and terminal as well as equipment was used, except the 1:30 sloping bottom had been removed and force measurements were not made.

9.2.1 Model test set-up and test conditions

A schematic overview of the set-up is presented in Figure 9.5 and pictures are shown in Figure 9.6. Expecting large fluid motions in the terminal gap in resonant condition, the glass wall gap was attempted sealed with rubber bands at the expense of loosing force measurements. Wave elevation was measured at twelve locations, denoted by w1 - w12 as before, but at slightly different locations due to re-rigging. See Table E.1. New to the November tests was video recordings by a high-speed camera acquiring images with resolution 1280×1024 at 200Hz, as well as video by an ordinary digital camera.

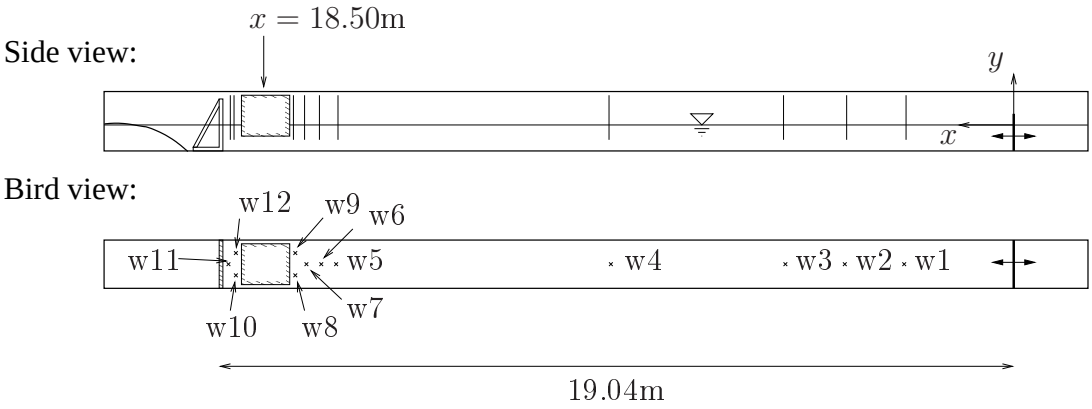

Figure 9.5: Schematics of wave flume in the November 2006 tests, same as that used in the September 2006 tests (see Figure 9.4). See Table E.1 for positions of the wave gauges w1 - w12. Mid-ship position is $x = 18.50$m as indicated. The terminal gap width b was varied by changing the position of the terminal.

As in the September tests, the water depth h, the terminal gap width b, the wave period T and the wave steepness $\epsilon = H_0/\lambda_0$ were varied in a systematic manner and wave calibration tests without the model were performed for all waves used. The wave steepness was lower in the present model tests due to expected large resonant motion as well as higher wave periods. We group the tests into three cases denoted by Case 1 - 3 with the specifics given in Table 9.3. More details are provided in the test matrix as given in Table E.3. There, the theoretical resonance periods calculated from the theory by Faltinsen et al. (2007) are indicated by a dark grey background. The resonance period in general increases with decreasing depth h and increasing terminal gap width b. Those tests with shaded numbers were not successfully run simply due to a limitation of the maximum possible stroke length of the paddle which was $S = 0.3$m.

Table 9.3: Specifics of the three cases denoted Case 1 - 3 in the November 2006 model tests. In the case denoted (x) the free surface in the terminal gap reached below the ship section bilge, introducing violent sloshing in the gap.

	h/B	b/B	$\epsilon_1 = 1/170$	$\epsilon_2 = 1/115$	$\epsilon_3 = 1/70$
Case 1	0.625	0.34	x	x	(x)
Case 2	0.45	0.34	x	x	-
Case 3	0.45	0.17	x	x	-

Repetition tests were not performed in the November 2006 tests, as good repeatability was found from the September 2006 tests.

9.2.2 Wave generation capability

Analysis of the results from the wave calibration tests after performing the model tests, showed a discrepancy between the theoretical and achieved waveheight given by the wave-maker stroke an the Bièsel transfer functions (3.4). Although (3.4) is based on linear theory it should adequately describe the situation at least in the majority of our regime

Figure 9.6: November 2006 model tests. Left: Model test set-up. Terminal seen to the far left. Clay and rubber bands were used to seal gap between glass wall and models. The black cloths reduced reflections when acquiring high-speed photos. Right: Sample of high speed camera.

of periods and steepness. This introduced a practical problem when attempting to reproduce the model test results using the recorded wavemaker signal as input to the numerical wavetank. Some effort was made in order to understand the discrepancy, including revisiting the laboratory, checking wave gauge calibrations and manually measuring the paddle stroke in order to check the recorded wavemaker signal. No negative observations were made in this respect. One question was why the DHI software came with an option "amplification factor" controlled entirely by the user. In the current model tests, the wavemaker signal was multiplied by a factor of 1.28 in all tests, with its choice based on one single wave calibration test from the beginning of the model tests without further thoughts on the matter. Our post-processing analysis showed, however, a significant variation between the tests, with an ideal value for the amplification factor being between about 1.05 to 1.35, depending on all parameters h, H and T. A phone call to DHI revealed that in general, and in particular for shallow water wave flumes, the desired waveheight is not achieved using (3.4) only, thereby for practical purposes allowing for a user specified amplification factor (or calibration factor) depending on the actual test condition. The phone call was followed by a literature search, and a discussion of the wave generation capability of a paddle wavemaker was found in Madsen (1970). They analysed the flow due to leakage around the sides and bottom of the paddle and found this to explain most of the observed discrepancies between wavemaker theory and their model tests. The wave flume was in those model tests similar to that used in the present model tests, and with similar gap width of about 0.5cm between the paddle and the walls and bottom of the tank. A more general discussion of the problem is given in Hughes (1993) with the conclusion that the wave generation capability of the wavemaker is in general less than that predicted by two-dimensional potential theory, and decreases in practice with decreasing water depth. The discrepancy is, however, significantly reduced when sealing the gaps between the paddle and the walls and the floor. Intuitively, letting $\omega \to 0$, effectively allowing the free surface to act as a rigid lid, the fluid will prefer flowing through the gaps. A practical implication is that when reproducing the wave in a two-dimensional numerical

wavetank, the wavemaker signal must be adjusted according to this amplification factor.

This discussion also in principal applies to the September tests, but as these were not equally in-depth analysed nor the results compared to numerical simulations, this was not an issue.

Note that the purpose of the November model tests was to investigate the resonance in the terminal gap, so the main focus was on the excitation period, and not on the exact shape of the waves. When disregarding the AWACS, the paddle motion was harmonic, so waves of permanent shape, or Cnoidal waves, were not generated. The waveheight is therefore not uniquely defined as the wave may have typically two local minima per period, basically due to free traveling second order waves, but it is hereby defined as the vertical distance from the minimum to the maximum free-surface elevation during each period.

9.2.3 Short discussion on error sources

The same discussion on sources of error and their estimated significance to the results applies here as in the September tests. We do, however, make some further remarks on the possible three dimensional leakage effects around the ship section in light of the above discussion on reduced wave making capability. Also, we emphasize the possibly significant influence from deflections of the side of the ship section on the piston-mode amplitude in resonant conditions. The deflections occurred also in the November 2006 tests.

The gap between the glass wall and the ship section was sealed with rubber bands and clay along the vertical sides of the ship section. The horizontal part was not. Leakage-like behaviour thus occured along the horizontal part of the ship model, where the dynamic fluid pressure in the area below the ship section created fluid motion in the glass wall gap. Although the sealing of the vertical parts significantly reduced the flow in the glass wall gap, leaving the horizontal part open only partly gave the desired sealing effect. Thinking in terms of this being in reality a passive wavemaker by means of reflecting waves, the same gap effects as those discussed with regard to the wave paddle may have been of relevance.

We believe that a more important source of error was introduced by the ship side deflections. This was most likely rather insignificant in the September tests as the conditions were not resonant. However, in case of resonant piston-mode motion, this most probably acted effectively as a damping. This matter is discussed in detail, and quantitative analysis performed, in connection with the model tests of a moored ship in the next section. There, small deflections of the terminal was in fact the reason for re-running those experiments. We have not made a quantitative analysis of the possible effects on the results from the present model tests. But discrepancies with respect to linear and nonlinear simulations of approximately 20 - 25% around resonance as presented in our studies on resonant behaviour in Section 10.1 indicates a possible effect. The KC-numbers indicate that flow separation may have occured to some extent around resonance, but then an effect of wave steepness should have been more pronounced than that found. More thorough discussion on this matter is presented there.

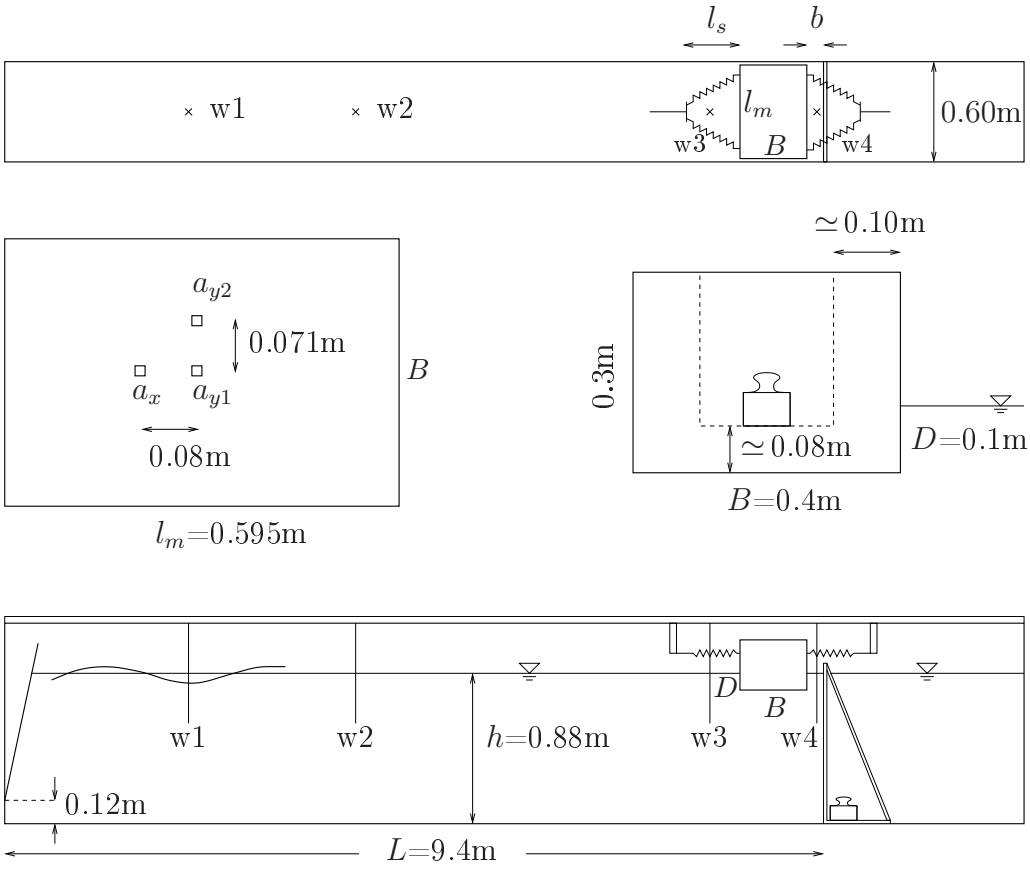

Figure 9.7: Schematics of the April 2008 model test set-up which involved a moored ship section by a terminal. The sketches are not to scale.

9.3 Moored ship section in resonant motion - April and June 2008

Two sets of model tests considering a moored ship by a bottom mounted terminal subject to incoming waves were performed in April and June 2008. The focus was the coupled resonant ship section and piston-mode motion.

Basically, the June tests were re-runs of the April tests as the results of the latter were contaminated by bias error due to a slight flexing of the terminal causing a large reduction in the response of the system in resonant condition. In this section we report both sets of model tests together. We point out main differences and associated improvements, with the main improvement being a thorough stiffening and horizontal support of the terminal as opposed to the unintentionally flexible terminal in the first tests. Although the results from the first set of experiments were unusable, we still report the test set-up along with some results. We justify this by arguing that negative results should in principle be reported not only through the odd comment, but in a manner allowing the reader to extract knowledge useful for his or her work, possibly avoiding making the same mistakes.

We proceed by reporting the model test set-ups, instrumentation, test conditions and a qualitative investigation of the effect of a flexing terminal.

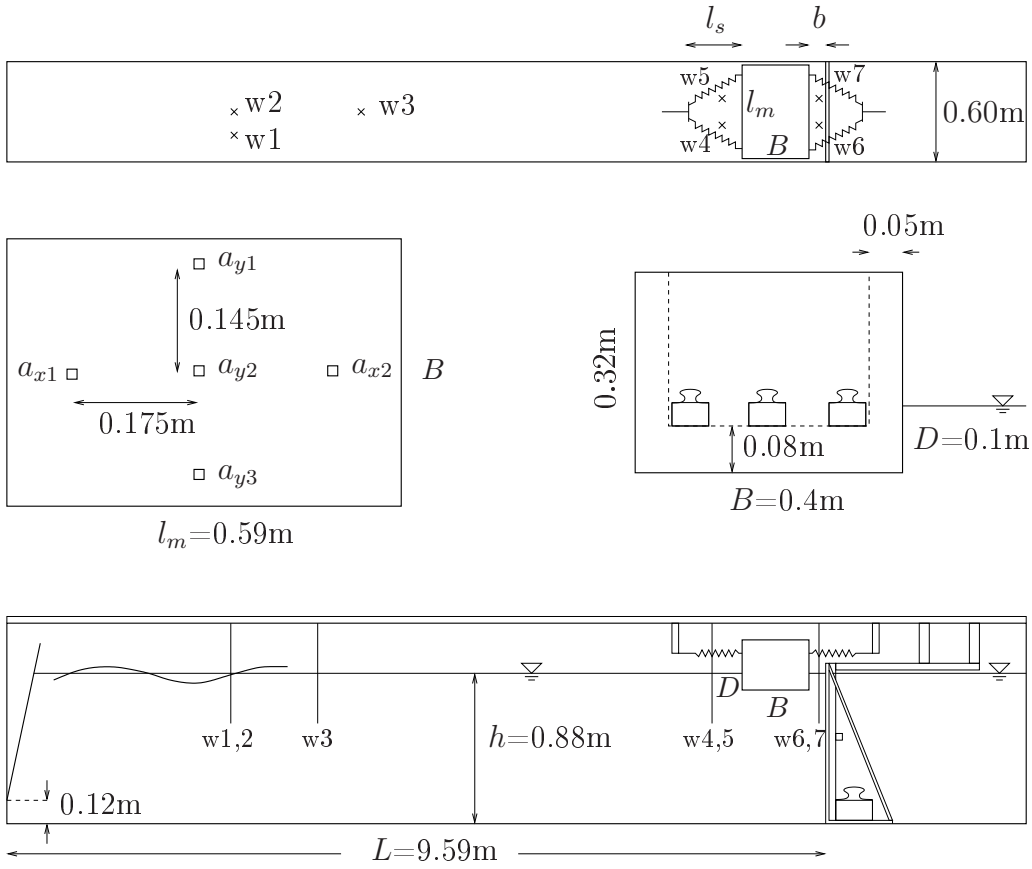

Figure 9.8: Schematics of the June 2008 model test set-up which involved a moored ship section by a terminal. The sketches are not to scale.

9.3.1 Model test set-up and test conditions

Schematics of the test facility, test set-up and ship sections for the April tests are presented in Figure 9.7, and those for the June tests in Figure 9.8. Main specifications for both sets are given in Table 9.4. The tests were performed in a wave flume at MARINTEK with glass walls and bottom, of total length 13.67m and breadth 0.60m, essentially in deep water conditions with fixed water depth $h = 0.88$m, wave period range $T = 0.6\text{s} - 1.0\text{s}$ and with fixed beam to draught ratio $B/D = 4$. The wavemaker was of hinged flap type with dry backside, hinged 0.12m above the flat flume bottom, having a slight initial forward tilt, and was controlled by a Rexroth system.

In up-right position we found the flap to be slightly skewed, producing transverse waves of significance, particularly pronounced in some pre-tests with terminal and without ship section. This resembles a "sloshing tank" which is vulnerable to any transverse excitation. After some trial and error we found the transverse waves to be acceptably low using an initial forward tilt of approximately 5 deg, as indicated in the figures, as the skewness of the flap was there at a minimum. The small amplitude waves generated during the tests required flap stroke of less than 1cm, and hence the transverse wave generation was kept at a minimum, although not completely removed. The transverse fluid motion will be discussed later in the section.

In the April tests, the input to the wave making system was merely an amplitude

Table 9.4: Relevant measures of moored ship section model tests. The tank length L is the distance from the flap top, i.e. the intersection between the wavemaker flap and the free surface in still conditions, to the terminal. The water depth range indicate a slight variation along the flume, assumed negligible for the present model tests.

	April 2008 tests	**June 2008 tests**
Tank length L (from flap top)	9.40m	9.515m
Tank width (transverse)	0.60m	0.60m
Water depth h	0.880m - 0.882m	0.880m - 0.882m
Initial forward tilt angle wm flap	4.3deg	5.5deg
Ship section breadth B	0.40m	0.4m
Ship section draft D	0.099m	0.10m
Ship section width l_w	0.595m	0.590m
Ship COG y_G (above still water line)	0.034m	0.025m
Ship roll moment of inertia I	0.21kgm	0.31kgm
Spring stiffness (4 springs)	21.95 - 22.30N/m	21.95 - 22.30N/m

in voltage along with desired wave frequency, and the flap motion had a sudden start-up, i.e. no initial ramping period, and also a sudden stop taking the flap back to zero position. Although parasitic disturbances were hence created, steady-state was in our opinion adequately reached during all the tests within the range of periods tested. In the June tests a signal in voltage was produced a priori, and we used a linearly varying start-up during the first three seconds and a similar ramp down by the end of the signal. The smooth ramp down helped avoiding rather large transients to be generated, practical with respect to reduced waiting time in between tests. Unfortunately there was no active wave absorption implemented on the wavemaker system, and slow dissipation of the fluid disturbances in between runs was experienced as expected. A calm free surface was in general reached after about 7 - 12 minutes, with the longest waiting time for the shortest wave tests with the ship hardly moving, acting as a total reflecting wall, and shortest around resonance where the ship motion caused damping.

For all tests, the recording time was one minute, with re-reflections from the wavemaker reaching the ship section within that amount of time.

The test matrix for the June tests is presented in Table E.4, where hyphens indicate repetition tests. The test program included two terminal gap widths of $b = 0.08$m and $b = 0.06$m, 16 wave periods and two wave steepnesses $\epsilon_1 = H/\lambda \simeq 1/170$ and $\epsilon_2 = H/\lambda \simeq 1/85$. We group the tests into two cases denoted by Case A and B with the specifics given in Table 9.5.

Table 9.5: Specifics of the two cases denoted Case A and Case B in the June 2008 model tests. Here, $\epsilon = H/\lambda$. The water depth was $h/B = 2.2$.

	b/B	$\epsilon_1 \simeq 1/170$	$\epsilon_2 \simeq 1/85$
Case A	0.2	x	x
Case B	0.15	x	x

The same two terminal gaps and range of wave period and steepness were used in the April tests. We do not report the exact test matrix here. The test conditions were then

determined more or less ad-hoc during the testing, with the eigenperiods estimated from free decay tests of the ship section in the initial phase of the testing since no simulations or other estimates had been done prior to the testing for that particular geometry. We believe a proper investigation of the system to be tested prior to model testing is important. The ad-hoc procedure followed in the April tests are not, in general, recommended. It was, however, a question of availability of the laboratory which was very limited in time and somewhat earlier than originally planned.

Once the test set-up was completed, meaning the weights inside the model was properly positioned, the spring arrangement fine-tuned, wave gauges positioned and sensible camera arrangements including adequate lighting found, the actual testing went quite smooth. For the June tests we spent about one week for the set-up while three days completing the test runs, including the repetition tests. In the cases of more than one repetition, the repetition tests were run both just before and just after each of the four test series, meaning the repetition tests were basically run over 4 - 5 hours, and should therefore include any drift in the gain of the instrumentation. The drift was according to this argumentation found to be small, and any observed variability of significance caused by other factors.

9.3.2 Rigging and instrumentation

A description of the rigging of the ship section and terminal as well as instrumentation now follows.

Ship section, moorings and terminal. The ship section used in the June tests had only slightly different measures relative to that used in the April tests. The measures are given in Table 9.4. They both consisted of painted blocks of divinicell (compressed foam) that were hollowed out. A 4mm aluminum plate was used as lid for the ship section model. Two photos of the ship section from the June tests are shown in the upper part of Figure 9.9. Weights were positioned inside the ship section for correct draught, positioned such as to give a somewhat realistic roll moment of inertia I_{44}. The roll moment of inertia as well as the center of gravity y_G were, as is usual, calculated by summation of weights to $I_{44} = 0.21$kgm around COG, and $y_G = 0.034$m above the still water line in the April tests, whereas $I_{44} = 0.34$kgm around COG, and $y_G = 0.025$m above the still water line in the June tests. A certain level of pitch and yaw moment of inertia was found to be important with respect to stability in those modes such as to avoid mechanical contact with the glass walls due to transverse disturbances. In the preliminary stages of the testing this was not considered. The weights were positioned near the mid-ship position only, leaving the model prone to in particular yaw motion under minor disturbances. The implication was that mechanical contact occurred between the ship section and the glass walls. The problem was remedied before the actual testing started by re-distributing the weights, hence achieving higher moments of inertia in pitch and yaw. These two quantities were not measured or calculated, but found during model testing large enough for the ship section model to be stable.

The mooring arrangement was as simple as possible, consisting of four horizontal linear springs with two on each side of the ship section fixed 20cm apart for stability in the transverse direction. The distance from the ship side to the connection between the springs and the extending rope, denoted by l_s in Figures 9.7 - 9.8 was $l_s = 0.62$m in

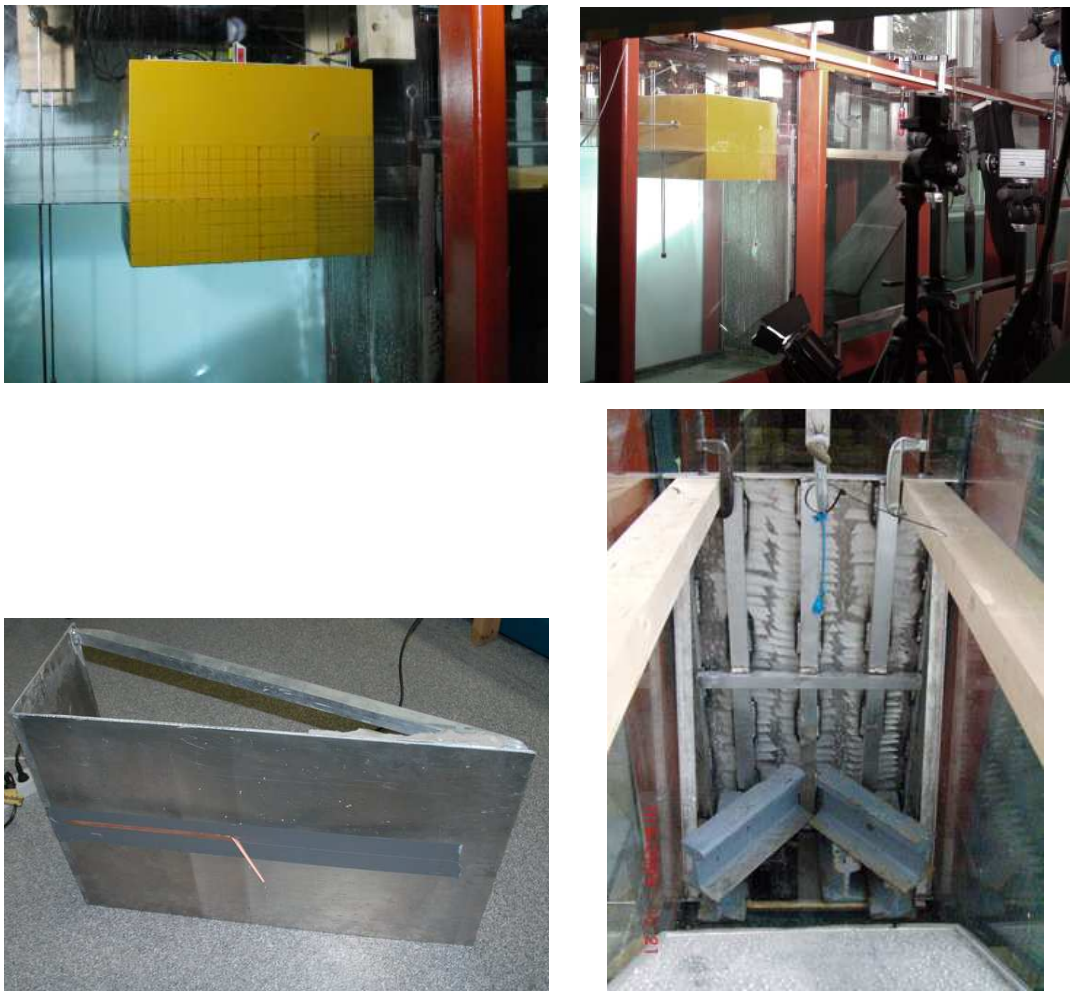

Figure 9.9: Pictures from the 2008 moored ship section model tests. Upper: The June test set-up. Lower: unstiffened terminal from the April tests (left), and the stiffened and supported terminal from the June tests (right).

the case of terminal gap width $b = 0.06$m and extended by 2cm on each side in the case of terminal gap width $b = 0.08$m. There was a variation of the spring stiffnesses of the four springs of about 1.5%, and the length at rest with about 3.5%. Given their slightly unequal properties we chose pairs as equal as possible in order to obtain transverse spring forces and moments on the ship section at a minimum. The total pre-tension in each spring pair was 16.3N in the case of terminal gap width $b = 0.06$m.

As will be discussed somewhat further below, the ship section preferred a position close to either of the glass walls, choosing one or the other side according to only small perturbations of the position of the far end mounting point of the springs. Based on observations the model kept that side during an entire test, and further, no mechanical contact between model and wall did, according to our observations, occur.

The terminal is depicted in the two lower pictures of Figure 9.9 and presented schematically in Figure 9.10. The terminal was in fact the same as that used in the fixed ship section tests of 2006, but described in more detail here. The terminal consisted of three main parts; a vertical aluminum plate of 3mm thickness, 0.595m width and 0.90m height

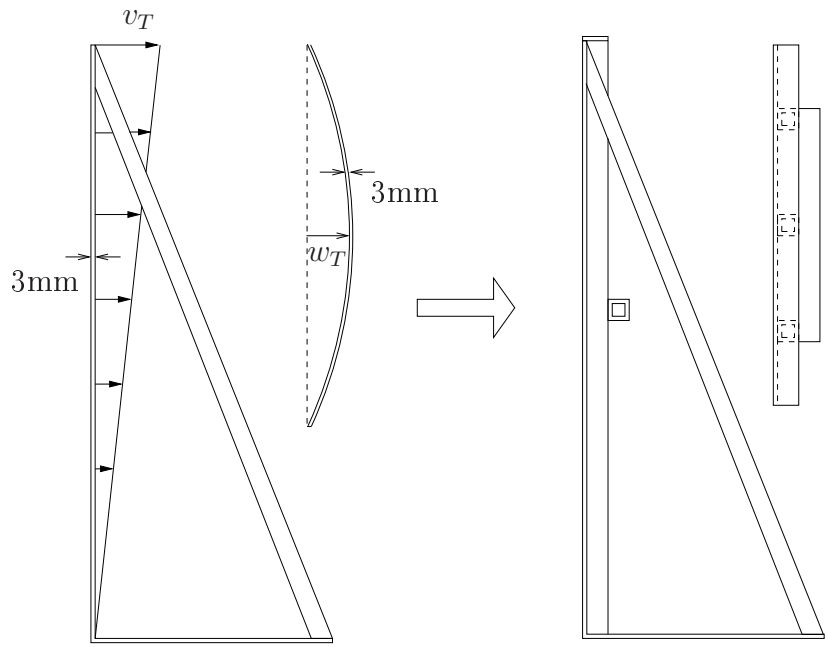

Figure 9.10: Left: The terminal being a 3mm thick aluminum plate as used in the April tests before stiffeners were mounted, with deflection w_T and associated velocity v_T as indicated. Right: Three vertical pipes are welded onto the vertical aluminum plate as well as to the bottom plate and an added top plate, and an additional horizontal pipe. Based on flat plate theory, the estimated maximum deflection given the conditions in the current tests were reduced from 1 - 2mm to $\mathcal{O}(10^{-6}\text{m})$ when including stiffeners.

welded onto a similar horizontal plate of approximately 0.3m length, and with two skew-mounted stiffeners extending from the top corners of the vertical plate and to the far end corners of the horizontal plates. As we mentioned earlier, the aluminum plate that represented the bottom mounted terminal flexed during the testing. The flexing occurred due to the hydrodynamic pressure from the water motion in the terminal gap, and was of static character since the frequencies were far from any natural structural frequency. There was obviously a lack of stiffening, as is indicated in the left of Figure 9.10. For this reason, in the June tests three vertical pipes were welded onto the vertical plate as well as to the bottom plate and an added top plate, and an additional horizontal pipe was added near the middle part, as shown in the right part of the figure. Further, the reinforced terminal model was next supported by horizontal wooden piles clamped to the terminal top plate at one end and to the fixed wave beach at the other end. This is shown in the two right photos of Figure 9.9. The terminal was after the reinforcement and support considered to adequately represent a fixed and rigid bottom mounted structure. A layer of rubber bands provided a sealed gap between the terminal and the wave flume floor, and for the same purpose clay was used along the gaps between the terminal and the glass walls of the flume. The sealing property was tested when filling the wave flume with water and found close to absolute. In comparison, no rubber bands towards the flume floor were used in the April tests, and only the top 30 - 40cm was then sealed with clay.

Wave elevation and ship section motions. Relevant information of the instru-

Table 9.6: Instrumentation in April and June 2008 model tests. Positions and relevant specifics of instrumentation of the moored ship section model tests. D_w means diameter of the wave gauge wires. Range indicates the maximum measurable acceleration of each accelerometer where g is the acceleration of gravity. Position of accelerometers are pairs of transverse/longitudinal distances relative to the lower left corner of the ship section as seen from above when keeping your head pointing along the incoming wave direction. Text in brackets indicate from where the distance is measured.

	April tests		**June tests**	
	D_w[mm]	**Position [m]**	**D_w[mm]**	**Position [m]**
w1	4.0	2.232 (flap top)	1.5	2.345 (flap top)
w2	4.0	$\simeq$ 5.1 - 5.18 (flap top)	1.5	"
w3	4.0	0.62 (terminal)	4.0	3.42 (flap top)
w4	4.0	0.025 (terminal)	4.0	0.624 (terminal)
w5	-	-	4.0	"
w6	-	-	4.0	0.037 (terminal)
w7	-	-	4.0	"
	Range	**Position [m]**	**Range**	**Position [m]**
a_{x1}	100g	(0.217 , 0.20)	20g	(0.172 , 0.20)
a_{x2}	-	-	20g	(0.418 , 0.20)
a_{y1}	100g	(0.2975 , 0.20)	20g	(0.295 , 0.345)
a_{y2}	100g	(0.2975 , 0.271)	20g	(0.295 , 0.20)
a_{y3}	-	-	5g	(0.295 , 0.055)
	Freq. [Hz]	**Resolution**	**Freq. [Hz]**	**Resolution**
HS	100	1280×1024 bw	100	1280×1024 bw
Ixus	32	640×400	32	640×400
Casio	-	-	60	6Mp

mentation is given in Table 9.6. Wave elevation was measured by capacitance type wave gauges, four in the April tests and seven in the June tests, while ship motion was measured by accelerometers mounted on the aluminum top plate, three in the April tests and five in the June tests. The diameter of each wire of the wave gauges was for the main part 4mm, except for w1 and w2 in the June tests having a diameter of 1.5mm in an effort to investigate the influence from wire diameter on the meniscus effect, that is, the characteristic curved fluid surface at the intersection between the fluid and the wire due to surface tension. We were not able to detect or conclude on any measurable difference between wave measuring capability of the 1.5mm and 4mm diameter wave gauges in our tests based on pre-tests with wave only using first the 4mm diameter wave gauges as w1 and w2.

In the April tests two accelerometers in the vertical direction gave heave and roll, while one in the horizontal direction gave sway. The accelerometers used in the April tests had maximum range of 100g, far beyond the accelerations experienced in our tests which was in the order of 0.1g, and typically showed drift of some significance during a single run. Significant low-frequency noise disallowed measurements of the slowly varying motion as well as the mean drift in sway. Also, noise in the wave period range gave, when integrated twice to motion, approximately 0.5mm amplitude motions. Further, noticeable zero drift during one single run was observed, and although filtered out in the post-processing, we

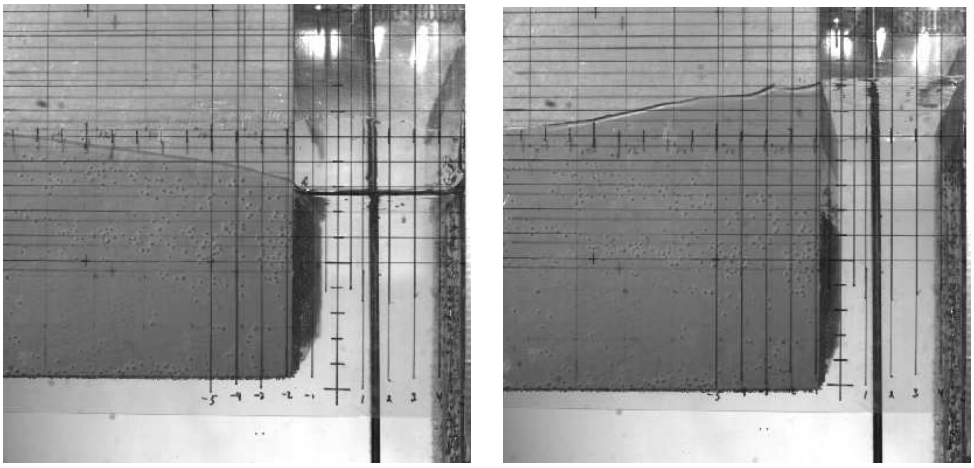

Figure 9.11: Two examples of photos from the high-speed (HS) camera capturing the terminal gap kinematics. Number marks are in centimeter. Resonant condition of coupled ship and piston-mode motion. Free surface at lower (left) and upper (right) position during a wave period.

felt that the equipment was somewhat improper. The three 100g accelerometers were therefore changed with one 5g and four 20g accelerometers for the June tests. Although much more stable during the test period as well as with hardly any drift during a run, the low-frequency noise still disallowed direct integration to motion without band-pass filtering, and the noise in the wave frequency range was also for these about 0.5mm. This meant that e.g. roll less than 0.5deg was dominated by noise. In the tests with wave period below about 0.8s, the roll was based on visual observations from video recordings, well below 0.5deg, and therefore in reality not measured. Other measuring techniques could have been chosen, such as optical systems, in order to reduce noise as well as getting the low-frequency and mean sway position, but this type of equipment was not available. A force ring connected to the spring arrangement was used in the April tests, and would in principle give combined mean roll and sway, but too much noise precluded also this signal, and the force ring was not used in the June tests. However, we believe the wave frequency motion was captured satisfactorily well by the accelerometers used, in particular those of range 5g and 20g.

Flow visualization. Three different cameras with slightly different purposes were utilized during the tests, denoted here as the high-speed (HS) camera, the Ixus and the Casio.

First, the wave kinematics and ship section motion in the terminal gap area was captured by a high-speed camera with frequency chosen at 100Hz and resolution 1280×1024 giving tiff-images in black and white. Two examples of HS images are presented in Figure 9.11. The model and glass wall were both marked with grids so that both ship motion and terminal gap elevation were monitored in detail. We mention that a white plate positioned laterally, that is on the back side of the wave flume relative to the camera side, was found essential with respect to setting the lighting for clear high-speed photos. With no such background plate, or dark background, the free surface was not captured well.

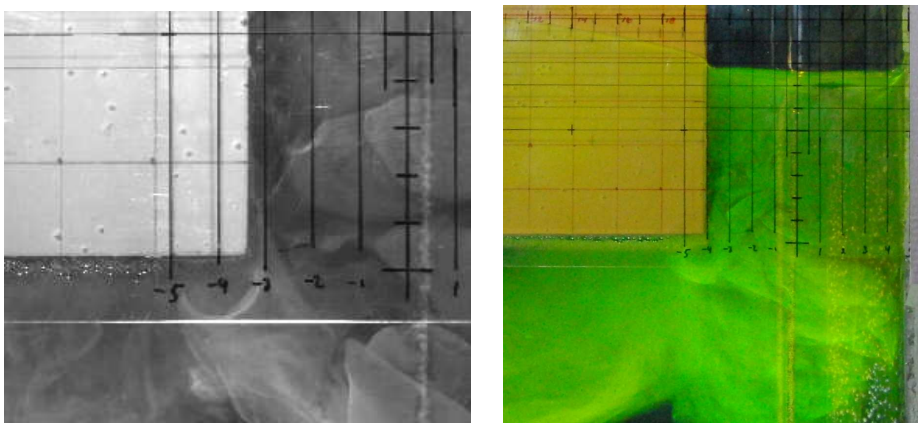

Figure 9.12: Attempts to capture vortical structures using a green colour mixed in the water. HS camera (left image) and Casio camera (right photo). One may vaguely observe a vortex just below the ship corner of approximately 2cm extent.

Second, the whole set-up was captured by a standard digital camera of type Canon Ixus 60 for a more qualitative observation of the global behaviour of the system.

Third, a Casio Exilim EX-F1 camera able to record a total of 60 colour images over one second with resolution of 6Mp along with powder providing green colour (bottle labeled *Fluorescenium Natricum*) mixed in the tank was used in an attempt to capture vortical structures. This turned out not to be successful to any satisfactory degree. The high-speed camera was also used during repetition runs by the end of the model testing in further attempts to study the flow separation. The green colour was hardly visible on the black and white high speed photos using the white background due to the light appearance of the coloring, something a black background improved. The green colour was, however, in general too evenly distributed throughout the fluid, so any clear vortical structures were in general not captured. We therefore tried mixing the colour with syrup and/or honey, sticking a lump on the ship corner just prior to a run using a ruler, resulting in relatively nicely visualized vortices during the initial stages, but dissolving almost completely before any steady-state motion was reached. An example from the Casio camera with white background and one from the high-speed camera with dark background, both in steady-state conditions, are shown in Figure 9.12. Although nearly dissolved, the colouring indicates some vortical structures of about 2cm extent just below the ship section corner, in particular in the high-speed photo.

We conclude that the free surface and ship motions were captured well by the cameras, while the flow separation not so well.

9.3.3 Main differences between April and June tests

In Table 9.7 we summarize the main differences between the April and June tests with possible improvement indicated in the right column. We have already touched upon most of these through the above description of models and test set-up, but still dwell somewhat on this matter to emphasize the importance of taking previous experience into account when designing experiments.

The main and decisive improvement in the June tests relative to the April tests was

Table 9.7: Main differences between the June and April tests. Potential improvements are indicated in the right column. The main improvement in the June tests relative to the April tests was that the terminal was thoroughly stiffened and supported.

	April tests	**June tests**	**Improvement**
Terminal plate	Stiff and supported	Unstiffened	Yes - major
No. of wave gauges	4	7	Yes
Calibration	First day only	Each day	Yes
No. of acc.meters	3	5	Some
Wavemaker signal	Abrupt start-up	Smooth start-up	Some
Test program	ad-hoc	Planned	Some
Terminal sealing	Top 30 - 40cm	All boundaries	Little
HS Lighting	No background	White background	Little
Ship section marks	Ticks	2cm x 2cm grid	Little
Model length	0.595m	0.590m	Unknown

by all means the stiffening and support of the terminal. Two other improvements not regarded crucial, although still providing results of what we believe is somewhat higher in quality than in the first tests were that (1) three pairs of wave gauges in side-by-side arrangements allowed identification of transverse oscillations, and (2) the wave gauges and the accelerometers were calibrated each morning. Also, a new set of accelerometers which proved to have less drift, and with a redundancy of one in each direction, gave more trustable body motion measurements. For example, calculating roll using three different combinations of the vertically positioned accelerometers gave differences only within 1-2%.

As far as the wavemaker motion goes, a smooth wavemaker start-up is considered an improvement in particular with respect to reproduction by a numerical wavetank, avoiding transients of non-smooth character.

Following a well defined model test plan is considered an advantage as opposed to the approach of more or less ad-hoc type of testing. It is on the other hand of course the danger of being biased towards the acquired results when expecting certain results. We feel, though, that we have treated both sets of data neutrally during the testing and post-processing.

Proper sealing of the terminal intersections with the flume bottom and walls is regarded a decent action, although the deep water conditions and relatively small gaps would indicate very small leakage in any case below about 30 - 40cm from the free surface.

Improved image quality in terms of better lighting as well as grid on both the ship and the glass wall provided an opportunity to qualitatively double check both the ship section motion and the free-surface elevation in the terminal gap, in particular the former.

Lastly, a 0.5cm shorter length of the ship section l_w (in the transverse direction of the wave flume) may have reduced possible, yet quite unlikely, glass wall friction. By glass wall friction we mean the shear forces acting on the ship section due to the boundary layer flow in between this and the glass walls. On the other hand, it did most likely introduce additional three-dimensional effects, therefore the indication "unknown" in Table 9.7. By three-dimensional effects we mean the following. In the April tests the section length was 0.595m, leaving a 2 - 3mm gap between the ship section and glass walls on each side, while in the June tests there was a total gap of about 1cm. The frictional forces were in the April tests a priori estimated using a Stokes second problem approach. In Stokes second

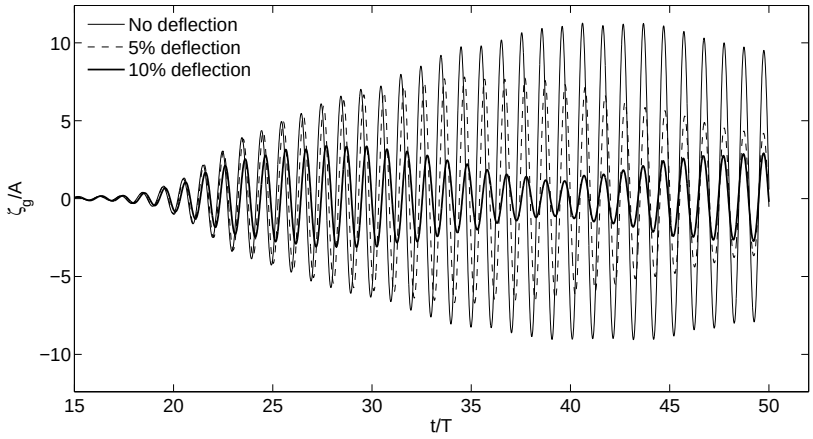

Figure 9.13: Numerical investigation of the effect of flexing terminal wall. Time-series of terminal gap elevation from simulations using the numerical wavetank without flow separation. Results from numerical simulations with no deflection of the terminal and with deflection according to $w_T = 0.05\,\zeta_g$ and $w_T = 0.1\zeta_g$ are shown.

problem there is a semi-infinite fluid over a flat plate of infinite extent. In our approach there were two parallell plates a distance d apart. Both plates were of infinite extent, one at rest and the other one oscillating laterally in harmonic motion. No-slip condition was prescribed on both plates. The resulting shear force was obtained by integration over an area equal to BD and multiplied by 2 due to the two sides of the ship section. The opening effects near the ends of the ship section sides were thus not accounted for. We mention that the resulting frictional force was not significantly different from that estimated using the classical approach. This goes for the given oscillation periods and gaps of 2 - 3mm. For smaller gaps, the two estimates deviated. The force estimation indicated the shear forces to be by all means negligible relative to other forces acting, even with respect to roll damping. However, adding an extra 5mm gap was nevertheless chosen in case of miscalculation or lack of validity of the simplified approach. During the June tests it turned out, however, that the ship section always preferred a position approximately 2 - 3mm from one of the sides, leaving a 7 - 8mm gap on the other. This introduced some three-dimensionality through the ship sections' role as wave making device. The measured wave elevation at w6 and w7 in the terminal gap differed in some cases around resonance by up to 15%, with the lowest on the side with the largest gap. Slight justifications of the spring arrangement between runs allowed control of which of the glass walls the model preferred being close to, and we found that changing sides also changed the side on which the highest terminal gap amplitude was measured. We believe that a model length of $l_w = 0.595$m, leaving a gap of about 2 - 3mm on each side, would have resulted in somewhat higher responses, say maybe 7 - 8% higher than those acquired during the present tests.

9.3.4 The effect of a flexing terminal

We here present a qualitative investigation of the effect of a statically flexing terminal. The flexing amplitude w_T (cf. Figure 9.10) of about 1 - 2mm as observed during the

experiments is first substantiated by estimates using beam theory on a horizontal strip of the terminal. The actual flexing and its effect of reducing the amplitude of the resonant ship and piston-mode motion is next modelled by use of the nonlinear numerical wavetank.

We assume that the terminal plate is free at the ends towards the wave flume wall, that is, neglect the stiffeners connecting the vertical and horizontal aluminum plates. We further assume a uniform hydrodynamic pressure over the breadth and consider a horizontal strip at the top of the terminal. The maximum deflection is then given by $w_T = (5/384)ql^4/EI$, where for aluminium $E = 0.7 \cdot 10^5 MPa$, $I = t^3/12$ with $t = 0.003$m being the plate thickness, $l = 0.6$m the breadth of the tank and $q = p \times 1$ is the pressure times a unit section. The back of the plate was wetted, such that the net pressure acting was the dynamic pressure in the terminal gap, and we estimate q from the amplitude of the dynamic pressure near the free surface $\rho\phi_t \simeq \rho g A_g$. As defined earlier in the text, A_g is the amplitude of the piston-mode motion. As an example, for one test near resonance with $A_g \simeq 9$mm, meaning $\rho\phi_t \simeq 100$Pa, we get that the deflection amplitude would be $w_T \simeq 1$mm, which corresponds well with that observed. The averaged deflection over the breadth is then $2w_T/\pi \simeq 0.64$mm which is about 7% of the piston-mode motion.

Next, we assume the plate deflection to vary linearly along its height as indicated in Figure 9.10, with deflection w_T at the top due to the dynamic pressure acting there, and zero at the bottom. Since the range of wave periods was away from that providing any plate dynamics, we may further safely assume the plate deflection to have been quasi-static. This means we may express the plate deflection as $w(y,t) = w_T(1 + y/h)$, with $w_T = a\zeta_g$ The fraction a is chosen based on observation and the above estimates of the deflection. The time derivative of w serves as body boundary condition (2.5) along the terminal, i.e. $\varphi_n = -\dot{w}$ in the numerical wavetank. Examples of terminal gap elevation time-series from running the nonlinear numerical wavetank is shown Figure 9.13. Flow separation is not included. In the figure, the thin solid curve corresponds to no deflection of the terminal, and the other two curves corresponds to deflections of $w_T = 0.05\zeta_g$ and $w_T = 0.1\zeta_g$. The effect of the deflection is significant. Although steady-state is not reached, the results indicate that the terminal gap amplitude is reduced to about 60% and 30% of that without deflection in the two cases respectively.

Condensed results from both the April and June tests by means of steady-state terminal gap amplitudes normalized by the amplitude of the incoming wave is shown in Figure 9.14. These show that the near resonance amplitudes of the April tests were about 60% of those in the June tests. This fraction of about 60% corresponds well with the numerical results combined with the estimates and observations of the flexing amplitude.

The above discussion provides clear evidence of the significant reduction effect of a flexible terminal. We conclude that emphasis must be made on modelling boundaries that are supposed to be fixed and solid thoroughly stiff when investigating resonance phenomena.

Last, we suggest that this effect could also be utilized in practice in design. For example, a plate hinged near the bottom of a terminal or inside a moonpool, allowed to under-go quasi-static motion might be an effective device to reduce motions around resonance. The spring effect could be achieved for example by placing pieces of rubber or similar between the hinged plate and the terminal. The concept is based on a passive system, meaning no active control is needed.

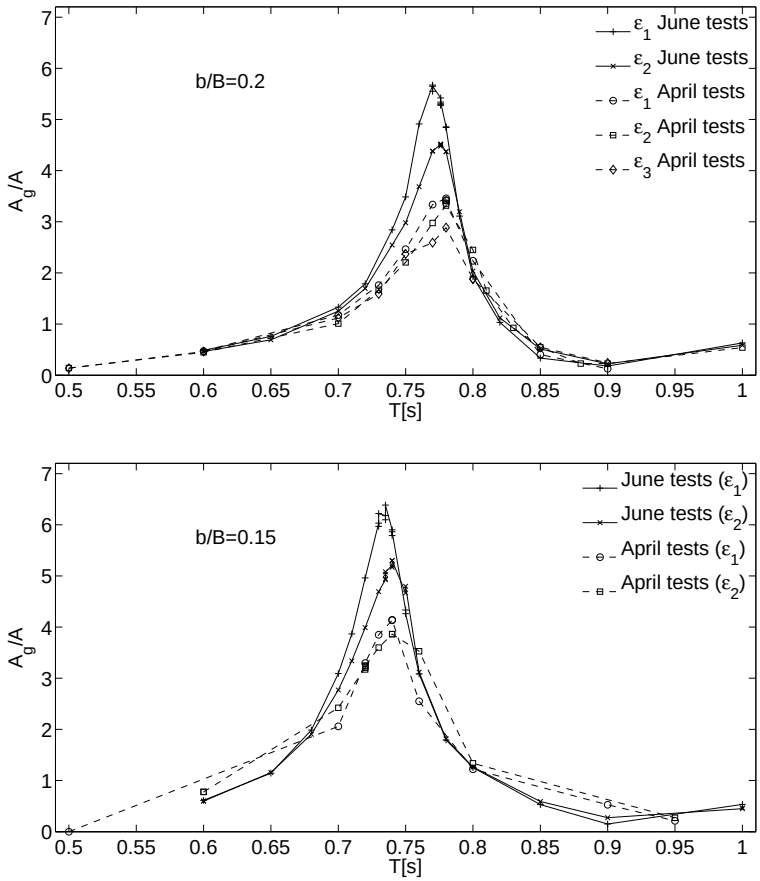

Figure 9.14: Comparison between the nondimensional terminal gap amplitude from the April tests with a slightly flexible terminal, and the June tests where the terminal was stiffened. $\epsilon = H/\lambda$ is the wave steepness and b/B the terminal gap width nondimensionalized by the ship section beam. Around resonance the results from the April tests are about 60% of those from the June tests.

9.4 Moonpool tests briefly recapitulated

The so-called moonpool model tests were performed in connection with the work by Faltinsen et al. (2007) during summer 2005, and results from these are reported therein. Time-series were provided electronically for use in the present work. A re-analysis was done as reported in Kristiansen and Faltinsen (2008) in order to investigate in-depth the rather surprising results that the piston-mode amplitude in the model tests in one case actually exceeded that predicted by linear theory. The re-analysis revealed that wave reflections from the far ends of the wave flume caused the discrepancies. This is presented briefly in the following.

9.4.1 Model test set-up and test conditions

Model tests involving forced heave of two rectangular sections with sharp corners were performed in the same wave flume described in connection with the moored ship section model tests, and the model test set-up is presented schematically in Figure 9.15. Under the

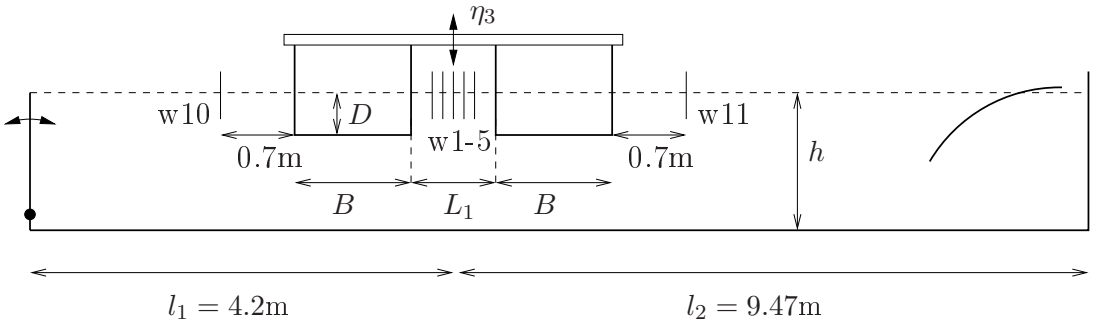

Figure 9.15: Schematics of model test set-up in the moonpool tests with a selection of the twelve wave gauges and dimensions. Note that the sketch is not to scale.

assumption of symmetry about the center-line of the moonpool, the set-up is equivalent to that of a single ship section by a wall at a distance half that between the two sections. The still water depth was $h = 1.03$m. The beach was of parabolic shape, approximately 2.3m long, and the wavemaker was at that time equipped with an active wave absorption system. The center-line of the model was $l_1 = 4.2$m away from the wavemaker and a distance $l_2 = 9.47$m from the tank wall behind the beach. There were twelve wave gauges, denoted by w1 - w12, where w3 was in the center-line, and w10 and w11 were 0.7m away from the model extremities on the wavemaker side and beach side respectively. w1 - w5 defined an array positioned longitudinally along the tank with 40mm cc distance between each.

As in Faltinsen et al. (2007) and Kristiansen and Faltinsen (2008) we group the results in three different cases denoted by Case I - III with variations in the draft D and the "terminal gap" width $b = L_1/2$, where L_1 is the distance between the two sections. There were two forcing amplitudes in Cases I and II, and one in Case III. The specifics of the three cases are summarized in Table 9.8. The normalized heave amplitude is denoted by $\epsilon = \eta_{3a}/B$, where η_{3a} is the amplitude of the forced heave motion with 2.5mm and 5mm used in the model tests, such that $\epsilon_1 = 1/144$ and $\epsilon_2 = 1/72$. A linear ramp during the first test seconds were used for the forced heave motion. We use the ship section beam $B = 0.36$m as characteristic length, rather than the quantity $L_1 = 2b$ in the mentioned works, and a nondimensional wave frequency $\omega/\sqrt{g/B}$, where ω is the circular frequency, rather than $\Lambda = \omega^2 L_1/g$. Redefining the characteristic length and nondimensional frequency is purely a matter of providing consistent presentation relative to the other studies in the present work.

Table 9.8: Specifics of the three cases denoted Case I - III in the moonpool model tests. $\epsilon = \eta_{3a}/B$ is nondimensional forced heave amplitude. The still water depth was $h/B = 2.86$.

	B/D	b/B	$\epsilon_1 = 1/144$	$\epsilon_2 = 1/72$
Case I	2	0.25	x	x
Case II	1.33	0.25	x	x
Case III	2	0.5	x	-

9.4.2 Wave reflections

Investigations of time-series showed clear indications of wave reflections in the wave flume, both from the beach side and from the wavemaker side. It seems that neither the wavemaker absorption system nor the beach was able to properly damp out waves radiated by the forced heave motion, and we speculate that this was due to the very low wave steepness, typically $H/\lambda \sim 1/1000 - 1/300$. As far as the beach goes, the waves will refuse to break at such low steepness, and for the wavemaker, the induced forces were perhaps in a lower range than the working range. The authors are not aware of the working range or the actual functionality of the absorption system of the wavemaker.

The existence of reflections is best illustrated by a few examples. In Figure 9.16 the time-series of w3, w10 and w11 from four tests (a-d) are presented. We denote the time instants when the wave train fronts are, roughly, to return from the two extremes of the tank by $T_{r1} = 2l_1/C_g$ and $T_{r2} = 2l_2/C_g$. The Hilbert envelopes, low-pass filtered at 1Hz, reflecting the energy in the signal, are superimposed as solid curves enclosing the time histories, and the time instants $t = T_{r1}$ and $t = T_{r2}$ are indicated by dash-dotted vertical bars. The solid vertical bars denote the time window used for estimation of the fluid elevation amplitudes. The spurious behaviour in the very beginning of each signal is due to band-pass filtering, and does not affect the following observation.

If there are no asymmetries inside the moonpool, the radiated waves to each side should evolve equivalently. This means that, given a symmetric behaviour of the fluid in the moonpool, the measured signals from w10 and w11 should be the same. From visual observations during the testing (oral communication) and from movies of the free surface elevation reconstructed using the signals from w1 - w5, there were no asymmetries in the moonpool of significance. This means that any discrepancy beyond measurement accuracy between w10 and w11 must be a consequence of reflections. Significant discrepancy between the signals from w10 and w11 is indeed observed in several cases such as that in Figure 9.16(c). We therefore conclude that reflections did occur at least in this test taken from Case III, but most likely in all tests to some extent. Modulations of the amplitudes occur around T_{r2} which is a clear indication that waves reflected from the beach side is the cause of the strong modulations in the particular test shown in Figure 9.16(c). A consequence of the reflected wave is an altering of the fluid behaviour also in the moonpool with a resulting lowering of the amplitude as seen from the bottom time-series of w3.

In Figure 9.16(d), the difference between w10 and w11 is not pronounced, but small amplitude modulations in w3 around both $t = T_{r1}$ and $t = T_{r2}$ are observed. In Figure 9.16(a) and (b) which are from Case I and Case II, there are some visible modulation around both T_{r1} and T_{r2}, although very small.

We conclude that wave reflections of some significance occured in Case III, while in Cases I and II, reflections did occur, although not that significant. This is taken into account in our study on resonant piston-mode motion due to forced heave in the next chapter.

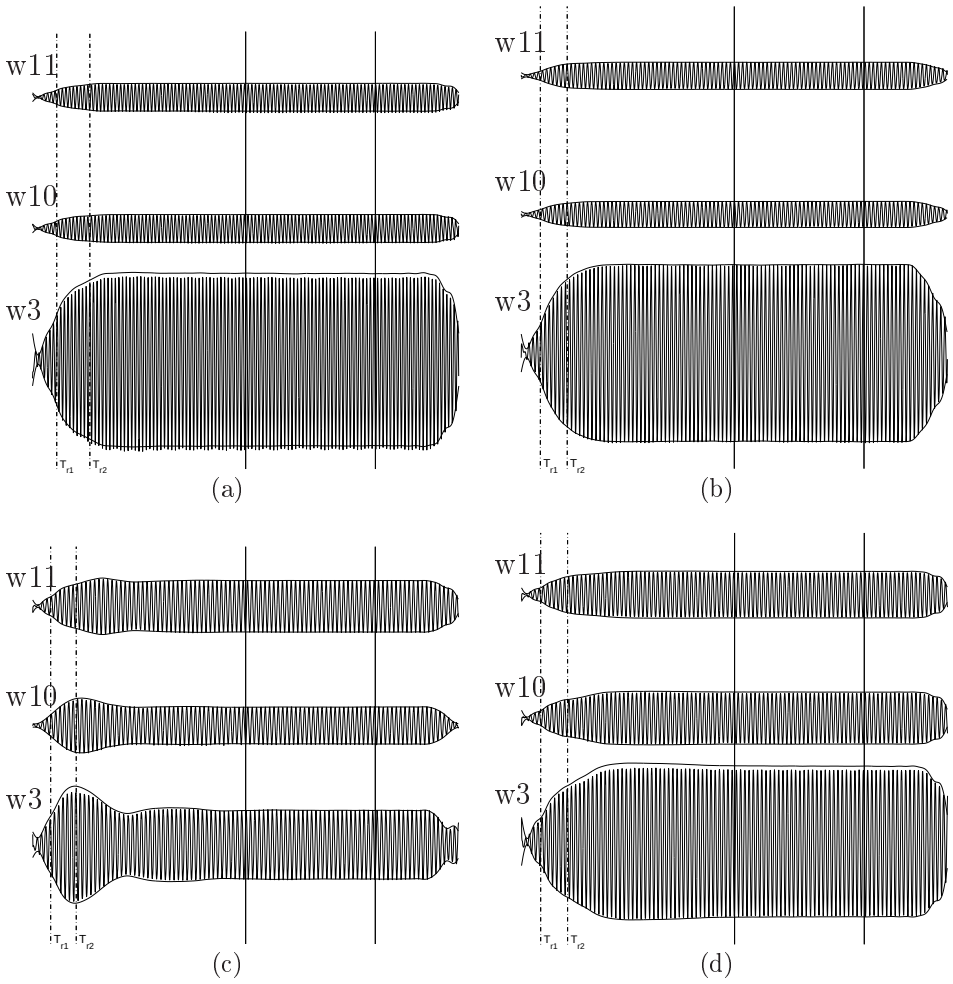

Figure 9.16: Time-series of w3, w10 and w11 from four tests: (a) Case I with ε_2 and $\omega/\sqrt{g/B} = 1.017$. (b) Case II with ε_2 and $\omega/\sqrt{g/B} = 0.885$. (c) Case III with $\omega/\sqrt{g/B} = 0.842$. (d) Case III with $\omega/\sqrt{g/B} = 0.872$. The Hilbert envelope reflecting the energy in the signal is superimposed.

Chapter 10

Studies on resonant behaviour

In this chapter the results from our studies of a ship section by a bottom mounted terminal in resonant conditions are presented. The studies are presented within the five sections of the present chapter. The first three sections represent the main work that includes both experimental and numerical results. Most of these results have already been published over three papers. The two last sections include numerical studies only, and are considered as supplement for the three preceding main studies. Results from these have not previously been published. A summary of the studies with main particulars is presented in Table 10.1. We further summarize the studies as follows.

In Section 10.1, a study on a fixed ship section with rounded bilges by a bottom mounted terminal subjected to incoming shallow water waves with focus on the piston-mode resonance is presented. The rounded bilges were such as to avoid flow separation as far as possible. The numerical part of the study involves simulations from both the linear wavetank as well as the nonlinear wavetank without flow separation. The results are compared with experimental results from the November 2006 model tests performed within this work as reported in Section 9.2. The majority of the results have been published in Kristiansen and Faltinsen (2009a).

In Section 10.2, a study on forced heave of a ship section with sharp bilges by a bottom mounted terminal with focus on the effect of flow separation on the amplitude of the piston mode near resonance is presented. The numerical part of the study involves simulations from both the linear wavetank as well as the nonlinear wavetank with and without flow separation. The considered case is equivalent to that of a moonpool, and the results are compared with experimental results from the moonpool tests briefly recapitulated in Section 9.4. The results have previously been published in Kristiansen and Faltinsen (2008).

In Section 10.3, a study of a moored ship section with sharp bilges by a bottom mounted terminal with focus on the effect of flow separation on the resonant coupled ship and piston-mode motion is presented. The numerical part of the study involves also here simulations from both the linear as well as the nonlinear wavetanks with and without flow separation. The results are compared with experimental results from the June 2008 model tests performed within this work as reported in Section 9.4. The results have previously been published in Kristiansen and Faltinsen (2009b).

In Section 10.4 we present numerical results of forced sway motion with otherwise the same set-up as in the work on forced heave reported in Section 10.2. This work involves simulations from both the linear wavetank as well as the nonlinear wavetank with flow

Table 10.1: Overview of the studies presented in Sections 10.1 - 10.5. By "Wave" forcing we mean incoming waves generated by a wavemaker.

Section:	10.1	10.2	10.3	10.4	10.5
Ship section	Fixed	Forced	Moored	(as 10.2)	(as 10.1)
Forcing	Wave	Heave	Wave	Sway	(as 10.1)
Flow separation	No	Yes	Yes	(as 10.2)	Yes
Model tests	Nov. 2006	"Moonpool"	June 2008	-	-
Water depth	Shallow	Deep	Deep	(as 10.2)	(as 10.1)
B/D	3.76	1.33 - 2	4	(as 10.2)	(as 10.1)
h/B	0.45 - 0.625	2.86	2.2	(as 10.2)	(as 10.1)
b/B	0.17 - 0.34	0.25 - 0.5	0.15 - 0.2	(as 10.2)	(as 10.1)
r/B	0.09	0	0	(as 10.2)	0 - 0.014
B [m]	0.64	0.36	0.40	(as 10.2)	(as 10.1)
T [s]	1.3 - 2.8	1.0 - 1.7	0.6 - 1.0	(as 10.2)	(as 10.1)

separation. In Section 10.5 we study numerically the effect of flow separation on the piston-mode resonance for a fixed ship section by a bottom mounted terminal subjected to incoming waves, with the same set-up as that reported in Section 10.1. We present numerical results involving simulations from both the linear as well as the nonlinear wavetanks with flow separation, and the ship section bilges are modelled both as sharp and with a finite curvature with fixed separation point.

10.1 Fixed ship section by a bottom mounted terminal

We now present and discuss the results from our first main study involving a fixed ship section with rounded corners by a bottom mounted terminal. The ship section and terminal are subject to incoming regular waves with wave periods around the piston-mode resonance period T_p. The study is based on the November 2006 model tests described in Section 9.2, and the particulars of the geometry and wave conditions are described there.

Before we proceed, we want to make the following three remarks. First, the relatively high piston-mode resonance period T_p implied rather shallow water waves ($h/\lambda_0 < 1/10$), with which one will typically associate large nonlinearities in the incoming waves. We do observe clear nonlinearities associated with the shallow water waves on the wave kinematics in the external part of the fluid. In the terminal gap itself, however, from observation during the model tests and video recordings we found that no higher modes of significance were triggered, except in some extreme cases where the terminal gap amplitude was large enough for the free surface to reach the rounded bilges, hence introducing significant disturbances. Video recordings from the high-speed camera shows clearly that violent sloshing, or run-up along the ship and terminal occured in these cases. The described disturbances were, however, introduced by the curved geometry, and not by the nonlinearity in the incoming waves. These tests were not considered in the following study. The terminal gap elevation, ζ_g, turned out to be nearly harmonic in all other cases. Second, this study involves a fixed ship section. This is not a realistic case, of course. It was, however, convenient to begin with a fixed ship section. Third, the results of this study and the discussion of these must be viewed in light of being our first study on the resonant

behaviour and the first real study applying the numerical models. More knowledge on the resonant behaviour was naturally acquired throughout the later studies. This goes both for the model testing and the application of the numerical wavetanks. For the former, the level of response is highly sensitive to additional damping which may easily be introduced by bias errors. For the latter, in the later studies we were typically more careful with studying the necessary resolution in time and space.

We now present the parameters in the numerical simulations and next compare the numerical results to those acquired from the model tests.

10.1.1 Parameters in the numerical simulations

The length from the mean position to the terminal is denoted L. The exact wave flume geometry from the model tests was reconstructed in both the linear wavetank and nonlinear wavetank, except for the beach. This means that in the simulations including the ship section and terminal, the exact geometry was reconstructed. In the wave calibration runs, however, the part from the position of the terminal and onwards was not reconstructed as this would involve wave breaking over the parapolic beach as in the physical tank. Wave absorbtion was done by using the numerical beach approach, that is, using (5.5).

The motion of the wave paddle in the numerical wavetank was that recorded during the model tests with the signal divided by the amplification factor discussed in sub-section 9.2.2.

Although the ship section in the model test had rounded corners of radius $r/B = 0.09$, the ship was in the numerical model taken as a rectangle. The argument was that quantities such as added mass and damping of this structure of area ratio $A_S/(BD) \simeq 0.986$, where A_S is the actual area of the ship section with rounded bilges, would not be affected to any significant degree.

Table 10.2: Numerical parameters in simulations of a fixed ship section by a bottom mounted terminal. Initial number of elements on the different parts of the boundary S.

Free surface (external + terminal gap)	$N_F = 357 + 3 = 360$
Ship section (side + bottom + side)	$N_B = 5 + 5 + 5 = 15$
Bottom of wavetank	$N_{BOT} = 240$
Terminal	$N_{TERM} = 7$
Wavemaker	$N_{WM} = 10$
Numerical beach length	$L_d = 3\lambda$
Dissipation parameter	$\nu_{max} = 0.8$
No. of time-steps per period	$N_P = 20 - 80$

The initital number of elements used on the different parts of the geometry, the numerical beach parameters and the time discretization parameter are tabulated in Table 10.2. These parameters applied to both the linear wavetank and nonlinear wavetank. Typically 30 periods were run, but in some cases the simulations broke down earlier. The CPU time for a single run on a 2.67GHz PC ranged from about 6min for the linear runs without beach and up to 40min for the nonlinear runs including the beach.

No formal convergence testing with respect to the beach length L_d was performed for the specific cases in the present study. Rather extensive testing of the parameter L_d

was done during the implementation of the numerical beach prior to the study. We then found that $L_d = 3\lambda$ in general gave reflections less than 1% of the incoming waves. This was done in intermediate to deep water conditions. We have no reason to believe that an extensive amount of reflection did occur in the present study. However, since the present damping strategy is not valid in the shallow water limit, we expect that $L_d = 3\lambda$ might have been a little too short to achieve less than 1% reflection for the longest waves in the study.

A selection of numerical tests involving the ship section and the terminal were checked for convergence with respect to resolution in time and space. These indicated that the numerical error associated with the present simulations were within 1 - 3%. Note that this was for tests including the ship section and terminal. A similar convergence study was not done for the wave calibration runs.

As pointed out in Section 5.4.2, the total fluid mass showed an oscillatory behaviour. In the present study this had an oscillation amplitude of $\mathcal{O}(10^{-4})$. There was never any sign of mean mass loss. This holds also for the wave calibration runs when the artificial damping was applied. We remark that in later studies the amplitude of oscillation was $\mathcal{O}\{10^{-6}\}$.

10.1.2 Results - Piston-mode resonance

The results from our study are organized as follows. First, time-series and snapshots of the free-surface elevation in two selected conditions are presented. Next reduced data are presented as function of wave frequency. As described in connection with the model tests we grouped the tests into three cases, called Case 1 - 3, with specifics given in Table 9.3. Since in Kristiansen and Faltinsen (2009a) the work was limited to investigating Cases 1 and 2 only, we present these results in the same detail as therein in connection with Figures 10.3 - 10.5. We also shortly present some results from Case 3, including piston-mode amplitudes from linear simulations and model tests, shown in the left part of Figure 10.6. In the right part of the same figure we include some results also from the September 2006 tests for frequencies higher than the resonance frequency.

Time-series. We first present the selected time-series from the model tests and nonlinear numerical simulations. Time-series at five locations along the wave flume from wave calibration tests are presented in Figures F.1 and F.2, and from corresponding tests with ship section and terminal in Figures F.3 and F.4. The wave condition in Figures F.1 and F.3 represent near piston-mode resonant condition in Case 1. The wave frequency is $\omega/\sqrt{g/B} = 0.791$. The nominal wave steepness in deep water is $\epsilon_2 = H_0/\lambda_0 = 1/115$. In the actual water depth where the wavelength and waveheight have both changed, we have $H/\lambda = 1/115$ and $H/h = 1/10$. Figures F.2 and F.4 present near piston-mode resonant condition in Case 2. The wave frequency is $\omega/\sqrt{g/B} = 0.707$. In this case we also have $\epsilon_2 = H_0/\lambda_0 = 1/115$, but $H/\lambda = 1/73$ and $H/h = 1/6$. The wave calibration time-series compare in our opinion quite well. Exceptions are the troughs at w8 and w12 in Figure F.2. This discrepancy might just as well be due to beach reflections in the wave calibration tests during the physical model as well as due to inaccuracies in the numerical model.

In all the considered tests, we have a similar level of comparison as in Figures F.1 - F.4. The troughs at w8 and w12 in Figure F.2 represent the worst level of comparison.

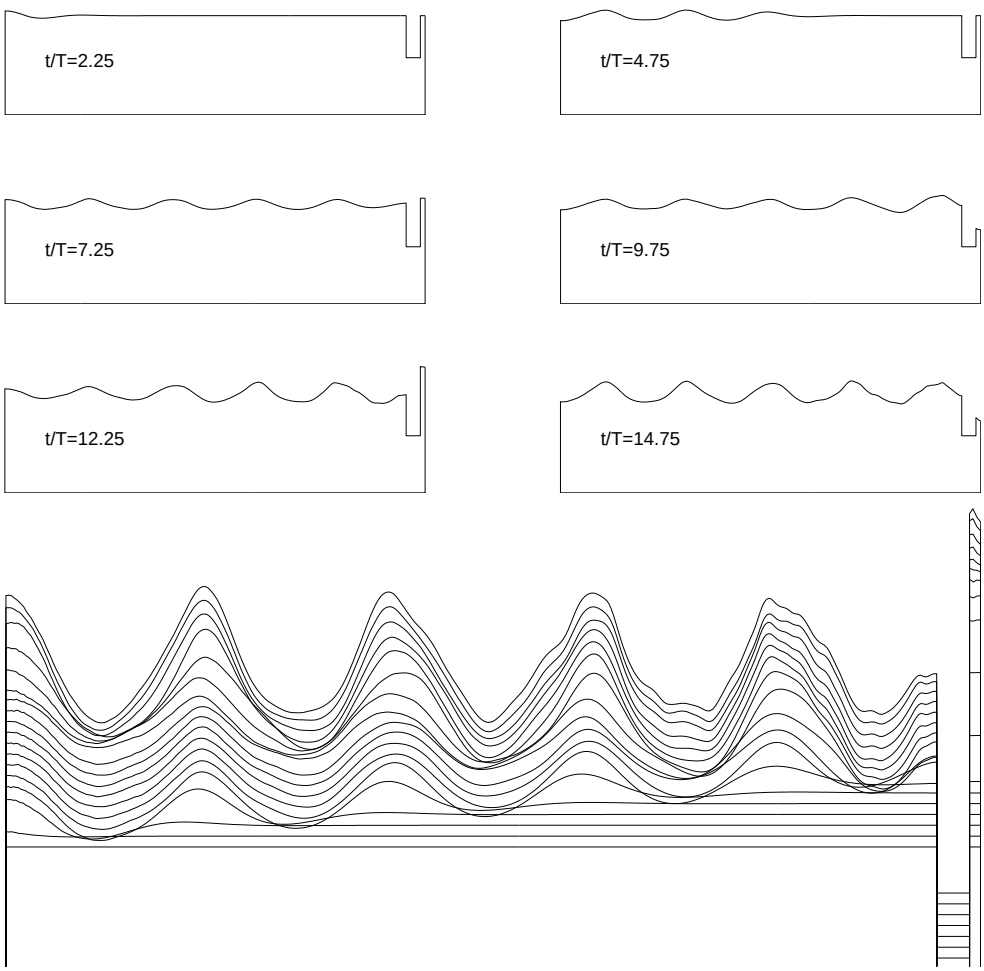

Figure 10.1: Snapshots of wave elevation in the run corresponding to that in Figure F.3. The lower plot represents other time-steps than the upper plots.

In other words, we feel the results compare reasonably well.

When the ship and terminal is present, the time series for w1 - w8 compare quite well up to the stage when the wave is re-reflected from the wavemaker to the wave gauges. The discrepancies after this stage is due to the leakage effect around the wave paddle which was discussed in sub-section 9.2.2. The AWACS adjusts the motion of the paddle continuously in order to damp out the reflected waves, and does so rather successfully in the physical tank. However, the recorded wavemaker motion will not effectively damp out the reflected waves in the numerical model due to the leakage in the physical tank. It will partly work, though, one may say, and the behaviour of the simulated free-surface elevation is qualitatively similar to that in the model tests. See for instance w1 after about $t/T = 15$ in Figure F.3 and w4 after about $t/T = 12$ in Figure F.4. The kinematics in the terminal gap (w12), however, is over-predicted right from the start. The discrepancy stays constant for some time, until it increases about when the re-reflected wave reaches the model. This last increase is due to the leakage around the paddle. The discrepancy in the first steady-state part is the core of the present study. We discuss this in detail below, in connection with the reduced data.

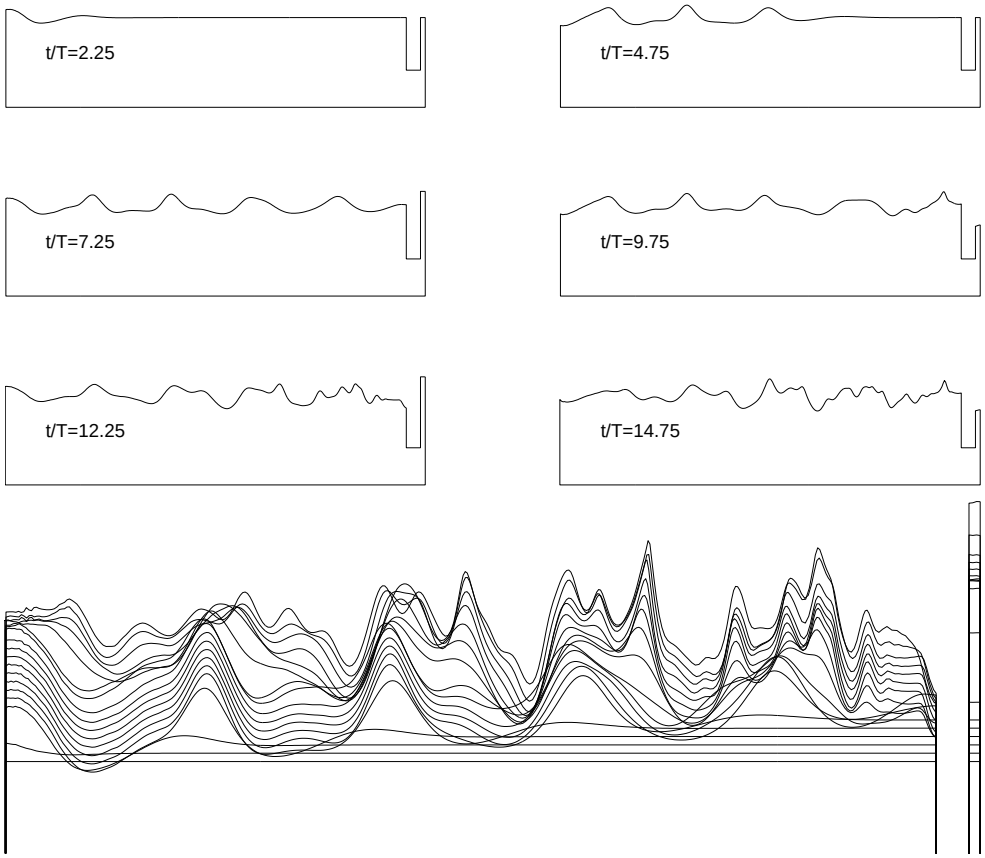

Figure 10.2: Snapshots of wave elevation in the run corresponding to that in Figure F.4. The lower plot represents other time-steps than the upper plots.

Snapshots. In Figures 10.1 and 10.2 snapshots of the simulated wave elevation for the two conditions are presented. The geometry is stretched in the vertical direction for illustration purposes. From the figures it is clear that nonlinearities in the wave in the up-stream part of the wavetank are more pronounced in the latter case. The free surface becomes very messy in the second case as illustrated in Figure 10.2, but the time series nevertheless compare quite well, ref. Figure F.4. Note that the steepness H/λ is roughly the same for the two conditions. However, H/h is not the same. The values are $H/h = 1/10$ and $1/6$ in the two cases, respectively. The large motion in the terminal gap is clear, and dominated by the piston motion. Some disturbances other than the piston mode are also seen. So, as discussed in Chapter 4, the behaviour is piston-like, and not that of pure piston-mode motion. We take $\zeta_g = 0.5(\mathrm{w11} + \mathrm{w12})$ as a representative measure of the piston-mode elevation. The positions of these are given in Table E.1. Wave gauge w10 gave a few spurious results, and was not included in the analysis. For consistency, we use the same measure in the numerical simulations.

Reduced data. Steady-state values of the free-surface elevation are taken from steady parts of the time-series. The simulated time-series were only stationary until the re-reflected waves reached the position of each wave gauge, but we found that the free-surface elevation at w11 and w12 were steady in the time-interval $t = 25 - 35$s. This was a matter

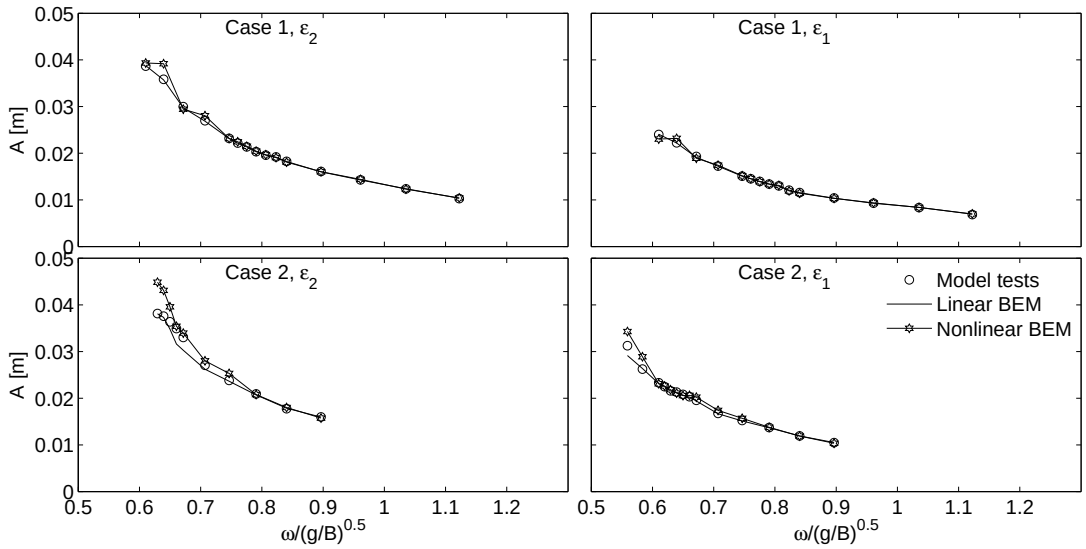

Figure 10.3: Wave amplitude $A = H/2$ from wave calibration runs. H is taken as the average of the trough-to-crest heights of w8, w11 and w12.

of visual inspection combined with arguments using the group velocity C_g. The value of H_g is in this way estimated using 3 - 7 periods, depending on the wave period. The mean undisturbed waveheight H was taken as the crest-to-trough distances taken from the wave calibration runs, using the same time interval for consistency.

In Figures 10.3 - 10.5 there are four sub-plots in each of the figures, representing Case 1 by the two upper and Case 2 by the two lower plots. The left plots represent the highest wave steepness ϵ_2, while the right plots the lowest wave steepness ϵ_1.

In Figure 10.3, the wave amplitude A is presented. As explained earlier, $A = H/2$. In the model tests, the wave gauges were positioned equally in the wave calibration tests and the tests with ship section and terminal. The waveheight H is taken as the mean of those from w8, w11 and w12 from the wave calibration runs. The wave amplitude from the nonlinear simulations compares well with those from the model tests, except for some of the longest waves. The discrepancies might be due to beach reflections in both the physical and the nonlinear wavetank. The nonlinear wavetank length was in the wave calibration tests not the same as the physical wavetank length, so reflections would influence the solution differently in the measured and simulated wavetanks.

In Figure 10.4, the terminal gap elevation A_g is presented. We note that some data points seem to be "missing" in the lower left plot for Case 2 with ϵ_2. This is due to the following. First, the model tests could not be run for lower wave frequencies than those shown due to limitations in the wave paddle stroke S. The "missing" nonlinear simulations broke down before steady-state was reached due to entanglement of the free-surface elements near the sharpest peaks of the free surface up-stream of the ship. The break-down may perhaps be avoided by using a re-gridding algorithm of the whole free surface, but this has not been done in this work. We mention that this sharp crest was denoted "fountain" by Buchner et al. (2004), something they observed during model testing of a ship by a terminal in shallow water. The same fountain effect was observed during our model testing.

In Figure 10.5, the nondimensional terminal gap amplitude A_g/A is presented. The

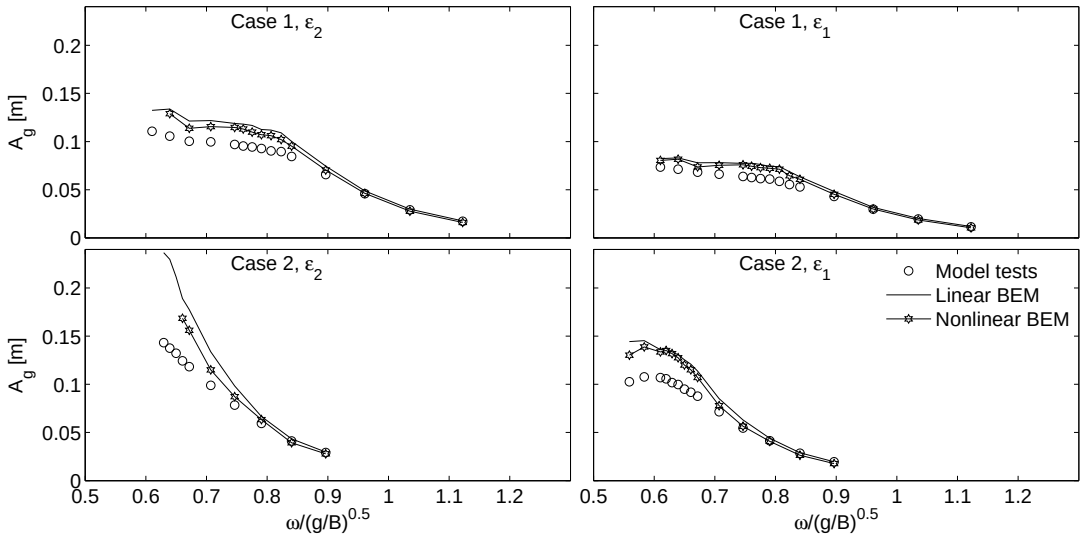

Figure 10.4: Piston-mode amplitude $A_g = H_g/2$. H_g is taken as the average of the trough-to-crest heights of w11 and w12.

four main observed features are the following. First, the linear results over-predict around the resonance frequency, with predicted nondimensional terminal gap amplitudes $A_g/A \simeq 6$ in both Cases 1 and 2 while the ratio from the model tests lie between four and five. Second, the nonlinear results in general lie between the measured and linear, also over-predicting with respect to the measured values. Third, there is close to no effect of steepness in Case 1 with the largest water depth $h/B = 0.625$, while there seemingly is an effect in the Case 2 with the smallest water depth $h/B = 0.43$. This applies to both the experiments and the nonlinear simulations. Last, for the frequencies higher than resonance the measured and simulated results compare well, as expected, while for lower frequencies some discrepancies are observed. We discuss these discrepancies in the following.

The fact that linear theory over-predicted was expected, but the nature of the nonlinear behaviour was not known a priori. From Figure 10.5 we can see that there is an effect of the nonlinearity parameter H/h, while there is seemingly no effect of the other nonlinearity parameter, the wave steepness $\epsilon = H_0/\lambda_0$. The results from the nonlinear simulations leave the linear to an appreciable degree when H/h is higher than, say, $1/6$. This may be seen from a combination of the lower left sub-plots of Figures 10.4 and 10.5. In the latter figure, the discrepancy between the linear and nonlinear behaviour is non-negligible for $\omega/\sqrt{g/B} \lesssim 0.7$. For these wave frequencies, we see from Figure 10.4 that the waveheight $H = 2A \gtrsim 0.05$. With the water depth $h = 0.29$m, this means $H/h \gtrsim 1/6$. This is about the limit when we start observing significant nonlinearities in the external fluid kinematics as illustrated above in connection with the time-series and snapshots.

The fact that the nonlinear results are in general closer to the linear than to the measured around resonance means that the majority of the discrepancy between measured and linear values are explained by other effects than those associated with the nonlinear free-surface conditions, assuming that the simulated results are accurate. We propose four candidates. First, flow separation from the ship section bilges did probably occur. Second, the slight flexing of the side of the ship section in the model tests as was observed

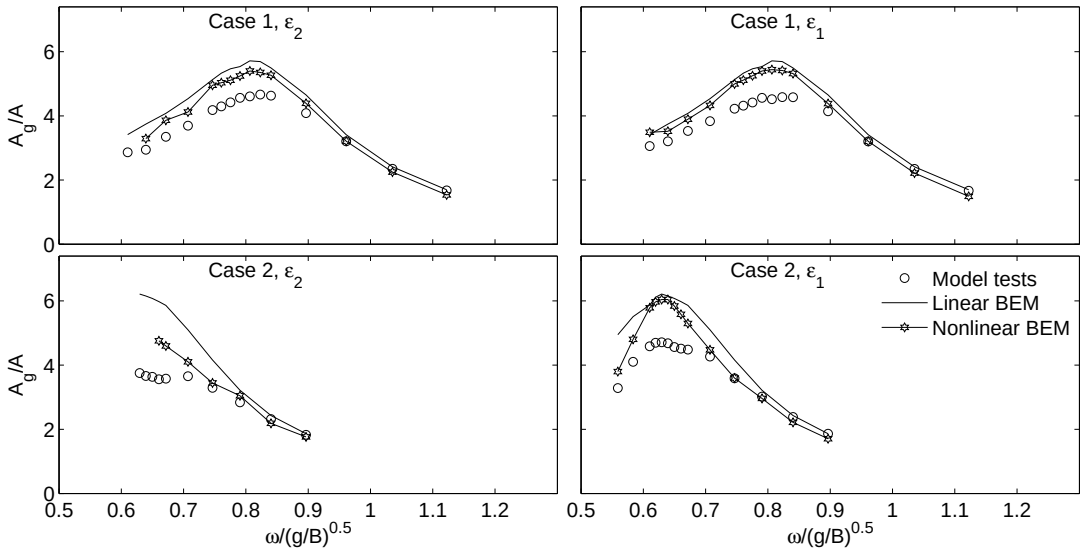

Figure 10.5: Nondimensional piston-mode amplitude A_g/A.

is a candidate. Third, the leakage between the glass wall and ship section might have been a contributor. Last, wave reflections was most probably of some importance for the longest waves. The three last candidates represent bias errors in the model tests. This illustrates the importance of discussing this matter as we did in the presentation of the model tests. The leakage effect and possible wave reflections are not discussed further here. We do, however, discuss the two other.

In the present model tests the corners were rounded in order to avoid flow separation as far as possible. However, using $2r = 0.12$m as a characteristic length, $U_m = \pi H_g/T$ as the maximum fluid velocity and a kinematic viscosity of $\nu = 10^{-6}$ we get e.g. near resonance in Case 1 ($T = 2$s) that the Keulegan-Carpenter number $KC = U_m T/2r \simeq 5$. Futher, the Reynolds number $R_n = 2rU_m/\nu \simeq 4 \cdot 10^4$ and $\beta = Rn/KC \simeq 7000$. For these conditions flow separation probably occurs, although it is not easily observable, as discussed in Faltinsen (1990) (see discussion on p. 229). The flow will separate for $KC \gtrsim 1$, but the separated flow will not break strongly away from the body as visible vortices unless $KC \gtrsim 5$. So, even though we did not observe vortices breaking away from the rounded ship bilge, some contribution to the discrepancies may nevertheless have been due to flow separation, due to the achieved KC-numbers. If flow separation was the main contributor, however, there should have been a more clear effect of wave steepness than that observed for Case 2 in the two upper plots.

We therefore speculate that the observed slight flexing of the ship side is the main contributor. We base this on the fact that the piston-mode amplitudes A_g around resonance were higher in Case 2 than in Case 1, around 50 - 60% higher. This was due to the chosen fixed wave steepness and longer waves in Case 2. The ability to indent the ship section side was therefore about twice as large in the Case 2 than in Case 1. Referring to the discussion on the rather significant motion reduction effect of flexing walls in connection with the study on a moored ship section in Section 10.3, we find this a plausible cause of the observed discrepancies.

Last, we briefly present in Figure 10.6 (left plot) results from Case 3 with the smaller terminal gap width $b/B = 0.17$, and in Figure 10.6 (right plot) some results from the

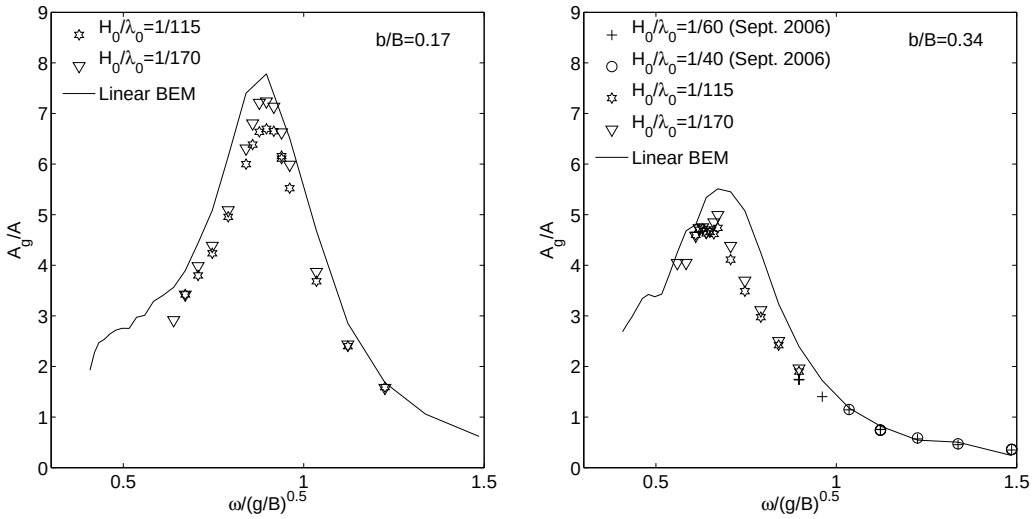

Figure 10.6: Additional results from the study of a fixed ship section. Left: Half the terminal gap width $b/B = 0.17$ relative to that presented in Figure 10.5 (Case 3). Right: Results from September 2006 model tests as indicated in the legend. The other results from the November 2006 tests as presented in Figure 10.5.

September 2006 model tests with $b/B = 0.34$, overlapping those in the November 2006 tests. We see from the left plot of the figure that the piston-mode amplitude is higher in Case 3 relative to those in Cases 1 and 2. We note that in Case 3, the terminal gap width b is half that of Cases 1 and 2. Linear theory predicts piston-mode amplitudes of $A_g/A \simeq 8$, while we measure about 6.5 - 7.5. Nonlinear simulations were not performed for Case 3. There seems to be a slight effect of wave steepness, but quite small. The terminal gap amplitudes around resonance were (in dimensional form) smaller in Case 3 than in Cases 1 and 2 due to shorter wavelengths. The ability to indent the ship section side was therefore smaller. This seems consistent with a somewhat less over-prediction by linear theory in this case, and supports our suspicion of the flexing being the main contributor to the discrepancy.

In the right part of Figure 10.6 nondimensional terminal gap amplitude from the September 2006 tests for higher wave frequencies than the resonance frequency is presented and compared with the slightly overlapping November 2006 tests. The water depht is $h/B = 0.45$. We note that the results from the November tests are the same as those presented in the lower parts of Figure 10.5. The reason we did not include the results from the September 2006 tests there was that the wave steepness was higher, being $H_0/\lambda_0 = 1/40$ and $H_0/\lambda_0 = 1/60$, and the incoming waves were subject to a 1:30 sloping bottom. The behaviour seems, however, in general to be consistent in the two sets of model tests. For the one overlapping wave frequency ($\omega/\sqrt{g/B} \simeq 0.897$), the nondimensional amplitude is about 11% higher in the November tests. This is probably due to the smaller wave steepness.

10.1.3 Summary of the study

We summarize the present study as follows. The study involved a fixed ship section by a bottom mounted terminal. The ship section had rounded corners in order to avoid flow separation. The ship section and terminal were subjected to incoming shallow water waves. The wave periods T were chosen to be around the piston-mode resonance period T_p. We varied the water depth h, the terminal gap width b and the wave steepness H/λ. The studied cases are summarized in Table 9.3. The primary goal was to study the piston-mode amplitude around piston-mode resonance. A secondary goal was to study the effects of the shallow water wave conditions.

The main results from the studied cases are briefly summarized as:

- The present linear simulations predicted piston-mode amplitudes $A_g/A \simeq 6 - 8$ at the piston-mode resonance period T_p.
- Piston-mode amplitudes in the model tests were around resonance 10 - 30% lower than that predicted by linear theory.
- The present nonlinear simulations predicted values in between that predicted by the linear simulations and measured in the model tests.
- Shallow water wave effects seemed to slightly affect the piston-mode amplitude for large H/h, say $H/h \gtrsim 1/6$ in the investigated cases.
- Flexing of the ship side probably introduced a reduction of the piston-mode motion in the model tests. We believe this caused a major part of the discrepancies.
- Flow separation is thought not to have been important in the present study.

There seemed to be a relatively small effect on the piston-mode amplitude due to nonlinearity associated with the free-surface conditions, despite the rather nonlinear behaviour of the external wave field in the shallow water conditions. We believe that for the most part, the discrepancies between measurements and nonlinear simulations are explained by flexing of the ship sides rather than by flow separation from the rounded bilges.

10.2 Forced heave of a ship section by a bottom mounted terminal

Our second main study involves forced heave motion of a ship section with sharp bilges by a bottom mounted terminal in deep water conditions. The ship section is forced at periods around the piston-mode resonance period T_p. Although the deep water conditions are not realistic regarding offshore LNG terminals, the study is directly relevant to the problem. We investigate the discrepancies between the piston-mode amplitude predicted by linear theory and that observed in experiments. The experiments we refer to were carried out to investigate resonant fluid behaviour in moonpools, and originally reported in Faltinsen et al. (2007). They also presented a newly developed linear theory for this problem. The solution procedure involves domain decomposition and Green functions distributed along

the so-called Neumann traces defining the fictitious boundaries of each domain. We use this theory to verify the present results from application of our linear wavetank.

In the present section we present results from our numerical simulations using both the linear wavetank and the nonlinear wavetank, where in the former case, both with and without in- and out-flow of boundary layers, and for the latter both with and without flow separation from the ship section bilges. The numerical results are compared to the above mentioned linear theory and experiments. All results presented in the present section are previously published in Kristiansen and Faltinsen (2008). There, the experimental data were re-analyzed and reflections in the wave flume were found to cause some surprising results in some cases. This discussion is also found in Section 9.4. The results include piston-mode amplitude, A_g, the "far-field" amplitude, denoted by A_f, as well as phases of the free-surface elevation relative to the heave motion.

We proceed with a description of the parameters used in the present numerical work, and next present and discuss the results of the study.

Table 10.3: Numerical parameters in the simulations of forced heave of a ship section by a bottom mounted terminal. Initial number of elements on the different parts of the boundary S.

Free surface (external + terminal gap)	$N_F = 184 + 16 = 200$
Ship section (side + bottom + side)	$N_B = 30 + 60 + 30 = 120$
Bottom of wavetank	$N_{BOT} = 30$
Terminal	$N_{TERM} = 40$
Far end of damping zone	$N_{WM} = 4$
Tank length	$L \simeq 47B$
Numerical beach length	$L_d = L/2$
Dissipation parameter	$\nu_{max} = 0.4$
No. of time-steps per period	$N_P = 120$ or 600

10.2.1 Parameters in the numerical simulations

The exact geometry of the physical wave flume was not reproduced in this case as it was in the study of the fixed ship described in the previous section. Only one ship section was modelled due to symmetry of the flow under forced heave in otherwise calm conditions. The terminal gap width b was thus half the distance between the two hulls in the model tests. The tank length in the numerical work was $L/B \simeq 47$. The gridding and time-step was similar for all tests and both the linear and nonlinear wavetanks, with cosine spacing for refinement near the intersections between the free surface and solid boundaries, and in particular near the convex corners of the body. The ratio of the element lengths on the mid-part of the body to those at the corners were 200 in the simulations with flow separation, while 25 in the other simulations. A close-up of the body and its near vicinity is shown in Figure 10.7. As described earlier, dynamic re-gridding of the geometry was used. The inital number of elements, numerical beach parameters and temporal discretization is presented in Table 10.3. The number of time-steps per period was $N_p = 120$ in simulations without flow separation. In the simulations with flow separation this was changed to $N_p = 600$ at the onset of the free shear layer. We chose to initiate the flow separation at minimum ambient velocity during the fourth period. This means that the flow separation

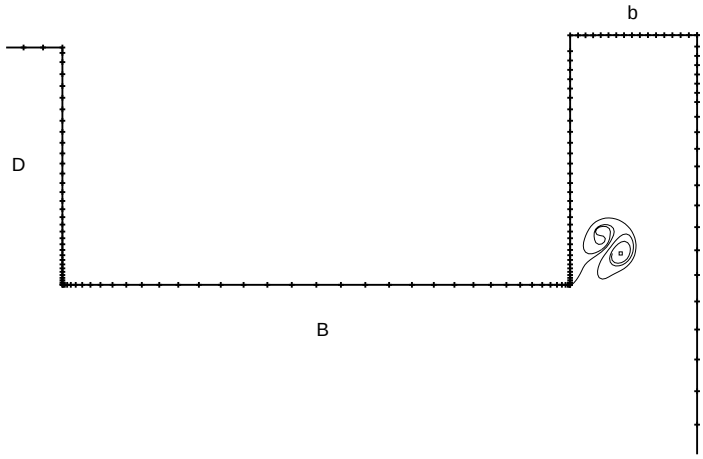

Figure 10.7: An example of discretization of the boundary with refined grid near the ship section bilges.

inititated when the piston-mode elevation was at its maximum during the fourth period. In practice this meant after approximately 3.75 periods. In the simulations with the nonlinear numerical wavetank the forced heave motion of the ship section was as recorded during the model tests, whereas in the linear simulations simply a linear ramp of the first two periods were used. Running 20 - 30 wave periods on a 2.4GHz computer took for the simulations with free shear layer typically 1.5 hours, the nonlinear simulations without free shear layer about 20 minutes and the linear simulations about 10 minutes.

In some cases the simulations with free shear layer broke down during the first critical period, but the majority of the runs finalized, in particular those around the natural period with appreciable gap amplitude. Flow separation was suppressed at the corner of the ship opposite to the moonpool. Although the computer code may handle an arbitrary number of free shear layers simultaneously, the simulation easily breaks down if the ambient velocity is very low. Small induced vorticity in the free shear layer will then result in devastating short wave instabilities. We ran one test successfully with separation at both corners, but the effect of the second free shear layer was negligible both on the piston-mode and far-field behaviour and we therefore decided not to include flow separation there.

10.2.2 Results - Piston-mode resonance due to forced heave

Three different cases were considered. The draft D, terminal gap width b and the amplitude of the forced motion $\epsilon = \eta_{3a}/B$ were varied. The specifics are given in Table 9.8, where the three cases are denoted Case I - III.

In Cases I and II, the piston-mode motion is represented by the mean signal of w1 - w5, whereas in Case III, where the gap width is doubled, and the array w1 - w5 is thought not to represent the piston mode as well, only the signal from w3 is used. For consistency, the results from theory and simulations are taken as the averaged amplitude across the moonpool in Cases I and II, while that at the center-line of the moonpool (or on the terminal wall in our terminology) in Case III. The phase of a signal is computed by identifying the time of zero up-crossing, t_0, in a steady part of the time-series yielding

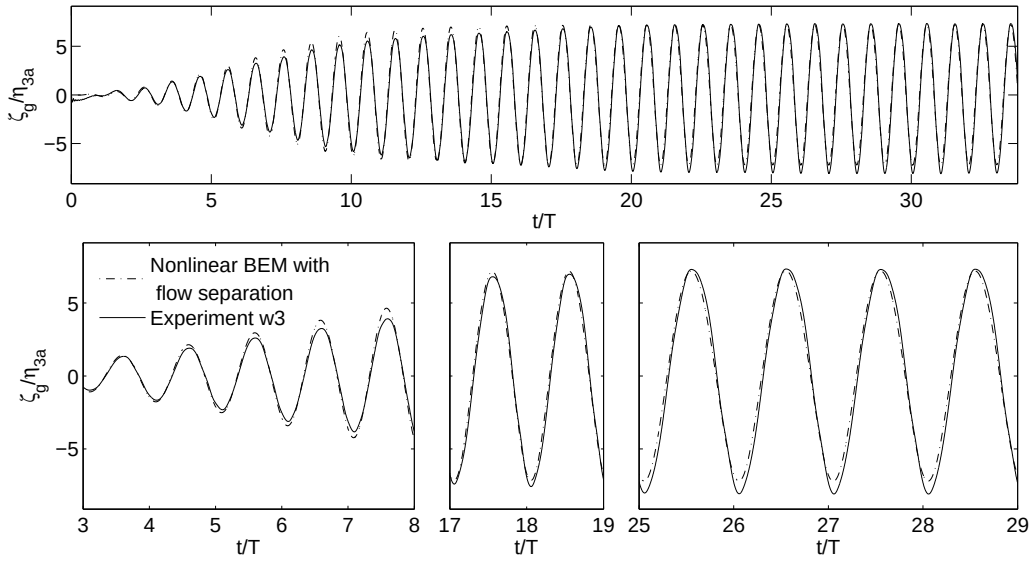

Figure 10.8: Time-series of the piston-mode elevation ζ_g from Case I with $\epsilon_2 = \eta_{3a}/B = 1/72$ and $\omega/\sqrt{g/B} \simeq 1.017$. Experiments and nonlinear simulations where flow separation is included. The recorded ship heave motion was used as input to the numerical model. The onset of the free shear layer is after 3.775 periods.

the phase $\theta = \omega\Delta t_0$, where Δt_0 is the time difference between t_0 for the signal and heave motion.

Time-series. An example of comparison between experimental and simulated piston-mode time-series for a test near resonance in Case I with the highest forcing amplitude $\epsilon_2 = \eta_{3a}/B = 1/72$ is presented in Figure 10.8. The time of onset of the free shear layer is in this test $t/T = 3.775$. The steady-state results were found not to be sensitive to the time of onset, but a certain flow magnitude is required in order for the model to be valid, i.e. the Reynold's number to be sufficiently large. The simulation over-predicts in the beginning, which is natural as the onset of the free shear layer is delayed, whereas in reality the flow separates immediately. The two time-series converge fairly well after a while (lower middle plot). Some time after this a modulation of the trough in the experimental time-series occurs (lower right plot), whereas not in the simulations. The modulations observed there occur just after $t = T_{r2} \simeq 19T$ (see upper sub-plot), and we want to elaborate somewhat on this phenomenon, which is most likely explained by slight reflections in the flume, as discussed in Section 9.4. We mentioned there that the reflections were of smaller relative importance in Cases I and II than in Case III. The argumentation for this is as follows. In the two examples in the lower part of Figure 9.16, taken from Case III, the amplitudes of the radiated waves A_f are in the same order as the piston-mode amplitude A_g, more specifically $A_f/A_g \simeq 2$. For the tests in Case III we have in general that $A_f/A_g \simeq 2-3$. For Case I and II, however, this ratio is much larger around resonance, it is $A_f/A_g \simeq 7-10$. Therefore the potential of the reflections to affect the fluid behaviour in the moonpool is in general higher in Case III than in Cases I and II. In Figures 9.16(a) and (b) examples near resonance are presented from Case I and Case II respectively.

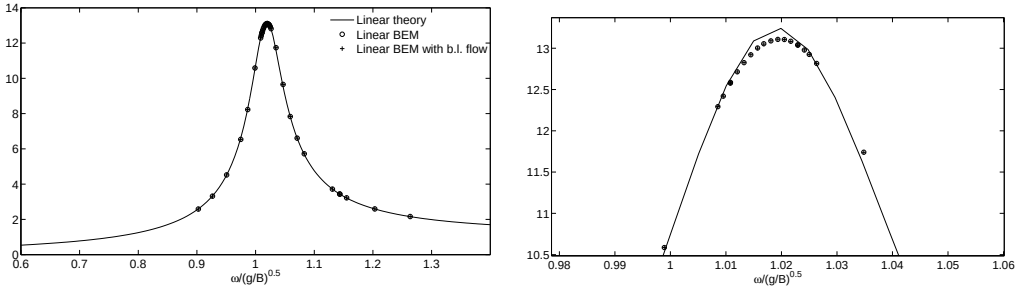

Figure 10.9: The effect of the boundary layer on the nondimensional piston amplitude is negligible. To the right is a close-up around the resonance frequency. Case I with ϵ_2.

Reduced data. With this discussion in mind, we choose to present the nondimensional amplitudes by means of "error bars", with one end being the value acquired from the steady-state part of the time-series indicated by the solid vertical bars in Figure 9.16, and the other end the value acquired using the time window extending from one period before and until one period after $t = T_{r2}$. This certainly is not a measure of measurement accuracy or a range over where the "real" values would reside. It is not any rigorous attempt to rule out the bias introduced by reflections, simply because this would not be possible. However, it gives a reasonable range for the values, and the reader should keep the above discussion in mind when using the data. Choosing the latter end of the error bar was a matter of observations from inspection of figures like Figure 9.16 for all tests, revealing a tendency that the system is closing in on steady-state around $t = T_{r2}$ in most of the tests. This means that we to a certain extent rule out reflections from the beach side (cf. Figure 9.15), but not reflections from the wavemaker side and we neglect in a way the fact that steady-state in general is not perfectly reached.

We stress that, as we have argued, reflections most likely have not affected the results for Case I and II to a very high degree due to the small amplitudes of the radiated waves.

As in the work by Faltinsen et al. (2007) and Kristiansen and Faltinsen (2008), we consider the nondimensional piston-mode amplitudes A_g/η_{3a}, the "far-field" amplitudes A_f/η_{3a} at the position of w11 (see Figure 9.15), the phases as well as the added mass and damping.

We first discuss the results from the linearized problem. Results from present linear, inviscid simulations and from the theory are presented and compared with respect to free-surface kinematics in Figures 10.10 - 10.14. Added mass and damping coefficients are presented in Figures 10.15 - 10.17. The theoretical results are represented by solid curves, while the present linear simulations are represented by markers. The agreement between the present linear simulations and the linear theory is obvious for both the piston-mode and far-field amplitudes as well as the added mass and damping. This serves as a verification of the basic linear wavetank on which the other numerical wavetanks are built. We note the occurrence of negative added mass which is typical of resonant behaviour. The added mass and damping coefficients are calculated from the present linear simulations by numerical evaluation of the expressions

$$A_{kj} = -\frac{\int_0^T F_{kj}\,\ddot{\eta}_j\,\mathrm{d}t}{\int_0^T (\ddot{\eta}_j)^2\,\mathrm{d}t}, \quad B_{kj} = -\frac{\int_0^T F_{kj}\,\dot{\eta}_j\,\mathrm{d}t}{\int_0^T (\dot{\eta}_j)^2\,\mathrm{d}t}, \tag{10.1}$$

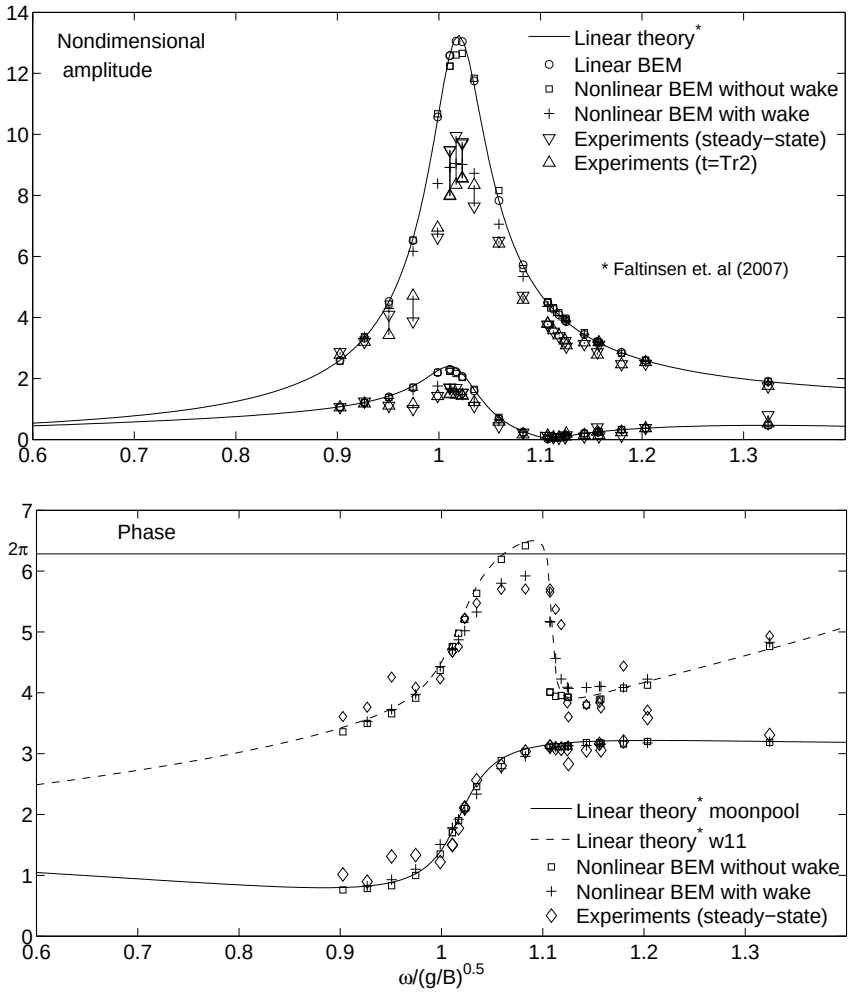

Figure 10.10: Case I ($B/D = 2$ and $b/B = 0.25$) with forcing amplitude $\epsilon_1 = \eta_{3a}/B = 1/144$. Upper: Nondimensional amplitude of the piston mode (average of w1 - w5) and "far-field" (at w11). Lower: Phases. The two sets of experimental values are connected with vertical bars. These bars should not be interpreted directly as error bars, cf. the discussion.

where $F_{kj} = \rho \int_{S_B} \varphi_t \, n_k \, \mathrm{d}s$ is the part of the force due to the unsteady term in the Bernoulli equation, φ_t, in the k'th direction due to forced motion in the j'th degree of freedom and n_k is the corresponding component of the normal vector. Here, S_B is the fixed mean boundary of the ship section. φ_t is estimated by numerical differentiation of φ, in the present taken as $(\varphi^{n+1} - \varphi^n)/\Delta t$, where n is main time-step number. The expressions in (10.1) appear directly from the definition of added mass and damping, i.e. $F_{kj} = -A_{kj}\ddot{\eta}_j - B_{kj}\dot{\eta}_j$, upon multiplicating this by $\ddot{\eta}_j$ or $\dot{\eta}_j$, integrating over an integer number of wave periods and using the orthogonality properties of cos and sin. We have during the present work integrated over 5 - 10 periods. The added mass and damping are in the present nondimensionalized as $A_{33}/(\rho B^2)$ and $B_{33}/(\rho B^2\sqrt{g/B})$.

In Figure 10.9 a selection of results from the linear simulations with in- and outflow of the boundary layers, with Case I arbitrarily chosen, is compared to "standard" linear theory. The data points are close to indistinguishable, hence the damping due to

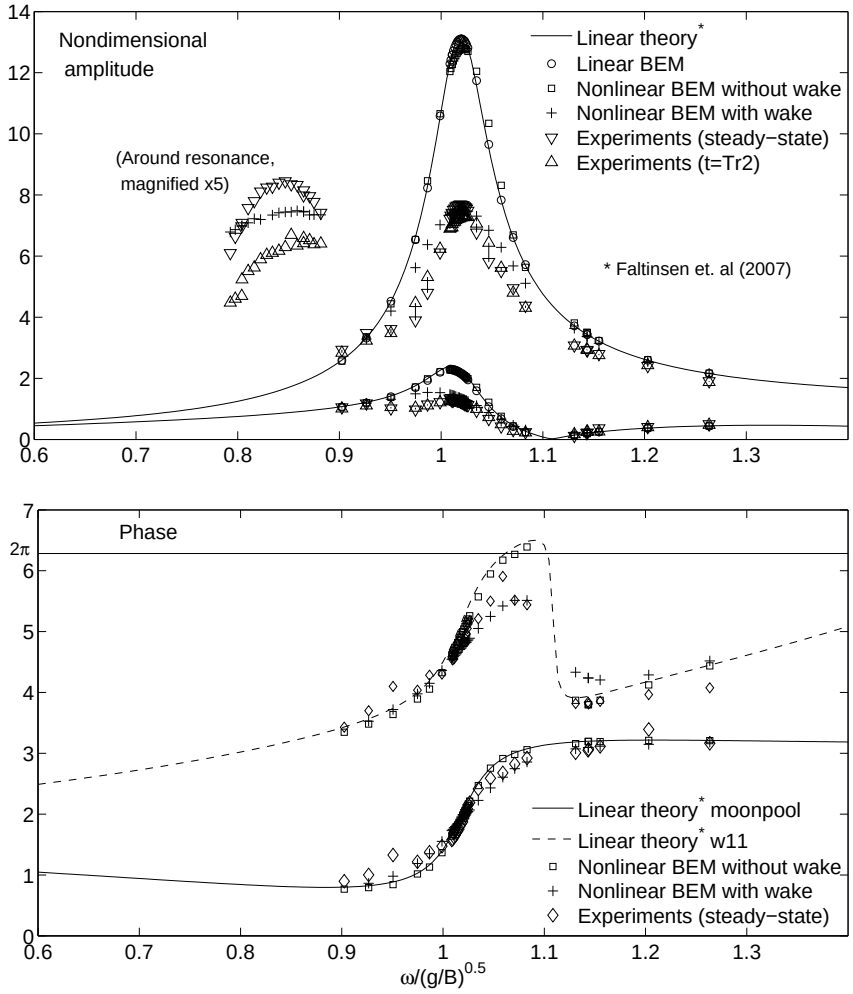

Figure 10.11: Same as in Figure 10.10, but for forcing amplitude $\epsilon_2 = \eta_{3a}/B = 1/72$.

(attached) boundary layer effects is negligible to all practical purposes, and will not be further considered in the present work.

Hereafter, we focus on the effects on the system associated with the free-surface conditions and those associated with the separated flow, with emphasis on the latter. These results are also presented in Figures 10.10 - 10.14. The discussion above on the wave reflections in the measurements must be kept in mind, but apart from Case III, one should not over-emphasize the effect this have had on the experimental results.

In short, from the figures our simulations clearly suggest that separation has a significant damping effect on both the piston-mode and far-field amplitudes. Further, our simulations without flow separation suggest that the nonlinearity associated with the free surface is quite insignificant. Believing the numerical results, and comparing to the experimental data, one may draw the main conclusion that flow separation at the corner of the ship section explains by far the major part of the discrepancies between the linear theory and the experimental results.

The results from Case I are presented in Figures 10.10 and 10.11, with the smallest and largest forcing amplitude $\epsilon = \eta_{3a}/B$ in the two figures respectively. The response curve of

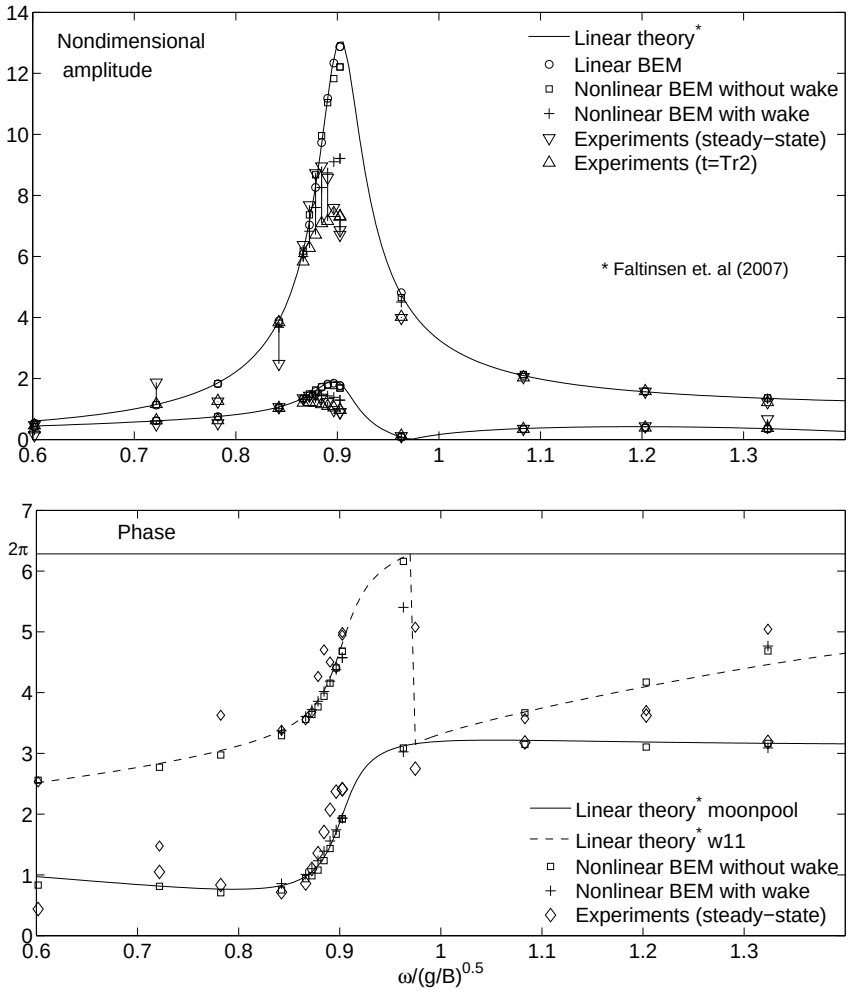

Figure 10.12: Case II ($B/D = 1.33$ and $b/B = 0.25$) with forcing amplitude $\epsilon_1 = \eta_{3a}/B = 1/144$. Upper: Nondimensional amplitude of the piston mode (average of w1 - w5) and "far-field" (at w11). Lower: Phases. The two sets of experimental values are connected with vertical bars. These bars should not be interpreted directly as error bars, cf. the discussion.

the piston-mode amplitude is somewhat narrower in the experiments than that estimated by the numerical results for both forcing amplitudes. The results are in good agreement around and far from resonance, but differ somewhat for frequencies in the vicinity of resonance. The same holds for the far-field amplitudes. The rapid phase shift around resonance is somewhat relaxed by the separation effect, as seen from the right sub-plots. The phase of the radiated wave is more affected by the separation than the phase of the free-surface elevation in the terminal gap, and there is a clear effect of forcing amplitude, as seen for the frequencies just above the resonance frequency. The phases of the radiated waves predicted by the simulations with separation for $\omega/\sqrt{g/B} \simeq 1.15$ differ somewhat from the linear theory, despite the seemingly small effect of the separation judging from the piston-mode amplitude. In these tests the amplitude of the radiated waves are very small, and perhaps the numerical modelling of these small waves were not completely

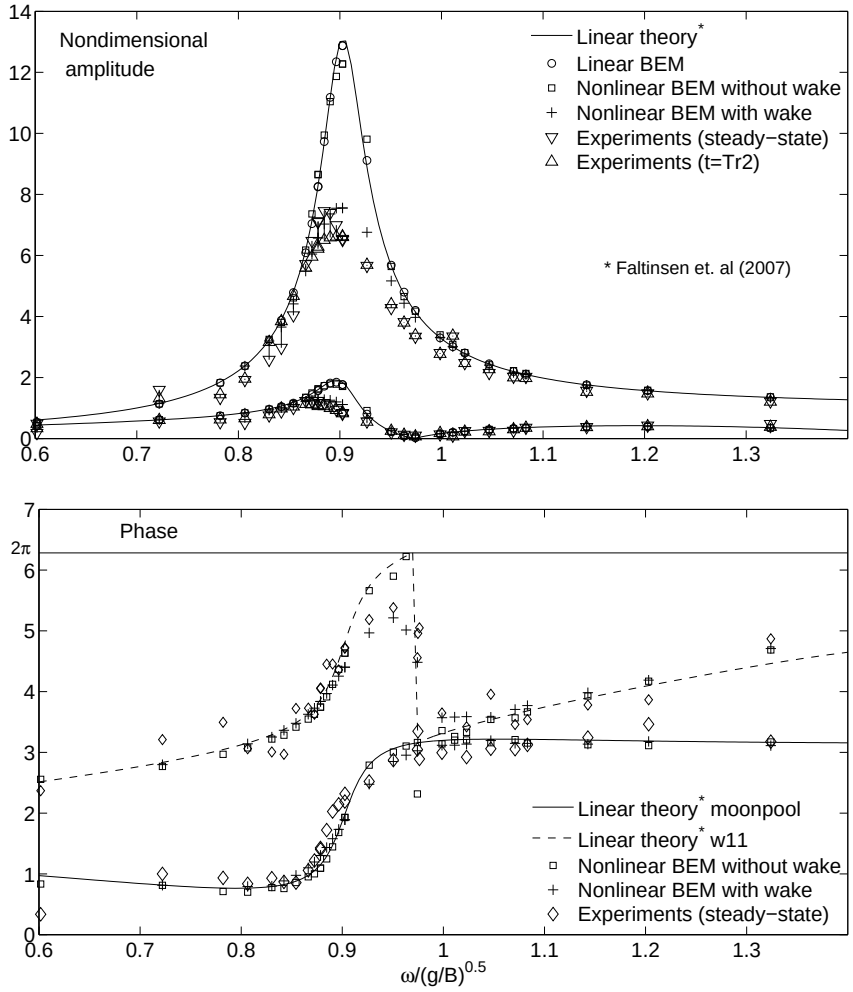

Figure 10.13: Same as in Figure 10.12, but for forcing amplitude $\epsilon_2 = \eta_{3a}/B = 1/72$.

successful. For the main part otherwise, the trends of the phases from experiments and simulated results are in good agreement.

We remark that an alternative to Equation (10.1) is to calculate the added mass and damping from F_3 using phases. Since the agreement between the added mass and damping coefficients from the present linear simulations and the theory is in general good, implicitly, the phasing is also good. Therefore, the phase from the linear simulations is not presented in Figures 10.10 - 10.14, although agreement has been checked by the author.

The results from Case II are presented in Figures 10.12 and 10.13, again with the smallest and largest forcing amplitude $\epsilon = \eta_{3a}/B$ in the two figures respectively. The simulated amplitudes and phases exhibit the same qualitative behaviour in Case II as in Case I. However, the experimental results from Case II show a slightly different behaviour to those in Case I. The response curve of the piston-mode amplitude in the experiments seemingly inhibits a shift to the left (lower frequency), whereas that from the simulations does not. We believe the shift in the experimental data is a bias error caused by the reflections in the wave flume, as the shift is towards the same wave frequency as where we observe strange behaviour in Case III as will be shown shortly. The frequency we speak

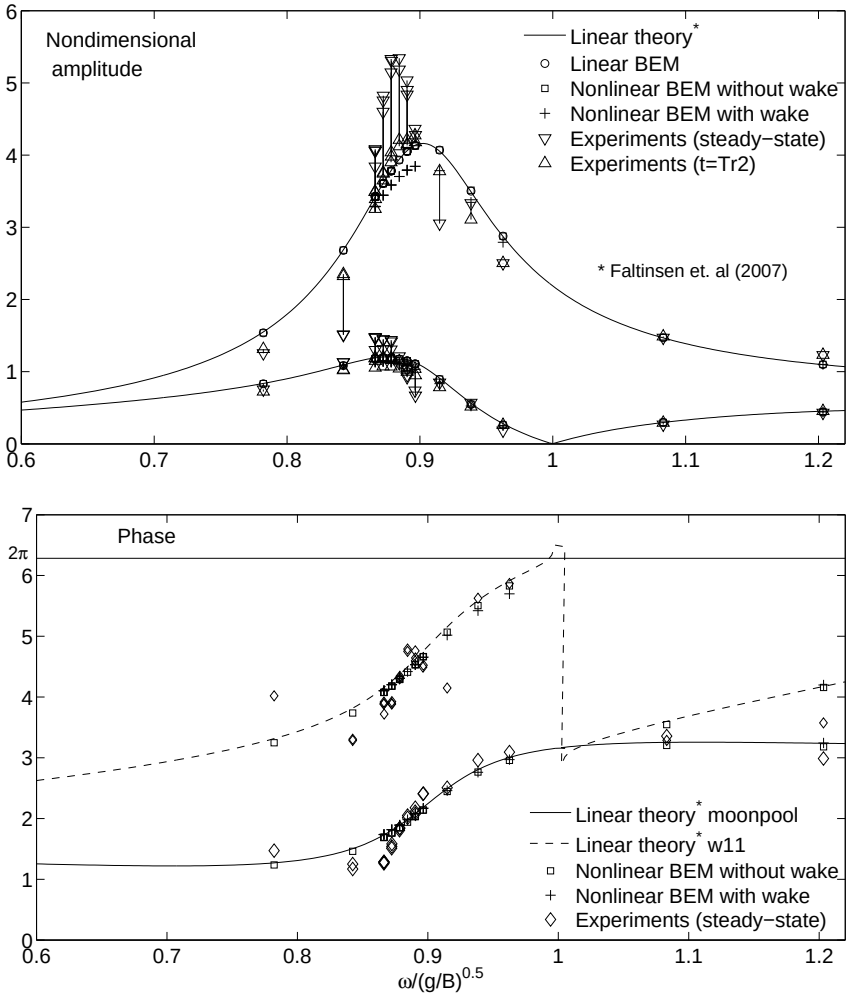

Figure 10.14: Case III ($B/D = 2$ and $b/B = 0.5$) (with forcing amplitude $\epsilon_1 = \eta_{3a}/B = 1/144$). Upper: Nondimensional amplitude of the piston mode (w3 only) and "far-field" (at w11). Lower: Phases. The two sets of experimental values are connected with vertical bars. These bars should not be interpreted directly as error bars, cf. the discussion.

of is $\omega/\sqrt{g/B} \simeq 0.87$. The simulations in general predict slightly higher response than that measured near and above the resonance frequency. The same holds for the far-field amplitudes. As for the phases, the rapid change of phase around resonance of the terminal gap motion is also somewhat shifted to the left in the experiments, whereas not in the simulations, and above the resonance frequency, the measured phases are somewhat lower than those simulated, although showing the same trend relative to linear theory.

The results from Case III are presented in Figure 10.14. In Case III the behaviour of the simulations are similar to that in Cases I and II, but less pronounced, and one may say that the behaviour is close to linear. The effect of flow separation is according to our results very modest in this case. The relatively large span in the "error-bar" for the majority of the presented model test results prohibits drawing conclusion about the correctness of the numerical results. However, the values taken from around $t = T_{r2}$

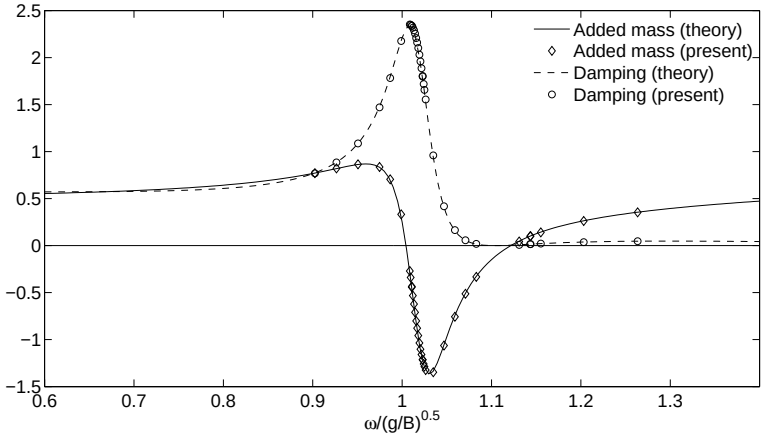

Figure 10.15: Heave added mass and damping of the ship section. The hydrodynamic coefficients are nondimensionalized as $A_{33}/(\rho B^2)$ and $B_{33}/(\rho B^2\sqrt{g/B})$. Case I ($B/D = 2$ and $b/B = 0.25$).

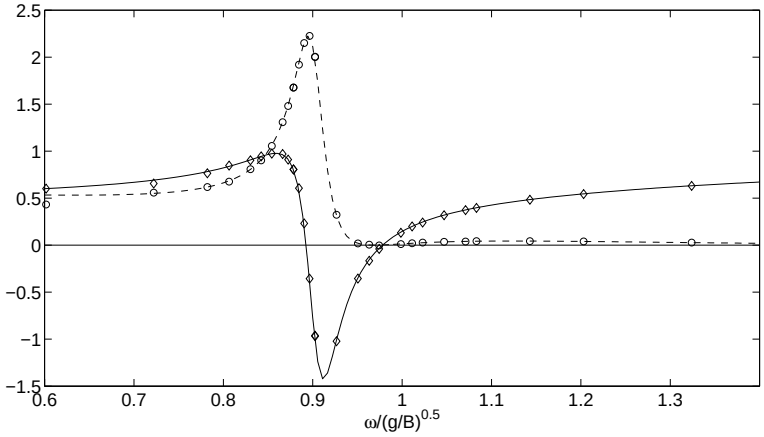

Figure 10.16: As Figure 10.15, but for Case II ($B/D = 1.33$ and $b/B = 0.25$).

in Figure 10.14 do suggest a relatively linear behaviour also in the model tests. It is not surprising that the behaviour is more linear in Cse III than in Cases I and II, when considering the vertical displacement relative to the horizontal dimensions. With double gap width b and approximately half the response A_g, we would expect less effect of flow separation in this case relative to the other two cases.

The relative difference between the linear theory and the present nonlinear simulations is presented in more detail in Figure 10.18. For the nonlinear simulations without free shear layer, results only from Cases I and III are included in order to avoid over-loading of the figure, but the behaviour in Case II is similar to that in Case I. Our simulations suggest that the altering of the piston-mode amplitude A_g as a result of the nonlinear free-surface conditions in Cases I and II is only around 3 - 4%, and is similar for both forcing amplitudes. We would in general expect an amplitude dependent behaviour, but this is small here, so perhaps this is due numerical inaccuracies. For the frequencies

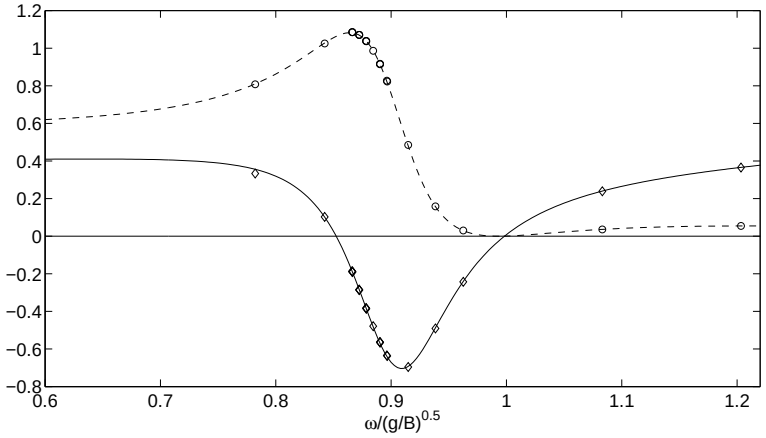

Figure 10.17: As Figure 10.15, but for Case III ($B/D = 2$ and $b/B = 0.5$).

just above resonance, or $\omega/\sqrt{g/B} \simeq 1.05$ the nonlinearity introduced by the free-surface conditions seem to amplify the response somewhat, meaning we see a slight broadening of the response. We see some amplitude dependency there. In Case III the nonlinearity introduced by the free-surface conditions gives no effect of practical interest. The effect of the flow separation is in Cases I and II a reduction of the amplitude around resonance of about 40% at the largest forcing amplitude and about 30% at the lowest forcing amplitude, both of which are quite significant. In Case III the effect of flow separation is a reduction near resonance of about 8% which is fairly moderate in comparison to the other two cases, meaning the response is significantly more linear.

10.2.3 Summary of the study

We summarize the present study as follows. The study involved forced heave of a ship section by a bottom mounted terminal. The ship section had sharp bilges in order to fix the separation point. The periods T of the forced heave motion were chosen to be around the piston-mode resonance period T_p. The goal was to study the effects from the nonlinear free-surface conditions, flow separation from the ship bilges as well as in- and out-flow of the boundary layers on the piston-mode amplitude around piston-mode resonance. We varied the ship section draft D, the terminal gap width b and amplitude of the forced heave motion η_{3a}. The studied cases are summarized in Table 9.8.

The main results from the present study are

- Linear theory (Faltinsen et al. (2007)) as well as the present linear simulations predicted A_g/η_{3a} ratios at resonance up to about 13 in Cases I and II and 4 in Case III.

- The corresponding ratios measured in the model tests were about 7 for the largest heave amplitude and about 8 for the smallest heave amplitude in Cases I and II. In Case III wave reflections made the data hard to interpret, but most probably, the ratios were very similar to those predicted by linear theory.

- The present nonlinear simulations without flow separation predicted A_g/η_{3a} ratios

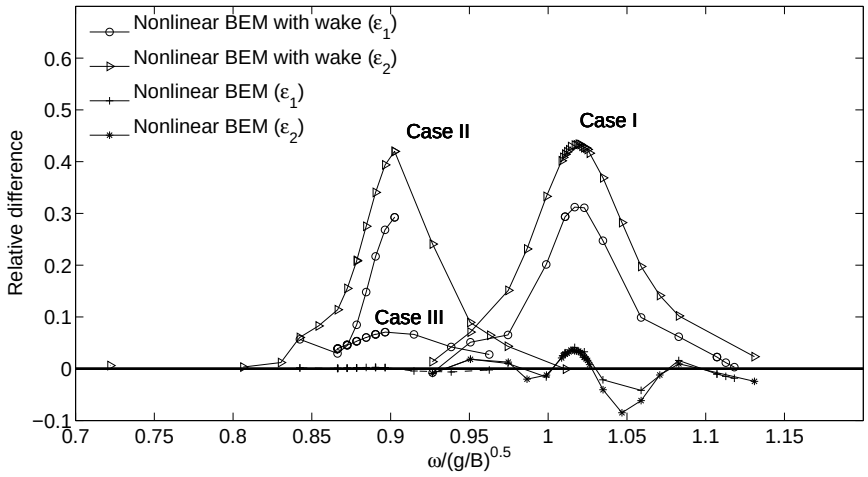

Figure 10.18: Relative difference between the piston-mode amplitude predicted by linear theory and simulations with and without flow separation. Only results from Cases I and III for simulations without free shear layer are presented for presentability.

very similar to the linear, so there were only very small effects of the nonlinear free-surface conditions.

- The present nonlinear simulations with flow separation predicted A_g/η_{3a} ratios very close to those measured in the model tests.
- The present linear simulations including in- and out-flow of the boundary layers showed that this effect was totally negligible in the present context.

The present study strongly indicates that flow separation is the main contributor to the observed discrepancies between linear theory and experiments around piston-mode resonance period T_p.

10.3 Moored ship by a bottom mounted terminal

Our third and last main study involves a ship section with sharp bilges moored by a bottom mounted terminal and subject to incoming waves in deep water conditions. Again, as in the study on forced heave as discussed in the previous section, the water depth is too large to give direct relevance to offshore LNG terminals. The study is nevertheless highly relevant and describes key features of the problem.

This last study is in a way more realistic than the previous two studies, as the ship section oscillates under influence from incoming waves, rather than being fixed or forced to move. An implication is that the problem is more demanding as the ship motion becomes a function of the surrounding fluid and vice versa. Despite the increased complexity we believe that through both the physical and numerical models, reliable and interesting results have been acquired. The model tests were described in Section 9.3. Also, some of the numerical work involving the linear wavetank was reported in Section 4.2, used there to exemplify the behaviour of the system. We proceed by reporting the relevant parameters of the numerical work before presenting the results.

10.3.1 Parameters in the numerical simulations

In the simulations with the nonlinear wavetank, both with and without flow separation, the exact geometry of the physical wave flume was modelled, including the initial tilt of the hinged wavemaker flap, and the flap motion was according to the flap signal in the model tests. The situation is described in Figure 9.8. For the linear wavetank, a tank length of $L = 18\lambda$ was used for each run, meaning the model test geometry was not reconstructed. Based on the group velocity C_g, re-reflections will occur after 108 periods with this tank length. In the linear simulations we attempted to reach closer to steady-state than in the runs with the nonlinear tank without flow separation where significant beating of the signals occurred. The beating behaviour in the numerical wavetanks is further discussed below. A sinusoidal signal with linear initial ramp of five periods was used in the linear case.

Typical spatial discretization as used in the present simulations is exemplified in the snapshots in Figure 10.19. The initial grid resolution is indicated by numbers in the figure. A somewhat finer body discretization was used in the simulations with flow separation than in those without. A finer resolution near the corners of separation was required in the former case. As in the study of forced heave, the element lengths followed a cosine squared distribution, with the length of the elements near the corner $1/200$ of those in the middle part of each body surface. On the free surface, a total of 300 elements was found adequate in order to propagate the waves properly, giving a number of elements per wavelength between 18 for the shortest waves of period $T = 0.6$s and 52 for the longest waves of period $T = 1.0$s. Around the resonance periods of $T \simeq 0.73\text{s} - 0.78\text{s}$ this was 25 to 33, which we have found represents both amplitude and group velocity well for such small-amplitude waves. Only two elements were used to describe the free surface in the terminal gap, reasoning that hardly any local disturbances in the terminal gap were observed in the experiments. The low resolution helped avoiding numerical instabilities related to frequent re-gridding of the free surface. The numerical instabilities are associated with the linear interpolation of the potential when splitting an element, which we suspect is too crude on the free surface. This was discussed in Section 5.5. The sway motion of the ship induced a slightly tilted terminal gap free-surface. This is, however, captured adequately using only two elements, and the chosen resolution therefore considered sufficient for our purpose. As before, re-gridding was applied in order to keep the resolution at a certain level, in particular along the ship side and terminal wall.

The number of time-steps was $N_p = 120$ per period in the runs without flow separation. In those with flow separation, 120 was used until the onset of separation, and 600 after the onset. The number 600 is considered near optimal in the sense that the free shear layer behaviour behaves well as discussed in detail earlier. The time of onset was in the present study chosen as the instant the free surface in the terminal gap, ζ_g, starts moving downwards from maximum positive elevation under the condition that $\zeta_g > 3A$, where A is the incoming wave amplitude. As mentioned in the previous section, the steady-state results are found not to be sensitive to the time of onset, but a certain flow magnitude is required in order for the model to be valid, i.e. the Reynold's number to be sufficiently large (cf. Section 2.2). The runs without free shear layer typically took two hours running 55 wave periods, while those with free shear layer about ten hours running 50 wave periods on a 2.4GHz processor. The additional CPU time in the latter was for the most part due to shorter time-step, but also due to somewhat higher resolution on the body as well as

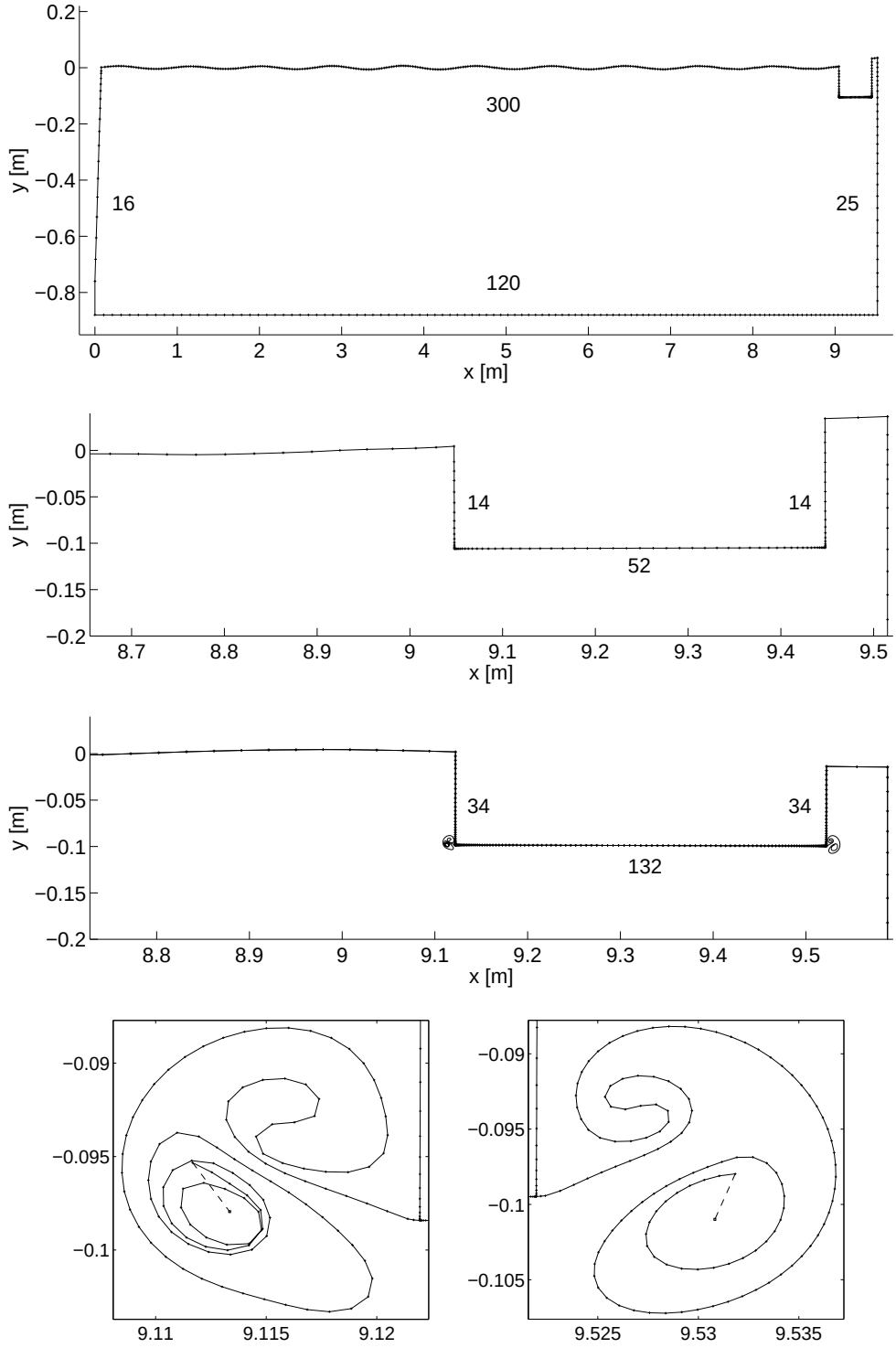

Figure 10.19: Snapshots from nonlinear wavetank runs. Top: Nonlinear wavetank without flow separation (not to scale). Second: Close-up of the ship section. Third: Close-up of body in a case with flow separation. Bottom: Close-up of the free shear layers emanating from the two bilges. Initial number of elements on each surface is indicated.

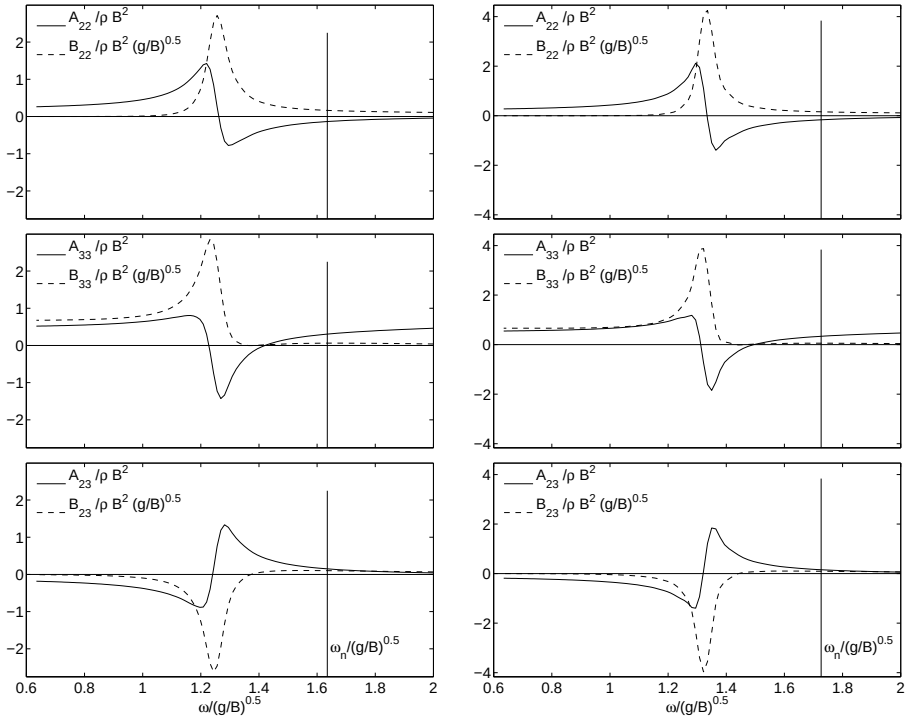

Figure 10.20: Added mass and damping calculated by using the linear wavetank. Left: Case A. Right: Case B.

additional CPU time associated with the free shear layer.

For the linear wavetank a similar spatial discretization as for the nonlinear wavetanks was used, except on the body only 36 elements, and along the bottom 80. The number of time-steps per period was 80. Each simulation took about about 25 minutes running 90 wave periods on a 2.4GHz processor.

Added mass and damping used to estimate resonance frequencies, were acquired from forced heave and sway simulations using the linear wavetank as described in the previous section. In these tests the resolution was somewhat lower, taken as in the forced heave study described in the previous section. The added mass and damping coefficients are presented as functions of nondimensional frequency in Figure 10.20. The coupled ship and piston-mode resonance frequency $\omega_n/\sqrt{g/B}$ is indicated for reference. Note the negative values of added mass and coupled damping coefficients.

For the highest steepness, only two runs with flow separation were successful. In all other runs breakdown occured about 2 - 6 periods after the onset of flow separation. The experience with forced heave was that if the simulations survived the first two periods it would proceed without breakdown. This is also the case with the present lowest steepness case. The reason for breakdown in the highest steepness case is probably associated with an appreciably larger body motion than in the forced heave simulations. The automatic simplification procedure was developed with small body motions. The breakdown is in general due to element crossing near the corner of separation. As discussed in the presentation of the automatic simplification procedure in Section 6.4, reducing the time-step was not feasible and therefore not done. More work is needed in order to provide a

more robust procedure, but this is left for future work.

Beating. As briefly mentioned above, the ship motion and terminal gap elevation as simulated with the nonlinear wavetank without flow separation and linear wavetank, for frequencies close to the natural frequency, exhibit pronounced beating due to the transient behaviour starting from initially calm conditions. This is a result of small damping. Therefore, steady-state is in general not reached within the time of simulation. Further, at resonance, the motion is still slightly increasing even after the 90 wave periods in the linear simulations. The condensed data presented in this study therefore must be seen as near steady-state values only. In order to extract data as consistent as possible, the average amplitude over one beating period, T_b, is used as long as the time-series are long enough. The beating period was taken as $T_b = 1/|f - f_n|$ where $f = 1/T$ and $f_n = 1/T_n$ with T_n calculated a priori. At the natural frequency the average amplitude of the last 10 periods were used. With the motion still increasing at resonance and with the beating behaviour as described, the values are not exactly the desired steady-state value, but do indicate reasonably well the steady-state values. In the model tests and simulations including flow separation, however, steady-state is reached in all cases.

10.3.2 Results - Coupled ship and piston-mode resonance

Two different cases were considered. The terminal gap width b and the wave steepness $\epsilon = H/\lambda$ were varied. The specifics are given in Table 9.5, where the three cases are denoted Case A and B.

In the following we present results from the above described numerical work as well as the model tests. We first present example time-series. Next, we present reduced data in terms of near steady-state amplitudes of the ship motion and piston-mode amplitude. These are nondimensionalized by the incoming wave amplitude and presented as function of the nondimensionalized wave frequency $\omega/\sqrt{g/B}$. The terminal gap amplitude is represented by the wave elevation 0.037m away from the terminal, taken in the model tests as $\zeta_g = 0.5(\mathrm{w6} + \mathrm{w7})$. What we refer to as terminal gap amplitude is thus not that averaged over the terminal gap width, but in all the considered tests, the free surface was observed to be near horizontal. This therefore represents the piston-mode amplitude quite well. For consistency, the terminal gap elevation in the numerical simulations are taken as the free-surface elevation at the same position.

Time-series. The time-series examples are presented in Figures 10.21 and 10.22. They are taken from Case B ($b/B = 0.15$). The nondimensional wave frequency is $\omega/\sqrt{g/B} \simeq 1.69$ (corresponding to $T = 0.75$s), and the steepness is $\epsilon_1 \simeq 1/170$ in the first figure and $\epsilon_2 \simeq 1/85$ in the second figure. From top to bottom we present sway, heave, roll, terminal gap elevation and the incoming wave. The vertical bars indicate the onset of flow separation in the numerical simulations denoted "BEM with vortex" in the legends. The nonlinear numerical simulations without flow separation is simply denoted "BEM". Time-series from the linear wavetank is not included since the model test geometry nor the wavemaker motion were reconstructed in those runs. Please note that the linear solution over-predicts significantly more than the nonlinear solution without flow separation. This will become clear when we present the reduced data.

We first discuss the time-series in Figure 10.21. The horizontal drift away from the ter-

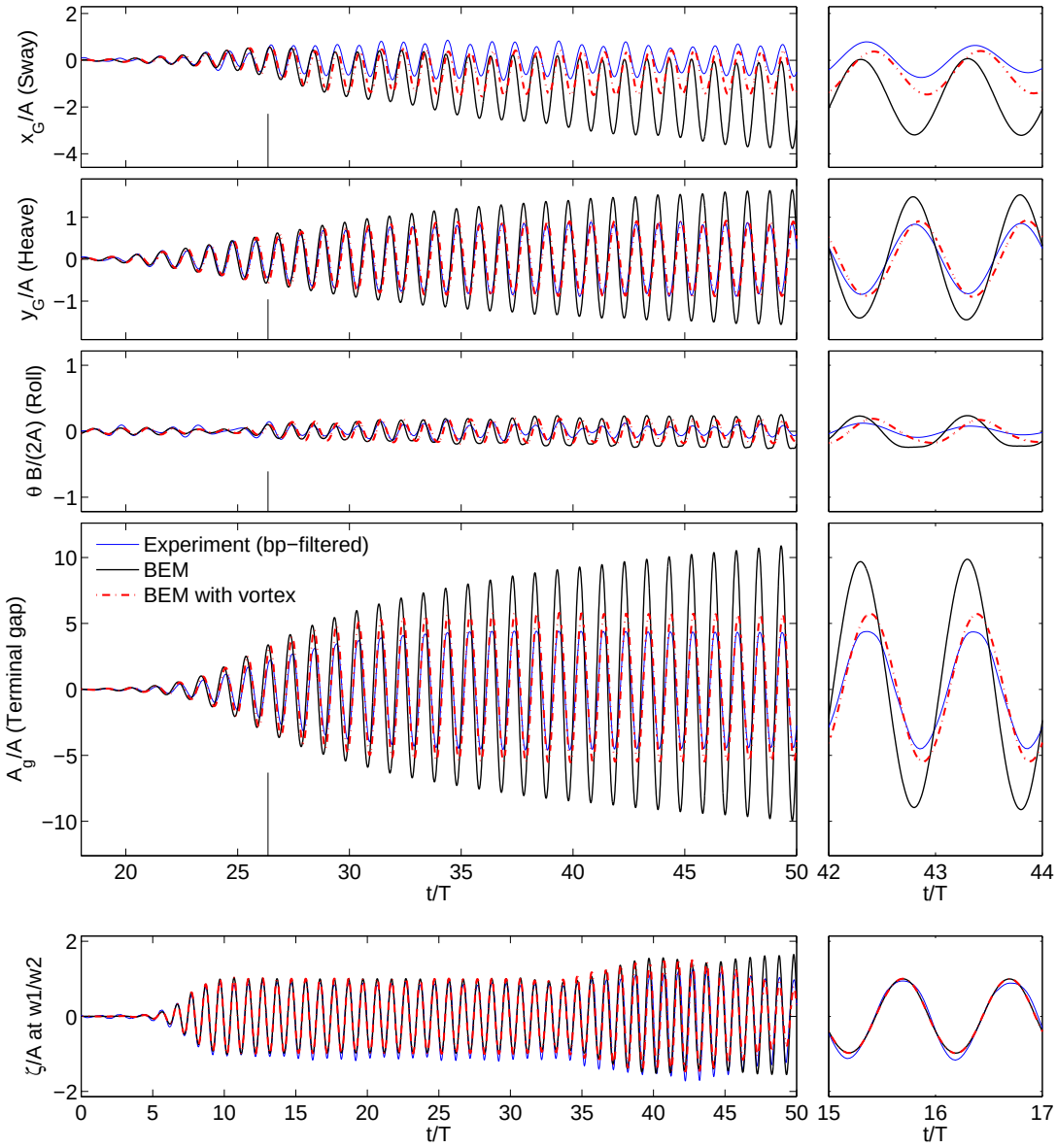

Figure 10.21: Time-series of the three degrees of freedom ship motion, terminal gap elevation and incoming wave elevation. From Case B. $\omega/\sqrt{g/B} \simeq 1.69$ and the lowest wave steepness $H/\lambda \simeq 1/170$. Nonlinear numerical wavetank without and with flow separation denoted by "BEM" and "BEM with vortex", respectively.

minal is clearly over-predicted by the simulation without flow separation relative to that with flow separation. Since the experimental data are band-pass filtered we are not able to compare the drift with that measured in the model tests. However, from the high-speed video it is quite evident that the drift is much closer to that predicted by the simulations including flow separation than to those without. The oscillation amplitude of the sway motion is also largely over-predicted by the simulations without flow separation, whereas only somewhat over-predicted by the simulations with flow separation. For heave, the simulations without flow separation clearly over-predict, while the simulations with flow separation compares well with the measured. Roll is very small and the experimental data

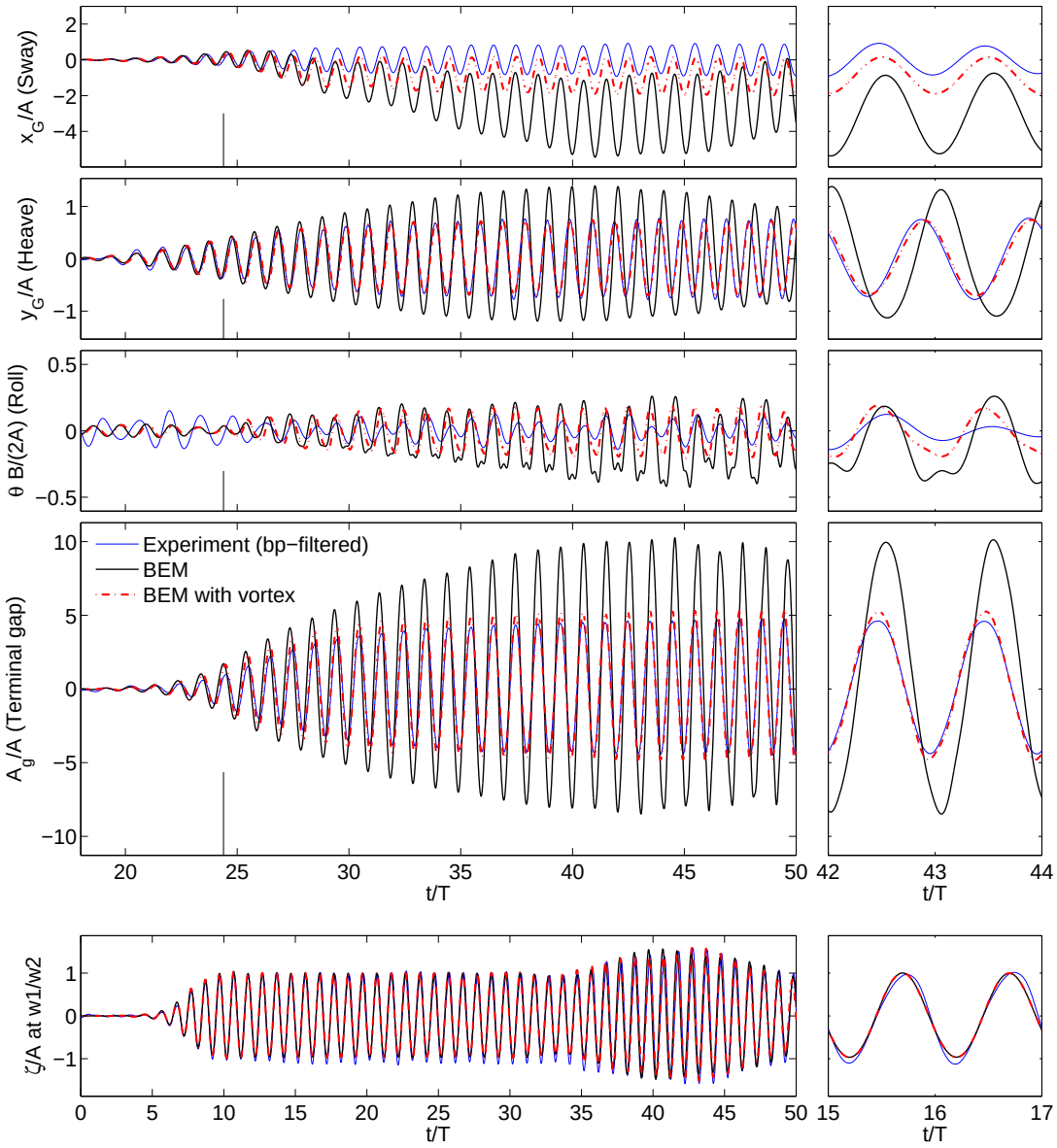

Figure 10.22: Time-series of the three degrees of freedom ship motion, terminal gap elevation and incoming wave elevation. From Case B. $\omega/\sqrt{g/B} \simeq 1.69$ and the highest wave steepness $H/\lambda \simeq 1/85$. Nonlinear numerical wavetank without and with flow separation denoted by "BEM" and "BEM with vortex", respectively.

here shown are dominated by noise in the accelerometers. The roll amplitude is somewhat smaller in the simulations with flow separation relative to those without flow separation, with the relative difference more or less as for sway and heave. The amplitude is approximately 0.5deg in the simulations including flow separation. The terminal gap amplitude is also clearly over-estimated by the simulations without flow separation. Including flow separation significantly improves the situation, although they still over-predict by about 25%. We note that for all main quantitities of the problem, i.e. sway, heave and terminal gap motion, steady-state is reached in a matter of about 12 - 15 periods in the model tests and the simulations with flow separation, whereas in those without flow separation,

steady-state is not yet reached by the end of the simulation. There is a clear beating in the signals from the nonlinear simulations without flow separation. The incoming wave time-series, taken as 0.5(w1 + w2), is presented in the bottom of the figure. The incoming wave is reasonably reproduced by the numerical wavetank. We mention that there are some small discrepancies as seen from the figure; the wave in the model tests exhibits some features that are not as expected. This includes slightly larger minima than maxima and slightly wider troughs than crests. The incoming wave amplitude was only 2.8mm in the presented case. The amplitude of these features are thus very small. We believe they are due to some transverse motion and possibly meniscus effects on the wave gauges.

Much the same discussion applies for the results in Figure 10.22. This corresponds to the same set-up, but for the highest wave steepness. An exception is that the results from the numerical model with flow separation over-predict less in this case. There is almost no over-prediction for heave and about 12% for the terminal gap amplitude corresponding to that in sway. The simulation without flow separation predicts a large drift away from the terminal. The motion then tends away from resonance due to the increased gap which is initially $b/B = 0.15$, while it increase to $b/B \simeq 0.19$ around $t/T = 35 - 38$. In reality a taut mooring will not allow this significant drift, and the over-prediction would most likely be higher in such a case.

As a supplement, we present time-series of the terminal gap elevation for a range of wave periods in Figures F.5 - F.8. These illustrate the beating behaviour for periods around the natural period in the nonlinear simulations where flow separation is not included. The vertical bars indicate initiation of flow separation in the tests where such simulations were made. Some of these break down quite early, as discussed. Also some of the nonlinear simulations without flow separation break down. When such large ship motions occur that re-gridding is applied in the terminal gap, saw-tooth instabilities arise with breakdown after a few periods as a consequence.

Reduced data. Reduced data in terms of near steady-state values are presented in Figures 10.23 and 10.24. The main observations are that linear theory clearly over-predicts around resonance as expected. Including flow separation (in the nonlinear simulations) seems to remedy the majority of the discrepancies. In the nonlinear simulations without flow separation the resonance frequency shifts somewhat to a lower value due to mean drift away from the terminal, with the effect being more pronounced in the cases with highest wave steepness, as one would expect. We note that this is not realistic in the case of taut mooring, and the behaviour would most likely be closer to the linear if restrained from drifting. If this is true, effects from the nonlinear boundary conditions are not important. Further, believing the results produced by the simulations including flow separation, the present results strongly indicate that flow separation is the main contributor to the discrepancy between linear theory and experimental data.

This is consistent with the findings in the previous section for the forced heave problem, where around the piston-mode resonance period T_p there was a clear effect of flow separation. It was, however, from that study not clear whether it would be so also in the case of a moored ship undergoing resonant *coupled* ship section and piston-mode motion. It turned out, as seen from the present results, that the flow separation effect is in fact appreciably more pronounced in the case of a moored ship than in the radiation problem, now around the coupled ship and piston-mode resonance period T_n. In the forced heave problem, linear theory over-predicted the piston-mode amplitude by about 45%

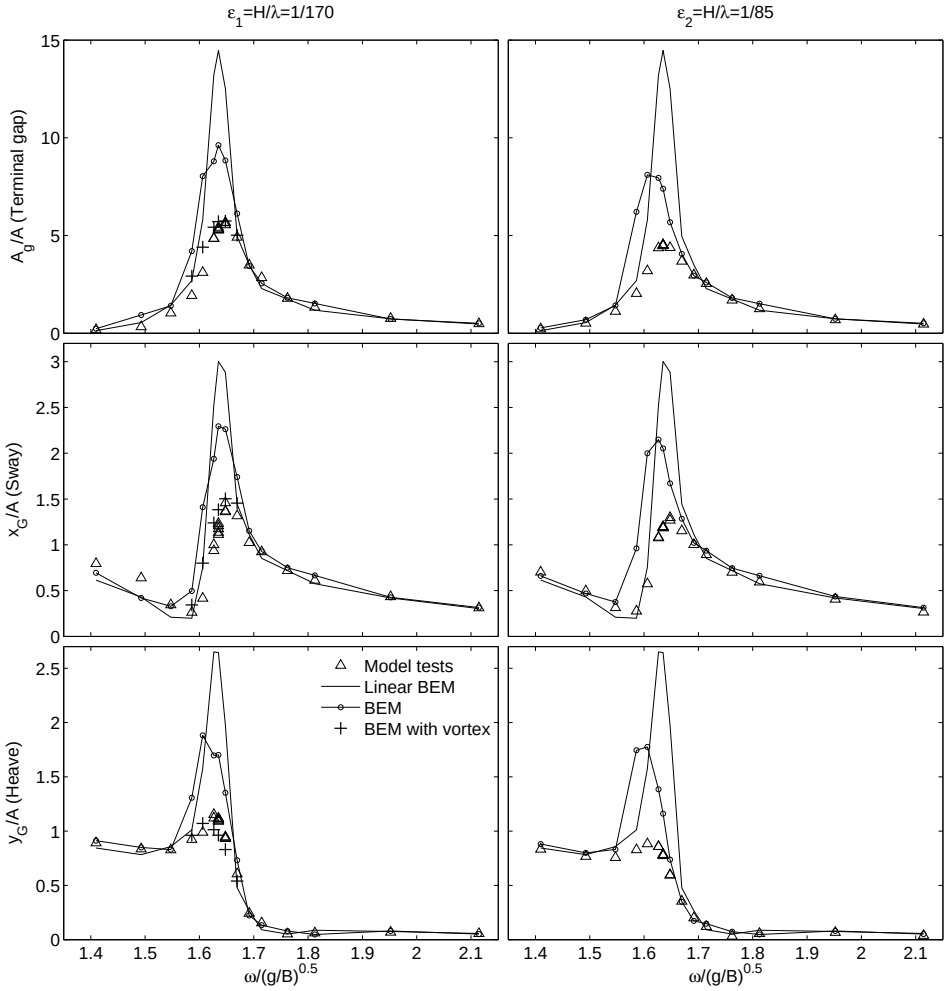

Figure 10.23: Piston-mode and ship motion steady-state or nearly steady-state amplitudes nondimensionalized by wave amplitude A. Case A ($b/B = 0.2$). Upper row: Piston-mode amplitude (A_g/A). Middle row: Sway (x_G/A). Lower row: Heave (y_G/A). Columns: Wave steepness ϵ_1 and ϵ_2.

and 65% in the lowest steepness and highest steepness cases respectively, while in the present moored ship section problem, by about 240% and 300% for the two steepnesses respectively.

We have no explanation for this observation. An explanation could perhaps have been the different *relative* velocity U_s at the corner of separation. It is the relative velociy which is relevant for the strength of the induced circulation, and thereby level of damping. The piston-mode amplitudes were in the present case comparable to that in the forced heave case presented in the preceding section. In both the forced heave study and the present moored ship section study, the piston-mode amplitudes at resonance were approximately $A_g/B \simeq 0.07$ in the lowest steepness case and $A_g/B \simeq 0.14$ in the highest steepness case. In the present case when the ship section is free to oscillate, there is a chance that the relative velocity is higher, despite a comparable piston-mode amplitude. We argue in the following, however, that this was not the case. We exemplify this as follows: In the

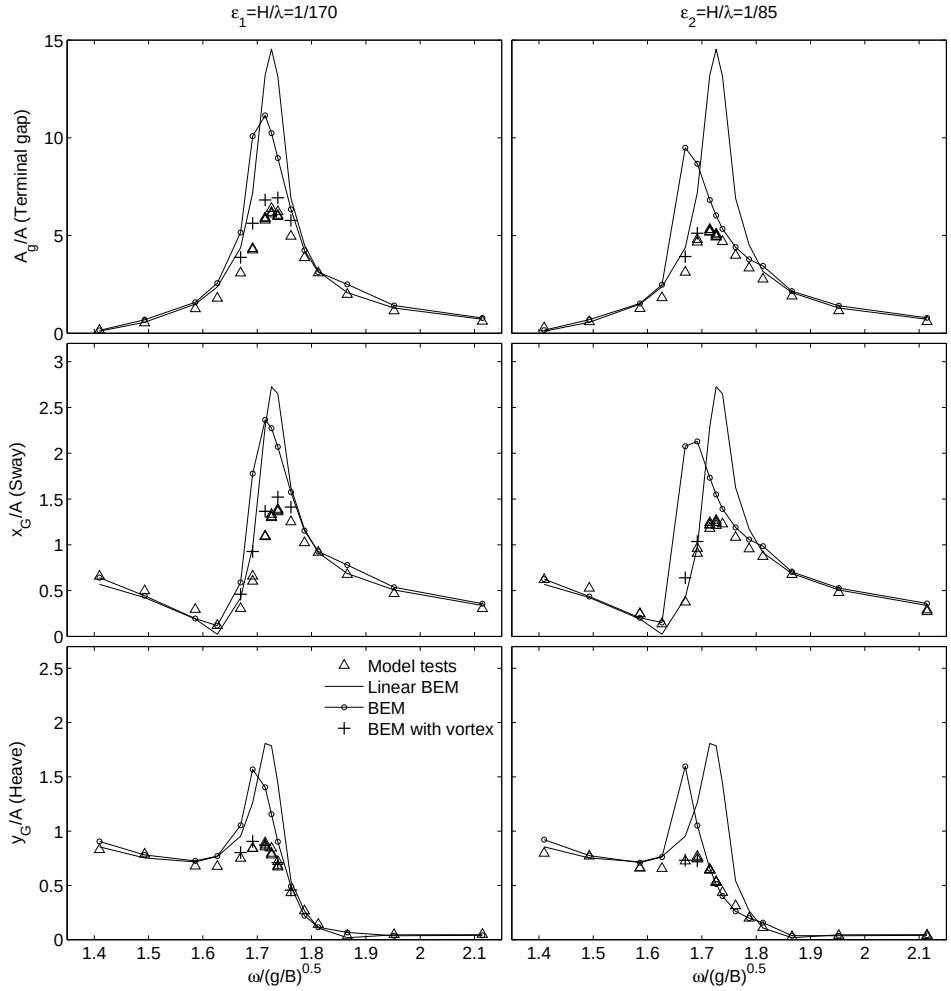

Figure 10.24: Piston-mode and ship motion steady-state or nearly steady-state amplitudes nondimensionalized by wave amplitude A. Case B ($b/B = 0.15$). Upper row: Piston-mode amplitude (A_g/A). Middle row: Sway (x_G/A). Lower row: Heave (y_G/A). Columns: Wave steepness ϵ_1 and ϵ_2.

forced heave case, we had e.g. for Case I in the lowest steepness case that $\eta_{3a}/A_g \simeq 1/10$. In Case A in the present moored ship section case, we have that $y_G/A_g \simeq 1/5$ and $x_G/A_g \simeq 1/4$. If we assume that the piston-like fluid motion is out of phase with the heave motion, the amplitude of the circulation should go like $(1+0.1)^2 = 1.21$ (for Case I) and $(1+0.2-0.25)^2 \simeq 0.9$ (for Case A) relative to the circulation with no ship motion and only fluid motion. This means the flow separation effect should be, according to this simple analysis about $0.9/1.21 \simeq 0.75$ times stronger in the moored ship case than in the forced heave case. That is, according to this reasoning, the induced circulation is lower in the moored ship case. Still, the effect is, as stated above, much more pronounced.

One should be careful with generalizations, but we believe that in a large number of applications in marine hydrodynamics with similar types of gap resonance phenomena where linear theory in general over-predicts relative to experiments or full-scale measurements, flow separation is the major cause to this discrepancy. Our feeling is also that

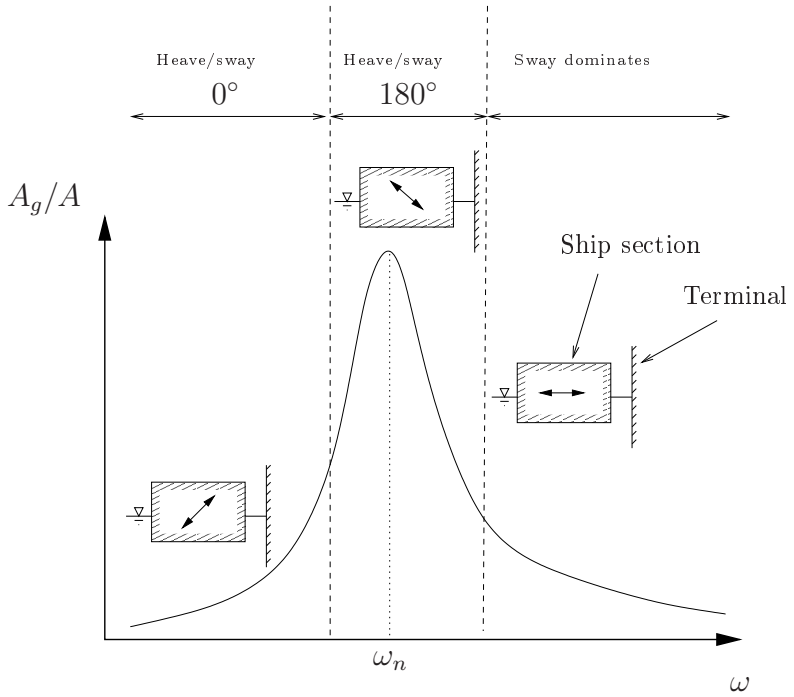

Figure 10.25: Observed ship motion behaviour as function of wave frequency.

effects associated with the nonlinear free-surface conditions is of minor importance, at least as long as the free surface behaves non-violent as in the present case.

Some further interesting observations partly based on the results from Figures 10.23 and 10.24, and partly from video recordings and investigation of corresponding time-series is presented schematically in Figure 10.25. For high wave frequencies basically only sway is excited. A rapid increase in heave occurs when tending to the natural frequency from above. Around resonance, the relative phase between heave and sway is as stated above, approximately 180deg. This decreases rapidly to nearly 0deg with decreasing frequency, with a near total canceling of the terminal gap motion.

In reality, bottom mounted GBS type of terminals are not built in water depths as large as that considered here. The choice of water depth in the present study was a matter of laboratory availability. The water depths in the present study was $h/B = 2.2$. The water depths are more typically $h/B \simeq 0.4-0.7$ for these types of installations. There are three main effects associated with decreasing the water depth h, given otherwise the same dimensions. First, as indicated in the discussion around Figure 4.4, T_p increases with decreasing water depth. Second, heave added mass of the ship section increases so that also the ship motion resonance period T_n increases. A relevant question is then whether T_n becomes closer to T_p or not. If they come close, substantially larger motion than that reported here may be a consequence. Third, since the ship motion resonance period increases, the associated incoming waves become longer and start communicating with the terminal gap flow more directly, and the resulting discussion becomes slightly more complicated than the above. Then comes the aspects of shallow water waves. Whether the nonlinearities associated with the incoming shallow water waves are important to the resonance problem is not clear at this stage. It was investigated for a fixed ship section in

Section 10.1. The results in that study were somewhat inconclusive due to possible bias errors in the model tests of that study. Our suggestion was, however, that the shallow water wave effect was small in that case.

10.3.3 Summary of the study

We summarize the present study as follows. The study involved a moored ship section by a bottom mounted terminal. The ship section had sharp bilges in order to fix the separation point. The ship section and terminal were subjected to deep water waves. The periods T of the incoming waves were chosen to be around the coupled ship and piston-mode resonance period T_n. We varied the terminal gap width b and wave steepness H/λ. The steepness was small. The studied cases are summarized in Table 9.5. The goal was to study the effects from the nonlinear boundary conditions and flow separation from the ship bilges on the amplitudes of the ship motions in sway, heave and roll as well as the piston-mode amplitude around coupled ship and piston-mode resonance.

The main results from the present study are

- The present linear simulations predicted A_g/A ratios at resonance up to about 15 in both Cases A and B. The sway and heave motion was $(x_g, y_g)/A \simeq 2-3$. The roll motion was very small.
- The A_g/A ratios measured in the model tests were about 5 for the largest wave steepness and about 6 for the smallest wave steepness in both Cases A and B. There is a significant discrepancy between those measured and predicted by linear theory. The sway and heave motion was $x_g/A \simeq 1-1.5$. The roll motion was close to zero.
- The present nonlinear simulations without flow separation predicted A_g/A ratios in between those predicted by the linear simulations and measured in the model tests. They were appreciably affected by large drift from the terminal. The drift was caused by the largely over-predicted piston-mode motion. With a more realistic taut mooring the drift would not occur and the results would probably be close to the linear results.
- The present nonlinear simulations with flow separation predicted both ship motions and piston-mode motion very close to those measured in the model tests.

The present study strongly indicates that flow separation is the main contributor to the observed discrepancies between linear theory and experiments around coupled ship and piston-mode resonance period T_n. The effect of flow separation is significantly more pronounced when the ship section is free to oscillate than when forced to oscillate. The latter was studied by means of a forced heave study in the previous section.

10.4 Forced sway of a ship section by a bottom mounted terminal

We study the resonant piston-mode behaviour in forced sway of a rectangular ship section with sharp bilges by a bottom mounted terminal. Forcing frequencies near the piston-mode resonance frequency T_p is applied. The numerical work related to forced sway was

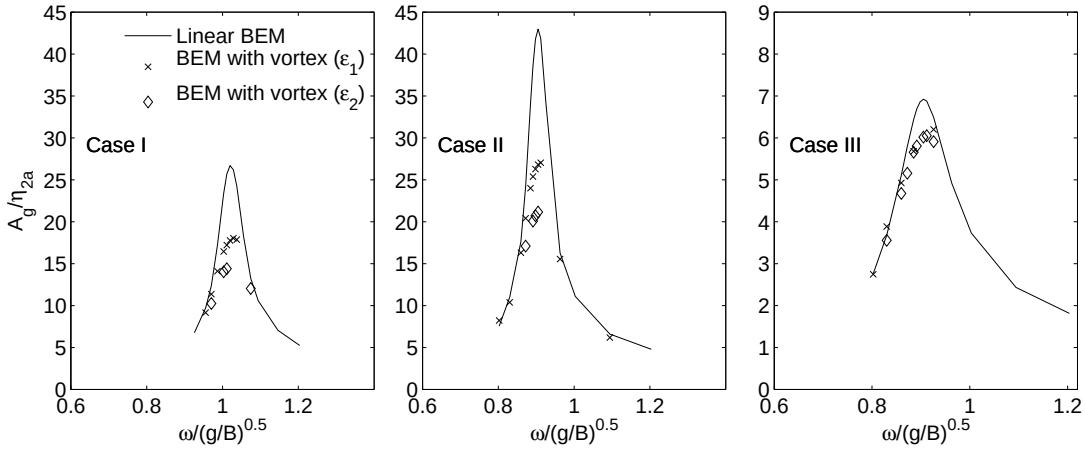

Figure 10.26: Nondimensional piston-mode amplitude A_g/η_{2a} in the case of a ship section undergoing forced sway motion. Note the different scales in the figure axis.

originally meant as part of a quantitative study on the shape of the vortical structure emanating from a sharp corner in collaboration with other researchers at NTNU. Model tests of forced sway were planned in the wave flume at MARINTEK described in the two previous sections, with measurements involving Particle Image Velocimetry (PIV). Software had been developed by these researchers for identification of the main vortical structures from the PIV images, suitable for direct comparison with the present simulations. However, the model tests could not be performed due to an unresolved problem of slight drift in the rig controlling the sway motion, so the present numerical work on forced sway has not previously been published.

We nevertheless find it interesting to present the results from the numerical study as a supplement to the study on forced heave presented in Section 10.2. The geometrical set-up is the same as in that study. The parameters are described in Table 9.8.

Also the same numerical parameters as those used in the forced heave tests were used, and forced sway amplitudes the same as the forced heave amplitudes. Not all simulations with the nonlinear wavetank with flow separation were successful, but we made no effort in improvements on this matter since the experimental work was stopped.

Reduced data by means of piston-mode amplitude A_g/η_{2a} taken as that averaged over the gap are presented in Figure 10.26. We note the considerable piston-mode amplitude resulting from the forced sway motion in Cases I and II. In Case III, the response is much lower. The results are hence sensitive to the ratio b/B. The response in Case II is higher than in Case I due to a larger draft D. The discrepancies between the linear simulations and the nonlinear simulations with flow separation are very similar to those in the forced heave study. The response is, however, significantly higher here, in particular in Case II. For forced heave, the ratio was from linear theory $A_g/A \simeq 13$ in the heave case, while it is $A_g/A \simeq 43$ in the present, sway case. Despite the different response, the relative damping effect due to flow separation is very similar in sway and heave.

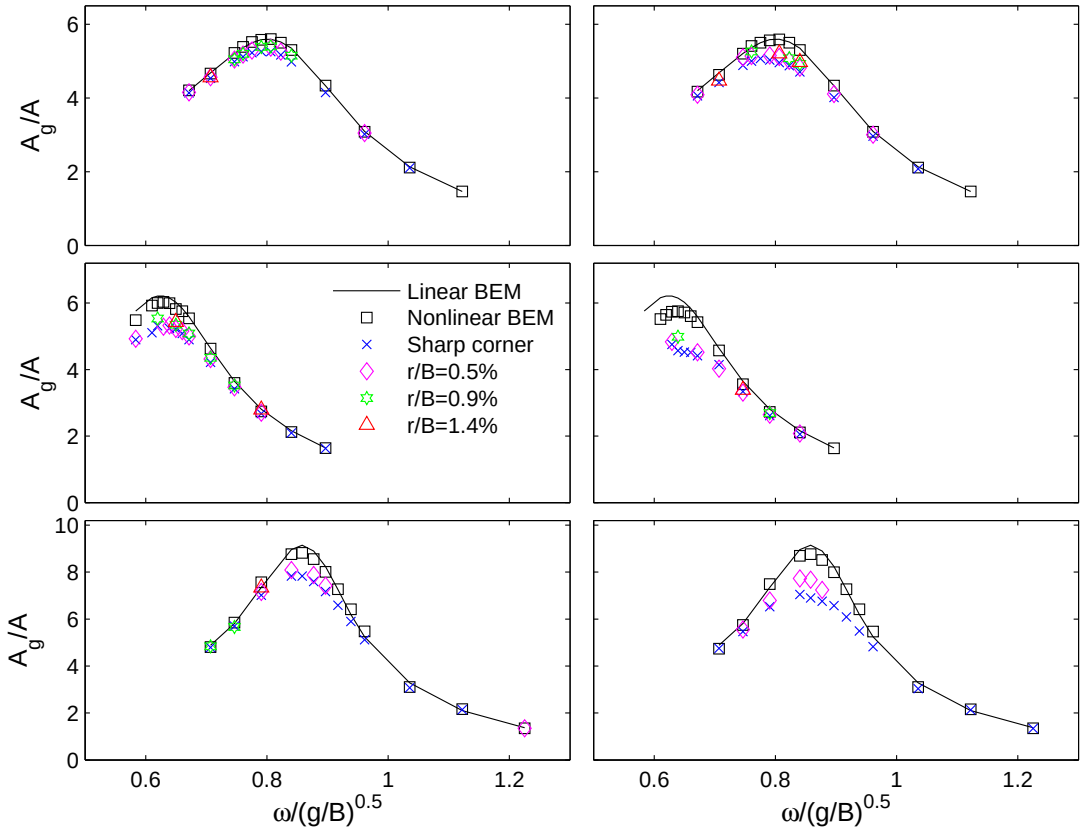

Figure 10.27: Nondimensional piston-mode amplitude A_g/A in the case of a fixed ship exposed to waves. Simulations include linear, nonlinear without flow separation and nonlinear with flow separation. The simulations with flow separation include sharp corner and rounded bilges of different radii r. Upper row: Case 1. Middle row: Case 2. Lower row: Case 3. Left column: Lowest wave steepness $\epsilon_1 = 1/600$. Right column: Highest wave steepness $\epsilon_2 = 1/300$

10.5 Fixed ship with flow separation

In light of the discrepancies between linear theory and model test results in the study on the fixed ship section by a bottom mounted terminal subject to incoming waves, we wanted to investigate the significance of possible flow separation on this system. As is discussed in Section 10.1, we expect that flexing of the ship section side caused a similar damping effect as that due to the flexing terminal in the moored ship section model tests. We therefore reached the conclusion that flexing of the ship section side caused a considerable damping in the fixed ship section model tests. The present study was, however, done prior to that conclusion, and we still consider that the acquired results are worth mentioning, showing trends as expected with respect to wave steepness and radius of the bilge keels.

In the model tests the bilge radius was $r/B = 0.09$, and we had at most $KC \simeq 5$. In that case, vortices will not break strongly away from the ship section, although the flow will separate. This was discussed in sub-section 10.1.2. With sufficiently low radius r, however, the KC-numbers will be high enough in order to achieve vortex shedding. Our

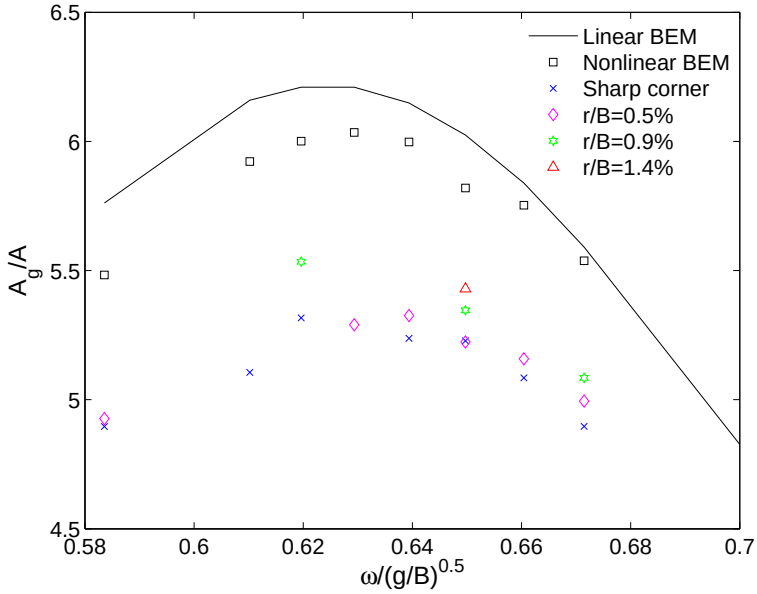

Figure 10.28: Zoom-up of the middle left sub-plot of Figure 10.27.

strategy to investigate the flow separation effect was to model the ship section bilge first as sharp and then with increasing bilge radius, r, with a fixed separation point at the mean apex angle. We realize the shortcomings of the method when fixing the separation point. Boundary layer calculations would be needed in case of estimating the separation point, but this was not done.

Suffering from numerical problems associated with the free shear layer entering the body when increasing the bilge radius we were only able to simulate for $r/B \lesssim 0.014$. We believe the problems were associated with the physics involved where, with decreasing KC-number, vortices breaking away from the body becomes less likely.

The simulations were done with the same set-up and numerical parameters as in the simulations of the study of the fixed ship section in Section 10.1, except the ship bilges were allowed to be rounded and a higher number of elements were used on the ship section. We considered all Cases 1 - 3, but had to reduce the steepness of the incoming waves to $\epsilon_1 = 1/600$ and $\epsilon_2 = 1/300$ as vortical structures with dimension D_0 in the order of the terminal gap width b and bottom clearance d evolved when using the original steepnesses. In such cases the automatic simplification algorithm still works, but its validity seizes. An example of this type of behaviour was presented and discussed in connection with Figure 6.8. We suspect that in such a case the free surface in the terminal gap as observed from above in an experiment would look rather chaotic, since an appreciable amount of vorticity would be advected towards the free surface.

In Figure 10.27 we present the nondimensional piston-mode amplitude A_g/A as that averaged over the free surface in the terminal gap. Note that with the wave steepness being only about one quarter of that in the original study, the amount of vorticity shed through flow separation and the KC-numbers are not directly comparable to those used in that study. Anyway, there is some effect of wave steepness, as seen when comparing the left and right column of sub-plots in the figure. Also, there is some effect of bilge keel radius. This is perhaps best illustrated by the lower right sub-plot. Those results suggest

that a bilge radius of only 0.5% of the ship beam removes about one third of the damping effect of flow separation. Further, from Figure 10.28, which is a zoom-up of the middle left sub-plot of Figure 10.27, we see that the results seem to approach those without flow separation when increasing the radius.

Chapter 11

Summary and further work

11.1 Summary of the present work

In the present work we investigated the gap resonance problems associated with a ship alongside a bottom mounted terminal. The gap between the ship and the terminal was denoted the terminal gap. The resonance problems were studied in a two-dimensional setting, which means we studied a mid-ship section. If the ship section is forced to move, or fixed and subjected to incoming waves, we have the *piston-mode resonance* problem. By piston-mode motion we mean the massive, near vertically oscillating flow of the fluid entrained between the ship and the terminal. If the ship section is free to oscillate, we have the *coupled ship and piston-mode resonance* problem. With each of these problems there is a resonance frequency.

The main focus was to investigate why linear theory in general over-predicts the ship and piston-mode motion near the resonance frequencies. Dedicated experimental as well as numerical work was performed and results compared. The present experimental work involved a fixed and a moored ship section. Results from previously published experiments on forced heave of two ship sections was also used. Geometrical parameters like theterminal gap width b, the water depth h, and wave steepness H/λ, were varied. The present numerical work involved two time-domain wavetanks based on a boundary element method, one linear wavetank and one fully nonlinear wavetank. We investigated the effect of the nonlinear boundary conditions. Further, the following two viscous effects were investigated: The in- and out-flow of boundary layers and flow separation from the ship bilges. Special effort was made in modelling the flow separation as well as calculating the ship motion in the nonlinear numerical wavetank.

Basic numerical wavetanks. We assumed potential flow. The boundary value problem involving the Laplace equation with the kinematic and dynamic boundary conditions were recast into a standard boundary integral equation based on Green's second identity. Two time-domain wavetanks applying the Boundary Element Method (BEM) were implemented, one linear and one fully nonlinear. By linear we mean that both linearized boundary conditions were satisfied at the mean position of the boundaries. Rankine singularities were distributed along the boundary. The Mixed Eulerian-Lagrangian (MEL) formalism was adopted, where the boundary value problem is solved given the instantaneous situation each time-step, and the unknowns, the free surface S_F and the potential

φ, are updated according to this solution. We chose a fourth order explicit Runge-Kutta scheme for time-integration. Re-gridding of the elements defining the intersections between the free surface and the solid boundaries was implemented in order to keep the grid resolution at a certain level. No explicit smoothing of any kind for the free surface was used.

Numerical modelling of viscous effects. The two viscous effects of in- and out-flow of boundary layers as well as flow separation were modelled. The former was implemented in the linear wavetank only, and the latter in the nonlinear wavetank only. Switches determined whether the two viscous effects be turned on or off. In this way, we were able to isolate the different effects. Laminar boundary layers were assumed, and a semi-analytical solution found as a convolution integral handling arbitrary outer flow. The in- and out-flow velocity was posed directly on the solid boundaries. Flow separation was modelled by an inviscid vortex tracking method where the shed vorticity is concentrated in thin free shear layers in the irrotational fluid. The assumption of a thin free shear layer requires high Reynold's numbers. The vorticity in the free shear layer was represented by a continuous distribution of dipoles. Re-gridding and automatic simplifications of the geometry of the free shear layer were applied each time-step. The automatic simplifications were based on an algorithm developed within the present work and considered crucial for the method to be applicable for long-time simulations in oscillatory flow. The procedure required in practice the vortical structures to be localized in the vicinity of the corner of separation.

Numerical modelling of ship motions. We considered rigid body motion in the three degrees of freedom sway, heave and roll. This involved solving the equations of motion. A challenge with evaluating the forces and moment was introduced by the adopted MEL approach, since in the MEL approach, the φ_t term in the Bernoulli equation is not defined. A simple differentiation in time gives an unstable numerical scheme. We derived an alternative formulation of the force and moment where the time derivative was moved outside the integrals. A closed control surface including the ship, the surrounding free surface and a connecting surface inside the fluid was introduced and Gauss' and Stokes' theorems used. Some numerical problems were encountered for roll. For large amplitude roll, the numerical scheme was unstable. For small roll amplitudes the solutions converged. In the present work only small roll amplitudes and no instabilities were experienced. For sway and heave the method worked well.

11.1.1 Studies of resonant ship and fluid motion

Three main studies and two supplementary studies were performed, all with a ship section by a bottom mounted terminal. All studies were within a two-dimensional setting. In the main studies we presented results from both model tests and present numerical simulations, while in the supplementary studies results from present numerical simulations only. The two first main studies involved resonant piston-mode motion of the fluid with the ship section fixed and subjected to incoming waves ("diffraction") or forced in heave ("radiation"). The third involved coupled ship and piston-mode motion of a moored ship section. In the first study the ship section had rounded bilges to avoid flow separation

as far as possible, while in the two last studies, sharp bilges in order to enforce flow separation and to ensure the separation point was fixed and known. Realistic water depths for an offshore terminal was considered in the first study only, which involved shallow water wave conditions. The other two main studies involved deep water conditions. In all studies a range of wave periods T around resonance were considered.

Fixed ship section with rounded bilges. In the first main study the ship section was fixed, and the model test set-up was originally meant for the study of shallow water wave effects on offshore terminals. This involved full scale periods in the range $T = 6\text{s} - 15\text{s}$ at full scale water depths of $h = 16\text{m} - 20\text{m}$. We next decided to investigate the resonant piston-mode motion. The wave period range was extended to include wave periods around the piston-mode resonance period T_p which in full scale was approximately 17s to 21s depending on the water depth. The water depth was extended to include also $h = 28\text{m}$. We defined the three Cases 1 - 3. The ratio between the water depths and ship beam were $h/B = 0.45 - 0.625$. The ship beam B and draft D were not varied. The beam to draft ratio was fixed to $B/D = 3.76$. In addition to h, the parameters b and wave steepness were varied. The steepness of the incoming waves were modest, with $H_0/\lambda_0 \simeq 1/115 - 170$, where subscript 0 means deep water limit. Flow separation was not yet modelled numerically. The bilges were rounded in the model tests in order to avoid flow separation as far as possible. The corner radius was $r/B = 0.09$. The KC-number was no more than 5, where $KC = \pi A_g/r$ with A_g the piston-mode amplitude. No vortex shedding will occur for these KC-numbers, although the flow may separate. No flow separation was observed visually during the experiments. Despite the low wave steepness, significant nonlinearities in the free surface up-stream of the ship were introduced by the shallow water, in particular for $H/h \gtrsim 1/6$. The kinematics up-stream of the ship was captured well by the nonlinear numerical wavetank. The linear simulations over-predicted the piston-mode amplitudes A_g relative to the measurements by 20 - 30% around piston-mode resonance. Candidates explaining the discrepancy were effects associated with the nonlinear free-surface conditions as well as flow separation from the rounded ship bilges. If these were responsible, there should have been a clear effect of wave steepness. This was not the case, however. We suspected that a bias error in terms of slight flexing of the ship side in the model tests caused a reduction in the piston-mode motion, explaining most of the discrepancy.

Forced heave of a ship section with sharp bilges. In the second main study a ship section of rectangular shape and sharp bilges was forced to oscillate in heave with amplitude η_{3a}. The parameters D, b and η_{3a} were varied. The water depth was $h/B = 2.86$. We defined three cases, Cases I - III with $b/B = 0.25$ in Cases I and II and $b/B = 0.5$ in Case III. Previously published model test results were re-visited and used. Results from a semi-analytical linear theory was also used. Our linear simulations were verified against this linear theory.

Linear theory predicted in Cases I and II about 30% higher piston-mode amplitudes around piston-mode resonance T_p relative to the measured for the lowest forcing amplitude η_{3a}, while 40% when doubling η_{3a}. In Case III only the lowest forcing amplitude was considered, and the linear theory over-predicted in that case only by about 10%. Also far-field amplitudes were compared, with similar discrepancies. The in- and out-flow of boundary layers were from our linear simulations with and without this effect turned on found insignificant to all practical purposes. Thus, the "friction", as one may think of

it, along the ship side and terminal was negligible. There were only negligible effects associated with the nonlinear free-surface conditions; the results from the nonlinear simulations without flow separation were very similar to those from the linear simulations. Steady-state amplitudes as well as time-series from the nonlinear simulations including flow separation compared well with those measured. Flow separation was thus found to explain the discrepancies. The circulation introduced by the shed vorticity induced a backflow acting like a damping. The study showed a rather weak dependence on η_{3a}, but rather pronounced dependence on b.

Moored ship section with sharp bilges. In the third main study the ship section had sharp bilges and was moored by linear, horizontal springs. The beam to draft ratio was $B/D = 4$. The parameters b and H/λ were varied. The water depth was $h/B = 2.2$. We defined two cases, Case A with $b/B = 0.2$ and Case B with $b/B = 0.15$. No higher modes or other local disturbances of significance were observed in the terminal gap during model testing, while large ship and piston-mode motion were experienced. This was so also in the numerical simulations. The results in Case A were very similar to Case B, indicating weak dependence with b in this range of b. However, a short investigation during model testing with $b/B = 0.25$ indicated a very different behaviour; the piston-mode motion was nearly canceled at ship motion resonance T_n in that case, although the ship motion was considerable. The phasing between the sway and heave motion of the ship was crucial in this respect. This last case was not studied further due to time limitations. Steady-state values were strictly speaking not obtained from the linear simulations nor the nonlinear simulations without flow separation due to considerable beating effects. Only near steady-state values were therefore presented. The system did reach steady-state, however, in the model tests as well as in the simulations with flow separation. This was so due to a significantly larger damping.

Linear simulations over-predicted both the ship motion and the piston-mode amplitude around the coupled ship and piston-mode resonance T_n by two - three times relative to that measured. The nonlinear simulations without flow separation also over-predicted, but somewhat less than the linear. In both the experiments and the simulations with flow separation some mean drift away from the terminal was observed. The mean drift was, as expected, towards the wave direction due to the large piston mode. In the nonlinear simulations without flow separation the mean drift was significantly over-predicted due to over-prediction of the piston-mode motion. In the more realistic case of taut mooring the experienced large drift would not be allowed. With such a mooring the nonlinear simulations without flow separation would most probably over-predict nearly as much as the linear simulations. We note that the ship may note drift in the linear case. As in the forced heave case, steady-state amplitudes as well as time-series from the nonlinear simulations including flow separation compared well with those measured. Based on this discussion, we concluded that the discrepancies between linear theory and that measured around ship motion resonance was due to flow separation.

The discrepancies between linear theory and that measured in the model tests were nearly an order of magnitude higher than in the forced heave study. This indicated a significantly stronger effect of flow separation in the resonant coupled ship and piston-mode than in the forced heave problem with only resonant piston-mode motion.

Other studies. We also performed two supplementary, numerical studies. One with

forced sway with the same parameters as in the forced heave case. The results were very similar to the forced heave case. In the second supplementary study the effect of flow separation was investigated in the setting of the first main study of a fixed ship section in shallow water. Also the effect of rounded bilges ($r/B = 0 - 0.014$), with flow separation from a the mean apex angle of the bilge, was investigated. A fixed separation point was questionable. However, from the simulations, the damping effect of flow separation was reduced by a third with r/B as small as 0.005 relative to a sharp corner.

11.2 Future work

Future work that could be carried out includes improvements of the present numerical wavetanks as well as further case studies using these, either as they are or after improvement. We also think an investigation of the three-dimensional problem would be interesting. Other aspects are mentioned last.

There are three numerical issues concerning the nonlinear wavetank as it is at the present, that should be further investigated:

- The automatic simplification procedure works reasonably well. It is, however, not very robust in cases with large ship motions. We believe that this could be improved by developing a more robust handling of the free shear layer element closest to the separation point to avoid entanglement when the direction of flow separation is turning. We also expect that a higher order representation of the free shear layer geometry would improve the matter. Less entanglement is then expected.

- When considering the coupled fluid and ship motion problem, a set of differential-algebraic equations must be solved. To the author's knowledge, this has not previously been explicitly noted in the literature. A further investigation of this matter in order to try to improve the order of accuracy of the present numerical scheme would be welcome.

- There is still an unresolved problem with roll. We are at the present time not sure whether the roll instabilities, which occur when roll motion is appreciable, are due to large terms that do not cancel due to numerical inaccuracies or simply a programming bug. Perhaps a higher order spatial accuracy is needed in the integration of the terms in the alternative expression for the moment.

Additional cases studies would be welcomed. With respect to a moored ship by an offshore bottom-mounted terminal, it would be interesting to perform an investigation such as the third main study in more realistic water depths of $h/B \simeq 0.4 - 0.8$. This would involve nonlinear effects associated with the shallow water waves as well as a more pronounced communication between the outer flow with that in the terminal gap. In the presented study, the communication was mainly via the ship. Further, nonlinear mooring and fender characteristics should also be introduced. In the time-domain approach adopted here, this should in principle be straight-forward to incorporate. The shallow water effects and nonlinear mooring and fender characteristics are expected to introduce challenges not considered in the present work. This could involve e.g. super-harmonic resonances.

The considered two-dimensional problem represents an infinitely long ship. In reality, there are three-dimensional effects. One is the nearly sinusoidal mode shape of the "piston mode" along the ship length. Another is flow separation at the longitudinal ends of the ship and terminal. The behaviour of the three-dimensional problem is not clear to us without further investigation. But it is not clear neither how such an investigation could be performed. The formulation using the boundary integral formulation does not, in principle, prohibit a direct three-dimensional investigation. The full three-dimensional problem would, however, be very CPU-demanding and, we expect, prone to numerical difficulties associated with the free shear layer. Consider e.g. the transverse instabilities of the free shear layer. One could perhaps develop some automatic smoothing procedure in that respect. Another possibility is a strip theory approach.

As described in the introduction, empirically based damping terms in the free-surface conditions have been applied to three-dimensional linear radiation-diffraction frequency plane codes in practice, and the magnitude of the damping terms are currently found from model tests. A future work would be to suggest and elaborate on a more physically based, possibly semi-empirical, method to resolve the practical problems associated with linear theory and gap resonances. It is, however, not clear to the author what this would involve.

We also note that the nonlinear wavetank including flow separation could be used in other problems involving near sinusoidal flow with separation from sharp corners. For example, the effect of baffles in a two-dimensional sloshing tank could be investigated in case of non-violent free-surface flow. In cases involving violent free-surface flow, more elaboration would, however, be needed with respect to the handling of the free surface in the nonlinear numerical wavetank.

Bibliography

Aarsnes, J. V. (1984). *Current forces on ships*. Ph. D. thesis, Norwegian Institute of Technology.

Baarholm, R. J. (2001). *Theoretical and Experimental Studies of Wave Impact underneath Decks of Offshore Platforms*. Ph. D. thesis, Norwegian University of Science and Technology (NTNU).

Bingham, H. B. (2000). A hybrid Boussinesq-panel method for predicting the motion of a moored ship. *Coastal Eng. 40*, 21–38.

Birkhoff, G. and J. Fisher (1959). Do vortex sheets roll up? *Rc. Circ. mat. Palermo Ser. 2 8*(1), 77–90.

Bisplinghoff, R. L., H. Ashley, and R. L. Halfman (1996). *Aeroelasticity*. New York: Dover Publications.

Braathen, A. (1987). *Application of a vortex tracking method to the prediction of roll damping of a two-dimensional floating body*. Ph. D. thesis, Norwegian Institute of Technology.

Brady, M., A. Leonard, and D. I. Pullin (1998). Regularized vortex sheet evolution in three dimensions. *J. Comp. Phys. 146*, 520–545.

Bryant, P. J. (1983). *Nonlinear Waves*. Cambridge University Press.

Buchner, B., G. de Boer, and J. de Wilde (2004). The interaction effects of mooring in close proximity of other structures. In *Proc. 14th Int. Offshore and Polar Eng. Conf.*

Buchner, B., G. E. Loots, G. Z. Forristall, and E. J. van Iperen (2004). Hydrodynamic aspects of gravity based structures in shallow water. In *Proc. Offshore Tech. Conf. (OTC)*.

Buchner, B., A. van Dijk, and J. de Wilde (2001). Numerical multiple-body simulations of side-by-side mooring to an FPSO. In *Proc. 11th Int. Offshore and Polar Eng. Conf.*

Chen, X.-B. (2005). Accurate computation of second-order low-frequency loads. In *Proc. 19th National Conf. on Hydr./ 7th National Congress on Hydr., Harbin, China*.

Chorin, A. J. and P. S. Bernard (1973). Discretization of a vortex sheet, with an example of roll-up. *J. Comp. Phys. 13*, 423–429.

Clement, A. (1996). Coupling of two absorbing boundary conditions for 2D time-domain simulations of free surface gravity waves. *J. Comp. Phys. 126*, 139–151.

Clements, R. R. (1973). An inviscid model of two-dimensional vortex shedding. *J. Fluid Mech. 57*(2), 321–336.

Cointe, R. (1989). *Quelques Aspects de la Simulation Numérique d'un Canal à Houle*. Ph. D. thesis, Thèse de Doctorat de l'Ecole Nationale des Ponts et Chaussées, Paris (in French).

Cointe, R., P. Geyer, B. King, B. Molin, and M. Tramoni (1991). Nonlinear and linear motions of a rectangular barge in a perfect fluid. In *18th Symp. on Naval Hydr.*, pp. 85–99.

Dean, R. G. and R. A. Dalrymple (1984). *Water wave mechanics for engineers and scientists*, Volume 2 of *Advanced series on ocean engineering*. World Scientific.

Downie, M. J., P. W. Bearman, and J. M. R. Graham (1988). Effect of vortex shedding on the coupled roll response of bodies in waves. *J. Fluid Mech. 189*, 243–264.

Eatock Taylor, R., L. Sun, and P. H. Taylor (2008). Gap resonances in focused wave groups. In *23rd Int. Workshop on Water Waves and Floating Bodies*.

Faltinsen, O. M. (1974). A nonlinear theory of sloshing in rectangular tanks. *J. Ship Res. 18*(4), 224–241.

Faltinsen, O. M. (1977). Numerical solution of transient nonlinear free-surface motion outside or inside moving bodies. In *Second Int. Conf. on Num. Ship Hydrodyn.*

Faltinsen, O. M. (1978). A numerical nonlinear method of sloshing in tanks with two-dimensional flow. *J. Ship Res. 22*, 193–202.

Faltinsen, O. M. (1990). *Sea Loads on Ships and Offshore Structures*. Cambridge University Press.

Faltinsen, O. M. (2005). *Hydrodynamics of High-Speed Marine Vehicles*. Cambridge University Press.

Faltinsen, O. M. and B. Pettersen (1987). Application of a vortex tracking method to separated flow around marine structures. *J. Fluids Struct. 1*, 217–237.

Faltinsen, O. M., O. F. Rognebakke, and A. N. Timokha (2003). Resonant three-dimensional nonlinear sloshing in a square-base basin. *J Fluid Mech. 487*, 1–42.

Faltinsen, O. M., O. F. Rognebakke, and A. N. Timokha (2005). Classification of three-dimensional nonlinear sloshing in a square-base tank with finite depth. *J. Fluids Struct. 20*, 81–103.

Faltinsen, O. M., O. F. Rognebakke, and A. N. Timokha (2007). Two-dimensional resonant piston-like sloshing in a moonpool. Linear inviscid statement. *J. Fluid Mech. 575*, 359–397.

Faltinsen, O. M. and B. Sortland (1987). Slow drift eddy making damping of a ship. *Appl. Ocean Res. 9*(1), 37–46.

Fredriksen, A. (2008). Ship motion in exposed harbours. Master's thesis, Norwegian University of Science and Technology (NTNU).

Fredsøe, J. and R. Deigaard (1992). *Mechanics of coastal sediment transport*, Volume 3 of *Advanced Series on Ocean Engineering*. World Scientific.

Fuhrman, D. R., H. B. Bingham, and P. A. Madsen (2005). Nonlinear wave-structure interactions with a high-order Boussinesq model. *Coastal Eng. 52*(8), 655–672.

Giesing, J. P. (1968). Nonlinear two-dimensional unsteady potential flow with lift. *J. Aircraft 5*(2), 135–143.

Gradshteyn, I. S. and I. M. Ryzhik (2000). *Table of Integrals, Series and Products*. Academic Press.

Greco, M. (2001). *A Two-Dimensional Study of Green-Water Loading*. Ph. D. thesis, Norwegian University of Science and Technology (NTNU).

Hairer, E., C. Lubich, and M. Roche (1989). *The numerical solution of differential-algebraic systems by Runge-Kutta methods*. Springer-Verlag.

Hughes, S. A. (1993). *Physical Models and Laboratory Techniques in Coastal Engineering*, Volume 7 of *Advanced Series on Ocean Engineering*. World Scientific.

Huijsmans, R. H. M., J. A. Pinkster, and J. J. Wilde (2001). Diffraction and radiation of waves around side-by-side moored vessels. In *Proc. 11th Int. Offshore and Polar Eng. Conf.*

Iserles, A. (1996). *A First Course in the Numerical Analysis of Differential Equations*. Cambridge University Press.

Jones, M. A. (2003). The separated flow of an inviscid fluid around a moving flat plate. *J. Fluid Mech. 496*, 405–441.

Kashiwagi, M. (2000). Non-linear simulations of wave-induced motions of a floating body by means of the mixed Eulerian-Lagrangian method. In *Proc. Instn. Mech. Engrs. C*, Volume 214.

Keulegan, G. H. (1959). Energy dissipation in standing waves in rectangular basins. *J. Fluid Mech. 6*, 33–50.

Koo, W. and M.-H. Kim (2004). Freely floating-body simulation by a 2D fully nonlinear numerical wave tank. *Ocean Eng. 31*, 2011–2046.

Kristiansen, T. and O. M. Faltinsen (2008). Application of a vortex tracking method to the piston-like behaviour in a semi-entrained vertical gap. *Appl. Ocean Res. 30*, 1–16.

Kristiansen, T. and O. M. Faltinsen (2009a). Resonant water motion between a ship and a terminal in shallow water. *J. Offshore Mech. and Arctic Eng. 131*.

Kristiansen, T. and O. M. Faltinsen (2009b). A two-dimensional numerical and experimental study of resonant coupled ship and piston-mode motion. *Appl. Ocean Res. (To be submitted)*.

Kvaalsvold, J. (1994). *Hydroelastic modelling of wetdeck slamming on multihull vessels*. Ph. D. thesis, Norwegian Institute of Technology.

Lalli, F. (1997). On the accuracy of the desingularized boundary integral method in free surface flow. *Int. J. Num. Meth. Fluids 25*, 1163–1184.

Landau, L. D. and E. M. Lifschitz (1987). *Fluid Mechanics* (2nd ed.). Elsevier, Butterworth Heinemann.

Landrini, M., G. Grytøyr, and O. M. Faltinsen (1999). A B-spline based BEM for unsteady free-surface flows. *J. Ship Res. 43*, 13–24.

Lian, W. (1986). *A numerical study of two-dimensional separated flow past bluff bodies at moderate KC-numbers*. Ph. D. thesis, Norwegian Institute of Technology.

Liu, P. L.-F. and A. Orfila (2004). Viscous effects on transient long-wave propagation. *J. Fluid Mech. 520*, 83–92.

Longuet-Higgins, M. S. and E. D. Cokelet (1976). The deformation of steep surface waves on water. I. A numerical method of computation. *Proc. R. Soc. Lond. A. 350*, 1–26.

Longuet-Higgins, M. S. and E. D. Cokelet (1978). The deformation of steep surface waves on water. II. Growth of normal-mode instabilities. *Proc. R. Soc. Lond. A. 364*(1716), 1–28.

Madsen, O. S. (1970). Waves generated by a piston-type wavemaker. In *Proc. 12th Coastal Eng. Conf.*, Volume 1, pp. 589–607.

Madsen, P. A., H. B. Bingham, and L. Hua (2002). A new Boussinesq method for fully nonlinear waves from shallow to deep water. *J. Fluid Mech. 462*, 1–30.

Maisondieu, C., B. Molin, O. Kimmoun, and L. Gentaz (2001). Simulation bidimensionnelle des écoulements dans une baie de forage: étude des modes de résonance et des amortissements. *Actes des Huitèmes Journées de l'Hydrodynamique, Nantes*, 251–264 (in French).

Maritime Administration (2007). Current/planned deepwater ports. (http://www.marad.dot.gov/dwp/LNG/deepwater_ports/index.asp).

McIver, M. (1996). An example of non-uniqueness in the two-dimensional linear water wave problem. *J. Fluid Mech. 315*, 257–266.

McIver, P. (2005). Complex resonances in the water-wave problem for a floating structure. *J. Fluid Mech. 536*, 423–443.

McLean, J. W., Y. C. Ma, D. U. Martin, P. C. Saffman, and H. C. Yuen (1981). Three dimensional stability of finite amplitude waves. *Phys. Rev. Letters 46*(13), 817–821.

Mei, C. C. (1989). *The Applied Dynamics of Ocean Surface Waves*, Volume 1 of *Advanced Series on Ocean Engineering*. World Scientific.

Milne-Thomson, L. M. (1968). *Theoretical Hydrodynamics* (fifth ed.). Dover Publications, Inc., New York.

Molin, B. (2001). On the piston and sloshing modes in moonpools. *J. Fluid Mech. 430*, 27–50.

Newman, J. N. (1977). *Marine Hydrodynamics*. The MIT Press, Cambridge, Massachusetts.

Newman, J. N. (2004). Progress in wave load computations on offshore structures. In *26th Int. Conf. on Offshore Mech. and Arctic Eng. (Oral presentation)*.

Newman, J. N. (2008). Linear analysis of wave basins and absorbers. In *23rd Int. Workshop on Water Waves and Floating Bodies*.

Newman, J. N. and C.-H. Lee (2005). *Numerical Models in Fluid-Structure Interaction*, Chapter : Computation of wave effects using the panel method, pp. 211–251. WIT Press, Southampton.

Ogilvie, T. F. (1967). Nonlinear high-Froude-number free-surface problems. *J. Eng. Math. 1*(3), 215–235.

Pauw, W. H., R. Huijsmans, and A. Voogt (2007). Advances in the hydrodynamics of side-by-side moored vessels. In *Proc. 26th Int. Conf. on Offshore Mech. and Arctic Eng.*

Peregrine, D. H. (1967). Long waves on a beach. *J. Fluid Mech. 27*(4), 815–827.

Pinto, F. T., F. V. Gomes, P. R. Santos, C. G. Soares, N. Fonseca, J. A. Santos, A. P. Moreira, P. Costa, and D. E. Brógueira (2008). Analysis of the behaviour of moored tankers. In *Proc. 27th Int. Conf. on Offshore Mech. and Arctic Eng.*

Rabiner, L. R. and B. Gold (1975). *Theory and Application of Digital Signal Processing*. Englewood Cliffs, New Jersey: Prentice-Hall, Inc.

Rienecker, M. M. and J. D. Fenton (1981). A Fourier approximation for steady water waves. *J. Fluid Mech. 104*, 119–137.

Roberts, A. J. (1987). Transient free-surface flows generated by a moving vertical plate. *Q. J. Mech. appl. Math. 40*(1), 129–158.

Rosenhead, L. (1932). The formation of vortices from a surface of discontinuity. *Proc. Roy. Sot. London, Ser. A 134*, 170–192.

Sarpkaya, T. (1975). An inviscid model of two-dimensional vortex shedding for transient and asymptotically steady separated flow over an inclined plate. *J. Fluid Mech. 68*(1), 109–128.

Schønberg, T. and R. C. T. Rainey (2002). A hydrodynamic model of green water incidents. *Appl. Ocean Res. 24*, 299–307.

Shukla, R. K. and J. D. Eldredge (2007). An inviscid model for vortex shedding from a deforming body. *Theor. Comput. Fluid Dyn. 21*, 343–368.

Skejic, R. (2008). (private communications).

Soh, W. K. and P. T. Fink (1971). On potential flow modelling of the action of ships' bilge keels. In *4th Aust. Conf. Hyd. Fluid Mech.*

Sørensen, O. R., H. A. Schäffer, and L. S. Sørensen (2004). Boussinesq-type modelling using an unstructured finite element technique. *Coastal Eng. 50*, 181–198.

Sun, H. and O. Faltinsen (2006). Water impact of horizontal circular cylinders and cylindrical shells. *Appl. Ocean Res. 28*, 299–311.

Tanizawa, K. (2000, October). The state of the art on numerical wavetank. In *4th Osaka Colloquium on Seakeeping of Ships*, pp. 95–114. Ship Research Institute, Tokyo, Japan.

Ursell, F. (1953). The long wave paradox in the theory of gravity waves. In *Proc. Cambridge Phil. Soc.*, Volume 49, pp. 685–694.

Venkatalaxmi, A., B. S. Padmavati, and T. Amaranath (2007). A general solution of Oseen equations. *Fluid Dyn. Res. 39*, 595–606.

Winckelmans, G. S. and A. Leonard (1993). Contributions to vortex particle methods for the computation of three-dimensional incompressible unsteady flows. *J. Comp. Phys. 109*, 247–273.

Wu, G. X. and R. Eatock Taylor (1996). Transient motion of a floating body in steep water waves. In *11th Int. Workshop on Water Waves and Floating Bodies*.

Wu, G. X. and R. Eatock Taylor (2003). The coupled finite element and boundary element analysis of nonlinear interactions between waves and bodies. *Ocean Eng. 30*, 387–400.

Yeung, R. W. (1982). The transient heaving motion of floating cylinders. *J. Engg. Math. 16*, 97–119.

Yeung, R. W. (2002). Fluid dynamics of finned bodies - from VIV to FPSO. In *Proc. 12th Int. Offshore and Polar Eng. Conf.*

Yeung, R. W., R. K. M. Seah, and J. T. Imamura (2008). Separated flow about a slender body in forward and lateral motion. In *Proc. 27th Int. Conf. on Offshore Mech. and Arctic Eng.*

Zhao, R. and O. M. Faltinsen (1993). Water entry of two-dimensional bodies. *J. Fluid Mech. 246*, 593–612.

Appendix A

The basic numerical wavetank

A.1 The discretized version of the boundary integral equation

Assuming linear variation of φ and its derivatives, the discretized version of (6.1) is

$$\alpha\varphi_i = \sum_{j=1}^{N}\left[\varphi_{j+1}\frac{I_{i,j}^{④}-\xi_j I_{i,j}^{②}}{\xi_{j+1}-\xi_j}+\varphi_j\frac{\xi_{j+1}I_{i,j}^{②}-I_{i,j}^{④}}{\xi_{j+1}-\xi_j}\right]-\sum_{j=1}^{N}\left[\sigma_{j+1}\frac{I_{i,j}^{③}-\xi_j I_{i,j}^{①}}{\xi_{j+1}-\xi_j}-\sigma_j\frac{\xi_{j+1}I_{i,j}^{①}-I_{i,j}^{③}}{\xi_{j+1}-\xi_j}\right], \tag{A.1}$$

where $\sigma_j = (\varphi_\eta)_j$ and

$$\begin{aligned} I_{i,j}^{①} &= \int_{S_j}\log r_i\,\mathrm{d}s, \quad I_{i,j}^{②} = \int_{S_j}\frac{\partial}{\partial n}\log r_i\,\mathrm{d}s,\\ I_{i,j}^{③} &= \int_{S_j}\xi\log r_i\,\mathrm{d}s, \quad I_{i,j}^{④} = \int_{S_j}\xi\frac{\partial}{\partial n}\log r_i\,\mathrm{d}s. \end{aligned} \tag{A.2}$$

The indefinite integrals are

$$\begin{aligned} I^{①} &= \xi\,(\log r-1)+\eta\,\tau, \quad I^{②} = \tau,\\ I^{③} &= \frac{1}{2}\,r^2\log r-\frac{1}{4}\,\xi^2, \quad I^{④} = \eta\log r, \end{aligned} \tag{A.3}$$

where $\tau = \operatorname{atan}(\xi/\eta)$.

In these expressions, the integration over each element is carried out in a Cartesian coordinate system (ξ,η) which is rotated and translated relative to the Earth-fixed coordinate system (x,y). The former is denoted by the auxiliary plane and the latter by the physical plane. The auxiliary plane is defined as follows. The positive ξ-direction coincides with the tangential direction of the element in the physical plane. This direction is defined by the unit tangential vector $\mathbf{s}$ of the element. Similarly, the positive η-direction coincides with the normal direction of the element in the physical plane. This direction is defined by the unit normal vector $\mathbf{n}$ of the element. This is a standard Jacobi rotation. The rotated coordinate system is next translated such that the field point is in the origin. Lengths are preserved in this procedure.

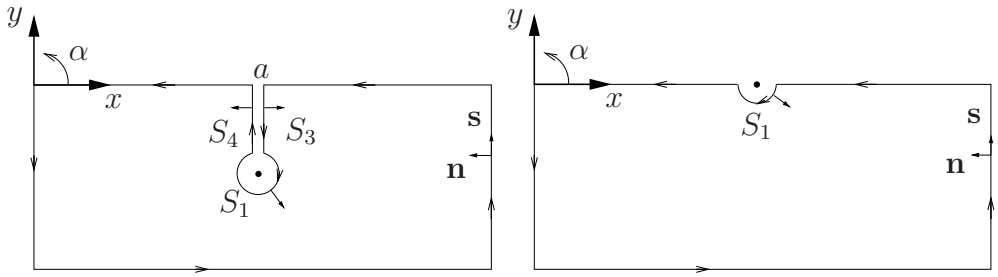

Figure A.1: The path of integration. Global direction of integration as well as α are positive in the counter-clockwise direction. The normal points into the fluid.

A.2 Exclusion of the singularity

The singularity at $r = 0$ from a source and/or dipole located inside the fluid domain is excluded by performing the integration along the path $S_3 + S_1 + S_4$ as shown in the left part of Figure A.1. Letting first the distance denoted by a go to zero, the integrals along S_3 and S_4 cancel each other exactly, as the potential is continuous while the sign of the normals are opposite. Next, letting the radius r of S_1 tend to zero, and noting that $\partial/\partial n = \partial/\partial r$ where r is the distance from the field point to the boundary S_1 and further that the integration direction is locally in the negative α direction, i.e. $ds = -R\,\mathrm{d}\alpha$, we are left with the expression in (5.3). In the present case of the field point inside the domain $\alpha = -2\pi$. When the field point is exactly on the boundary, we have the situation in the right part of Figure A.1, and the same discussion applies except the boundaries S_3 and S_4 are not introduced, and that $\alpha = -\pi$. Note that with $\mathbf{x}$ on the boundary, the first integral on the right hand side of (5.3) must be interpreted as a principal value integral, as the contribution from that point to the integral is, namely, $\alpha(\mathbf{x})\varphi(\mathbf{x})$.

A.3 Finite difference schemes for spatial differentials

Expressions for the first and second order derivatives correct to second order in the grid spacing are given in the following. It is assumed that $a/b \sim \mathcal{O}(1)$, where $a, b > 0$ are explained in Figure A.2. We define a function y as a function of the curvilinear coordinate s. For clarity in the notation we use $y_2 = y(s_{j+1})$, $y_1 = y(s_j)$ and $y_0 = y(s_{j-1})$. All expressions may be derived by direct expansion of the function y into Taylor series.

$$y\prime(s_j) \simeq \left(b^2 y_2 + (a^2 - b^2)y_1 - a^2 y_0\right)/\gamma \quad \text{(central)} \tag{A.4}$$

$$y\prime(s_j - b) \simeq \left(-b^2 y_2 + (a+b)^2 y_1 - \left(2ab + a^2\right) y_0\right)/\gamma \quad \text{(forward)} \tag{A.5}$$

$$y\prime(s_j + a) \simeq \left(\left(2ab + b^2\right) y_2 - (a+b)^2 y_1 + a^2 y_0\right)/\gamma \quad \text{(backward)} \tag{A.6}$$

$$y\prime\prime(s) \simeq \left(2b\, y_2 - (a+b)y_1 + a y_0\right)/\gamma \quad \text{(any)} \tag{A.7}$$

where the prime denotes derivative, $a = s_{j+1} - s_j$, $b = s_j - s_{j-1}$ and $\gamma = ab(a+b)$. Note that the expression for the second derivative is correct to second order in all the three nodes.

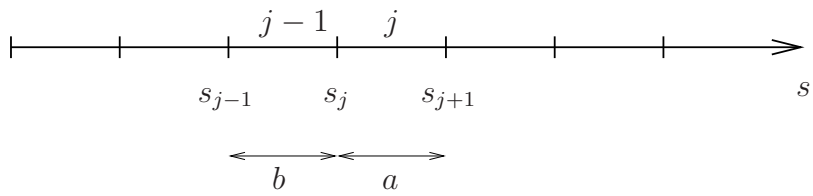

Figure A.2: The curvilinear s-axis. The indices below the curve indicate node number, while those above the curve indicate element number.

A.4 Expression for cosine spacing along boundaries

We use a cosine squared distribution of the element lengths. This may be expressed by

$$ds(x) = \left(1 - \beta \cos^2\left(\pi \frac{x}{L/2}\right)\right) \frac{ds_0}{1 - \beta/2}, \tag{A.8}$$

where $0 \leq \beta < 1$ must be given, the parameter L is the length over which one desires an uneven grid spacing and ds_0 is the element length according to an even distribution over the length L. The value of $1/(1-\beta)$ is the ratio between the longest and the shortest element. Note that with $\beta = 0$ we recover an even distribution of the nodes.

Appendix B

Inviscid vortex tracking model

B.1 The discretized version of the boundary integral equation including flow separation

Assuming linear variation of φ and its derivatives, the discretized version of (6.1) is

$$\alpha\varphi_i = \sum_{j=1}^{N}\left[\varphi_{j+1}\frac{I^{④}_{i,j}-\xi_j I^{②}_{i,j}}{\xi_{j+1}-\xi_j}+\varphi_j\frac{\xi_{j+1}I^{②}_{i,j}-I^{④}_{i,j}}{\xi_{j+1}-\xi_j}\right]-\sum_{j=1}^{N}\left[\sigma_{j+1}\frac{I^{③}_{i,j}-\xi_j I^{①}_{i,j}}{\xi_{j+1}-\xi_j}-\sigma_j\frac{\xi_{j+1}I^{①}_{i,j}-I^{③}_{i,j}}{\xi_{j+1}-\xi_j}\right]$$
$$-\sum_{j=1}^{N_V}\left[\Gamma_{j+1}\frac{I^{④}_{i,j}-\xi_j I^{②}_{i,j}}{\xi_{j+1}-\xi_j}+\Gamma_j\frac{\xi_{j+1}I^{②}_{i,j}-I^{④}_{i,j}}{\xi_{j+1}-\xi_j}\right], \tag{B.1}$$

following the same definitions of ξ, η, σ and the I-terms as in connection with equation (A.1).

B.2 The discretized version of the free shear layer velocity

The discretized version of (6.2) is, when considering the velocity $\boldsymbol{U_c}$ at the mid-point of element i of the unsimplified part of the free shear layer S_v,

$$-2\pi\,\nabla\varphi_i=\frac{1}{\pi}\frac{\Gamma_{i+1}+\Gamma_i}{\xi_{i+1}-\xi_i}+\sum_{j=1}^{N}\left[\varphi_{j+1}\frac{\mathbf{J}^{④}_{i,j}-\xi_j\mathbf{J}^{②}_{i,j}}{\xi_{j+1}-\xi_j}+\varphi_j\frac{\xi_{j+1}\mathbf{J}^{②}_{i,j}-\mathbf{J}^{④}_{i,j}}{\xi_{j+1}-\xi_j}\right]$$
$$-\sum_{j=1}^{N}\left[\sigma_{j+1}\frac{\mathbf{J}^{③}_{i,j}-\xi_j\mathbf{J}^{①}_{i,j}}{\xi_{j+1}-\xi_j}-\sigma_j\frac{\xi_{j+1}\mathbf{J}^{①}_{i,j}-\mathbf{J}^{③}_{i,j}}{\xi_{j+1}-\xi_j}\right]-\sum_{j\neq i}^{N_V}\left[\Gamma_{j+1}\frac{\mathbf{J}^{④}_{i,j}-\xi_j\mathbf{J}^{②}_{i,j}}{\xi_{j+1}-\xi_j}+\Gamma_j\frac{\xi_{j+1}\mathbf{J}^{②}_{i,j}-\mathbf{J}^{④}_{i,j}}{\xi_{j+1}-\xi_j}\right], \tag{B.2}$$

where

$$\mathbf{J}^{①}_{i,j}=\int_{S_j}\nabla\log r_i\,\mathrm{d}s,\quad \mathbf{J}^{②}_{i,j}=\int_{S_j}\frac{\partial}{\partial n_\xi}\nabla\log r_i\,\mathrm{d}s,$$
$$\mathbf{J}^{③}_{i,j}=\int_{S_j}\xi\nabla\log r_i\,\mathrm{d}s,\quad \mathbf{J}^{④}_{i,j}=\int_{S_j}\xi\frac{\partial}{\partial n_\xi}\nabla\log r_i\,\mathrm{d}s. \tag{B.3}$$

Here, $\nabla = (\partial/\partial x, \partial/\partial y)$ while $\partial/\partial n_\xi$ is the normal derivative with respect to the integration parameter $\boldsymbol{\xi}$. The indefinite integrals are

$$\begin{aligned} \mathbf{J}^{①} &= (-\log r,\, -\tau), \quad \mathbf{J}^{②} = \left(-\frac{\eta}{r^2},\, \frac{\xi}{r^2}\right), \\ \mathbf{J}^{③} &= (-\xi + \eta\,\tau,\, -\eta \log r), \quad \mathbf{J}^{④} = \left(-\frac{\eta\,\xi}{r^2} + \tau,\, \frac{\xi^2}{r^2} - \log r\right), \end{aligned} \tag{B.4}$$

where as in Appendix A, $\tau = \operatorname{atan}(\xi/\eta)$. In the derivation of the indefinite integrals we found Gradshteyn and Ryzhik (2000) useful (see Section 2.103 and formula (2.147)).

Appendix C

The in- and out-flow of boundary layers

C.1 Numerical integration of the convolution integral

We here derive (7.2), the numerical approximation of the convolution integral (7.1). In the derivation, a constant time-step Δt is assumed. We first separate the integral from (7.1) into two sub-integrals,

$$I(t) = \underbrace{\int_0^{t-h} \frac{f(\tau)}{\sqrt{t-\tau}}\,\mathrm{d}\tau}_{I_t(t)} + \underbrace{\int_{t-h}^{t} \frac{f(\tau)}{\sqrt{t-\tau}}\,\mathrm{d}\tau}_{I_h(t)}, \tag{C.1}$$

where $h < t$. We integrate I_h by parts,

$$I_h(t) = 2\left(f(t-h)\sqrt{h} + \int_{t-h}^{t} \frac{\mathrm{d}f}{\mathrm{d}\tau}(\tau)\sqrt{t-\tau}\,\mathrm{d}\tau\right). \tag{C.2}$$

This procedure removes the singularity. We choose $h = \Delta t$, and use the trapezoidal rule for time integration. Using the trapezoidal rule will give estimates correct to second order in time,

$$I_h(t) \simeq 2\left(f(t-\Delta t\,)\sqrt{\Delta t} + \frac{1}{2}\frac{\mathrm{d}f}{\mathrm{d}\tau}(t-\Delta t\,)\sqrt{t-(t-\Delta t\,)}\Delta t\right) \tag{C.3}$$

We approximate the derivative of f to first order in time by a backward difference scheme, but the expression is still second order in time. We get

$$\begin{aligned} I_h(t) &\simeq 2\left(f^{n-1}\sqrt{\Delta t} + \frac{1}{2}\frac{f^n - f^{n-1}}{\Delta t}\sqrt{\Delta t}\,\Delta t\right) \\ &= \left(f^n + f^{n-1}\right)\sqrt{\Delta t}\,. \end{aligned} \tag{C.4}$$

For I_t we get, using the trapezoidal rule, that

$$\begin{aligned} I_t(t) &\simeq \sum{}''_{i=1}^{n-1} \frac{f^i}{\sqrt{n\Delta t\, - i\Delta t}}\Delta t \;= \left(\sum{}''_{i=1}^{n-1} \frac{f^{n-i}}{\sqrt{i}}\right)\sqrt{\Delta t} \\ &= \left(\sum_{i=1}^{n-1} \frac{f^{n-i}}{\sqrt{i}} - \frac{1}{2}\left(f^{n-1} + \frac{f^1}{\sqrt{n-1}}\right)\right)\sqrt{\Delta t}\,, \end{aligned} \tag{C.5}$$

where by $\sum''$ we mean that the first and last terms are multiplied by one half. If we add (C.4) and (C.5) we obtain that of (7.2).

Appendix D

Force calculations

D.1 Rotational motion

In the following statements we consider three-dimensional space for the sake of using the cross-product, but with translational motion only in the x- and y-directions and rotational motion only in roll, denoted θ. The ship is thought to point towards the negative direction of the z-axis with the z-axis being the direction perpendicular to and positive out of the paper sheet with unit vector $\mathbf{k}$. The unit vectors in the positive x- and y-directions are denoted by the usual $\mathbf{i}$ and $\mathbf{j}$.

The normal and tangential unit vectors for the moments are the vectors $\mathbf{r} \times \mathbf{n}$ and $\mathbf{r} \times \mathbf{s}$ where $\mathbf{r} = \mathbf{x} - \mathbf{x}_G$ is the distance vector from the instantaneous center of gravity of the body $\mathbf{x}_G$ to a point $\mathbf{x}$ on the body surface. The third component, corresponding to roll in our case, are then

$$\begin{aligned} n_\theta &= (x - x_G)n_y - (y - y_G)n_x \quad \text{on } S_B, \\ s_\theta &= (x - x_G)s_y - (y - y_G)s_x \quad \text{on } S_B, \end{aligned} \tag{D.1}$$

The velocity of any point on the body is $\mathbf{v}_B = \dot{\mathbf{x}}_G + \boldsymbol{\omega} \times \mathbf{r}$ where in the case of roll only and using the usual right hand rule, $\boldsymbol{\omega} = \dot{\theta}\,\mathbf{k}$ such that $\boldsymbol{\omega} \times \mathbf{r} = (-y\mathbf{i} + x\mathbf{j})\,\dot{\theta}$. The normal velocity of the body is $\mathbf{v}_B \cdot \mathbf{n} = (\dot{\mathbf{x}}_G + \boldsymbol{\omega} \times \mathbf{r}) \cdot \mathbf{n} = \dot{\mathbf{x}}_G \cdot \mathbf{n} + \boldsymbol{\omega} \cdot \mathbf{r} \times \mathbf{n}$, where the last equality is due to the interchangeability of the terms in the triple product. The same applies for the tangential velocity except we consider $\mathbf{v}_B \cdot \mathbf{s}$. The normal and tangential velocities of the body are then

$$\begin{aligned} \frac{\partial \varphi}{\partial n} &= (\dot{x}_G - \dot{\theta}(y - y_G))n_x + (\dot{y}_G + \dot{\theta}(x - x_G))n_y \quad \text{on } S_B, \\ \frac{\partial \varphi}{\partial s} &= (\dot{x}_G - \dot{\theta}(y - y_G))s_x + (\dot{y}_G + \dot{\theta}(x - x_G))s_y \quad \text{on } S_B. \end{aligned} \tag{D.2}$$

D.2 The Gauss-, Stokes- and Transport-theorems

We consider a closed domain Ω enclosed by the surface S and define the normal vector $\mathbf{n}$ along S to be positive when pointing into Ω. The theorems known as Gauss' and Stokes' theorems may be written as

$$\int_S f \circ \mathbf{n}\, \mathrm{d}s = -\int_\Omega \nabla \circ f\, \mathrm{d}s, \tag{D.3}$$

where $\circ$ is either nothing, cross- or dot product. If $\circ$ is nothing, f is a scalar function. If $\circ$ is the dot- or cross-product, f is a vector function. In any case f must be defined over $\Omega \cup S$. Note the negative sign due to the direction of the normal. In the case that $\circ$ is nothing or dot-product, (D.3) is Gauss' theorem. In the case $\circ$ is cross-product (D.3) is Stokes' theorem.

The Transport theorem (see e.g. (Newman 1977)) is a special case of a more general law of conservation. It says

$$\frac{\mathrm{d}}{\mathrm{d}t}\int_{\Omega(t)} f \,\mathrm{d}s = \int_{\Omega} f_t \,\mathrm{d}s - \int_S fU \,\mathrm{d}s, \tag{D.4}$$

where f may be a scalar or vector function, and U is the normal velocity of the boundary S being positive into the domain with the current convention that the normal points into the domain.

As a special case of the Transport theorem, consider a curve $c(s,t) = (x(s,t), y(s,t))$ parametrised by the arc length s in two-dimensional space and define a continuous function $f(x,y,t)$ over this curve. The total time derivative of the integral of f over this curve is

$$\frac{\mathrm{d}}{\mathrm{d}t}\int_{a(t)}^{b(t)} f(s,t) \,\mathrm{d}s = \int_a^b f_t \,\mathrm{d}s + [uf]_a + [uf]_b \,, \tag{D.5}$$

where u_a and u_b are the tangential velocities of the end points of the curve c, or the rate at which the domain c expands or contracts, being positive in the direction of expansion. Note that this definition of positive direction is opposite to that in equation (D.4).

D.3 Contribution from the free shear layer

We show in the following the equality (8.7). First we let $S_V := S_V^-$. We then have that

$$\begin{aligned}\int_{S_V^{\pm}} &\left(\frac{1}{2}(\varphi_s^2 - \varphi_n^2)\mathbf{n} - \varphi_n\varphi_s\mathbf{s}\right) \,\mathrm{d}s \\ &= \int_{S_V} \left(\frac{1}{2}\left((\varphi_s^-)^2 - (\varphi_s^+)^2\right)\mathbf{n} - \varphi_n(\varphi_s^- - \varphi_s^+)\,\mathbf{s}\right) \,\mathrm{d}s,\end{aligned} \tag{D.6}$$

due to opposite sign of the unit vectors along S_V^- and S_V^+. We may rewrite the squared terms as

$$\frac{1}{2}\left((\varphi_s^-)^2 - (\varphi_s^+)^2\right) = \frac{1}{2}(\varphi_s^- + \varphi_s^+)(\varphi_s^- - \varphi_s^+). \tag{D.7}$$

We recognize that in both (D.6) and in (D.7) we have the term $\Gamma_s = \varphi_s^+ - \varphi_s^-$. We further recognize in (D.7) the tangential velocity of the free shear layer $U_{cs} = \frac{1}{2}(\varphi_s^- + \varphi_s^+)$. Lastly, since the normal velocity is continuous across the free shear layer we may write $\varphi_n = \boldsymbol{U_c} \cdot \mathbf{n} = U_{cn}$.

We need to pay extra attention to the Riemann cuts, the dashed line in Figure D.1, which has an essential singularity of the potential at the far end. We show here that the contribution over the Riemann cut to the integral (8.7) is zero. First note that the contributions along S_{R1} cancels that along S_{R3} due to opposite signs, i.e. $\mathbf{n}^- = -\mathbf{n}^+$ and

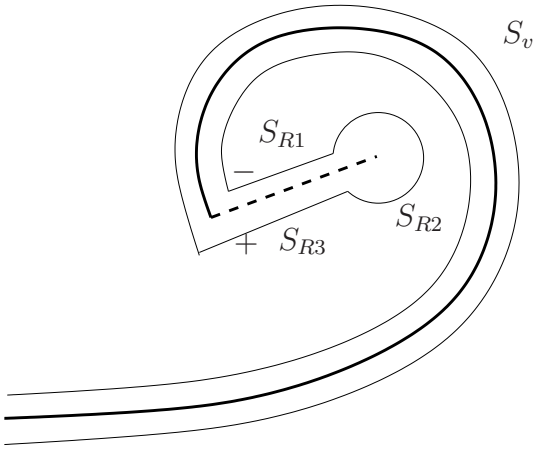

Figure D.1: Integration along the Riemann cut $S_R = S_{R1} + S_{R2} + S_{R3}$ after the limiting process.

$\varphi_n^- \varphi_s^- \mathbf{s}^- = -\varphi_n^+ \varphi_s^+ \mathbf{s}^+$ and $(\varphi_s^-)^2 = (\varphi_s^+)^2$. The only remaining contribution is over S_{R2}. Since near the point vortex, $\varphi_n \to 0$ due to the point vortex behaviour of zero normal velocity, the only possible contribution is from the term $\frac{1}{2}(\varphi_s)^2 \mathbf{n}$. Now, given a small, but finite radius of S_{R2}, φ_s is constant along the curve, and may be pulled outside the integral. But the integral over a complete circle of its normal is zero, hence the contribution is zero. And this shows the equality in equation (8.7)

D.4 Numerical integration of the K_j - terms

The integrals (8.12) are approximated by the following sums:

$$
\begin{aligned}
&K_1 \simeq \sum_{i=1}^{N_B} \varphi_{mi} \mathbf{n}_i \Delta s_i, \quad K_2 \simeq \sum_{i=1}^{N_F} \varphi_{mi} \mathbf{n}_i \Delta s_i, \; K_3 \simeq \sum_{i=1}^{N_B} y_{mi} \mathbf{n}_i \Delta s_i, \quad K_4 \simeq \sum_{i=1}^{N_F} y_{mi} \mathbf{n}_i \Delta s_i \\
&K_5 \simeq \sum_{i=1}^{N_B} f_{mi} \mathbf{n}_i \Delta s_i, \quad K_6 \simeq \sum_{i=1}^{N_F} f_{mi} \mathbf{n}_i \Delta s_i, \; K_7 \simeq u_A \varphi_A \mathbf{n}_A, \quad K_8 \simeq u_B \varphi_B \mathbf{n}_B \\
&K_9 \simeq \sum_{i=1}^{N_v} \mathbf{n}_i \Gamma_{mi} \Delta s_i + \sum_{i=1}^{N_R} \begin{pmatrix} -(y_{Ri+1} - y_{Ri}) \\ x_{Ri+1} - x_{Ri} \\ 0.5(x_{Ri+1}^2 - x_{Ri}^2 + y_{Ri+1}^2 - y_{Ri}^2) \end{pmatrix} \Gamma_i, \\
&K_{10} \simeq \sum_{i=1}^{N_v} ((-\boldsymbol{U}_{\boldsymbol{c}mi} \cdot \mathbf{s}_i)\, \mathbf{n}_i + (\boldsymbol{U}_{\boldsymbol{c}mi} \cdot \mathbf{n}_i)\, \mathbf{s}_i) \Delta \Gamma_i
\end{aligned}
\tag{D.8}
$$

where subscript m indicates values at the mid-point of an element, i.e. $\varphi_{mi} = 0.5\,(\varphi_{i+1} + \varphi_i)$, $y_{mi} = 0.5\,(y_{i+1} + y_i)$, $\Gamma_{mi} = 0.5\,(\Gamma_{i+1} + \Gamma_i)$, $\boldsymbol{U}_{\boldsymbol{c}mi} = 0.5\,(\boldsymbol{U}_{\boldsymbol{c}i+1} + \boldsymbol{U}_{\boldsymbol{c}i})$, $\Delta\Gamma_i = \Gamma_{i+1} - \Gamma_i$, Δs_i is the length of element number i, and (x_R, y_R) is the coordinate of the end points of each Riemann cut relative to the center of gravity of the body. The intersection points A and B will in general lie on a free-surface element. Only the part enclosed by the control

surface should be included in the calculation. The terms $u_A\varphi_A$ and $u_B\varphi_B$ are estimated by linear interpolation from the two end-points of the intersecting free surface elements.

Appendix E

Model tests - tables and selected results

The figures and tables presented here are referred to in the main text and not further explained within this appendix.

Table E.1: The locations of wave gauges and mid-ship positions in the September and November 2006 tests. Distances x measured from the mean position of piston wave flap as indicated in Figures 9.4 and 9.5.

	September 2006 x [m]	November 2006 x [m]
w1	3.50	3.50
w2	5.00	5.00
w3	6.50	6.52
w4	13.5	12.06
w5	16.91	16.90
w6	17.38	17.40
w7	17.65	17.87
w8	17.91	18.10
w9	17.91	18.10
w10	18.75	18.95
w11	18.70	18.98
w12	18.75	18.95
Mid-ship position	18.30	18.50

Table E.2: Test matrix September 2006 tests. Subscript 0 means deep water limit. Light grey background indicates shallow water waves ($\lambda_0/h > 10$).

Water depth $h = 0.23$m								
	$b = 0.22$m				$b = 0.32$m			
	$H_0/\lambda_0 = 1/40$		$H_0/\lambda_0 = 1/60$		$H_0/\lambda_0 = 1/40$		$H_0/\lambda_0 = 1/60$	
$T\,[s]$	test	wave	test	wave	test	wave	test	wave
0.72	3100	8105	3000	8005	2100	8105	2000	8005
0.84	3110	8115	3010	8015	2110	8115	2010	8015
0.96	3120	8125	3020	8025	2120	8125	2020	8025
1.08	3130 - 3134	8135	3030	8035	2130	8135	2030	8035
1.20	3140	8145	3040	8045	2140	8145	2040	8045
1.31	3150	8155	3050	8055	2150	8155	2050	8055
1.43	3160 - 3164	8165	3060 - 3064	8065	2160	8165	2060	8065
1.55	3170	8175	3070	8075	2170	8175	2070	8075
1.67	3180	8185	3080	8085	2180	8185	2080	8085
1.79			3090 - 3094	8095			2091	8095

Water depth $h = 0.29$m								
	$b = 0.22$m				$b = 0.32$m			
	$H_0/\lambda_0 = 1/40$		$H_0/\lambda_0 = 1/60$		$H_0/\lambda_0 = 1/40$		$H_0/\lambda_0 = 1/60$	
$T\,[s]$	test	wave	test	wave	test	wave	test	wave
0.72	3300	8305	3200	8205	2300	8305	2100	8205
0.84	3310	8315	3210	8215	2310	8315	2110	8215
0.96	3320	8325	3220	8225	2320	8325	2120	8225
1.08	3330 - 3334	8335	3230	8235	2330	8335	2130	8235
1.20	3340	8345	3240	8245	2340	8345	2140	8245
1.31	3350	8355	3250	8255	2350	8355	2150	8255
1.43	3360 - 3364	8365	3260 - 3264	8265	2360	8365	2160	8265
1.55	3370	8375	3270	8275	2370	8375	2170	8275
1.67	3380	8385	3280	8285	2380	8385	2180	8285
1.79			3290 - 3294	8295			2191	8295

Table E.3: Test matrix November 2006 tests. Subscript 0 means deep water limit.

Water depth $h = 0.40$m, terminal gap width $b = 0.22$m (Case 1)									
	$H_0/\lambda_0 = 1/70$			$H_0/\lambda_0 = 1/115$			$H_0/\lambda_0 = 1/170$		
$T\,[s]$	test	$H\,[m]$	wave	test	$H\,[m]$	wave	test	$H\,[m]$	wave
1.43	5000	0.033	8807	5500	0.022	9007	5700	0.018	9207
1.55	5010	0.038	8817	5510	0.025	9017	5710	0.021	9217
1.67	5020	0.043	8827	5520	0.029	9027	5720	0.025	9227
1.79	5030	0.048	8837	5530	0.032	9037	5730	0.029	9237
1.91	5040	0.054	8847	5540	0.036	9047	5741	0.030	9247
1.95	5051	0.060	8857	5550	0.040	9057	5750	0.032	9257
1.99	5060	0.062	8867	5560	0.041	9067	5760	0.033	9267
2.03	5071	0.064	8877	5570	0.042	9077	5771	0.035	9277
2.07	5080	0.066	8887	5580	0.044	9087	5780	0.036	9287
2.11	5091	0.068	8897	5590	0.045	9097	5790	0.038	9297
2.15	5100	0.070	8907	5600	0.047	9107	5800	0.043	9307
2.27	5110	0.072	8917	5610	0.048	9117	5810	0.048	9317
2.39	5120	0.079	8927	5620	0.053	9127	5820	0.054	9327
2.51	5130	0.086	8937	5630	0.057	9137	5830	0.060	9337
2.63	5140	0.093	8947	5640	0.062	9147	5840	0.066	9347

Water depth $h = 0.29$m												
Terminal gap width $b = 0.22$m (Case 2)							Terminal gap width $b = 0.11$m (Case 3)					
	$H_0/\lambda_0 = 1/115$			$H_0/\lambda_0 = 1/170$				$H_0/\lambda_0 = 1/115$			$H_0/\lambda_0 = 1/170$	
$T\,[s]$	test	$H\,[m]$	wave	test	$H\,[m]$	wave	$T\,[s]$	test	$H\,[m]$	wave	test	$H\,[m]$	wave
1.79	4000	0.033	8401	4500	0.022	8601	1.31	6000	0.018	8550	6200	0.012	8750
1.91	4010	0.038	8411	4510	0.025	8611	1.43	6010	0.021	8552	6210	0.014	8752
2.03	4020	0.043	8421	4520	0.029	8621	1.55	6020	0.025	8554	6220	0.017	8754
2.15	4030	0.048	8431	4530	0.032	8631	1.67	6030	0.029	8556	6230	0.019	8756
2.27	4040	0.054	8441	4540	0.036	8641	1.71	6041	0.030	8558	6240	0.020	8758
2.39	4050	0.060	8451	4550	0.040	8651	1.75	6050	0.032	8560	6250	0.021	8760
2.43	4060	0.062	8461	4560	0.041	8661	1.79	6060	0.033	8401	6260	0.022	8601
2.47	4070	0.064	8471	4570	0.042	8671	1.83	6071	0.035	8572	6270	0.023	8762
2.51	4080	0.066	8481	4580	0.044	8681	1.87	6080	0.036	8574	6280	0.024	8764
2.55	4090	0.068	8491	4590	0.045	8691	1.91	6090	0.038	8411	6290	0.025	8611
2.59	4100	0.070	8501	4600	0.047	8701	2.03	6100	0.043	8421	6300	0.029	8621
2.63	4110	0.072	8511	4610	0.048	8711	2.15	6110	0.048	8431	6310	0.032	8631
2.75	4120	0.079	8521	4620	0.053	8721	2.27	6120	0.054	8441	6320	0.036	8641
2.87	4130	0.086	8530	4630	0.057	8731	2.39	6130	0.060	8451	6330	0.040	8651
2.99	4140	0.093	8540	4640	0.062	8740	2.51	6140	0.066	8461	6340	0.044	8661

Table E.4: Test matrix June 2008 tests. Water depth $h = 0.88$m

Terminal gap width $b = 0.08$m (Case A)			Terminal gap width $b = 0.06$m (Case B)		
$T\,[s]$	$H/\lambda \simeq 1/170$	$H/\lambda \simeq 1/85$	$T\,[s]$	$H/\lambda \simeq 1/170$	$H/\lambda \simeq 1/85$
0.60	40010	40210	0.60	40510	40710 - 40711
0.65	40020	40220	0.65	40520	40720
0.70	40030	40230	0.70	40530	40730
0.72	40040	40240	0.71	40540	40740
0.74	40050	40250	0.72	40550	40750
0.75	40060	40260	0.73	40560	40760
0.76	40070	40270	0.735	40570 - 40572	40770
0.77	40080 - 40082	40280 - 40281	0.74	40580 - 40582	40780 - 40783
0.776	40090 - 40094	40290 - 40294	0.75	40590 - 40592	40790 - 40793
0.78	40100 - 40101	40300 - 40301	0.76	40600 - 40601	40800 - 40801
0.79	40110	40310	0.78	40610	40810
0.80	40120	40320	0.78	40620	40820
0.82	40130	40330	0.80	40630	40830 - 40831
0.85	40140	40340	0.85	40640	40840
0.90	40150	40350	0.90	40650	40850
1.00	40160	40360	1.00	40660	40860

Table E.5: Specifics of waves in September 2006 tests according to linear theory.

						$H_0/\lambda_0 = 1/60$			$H_0/\lambda_0 = 1/40$		
T	λ	λ_0	C_g	C_{g0}	h/λ_0	H_0	H	H/λ	H_0	H	H/λ
$h = 0.23$m											
0.72	0.77	0.81	0.63	0.54	0.28	0.014	0.012	1/60	0.020	0.019	1/40
0.84	0.99	1.10	0.77	0.59	0.21	0.018	0.016	1/59	0.028	0.024	1/39
0.96	1.20	1.44	0.90	0.63	0.16	0.024	0.020	1/55	0.036	0.030	1/37
1.08	1.41	1.82	1.00	0.65	0.13	0.030	0.025	1/51	0.046	0.037	1/34
1.20	1.61	2.25	1.08	0.67	0.10	0.038	0.030	1/46	0.056	0.044	1/31
1.31	1.79	2.68	1.14	0.68	0.09	0.045	0.035	1/42	0.067	0.052	1/28
1.43	1.99	3.19	1.19	0.69	0.07	0.053	0.041	1/39	0.080	0.061	1/26
1.55	2.18	3.75	1.23	0.70	0.06	0.063	0.047	1/35	0.094	0.071	1/23
1.67	2.37	4.35	1.27	0.71	0.05	0.073	0.054	1/32	0.109	0.081	1/21
1.79	2.56	5.00	1.30	0.71	0.05	0.083	0.062	1/30	0.125	0.093	1/20
$h = 0.29$m											
0.72	0.79	0.81	0.60	0.55	0.36	0.014	0.013	1/60	0.020	0.019	1/40
0.84	1.04	1.10	0.75	0.62	0.26	0.018	0.017	1/60	0.028	0.025	1/40
0.96	1.28	1.44	0.89	0.67	0.20	0.024	0.021	1/58	0.036	0.031	1/39
1.08	1.52	1.82	1.01	0.70	0.16	0.030	0.025	1/55	0.046	0.038	1/37
1.20	1.75	2.25	1.11	0.73	0.13	0.038	0.030	1/51	0.056	0.046	1/34
1.31	1.96	2.68	1.19	0.75	0.11	0.045	0.035	1/47	0.067	0.053	1/32
1.43	2.18	3.19	1.26	0.76	0.09	0.053	0.041	1/44	0.080	0.062	1/29
1.55	2.4	3.75	1.32	0.77	0.08	0.063	0.048	1/40	0.094	0.072	1/27
1.67	2.62	4.35	1.36	0.78	0.07	0.073	0.055	1/37	0.109	0.083	1/25
1.79	2.84	5.00	1.40	0.79	0.06	0.083	0.063	1/34	0.125	0.094	1/23

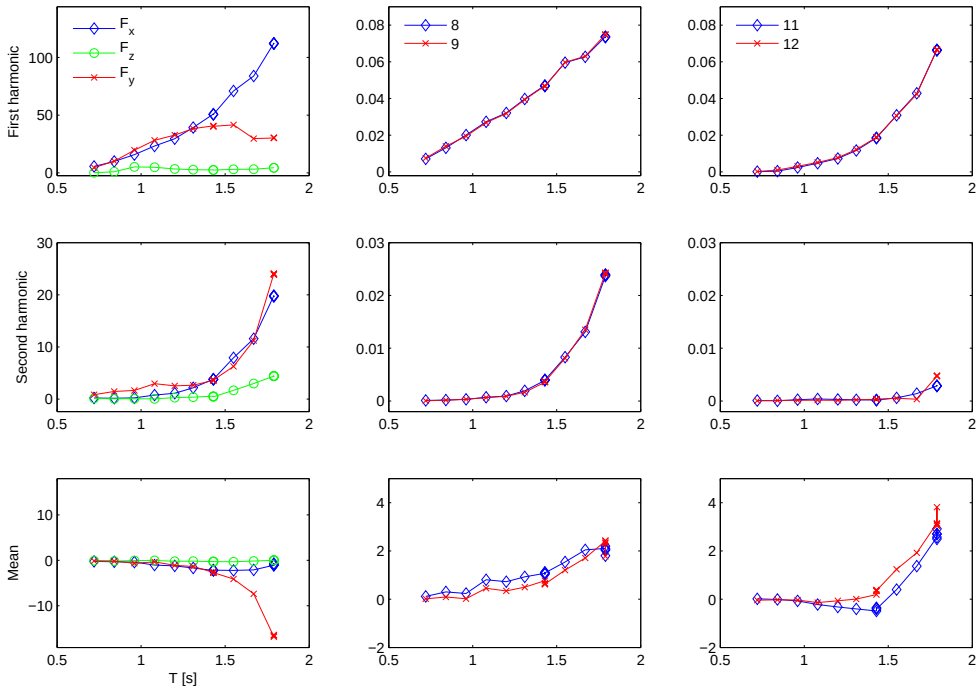

Figure E.1: Selection of condensed results from tests with fixed ship section (September 2006 tests), with particulars $b = 0.22$m, $h = 0.29$m and $H_0/\lambda_0 = 1/60$. The numbers in the legend correspond to wave gauge number. Force in [N] and wave elevation in [m]. Note that F_y is vertical force while F_z is transverse force in our coordinate system.

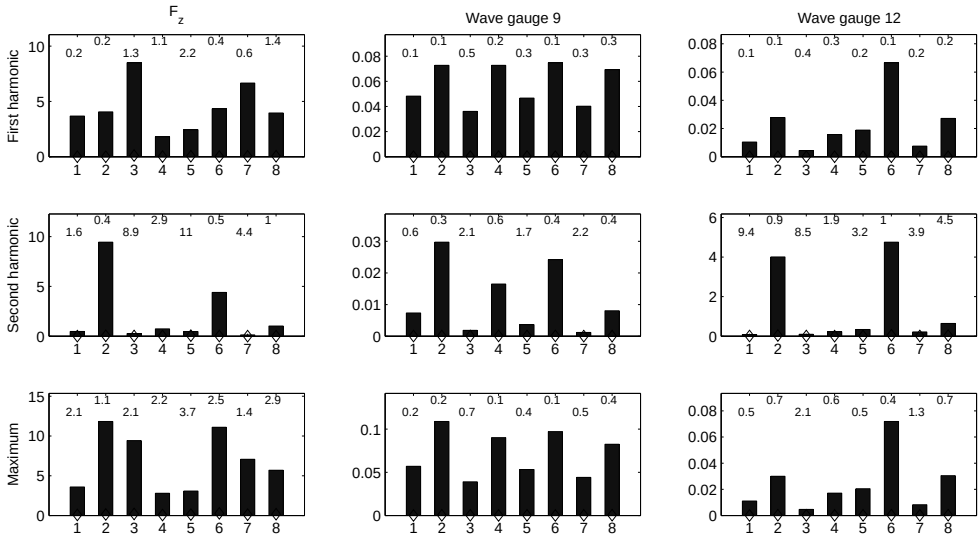

Figure E.2: Selection of results of repetition tests where the horizontal axis ticks 1-8 correspond to tests 3060, 3090, 3130, 3160, 3260, 3290, 3330 and 3360 and their respective four repetitions. Bars represent mean values and diamonds the standard deviation relative to the mean value in percentage, also given by numbers above the bars.

Appendix F

Time-series from the studies

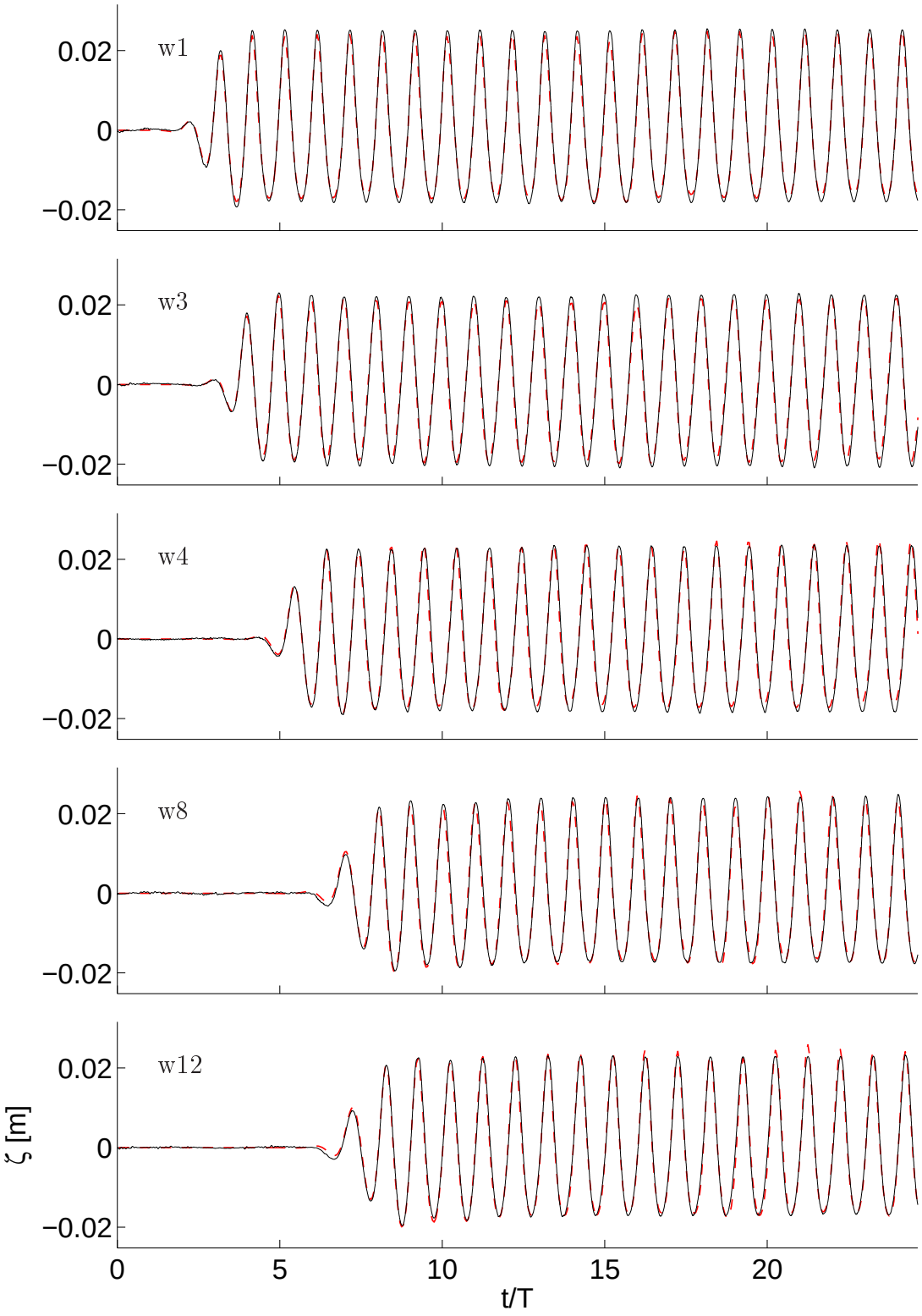

Figure F.1: Fixed ship section study. Wave calibration for a chosen test in Case 1 ($h/B = 0.625$ and $b/B = 0.34$) with wave frequency $\omega/\sqrt{g/B} = 0.791$. Solid curves represent model tests, dashed lines nonlinear simulations (BEM).

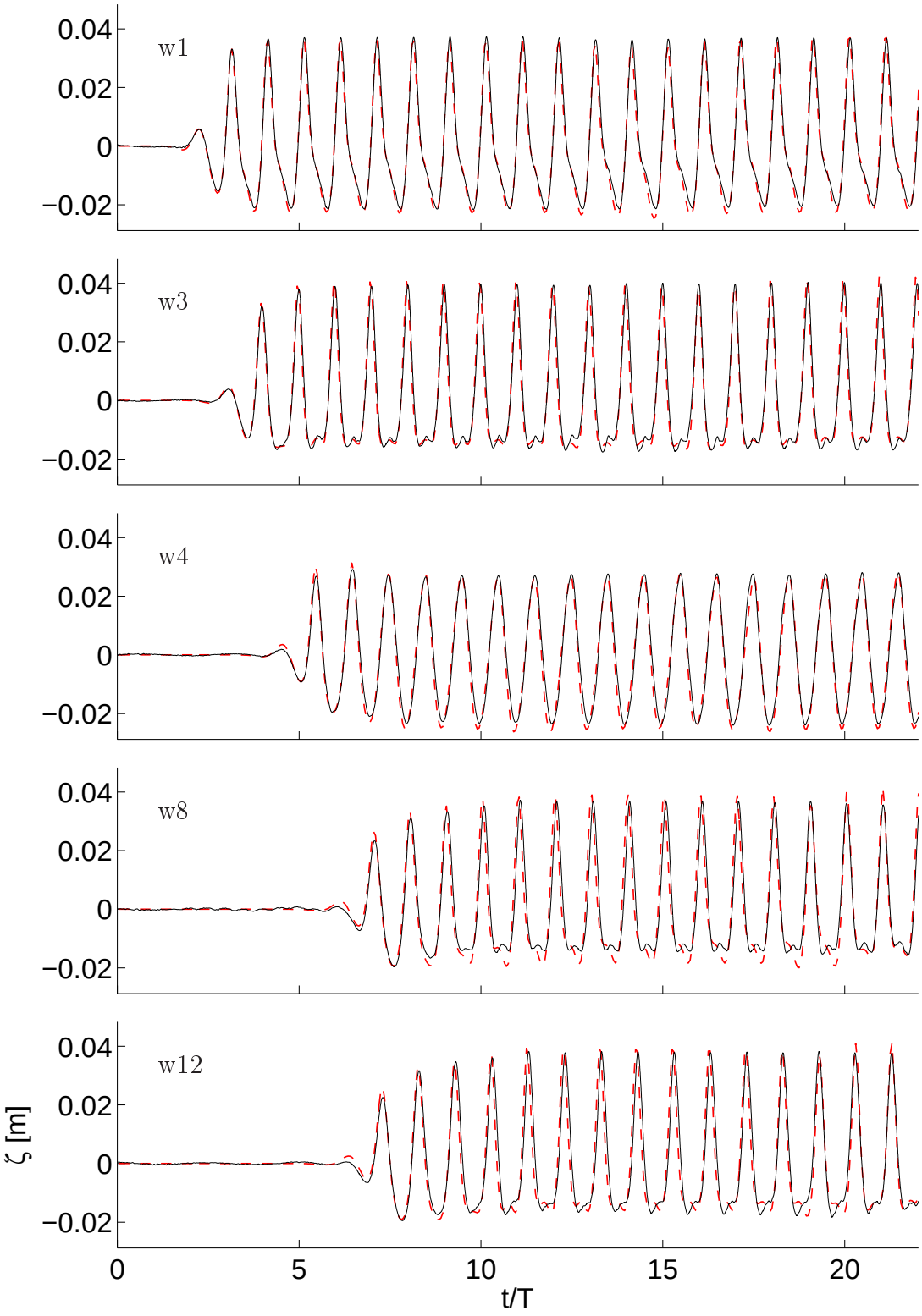

Figure F.2: Fixed ship section study. Wave calibration for a chosen test in Case 2 ($h/B = 0.43$ and $b/B = 0.34$) with wave frequency $\omega/\sqrt{g/B} = 0.707$. Solid curves represent model tests, dashed lines nonlinear simulations (BEM).

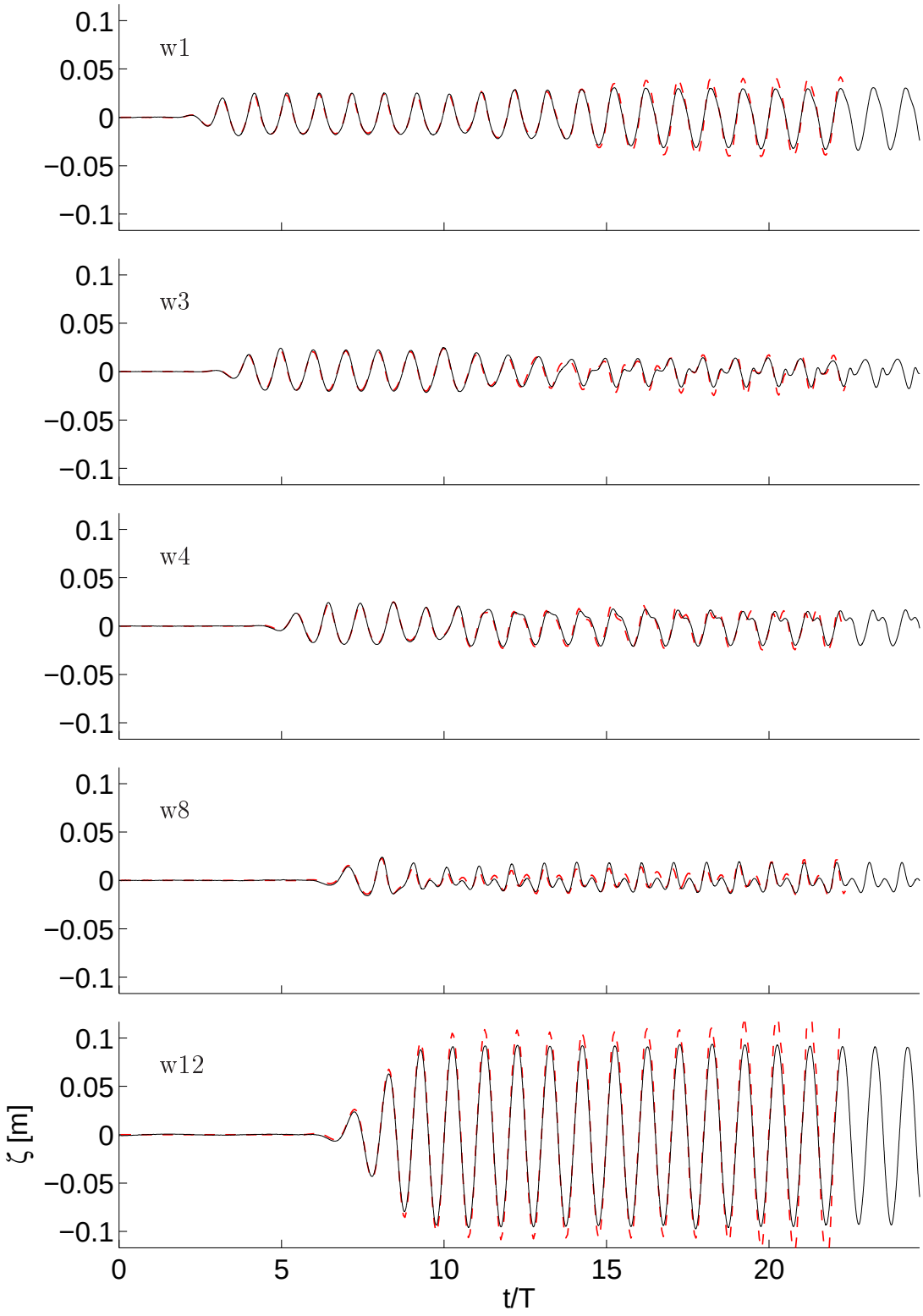

Figure F.3: Same case as in Figure F.1, but with ship section and terminal.

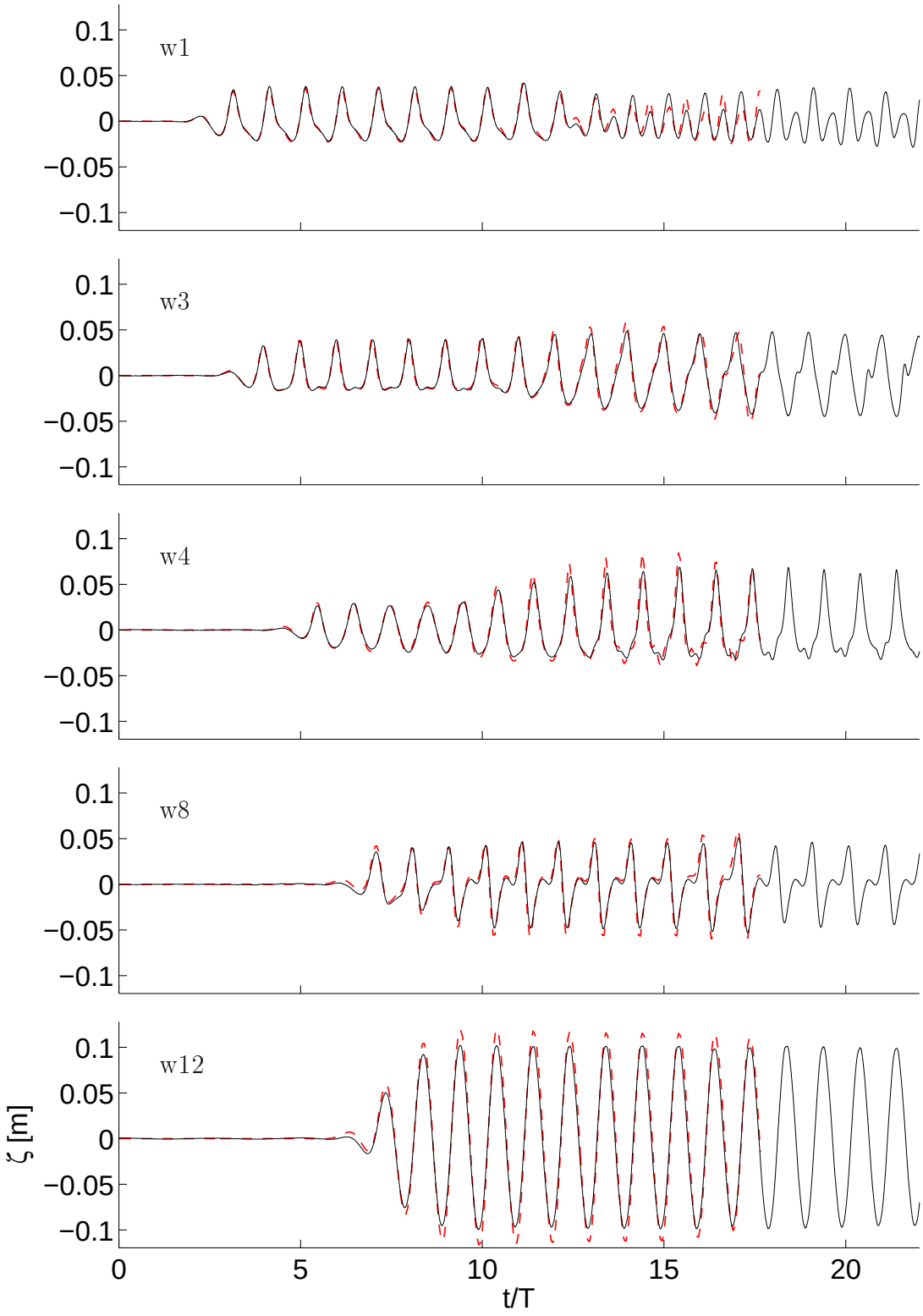

Figure F.4: Same case as in Figure F.2, but with ship section and terminal.

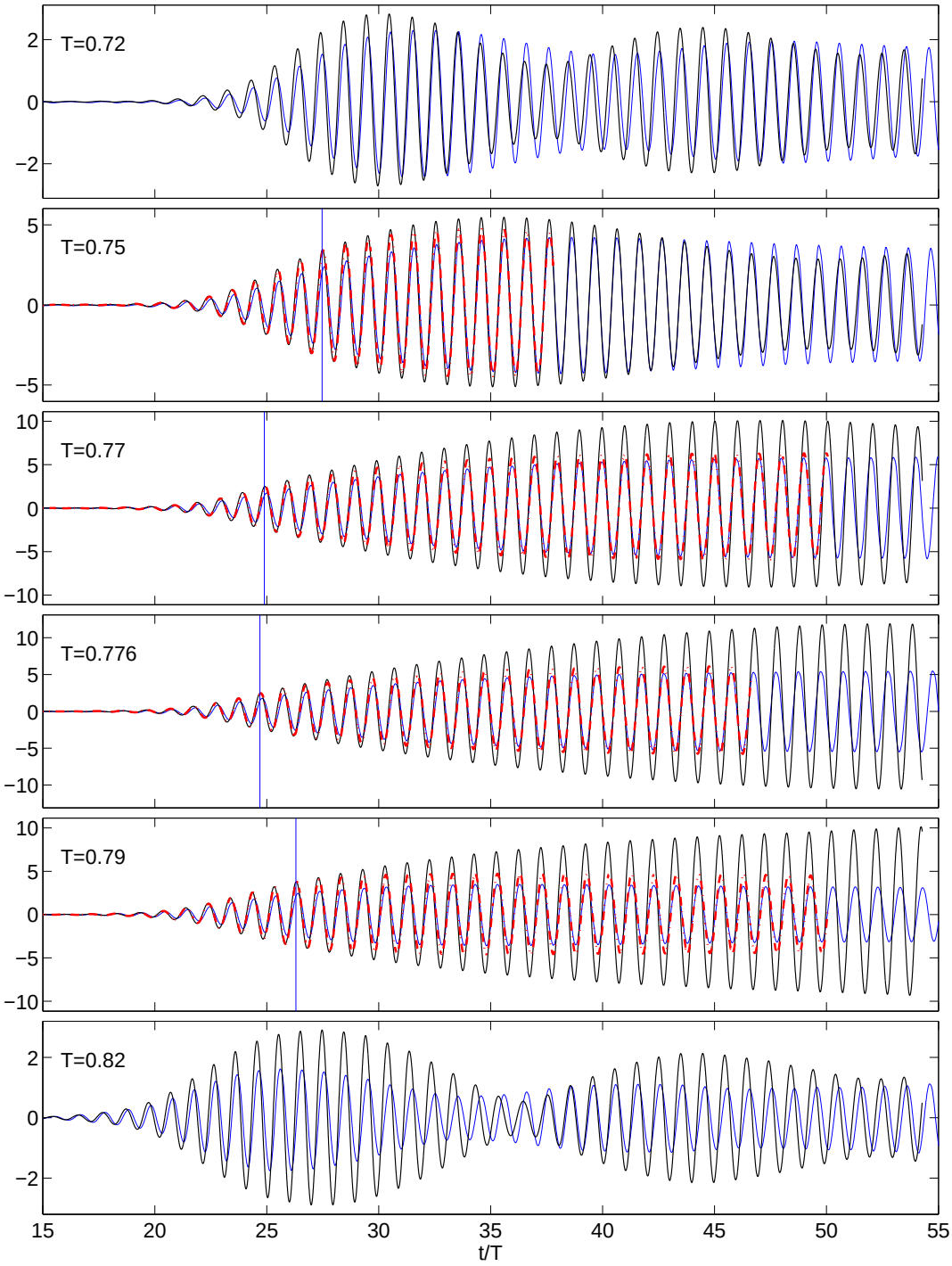

Figure F.5: Moored ship section study. Terminal gap time-series nondimensionalized by the incoming amplitude, ζ_g/A. Case A ($b/B = 0.2$) and wave steepness $\epsilon_1 \simeq 1/170$. Legend as in Figures 10.21 and 10.22. Vertical bar indicates initiation of the free shear layer.

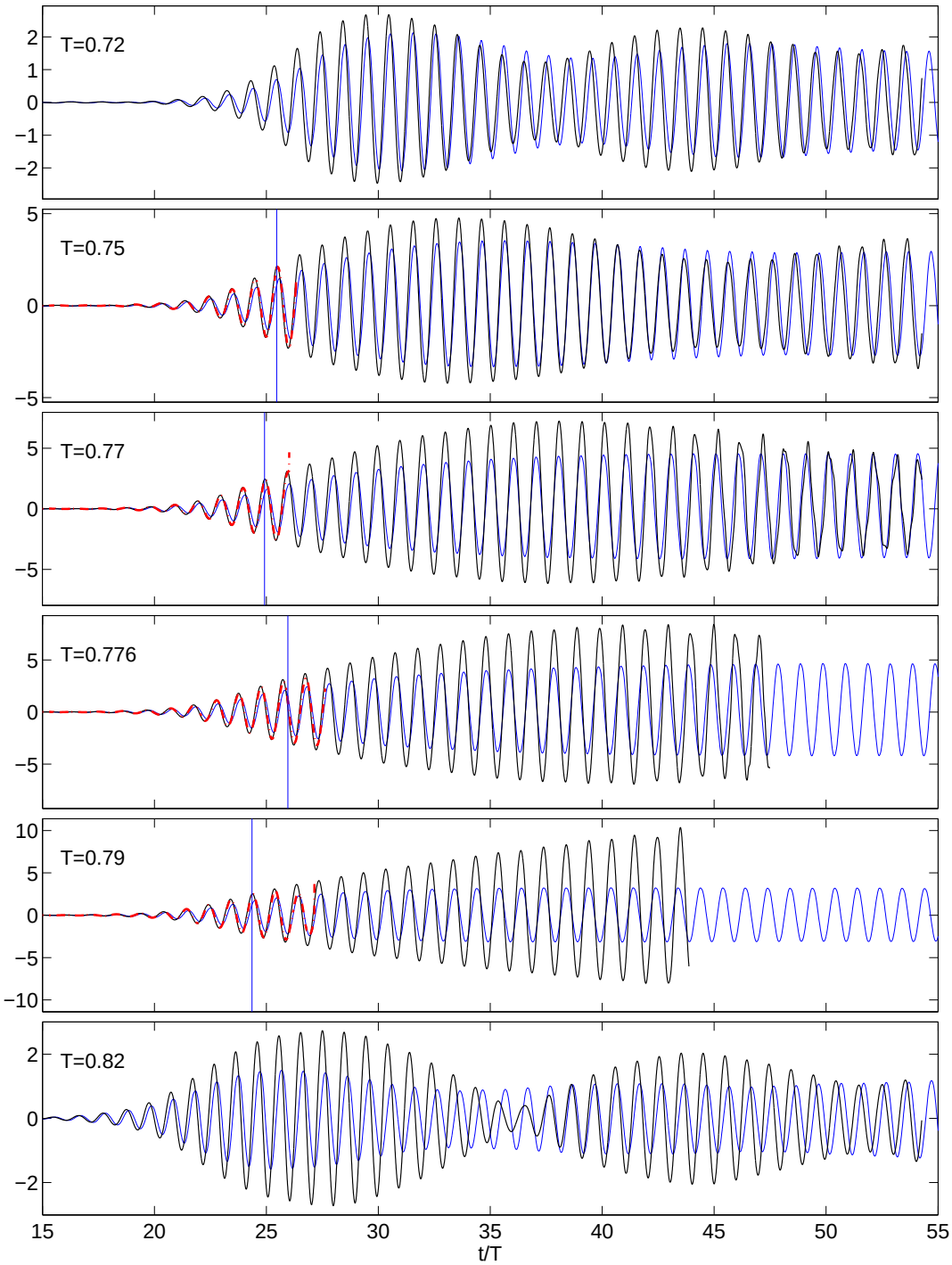

Figure F.6: Same as Figure F.5, but for wave steepness $\epsilon_2 \simeq 1/85$.

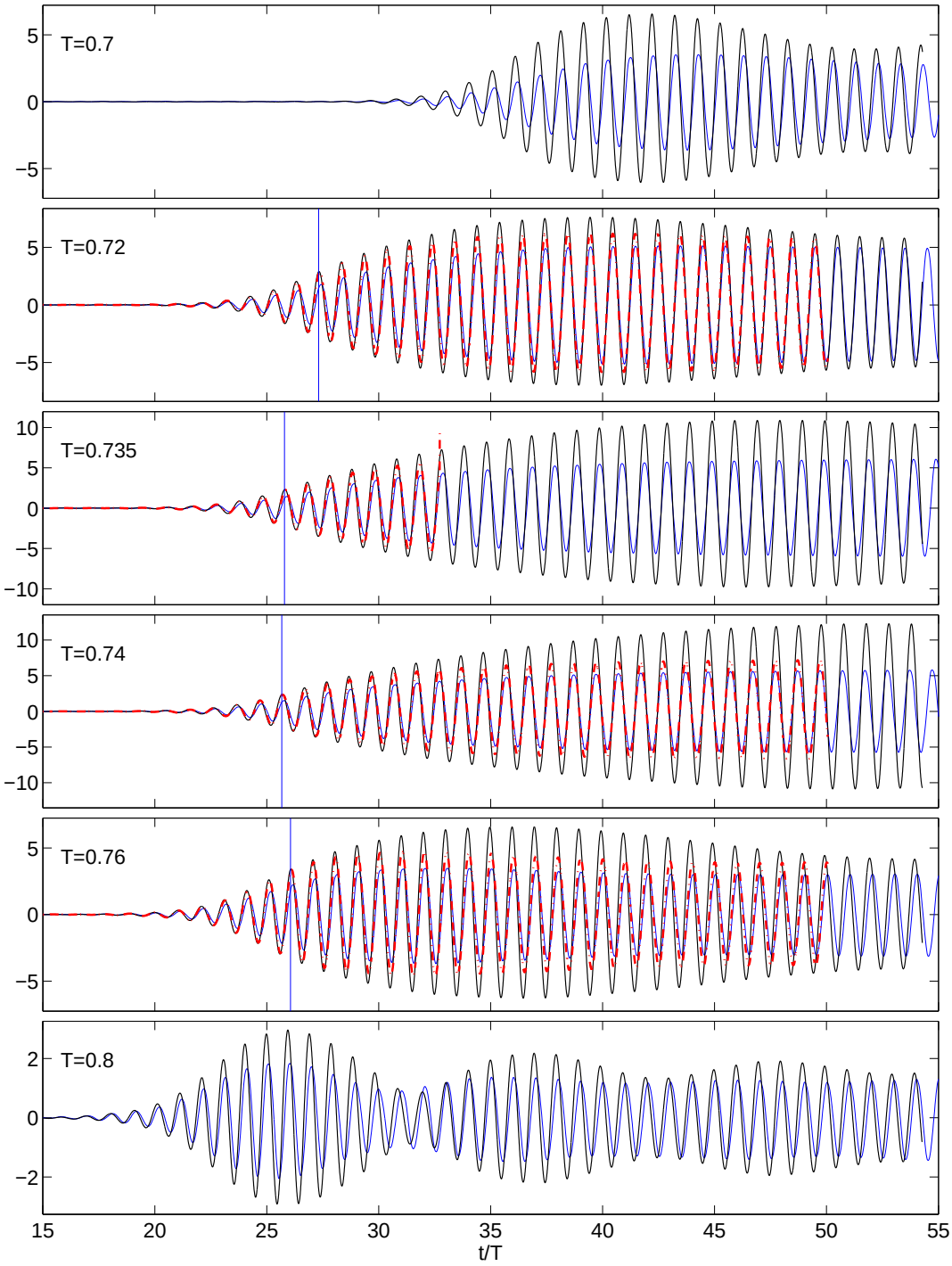

Figure F.7: Moored ship section study. Terminal gap time-series nondimensionalized by the incoming amplitude, ζ_g/A. Case B ($b/B = 0.15$) and wave steepness $\epsilon_1 \simeq 1/170$. Legend as in Figures 10.21 and 10.22. Vertical bar indicates initiation of the free shear layer.

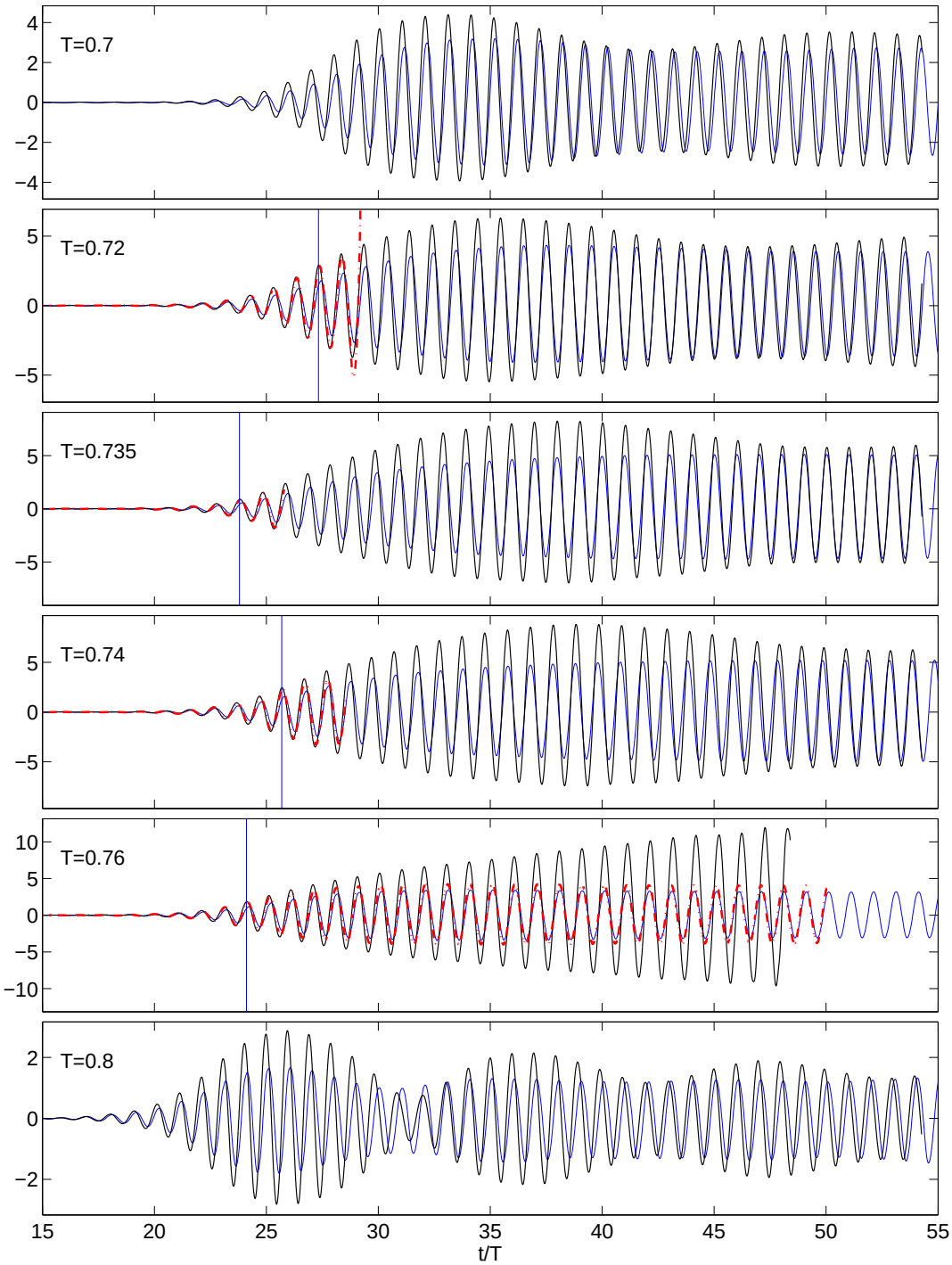

Figure F.8: Same as Figure F.7, but for wave steepness $\epsilon_2 \simeq 1/85$.

Previous reports published at the
Department of Marine Technology
(earlier: Faculty of Marine Technology)
Norwegian University of Science and Technology

UR-79-01 Brigt Hatlestad, MK:	The finite element method used in a fatigue evaluation of fixed offshore platforms. (Dr.Ing. Thesis)
UR-79-02 Erik Pettersen, MK:	Analysis and design of cellular structures. (Dr.Ing. Thesis)
UR-79-03 Sverre Valsgård, MK:	Finite difference and finite element methods applied to nonlinear analysis of plated structures. (Dr.Ing. Thesis)
UR-79-04 Nils T. Nordsve, MK:	Finite element collapse analysis of structural members considering imperfections and stresses due to fabrication. (Dr.Ing. Thesis)
UR-79-05 Ivar J. Fylling, MK:	Analysis of towline forces in ocean towing systems. (Dr.Ing. Thesis)
UR-80-06 Nils Sandsmark, MM:	Analysis of Stationary and Transient Heat Conduction by the Use of the Finite Element Method. (Dr.Ing. Thesis)
UR-80-09 Sverre Haver, MK:	Analysis of uncertainties related to the stochastic modelling of ocean waves. (Dr.Ing. Thesis)
UR-85-46 Alf G. Engseth, MK:	Finite element collapse analysis of tubular steel offshore structures. (Dr.Ing. Thesis)
UR-86-47 Dengody Sheshappa, MP:	A Computer Design Model for Optimizing Fishing Vessel Designs Based on Techno-Economic Analysis. (Dr.Ing. Thesis)
UR-86-48 Vidar Aanesland, MH:	A Theoretical and Numerical Study of Ship Wave Resistance. (Dr.Ing. Thesis)
UR-86-49 Heinz-Joachim Wessel, MK:	Fracture Mechanics Analysis of Crack Growth in Plate Girders. (Dr.Ing. Thesis)
UR-86-50 Jon Taby, MK:	Ultimate and Post-ultimate Strength of Dented Tubular Members. (Dr.Ing. Thesis)
UR-86-51 Walter Lian, MH:	A Numerical Study of Two-Dimensional

March. 2009, IMT

	Separated Flow Past Bluff Bodies at Moderate KC-Numbers. (Dr.Ing. Thesis)
UR-86-52 Bjørn Sortland, MH:	Force Measurements in Oscillating Flow on Ship Sections and Circular Cylinders in a U-Tube Water Tank. (Dr.Ing. Thesis)
UR-86-53 Kurt Strand, MM:	A System Dynamic Approach to One-dimensional Fluid Flow. (Dr.Ing. Thesis)
UR-86-54 Arne Edvin Løken, MH:	Three Dimensional Second Order Hydrodynamic Effects on Ocean Structures in Waves. (Dr.Ing. Thesis)
UR-86-55 Sigurd Falch, MH:	A Numerical Study of Slamming of Two-Dimensional Bodies. (Dr.Ing. Thesis)
UR-87-56 Arne Braathen, MH:	Application of a Vortex Tracking Method to the Prediction of Roll Damping of a Two-Dimension Floating Body. (Dr.Ing. Thesis)
UR-87-57 Bernt Leira, MR:	Gaussian Vector Processes for Reliability Analysis involving Wave-Induced Load Effects. (Dr.Ing. Thesis)
UR-87-58 Magnus Småvik, MM:	Thermal Load and Process Characteristics in a Two-Stroke Diesel Engine with Thermal Barriers (in Norwegian). (Dr.Ing. Thesis)
MTA-88-59 Bernt Arild Bremdal, MP:	An Investigation of Marine Installation Processes - A Knowledge - Based Planning Approach. (Dr.Ing. Thesis)
MTA-88-60 Xu Jun, MK:	Non-linear Dynamic Analysis of Space-framed Offshore Structures. (Dr.Ing. Thesis)
MTA-89-61 Gang Miao, MH:	Hydrodynamic Forces and Dynamic Responses of Circular Cylinders in Wave Zones. (Dr.Ing. Thesis)
MTA-89-62 Martin Greenhow, MH:	Linear and Non-Linear Studies of Waves and Floating Bodies. Part I and Part II. (Dr.Techn. Thesis)
MTA-89-63 Chang Li, MH:	Force Coefficients of Spheres and Cubes in Oscillatory Flow with and without Current. (Dr.Ing. Thesis)
MTA-89-64 Hu Ying, MP:	A Study of Marketing and Design in Development of Marine Transport Systems.

	(Dr.Ing. Thesis)
MTA-89-65 Arild Jæger, MH:	Seakeeping, Dynamic Stability and Performance of a Wedge Shaped Planing Hull. (Dr.Ing. Thesis)
MTA-89-66 Chan Siu Hung, MM:	The dynamic characteristics of tilting-pad bearings.
MTA-89-67 Kim Wikstrøm, MP:	Analysis av projekteringen for ett offshore projekt. (Licenciat-avhandling)
MTA-89-68 Jiao Guoyang, MR:	Reliability Analysis of Crack Growth under Random Loading, considering Model Updating. (Dr.Ing. Thesis)
MTA-89-69 Arnt Olufsen, MK:	Uncertainty and Reliability Analysis of Fixed Offshore Structures. (Dr.Ing. Thesis)
MTA-89-70 Wu Yu-Lin, MR:	System Reliability Analyses of Offshore Structures using improved Truss and Beam Models. (Dr.Ing. Thesis)
MTA-90-71 Jan Roger Hoff, MH:	Three-dimensional Green function of a vessel with forward speed in waves. (Dr.Ing. Thesis)
MTA-90-72 Rong Zhao, MH:	Slow-Drift Motions of a Moored Two-Dimensional Body in Irregular Waves. (Dr.Ing. Thesis)
MTA-90-73 Atle Minsaas, MP:	Economical Risk Analysis. (Dr.Ing. Thesis)
MTA-90-74 Knut-Aril Farnes, MK:	Long-term Statistics of Response in Non-linear Marine Structures. (Dr.Ing. Thesis)
MTA-90-75 Torbjørn Sotberg, MK:	Application of Reliability Methods for Safety Assessment of Submarine Pipelines. (Dr.Ing. Thesis)
MTA-90-76 Zeuthen, Steffen, MP:	SEAMAID. A computational model of the design process in a constraint-based logic programming environment. An example from the offshore domain. (Dr.Ing. Thesis)
MTA-91-77 Haagensen, Sven, MM:	Fuel Dependant Cyclic Variability in a Spark Ignition Engine - An Optical Approach. (Dr.Ing. Thesis)
MTA-91-78 Løland, Geir, MH:	Current forces on and flow through fish farms. (Dr.Ing. Thesis)

MTA-91-79 Hoen, Christopher, MK:	System Identification of Structures Excited by Stochastic Load Processes. (Dr.Ing. Thesis)
MTA-91-80 Haugen, Stein, MK:	Probabilistic Evaluation of Frequency of Collision between Ships and Offshore Platforms. (Dr.Ing. Thesis)
MTA-91-81 Sødahl, Nils, MK:	Methods for Design and Analysis of Flexible Risers. (Dr.Ing. Thesis)
MTA-91-82 Ormberg, Harald, MK:	Non-linear Response Analysis of Floating Fish Farm Systems. (Dr.Ing. Thesis)
MTA-91-83 Marley, Mark J., MK:	Time Variant Reliability under Fatigue Degradation. (Dr.Ing. Thesis)
MTA-91-84 Krokstad, Jørgen R., MH:	Second-order Loads in Multidirectional Seas. (Dr.Ing. Thesis)
MTA-91-85 Molteberg, Gunnar A., MM:	The Application of System Identification Techniques to Performance Monitoring of Four Stroke Turbocharged Diesel Engines. (Dr.Ing. Thesis)
MTA-92-86 Mørch, Hans Jørgen Bjelke, MH:	Aspects of Hydrofoil Design: with Emphasis on Hydrofoil Interaction in Calm Water. (Dr.Ing. Thesis)
MTA-92-87 Chan Siu Hung, MM:	Nonlinear Analysis of Rotordynamic Instabilities in High-speed Turbomachinery. (Dr.Ing. Thesis)
MTA-92-88 Bessason, Bjarni, MK:	Assessment of Earthquake Loading and Response of Seismically Isolated Bridges. (Dr.Ing. Thesis)
MTA-92-89 Langli, Geir, MP:	Improving Operational Safety through exploitation of Design Knowledge - an investigation of offshore platform safety. (Dr.Ing. Thesis)
MTA-92-90 Sævik, Svein, MK:	On Stresses and Fatigue in Flexible Pipes. (Dr.Ing. Thesis)
MTA-92-91 Ask, Tor Ø., MM:	Ignition and Flame Growth in Lean Gas-Air Mixtures. An Experimental Study with a Schlieren System. (Dr.Ing. Thesis)
MTA-86-92 Hessen, Gunnar, MK:	Fracture Mechanics Analysis of Stiffened

	Tubular Members. (Dr.Ing. Thesis)
MTA-93-93 Steinebach, Christian, MM:	Knowledge Based Systems for Diagnosis of Rotating Machinery. (Dr.Ing. Thesis)
MTA-93-94 Dalane, Jan Inge, MK:	System Reliability in Design and Maintenance of Fixed Offshore Structures. (Dr.Ing. Thesis)
MTA-93-95 Steen, Sverre, MH:	Cobblestone Effect on SES. (Dr.Ing. Thesis)
MTA-93-96 Karunakaran, Daniel, MK:	Nonlinear Dynamic Response and Reliability Analysis of Drag-dominated Offshore Platforms. (Dr.Ing. Thesis)
MTA-93-97 Hagen, Arnulf, MP:	The Framework of a Design Process Language. (Dr.Ing. Thesis)
MTA-93-98 Nordrik, Rune, MM:	Investigation of Spark Ignition and Autoignition in Methane and Air Using Computational Fluid Dynamics and Chemical Reaction Kinetics. A Numerical Study of Ignition Processes in Internal Combustion Engines. (Dr.Ing. Thesis)
MTA-94-99 Passano, Elizabeth, MK:	Efficient Analysis of Nonlinear Slender Marine Structures. (Dr.Ing. Thesis)
MTA-94-100 Kvålsvold, Jan, MH:	Hydroelastic Modelling of Wetdeck Slamming on Multihull Vessels. (Dr.Ing. Thesis)
MTA-94-102 Bech, Sidsel M., MK:	Experimental and Numerical Determination of Stiffness and Strength of GRP/PVC Sandwich Structures. (Dr.Ing. Thesis)
MTA-95-103 Paulsen, Hallvard, MM:	A Study of Transient Jet and Spray using a Schlieren Method and Digital Image Processing. (Dr.Ing. Thesis)
MTA-95-104 Hovde, Geir Olav, MK:	Fatigue and Overload Reliability of Offshore Structural Systems, Considering the Effect of Inspection and Repair. (Dr.Ing. Thesis)
MTA-95-105 Wang, Xiaozhi, MK:	Reliability Analysis of Production Ships with Emphasis on Load Combination and Ultimate Strength. (Dr.Ing. Thesis)
MTA-95-106 Ulstein, Tore, MH:	Nonlinear Effects of a Flexible Stern Seal Bag on Cobblestone Oscillations of an SES. (Dr.Ing. Thesis)
MTA-95-107 Solaas, Frøydis, MH:	Analytical and Numerical Studies of Sloshing in

	Tanks. (Dr.Ing. Thesis)
MTA-95-108 Hellan, øyvind, MK:	Nonlinear Pushover and Cyclic Analyses in Ultimate Limit State Design and Reassessment of Tubular Steel Offshore Structures. (Dr.Ing. Thesis)
MTA-95-109 Hermundstad, Ole A., MK:	Theoretical and Experimental Hydroelastic Analysis of High Speed Vessels. (Dr.Ing. Thesis)
MTA-96-110 Bratland, Anne K., MH:	Wave-Current Interaction Effects on Large-Volume Bodies in Water of Finite Depth. (Dr.Ing. Thesis)
MTA-96-111 Herfjord, Kjell, MH:	A Study of Two-dimensional Separated Flow by a Combination of the Finite Element Method and Navier-Stokes Equations. (Dr.Ing. Thesis)
MTA-96-112 Æsøy, Vilmar, MM:	Hot Surface Assisted Compression Ignition in a Direct Injection Natural Gas Engine. (Dr.Ing. Thesis)
MTA-96-113 Eknes, Monika L., MK:	Escalation Scenarios Initiated by Gas Explosions on Offshore Installations. (Dr.Ing. Thesis)
MTA-96-114 Erikstad, Stein O., MP:	A Decision Support Model for Preliminary Ship Design. (Dr.Ing. Thesis)
MTA-96-115 Pedersen, Egil, MH:	A Nautical Study of Towed Marine Seismic Streamer Cable Configurations. (Dr.Ing. Thesis)
MTA-97-116 Moksnes, Paul O., MM:	Modelling Two-Phase Thermo-Fluid Systems Using Bond Graphs. (Dr.Ing. Thesis)
MTA-97-117 Halse, Karl H., MK:	On Vortex Shedding and Prediction of Vortex-Induced Vibrations of Circular Cylinders. (Dr.Ing. Thesis)
MTA-97-118 Igland, Ragnar T., MK:	Reliability Analysis of Pipelines during Laying, considering Ultimate Strength under Combined Loads. (Dr.Ing. Thesis)
MTA-97-119 Pedersen, Hans-P., MP:	Levendefiskteknologi for fiskefartøy. (Dr.Ing. Thesis)
MTA-98-120 Vikestad, Kyrre, MK:	Multi-Frequency Response of a Cylinder Subjected to Vortex Shedding and Support Motions. (Dr.Ing. Thesis)

MTA-98-121 Azadi, Mohammad R. E., MK:	Analysis of Static and Dynamic Pile-Soil-Jacket Behaviour. (Dr.Ing. Thesis)
MTA-98-122 Ulltang, Terje, MP:	A Communication Model for Product Information. (Dr.Ing. Thesis)
MTA-98-123 Torbergsen, Erik, MM:	Impeller/Diffuser Interaction Forces in Centrifugal Pumps. (Dr.Ing. Thesis)
MTA-98-124 Hansen, Edmond, MH:	A Discrete Element Model to Study Marginal Ice Zone Dynamics and the Behaviour of Vessels Moored in Broken Ice. (Dr.Ing. Thesis)
MTA-98-125 Videiro, Paulo M., MK:	Reliability Based Design of Marine Structures. (Dr.Ing. Thesis)
MTA-99-126 Mainçon, Philippe, MK:	Fatigue Reliability of Long Welds Application to Titanium Risers. (Dr.Ing. Thesis)
MTA-99-127 Haugen, Elin M., MH:	Hydroelastic Analysis of Slamming on Stiffened Plates with Application to Catamaran Wetdecks. (Dr.Ing. Thesis)
MTA-99-128 Langhelle, Nina K., MK:	Experimental Validation and Calibration of Nonlinear Finite Element Models for Use in Design of Aluminium Structures Exposed to Fire. (Dr.Ing. Thesis)
MTA-99-129 Berstad, Are J., MK:	Calculation of Fatigue Damage in Ship Structures. (Dr.Ing. Thesis)
MTA-99-130 Andersen, Trond M., MM:	Short Term Maintenance Planning. (Dr.Ing. Thesis)
MTA-99-131 Tveiten, Bård Wathne, MK:	Fatigue Assessment of Welded Aluminium Ship Details. (Dr.Ing. Thesis)
MTA-99-132 Søreide, Fredrik, MP:	Applications of underwater technology in deep water archaeology. Principles and practice. (Dr.Ing. Thesis)
MTA-99-133 Tønnessen, Rune, MH:	A Finite Element Method Applied to Unsteady Viscous Flow Around 2D Blunt Bodies With Sharp Corners. (Dr.Ing. Thesis)
MTA-99-134 Elvekrok, Dag R., MP:	Engineering Integration in Field Development Projects in the Norwegian Oil and Gas Industry. The Supplier Management of Norne. (Dr.Ing. Thesis)

MTA-99-135 Fagerholt, Kjetil, MP:	Optimeringsbaserte Metoder for Ruteplanlegging innen skipsfart. (Dr.Ing. Thesis)
MTA-99-136 Bysveen, Marie, MM:	Visualization in Two Directions on a Dynamic Combustion Rig for Studies of Fuel Quality. (Dr.Ing. Thesis)
MTA-2000-137 Storteig, Eskild, MM:	Dynamic characteristics and leakage performance of liquid annular seals in centrifugal pumps. (Dr.Ing. Thesis)
MTA-2000-138 Sagli, Gro, MK:	Model uncertainty and simplified estimates of long term extremes of hull girder loads in ships. (Dr.Ing. Thesis)
MTA-2000-139 Tronstad, Harald, MK:	Nonlinear analysis and design of cable net structures like fishing gear based on the finite element method. (Dr.Ing. Thesis)
MTA-2000-140 Kroneberg, André, MP:	Innovation in shipping by using scenarios. (Dr.Ing. Thesis)
MTA-2000-141 Haslum, Herbjørn Alf, MH:	Simplified methods applied to nonlinear motion of spar platforms. (Dr.Ing. Thesis)
MTA-2001-142 Samdal, Ole Johan, MM:	Modelling of Degradation Mechanisms and Stressor Interaction on Static Mechanical Equipment Residual Lifetime. (Dr.Ing. Thesis)
MTA-2001-143 Baarholm, Rolf Jarle, MH:	Theoretical and experimental studies of wave impact underneath decks of offshore platforms. (Dr.Ing. Thesis)
MTA-2001-144 Wang, Lihua, MK:	Probabilistic Analysis of Nonlinear Wave-induced Loads on Ships. (Dr.Ing. Thesis)
MTA-2001-145 Kristensen, Odd H. Holt, MK:	Ultimate Capacity of Aluminium Plates under Multiple Loads, Considering HAZ Properties. (Dr.Ing. Thesis)
MTA-2001-146 Greco, Marilena, MH:	A Two-Dimensional Study of Green-Water Loading. (Dr.Ing. Thesis)
MTA-2001-147 Heggelund, Svein E., MK:	Calculation of Global Design Loads and Load Effects in Large High Speed Catamarans. (Dr.Ing. Thesis)
MTA-2001-148 Babalola, Olusegun T., MK:	Fatigue Strength of Titanium Risers - Defect

	Sensitivity. (Dr.Ing. Thesis)
MTA-2001-149 Mohammed, Abuu K., MK:	Nonlinear Shell Finite Elements for Ultimate Strength and Collapse Analysis of Ship Structures. (Dr.Ing. Thesis)
MTA-2002-150 Holmedal, Lars E., MH:	Wave-current interactions in the vicinity of the sea bed. (Dr.Ing. Thesis)
MTA-2002-151 Rognebakke, Olav F., MH:	Sloshing in rectangular tanks and interaction with ship motions. (Dr.Ing. Thesis)
MTA-2002-152 Lader, Pål Furset, MH:	Geometry and Kinematics of Breaking Waves. (Dr.Ing. Thesis)
MTA-2002-153 Yang, Qinzheng, MH:	Wash and wave resistance of ships in finite water depth. (Dr.Ing. Thesis)
MTA-2002-154 Melhus, Øyvin, MM:	Utilization of VOC in Diesel Engines. Ignition and combustion of VOC released by crude oil tankers. (Dr.Ing. Thesis)
MTA-2002-155 Ronæss, Marit, MH:	Wave Induced Motions of Two Ships Advancing on Parallel Course. (Dr.Ing. Thesis)
MTA-2002-156 Økland, Ole D., MK:	Numerical and experimental investigation of whipping in twin hull vessels exposed to severe wet deck slamming. (Dr.Ing. Thesis)
MTA-2002-157 Ge, Chunhua, MK:	Global Hydroelastic Response of Catamarans due to Wet Deck Slamming. (Dr.Ing. Thesis)
MTA-2002-158 Byklum, Eirik, MK:	Nonlinear Shell Finite Elements for Ultimate Strength and Collapse Analysis of Ship Structures. (Dr.Ing. Thesis)
IMT-2003-1 Chen, Haibo, MK:	Probabilistic Evaluation of FPSO-Tanker Collision in Tandem Offloading Operation. (Dr.Ing. Thesis)
IMT-2003-2 Skaugset, Kjetil Bjørn, MK:	On the Suppression of Vortex Induced Vibrations of Circular Cylinders by Radial Water Jets. (Dr.Ing. Thesis)
IMT-2003-3 Chezhian, Muthu	Three-Dimensional Analysis of Slamming. (Dr.Ing. Thesis)
IMT-2003-4 Buhaug, Øyvind	Deposit Formation on Cylinder Liner Surfaces in Medium Speed Engines. (Dr.Ing. Thesis)

IMT-2003-5 Tregde, Vidar	Aspects of Ship Design: Optimization of Aft Hull with Inverse Geometry Design. (Dr.Ing. Thesis)
IMT-2003-6 Wist, Hanne Therese	Statistical Properties of Successive Ocean Wave Parameters. (Dr.Ing. Thesis)
IMT-2004-7 Ransau, Samuel	Numerical Methods for Flows with Evolving Interfaces. (Dr.Ing. Thesis)
IMT-2004-8 Soma, Torkel	Blue-Chip or Sub-Standard. A data interrogation approach of identity safety characteristics of shipping organization. (Dr.Ing. Thesis)
IMT-2004-9 Ersdal, Svein	An experimental study of hydrodynamic forces on cylinders and cables in near axial flow. (Dr.Ing. Thesis)
IMT-2005-10 Brodtkorb, Per Andreas	The Probability of Occurrence of Dangerous Wave Situations at Sea. (Dr.Ing. Thesis)
IMT-2005-11 Yttervik, Rune	Ocean current variability in relation to offshore engineering. (Dr.Ing. Thesis)
IMT-2005-12 Fredheim, Arne	Current Forces on Net-Structures. (Dr.Ing. Thesis)
IMT-2005-13 Heggernes, Kjetil	Flow around marine structures. (Dr.Ing. Thesis)
IMT-2005-14 Fouques, Sebastien	Lagrangian Modelling of Ocean Surface Waves and Synthetic Aperture Radar Wave Measurements. (Dr.Ing. Thesis)
IMT-2006-15 Holm, Håvard	Numerical calculation of viscous free surface flow around marine structures. (Dr.Ing. Thesis)
IMT-2006-16 Bjørheim, Lars G.	Failure Assessment of Long Through Thickness Fatigue Cracks in Ship Hulls. (Dr.Ing. Thesis)
IMT-2006-17 Hansson, Lisbeth	Safety Management for Prevention of Occupational Accidents. (Dr.Ing. Thesis)
IMT-2006-18 Zhu, Xinying	Application of the CIP Method to Strongly Nonlinear Wave-Body Interaction Problems. (Dr.Ing. Thesis)
IMT-2006-19 Reite, Karl Johan	Modelling and Control of Trawl Systems. (Dr.Ing. Thesis)

IMT-2006-20 Smogeli, Øyvind Notland	Control of Marine Propellers. From Normal to Extreme Conditions. (Dr.Ing. Thesis)
IMT-2007-21 Storhaug, Gaute	Experimental Investigation of Wave Induced Vibrations and Their Effect on the Fatigue Loading of Ships. (Dr.Ing. Thesis)
IMT-2007-22 Sun, Hui	A Boundary Element Method Applied to Strongly Nonlinear Wave-Body Interaction Problems. (PhD Thesis, CeSOS)
IMT-2007-23 Rustad, Anne Marthine	Modelling and Control of Top Tensioned Risers. (PhD Thesis, CeSOS)
IMT-2007-24 Johansen, Vegar	Modelling flexible slender system for real-time simulations and control applications.
IMT-2007-25 Wroldsen, Anders Sunde	Modelling and control of tensegrity structures. (PhD Thesis, CeSOS)
IMT-2007-26 Aronsen, Kristoffer Høye	An experimental investigation of in-line and combined in-line and cross flow vortex induced vibrations. (Dr.Ing.Thesis, IMT)
IMT-2007-27 Zhen, Gao	Stochastic response analysis of mooring systems with emphasis on frequency-domain analysis of fatgue due to wide-band processes. (PhD Thesis CeSOS)
IMT-2007-28 Thorstensen, Tom Anders	Lifetime Profit Modelling of Ageing Systems Utilizing Information about Technical Condition. (Dr.ing. Thesis, IMT.)
IMT-2008-29 Berntsen, Per Ivar B.	Structural Reliability Based Position Mooring. (PhD Thesis, IMT)
IMT-2008-30 Ye, Naiquan	Fatigues Assessment of Aluminium Welded Box stiffener Joints in ships. (Dr.Ing. Thesis, IMT)
IMT-2008-31 Radan, Damir	Integrated Control of Marine Electrical Power Systems. (PhD Thesis, IMT)
IMT-2008-32 Norum, Viggo L.	Analysis of Ignituin and Combustion in Otto Lean-Burn Engines with Prechambers. (Dr.Ing. Thesis, IMT)
IMT-2008-33 Pákozdi, Csaba	A Smoothed Particle Hydrodynamics Study of Two-dimensional Nonlinear Sloshing in Rectangular Tanks. (Dr.Ing. Thesis, IMT)

IMT-2008-34 Grytøyr, Guttorm	A Higher-Order Boundary Element Method and Applications to Marine Hydrodynamics. (Dr.ing. Thesis, IMT)
IMT-2008-35 Drummen, Ingo	Experimental and Numerical Investigation of Nonlinear Wave-Induced Load effects in Containerships Considering Hydroelasticity. (PhD Thesis, CeSOS)
IMT-2008-36 Skejic, Renato	Maneuvering and Seakeeping of a Singel Ship and of Two Ships in Interaction. (PhD Thesis, CeSOS)
IMT-2008-37 Harlem, Alf	An Age-Based Replacement Model for Repairable Systems with Attention to High-Speed Marine Diesel Engines. (PhD Thesis, IMT)
IMT-2008-38 Alsos, Hagbart S.	Ship Grounding. Analysis of Ductile Fracture, Bottom Damage and Hull Girder Response. (PhD Thesis, IMT)
IMT-2008-39 Graczyk, Mateusz	Experimental Investigation of Sloshing Loading and Load Effects in Membrane LNG Tanks Subjected to Random Excitation. (PhD Thesis, CeSOS)
IMT-2008-40 Taghipour, Reza	Efficient Prediction of Dynamic Response for Flexible amd Multi-body Marine Structures. (PhD Thesis, CeSOS)
IMT-2008-41 Ruth, Eivind	Propulsion Control and Thrust Allocation on Marine Vessels. (PhD Thesis, CeSOS)
IMT-2008-42 Nystad, Bent Helge	Technical Condition Indexes and Remaining Useful Life of Aggregated Systems. (PhD Thesis, IMT)
IMT-2008-43 Soni, Prashant Kumer	Hydrodyynamic Coefficients for Vortex Induced Vibrations of Flexible Beams, (PhD Thesis, CeSOS)
IMT-2009-43 Amlashi, Hadi K.K.	Ultimate Strength and Reliability-based Design of Ship Hulls with Emphasis on Combined Global and Local Loads. (PhD Thesis, IMT)
IMT-2009-44 Pedersen, Tom Arne	Bond Graph Modelling of Marine Power Systems. (PhD Thesis, IMT)